Out-of-equilibrium dynamics of open quantum many-body systems

vorgelegt von
Leon Janek Droenner, M. Sc.
geb. in Achim

von der Fakultät II – Mathematik und Naturwissenschaften
der Technischen Universität Berlin
zur Erlangung des akademischen Grades
Doktor der Naturwissenschaften
– Dr. rer. nat. –

genehmigte Dissertation

Berlin, 2019

Abstract

Many-body localization, which prevents a many-body quantum systems from reaching thermal equilibrium has opened the possibility to study out-of-equilibrium dynamics of isolated quantum systems, leading to new phases of matter such as the discrete time crystal. However, little is known about these effects when the quantum many-body system is coupled to an external environment. An intuitive assumption is that out-of-equilibrium dynamics and quantum coherences would not survive due to thermalization with external degrees of freedom. The present work focuses on open quantum many-body systems and aims at the question how an external reservoir can preserve such out-of-equilibrium effects. In the first part, common generic reservoirs are assumed to focus on many-body effects of the systems of interest.

As a first many-body system, an optically driven many-emitter phonon laser is investigated. The full quantum mechanical treatment reveals additional resonances caused by collective effects of the many-emitter setup. Optically addressing these resonances results in an enhancement of phonon intensities within the acoustic cavity.

The Heisenberg spin-chain has achieved the role of a standard model to study many-body localization. As a second many-body system, the model is generalized to an open quantum system via boundary reservoirs which are driving the system out-of equilibrium and a spin-current is induced. When driven far from equilibrium, the transport is very much dependent on the external reservoirs. In contrast, it is demonstrated that a setup with long-range coupling between the spins shows transport behavior independent of the external environment.

In the second part of this work, the coupling to the reservoir is structured by assuming a boundary condition. Experimentally this is achieved by placing a distant mirror close to the system. A common Born-Markov approximation leading to factorizing system and reservoir states is insufficient to describe these feedback dynamics. In this work, an approach is used to treat the reservoir states as part of the many-body system which is based on matrix product states using the quantum stochastic Schrödinger equation.

Focusing on the reservoir statistics of a single two-level system, it is demonstrated that by combining time-dependent optical excitation with time-delayed feedback via structuring the reservoir, individual photon probabilities are controlled by changing external degrees of freedom.

Finally, this method is generalized to a many-body system including a coupling to an external reservoir beyond Born-Markov approximation. It is shown that feedback dynamics stabilize a discrete time crystal against dissipation to the environment. Out-of-equilibrium dynamics and many-body localization of the discrete time crystal survive for long times even in the presence of an external environment and become independent of the coupling to the reservoir. The developed method benefits from small entanglement entropy of the many-body localized system as well as from a suppression of entanglement between system and reservoir due to the feedback dynamics. This allows to consider up to forty spins with individual structured reservoirs in a numerically exact manner.

Kurzfassung

Das Verständnis von Lokalisierung in Vielteilchensystemen unter Berücksichtigung von Wechselwirkungen hat neue Möglichkeiten eröffnet, insbesondere die Erforschung von Nichtgleichgewichtsdynamiken in isolierten Quantensystemen. Dies hat zur Entdeckung neuer Nichtgleichgewichtsphasen, wie zum Beispiel den diskreten Zeitkristall, geführt.

Wenn das Vielteilchensystem mit einem externen Reservoir wechselwirkt, ist wenig bekannt darüber, ob etwaige Nichtgleichgewichtszustände erhalten bleiben. Eine intuitive Annahme wäre, dass Nichtgleichgewichtszustände und Quantenkohärenzen durch Thermalisierung mit externen Freiheitsgraden zerstört werden. Diese Arbeit berücksichtigt offene quantenmechanische Vielteilchensysteme und zielt darauf ab, Nichtgleichgewichtszustände unter Berücksichtigung von externen Reservoirs zu untersuchen.

Der erste Teil dieser Arbeit berücksichtigt einfache allgemeine Reservoirs, um genauer auf Vielteilcheneffekte im jeweiligen System einzugehen.

Ein Phononlaser, bestehend aus mehreren Emittern als aktives Medium, wird als erstes Vielteilchensystem untersucht. Eine voll quantenmechanische Beschreibung weist kollektive Effekte auf, welche zusätzliche optisch adressierbare Resonanzen hervorrufen. Durch optische Anregung dieser kollektiven Resonanzen, werden die erreichbaren Phonon-Intensitäten innerhalb des akustischen Resonators deutlich verbessert.

Die Heisenberg Spin-Kette ist ein bekanntes Modell, welches zur Beschreibung von Vielteilchenlokalisierung herangezogen wird. Als zweites untersuchtes Vielteilchensystem wird dieses Modell zu einem offenen Quantensystem verallgemeinert. Durch zwei Nichtgleichgewichts-Reservoirs an den Rändern der Kette wird ein Strom durch Spin-flips induziert. Im starken Nichtgleichgewicht ist der Transport abhängig von den Eigenschaften der externen Reservoirs. Dies ist nicht der Fall bei einer langreichweitigen Wechselwirkung zwischen den Spins, welche den Transport unabhängig von den Reservoir Parametern werden lässt.

Im zweiten Teil der Arbeit wird eine Randbedingung in der Kopplung ans Reservoir berücksichtigt. Dies kann experimentell zum Beispiel durch einen Spiegel realisiert werden. Das hat zur Folge, dass eine allgemeine Beschreibung des Reservoirs durch eine Born-Markov-Näherung nicht mehr durchgeführt werden kann, da für Rückkopplungseffekte ein Gedächtnis des Reservoirs angenommen werden muss. In dieser Arbeit wird das Reservoir innerhalb des Vielteilchenproblems beschrieben, basierend auf Matrix-Produkt-Zuständen und der Quantenstochastischen Schrödinger Gleichung. Mit Blick auf die Reservoirstatistik eines einzelnen Zweiniveausystems wird gezeigt, dass durch die Kombination von zeitabhängiger Anregung mit zeitverzögerter Rückkopplung einzelne Photonwahrscheinlichkeiten durch externe Kontrollparameter manipuliert werden.

Im letzten Teil wird diese Methode auf ein Vielteilchensystem verallgemeinert. Es wird gezeigt, dass Rückkopplungsdynamik einen Zeitkristall gegenüber Dissipation ins Reservoir stabilisiert. Nichtgleichgewichtszustände und Vielteilchenlokalisierung bleiben für lange Zeit erhalten, auch mit Ankopplung an externe Reservoirs. Die diskreten Oszillationen

des Zeitkristalls werden unabhängig von der Kopplung ans Reservoir. Die entwickelte Methode profitiert sowohl von kleiner Verschränkungsentropie des lokalisierten Vielteilchensystems, als auch von einer Unterdrückung der Verschränkung mit dem Reservoir durch zeitverzögerte Rückkopplung. Diese Kombination erlaubt eine Untersuchung von bis zu vierzig Spins mit individuellen strukturierten Reservoirs innerhalb einer numerisch exakten Beschreibung.

Contents

1.

Introduction

1.1. Motivation

Recent progress in experimental realizations of quantum simulators has enabled the possibility to study many-body quantum systems in an almost isolated and well controllable setup. In optical lattice systems, an ultra cold gas of atoms is loaded into the lattice potentials and the interactions between the atoms is manipulated by external controllable lasers [1, 2]. Another approach is to use trapped ions, where interactions between the sites are engineered via state-dependent optical dipole forces [3, 4]. The advantages of these experiments is that they open up the possibility to study out-of-equilibrium dynamics of many-body quantum systems [5, 6]. In solid-state setups, the loss of quantum coherences destroys most out-of-equilibrium effects on a comparable short time-scale [7, 8, 9]. One of the main reasons is pure dephasing resulting from phonon interactions. Due to the well controlled setup in optical lattices and trapped ions, decoherence is strongly suppressed. This leads to possible devices for quantum information protocols for quantum computation [10, 11].

However, even if a many-body quantum system is well isolated from the external environment it acts as its own heat bath for small subsystems as, e.g., a single spin. This leads to a thermalization of the subsystems with the rest of the many-body system [12, 13]. This implies that quantum information of local subsystems becomes highly non-local which is described by the spreading of entanglement entropy [14]. This process is called quantum thermalization, where expectation values of local observables become thermal in the long time limit, meaning that local observables are described by a thermodynamic ensemble. This process is described by the Eigenstate thermalization hypothesis which states that if thermalization occurs for some local Eigenstates, all local Eigenstates would become thermal [15]. The Eigenstate thermalization hypothesis is often referred to as quantum ergodicity hypothesis in analogy to the classical ergodicity hypothesis which states that a thermalizing system explores the whole phase space [16].

For the purpose of quantum information, thermalization of local observables is an unwanted process as it is equivalent to the loss of information about the initial state, which is fundamental for quantum computation protocols [17]. The question arises, how the process of thermalization can be prevented to preserve information about the initial state. A prominent example for the breaking of ergodicity is Anderson localization [18]. Originally investigated for a solid-state setup, Anderson found that disordered lattice potentials lead to the localization of particles at certain lattice positions. Disorder occurs naturally in solid-state systems due to impurities which deform the lattice potential. The scattering of particles on the deformed potentials leads to interference effects which localize the particle. This means when being localized, the initial information about the position of the particle is preserved which is in contrast to a thermalization process.

However, it was long believed that any interaction between particles would destroy this localization behavior [19]. The breakthrough discovery of localization for interacting systems, called many-body localization, opened a new field of present research [20, 21]. In contrast to Anderson localization, the entanglement entropy in many-body localized systems grows logarithmically as a function of time [22, 23]. This area-law scaling of entanglement [24] stands in strong contrast to the volume-law scaling of thermalizing systems [14, 16]. Thus, a many-body localized system provides a platform where initial conditions are preserved for long times even when information is exchanged between the local subsystems, making it a promising device for quantum memory storage.

From a theoretical point of view, the computation of many-body systems is very challenging as the number of states of the Hilbert space grows exponentially with the system size. The development of matrix product states [25] based on the powerful density matrix renormalization group methods [26] for the investigation of ground states provides a tool to explore larger system sizes in finding hints for the behavior in the thermodynamical limit. However, when simulating time evolution with matrix product states, it is limited to very small times due to the build up of entanglement entropy between local subsystems [27, 28]. The matrix product state method is based on the truncation of the Hilbert space, the idea is to truncate all states of the many-body system which are not relevant for the system dynamics. Thus, all states which are not entangled with relevant states for the dynamics are truncated [29]. The discovery of many-body localization opened up the possibility to explore much larger system sizes and/or times with matrix product state methods due to the strong suppression of entanglement growth [22, 23, 30].

Many-body localized systems allow to study out-of-equilibrium dynamics on long time-scales both theoretically [14, 30] and experimentally [31, 32, 33, 34] as ergodicity is broken due to the violation of the Eigenstate thermalization hypothesis. This is even true for systems which are periodically driven out-of-equilibrium with external lasers [35, 36, 37]. Without many-body localization the system would absorb the energy of the drive, resulting in thermal equilibrium [38, 39]. This was followed by the discovery of new phases of matter such as the discrete time crystal, where a many-body system breaks the time reversal symmetry of the governing Hamiltonian and returns back to its initial state after discrete periods [40, 41]. Time reversal symmetry breaking has recently been demonstrated experimentally on different platforms [42, 43, 44, 45].

Despite its success in many different areas, it is still under debate which aspects of many-body localization survive in case of open quantum systems [46, 47, 48, 49, 34]. Even when the system itself is many-body localized, interactions with external degrees of freedom naturally lead to decoherence and loss of initial information [50]. This is especially true for the common description of open quantum systems, where a Born-Markov approximation allows to formulate a trace-preserving Lindblad master equation [51].

The question of the suppression of decoherence is not only relevant for many-body localization, but also for any experimental setup and goes as far as fundamental quantum physics itself, because any measurement process is an interaction with external degrees of freedom [52, 53]. This is also true for the above mentioned experiments which are very well isolated from external environments.

The aim of this thesis is to formulate a theory based on matrix product state methods for open quantum many-body systems which can describe reservoirs beyond Born-Markov approximation [54]. The idea is to tailor the external environment such that decoherence is suppressed. This can be seen as a suppression of entanglement between states of the

system and states of the reservoir in analogy to many-body localization which suppresses entanglement growth within the many-body system itself.

1.2. Structure of the thesis

This thesis is divided into three parts. Part I describes the theoretical and phenomenological framework which is used in the following two parts. Part II focuses on many-body effects of two different systems with factorizing system-reservoir dynamics, which is describe by the common Lindblad formalism. In Part III, reservoirs beyond the Lindblad formalism are investigated without performing a Born-Markov approximation, describing entangled system-reservoir dynamics.

In chapter 2, the basic theoretical framework is introduced. In particular, the Hamiltonian for a two-level system interacting with an external mode continuum is derived, based on the Maxwell equations and the Lorentz force.

In chapter 3, the quantum stochastic Schrödinger equation is introduced. This formalism is especially relevant for Part III to describe entangled system-reservoir interactions. Furthermore, the Lindblad formalism is derived from the quantum stochastic Schrödinger equation which is used for Part II of this thesis.

In chapter 4, a phenomenological introduction to quantum ergodicity and many-body localization is given, which will be especially relevant for chapter 6 and chapter 9.

As a first many-body system, the many-emitter phonon laser is investigated in chapter 5, based on factorizing system-reservoir interactions via the Lindblad formalism. The focus lies on collective effects of the many-emitter setup.

The transport within the ergodic phase of the Heisenberg spin-chain is investigated in chapter 6. This is the most standard model to describe many-body-localization. The system is coupled to two boundary reservoirs, described by the Lindblad formalism, which induce an out-of-equilibrium situation. The focus lies on effects induced by the external reservoirs.

Matrix product states are introduced in chapter 7 as all computations in Part III are based on the matrix product state formalism.

As a first example, a single two-level system in front of a mirror is investigated in chapter 8. The self-feedback renders a description based on Lindblad dynamics impossible. This is why the surrounding reservoir is considered as a many-body problem, to describe it via matrix product states based on the quantum stochastic Schrödinger formalism. It will be shown that the reservoir statistics are controlled by external achievable parameters.

This formalism is generalized to a many-body system in chapter 9. An efficient algorithm is developed to stabilize a discrete time crystal against dissipation. The formalism based on matrix product states and the stochastic Schrödinger equation allows to consider efficiently a large system size together with a structured reservoir. Final remarks and an outlook conclude this thesis in chapter 10.

PART I

Theoretical background

2.

Basics

2.1. Quantum mechanics in the Schrödinger picture

The fundamental difference of quantum mechanics in contrast to classical mechanics lies in the description of systems via a probability distribution and the quantization of states. This implies that a theorist can well describe the probability of states of a given system but never predict with certainty the output of a single measurement. The probability distribution $\rho = |\psi\rangle\langle\psi|$ of a given system is described by its wavefunction $|\psi\rangle$, where

$$|\psi\rangle = \sum_i c_i |i\rangle \tag{2.1.1}$$

consists of a superposition of all possible states. The coefficients c_i describe the probability of the basis state $|i\rangle$.

Probably the most famous example of the superposition principle with a correctly determined probability distribution but uncertain result in a simple measurement process is Schrödinger's cat. The cat is put into a closed box with a mechanism which breaks a vial of poison with a probability of 50%. The system of the cat consists of two states where the cat is found dead in the state $|0\rangle$ with probability $|c_0|^2 = 1/2$ or found alive in the state $|1\rangle$ with probability $|c_1|^2 = 1/2$. The physicist as external observer does not know if the cat is alive or dead before opening the box, but he knows well that he will be sadly finding the cat dead with probability $|c_0|^2 = 1/2$. Before opening the box, to him, the cat is both dead and alive at the same time. Opening the box is a measurement process where the Hermitian operator $\hat{O}$ measures the state of the cat

$$\langle \hat{O} \rangle = \langle \psi | \hat{O} | \psi \rangle \ . \tag{2.1.2}$$

In the Copenhagen interpretation of quantum mechanics, this measurement process results in a collapse of the wavefunction to either the state $|0\rangle$ or $|1\rangle$ and the cat remains either dead or alive after opening the box.

How does the physicist know the probability distribution before opening the box? The answer to that lies in the Schrödinger equation. By solving the Eigenvalue problem of the time-dependent Schrödinger equation

$$i\hbar\partial_t|\psi(t)\rangle = \mathcal{H}|\psi(t)\rangle \ , \tag{2.1.3}$$

the coefficients of the wavefunction, i.e. probabilities of states, are determined. The solution is given by the expansion of the wavefunction in Eigenstates $|\varphi_n\rangle$

$$|\psi(t)\rangle = \sum_n c_n(t) e^{\frac{i}{\hbar} E_n t} |\varphi_n\rangle \tag{2.1.4}$$

with quantized Eigenenergies E_n to the corresponding Hamiltonian $\mathcal{H}$.

With a given Hamiltonian which describes the energies of the system of interest, the dynamics of the system are derived by solving the time-dependent Schrödinger equation.

2.2. Spin operator

Most of the magnetic moments measured in experiment result from the angular moment of electrons. Besides orbital momentum, there is also an intrinsic angular momentum of electrons which is called the spin [55]. The magnetic moment based on spins reads

$$\boldsymbol{\mu} = g\beta \boldsymbol{S} \tag{2.2.1}$$

with the Bohr magneton β, the spin $\boldsymbol{S}$ in units of $\hbar$ and the gyromagnetic ratio g [55]. The operator $\boldsymbol{S}$ describes the spin of the electron. Considering a single spin-1/2 it consists of the states spin up $|\uparrow\rangle$ and spin down $|\downarrow\rangle$. An arbitrary state of a single spin reads

$$|\psi\rangle = \alpha|\uparrow\rangle + \beta|\downarrow\rangle \ . \tag{2.2.2}$$

The spin operator consists of $\boldsymbol{S} = \{S^x, S^y, S^z\}$, where the z-component gives the Eigenvalues

$$S^z|\uparrow\rangle = \frac{\hbar}{2}|\uparrow\rangle \ , \tag{2.2.3}$$

$$S^z|\downarrow\rangle = \frac{-\hbar}{2}|\downarrow\rangle \ . \tag{2.2.4}$$

The action of the x-component and y-component on an Eigenstate results in a superposition state. However, by defining the raise S^+ and lower operator S^- [56]

$$S^+ = S^x + iS^y \ , \tag{2.2.5}$$
$$S^- = S^x - iS^y \ , \tag{2.2.6}$$

its application on the Eigenstate results in

$$S^+|\uparrow\rangle = 0 \quad S^+|\downarrow\rangle = |\uparrow\rangle \tag{2.2.7}$$

and the opposite for the lower operator S^-

$$S^-|\downarrow\rangle = 0, \quad S^-|\uparrow\rangle = |\downarrow\rangle \ . \tag{2.2.8}$$

The spin components have a cyclic commutation relation

$$\left[S_i^x, S_j^y\right] = i\hbar S_i^z \delta_{ij} \tag{2.2.9}$$

and, based on this, one yields for the raise and lower operators [55]

$$\left[S^z, S^+\right] = \hbar S^+ \ , \tag{2.2.10}$$

$$\left[S^z, S^-\right] = -\hbar S^- \ , \tag{2.2.11}$$

$$\left[S^-, S^+\right] = -2\hbar S^z \ . \tag{2.2.12}$$

Within this thesis, the spin operators will be described via

$$\boldsymbol{S} = \frac{\hbar}{2}\boldsymbol{\sigma} \ , \tag{2.2.13}$$

where $\boldsymbol{\sigma}$ are the typical Pauli-matrices

$$\sigma^x = \begin{pmatrix} 0 & 1 \\ 1 & 0 \end{pmatrix}, \quad \sigma^y = \begin{pmatrix} 0 & -i \\ i & 0 \end{pmatrix}, \quad \sigma^z = \begin{pmatrix} 1 & 0 \\ 0 & -1 \end{pmatrix} \ . \tag{2.2.14}$$

Note that a single spin is formally the same as a single two-level system which is why the Pauli-matrices will also be the basis to describe two-level systems later on.

2.3. Quantization of the Maxwell field

One of the main aspects within this thesis will be the consideration of open quantum systems. The quantum system of interest is coupled to an external reservoir, where interaction with the external degrees of freedom leads to dissipation.
The concept of an external mode continuum which is in a vacuum state forms the basis to describe the most simple open quantum system. The external vacuum is described on the basis of the microscopic Maxwell equations without source fields. For the open quantum system dynamics investigated in this thesis, a quantized (many-body) system and a quantized reservoir is considered. Thus, the quantization of the vacuum Maxwell field forms the theoretical background for the mode continuum of the surrounding reservoir. In this section, the Hamiltonian for the free evolution of the surrounding reservoir is derived. The starting point forms the Lagrange function L_M of the electromagnetic field [57]

$$L_M = \int d^3r \mathcal{L} \ , \quad \mathcal{L} = -\frac{1}{4\mu_0} F^{\alpha\beta} F_{\alpha\beta} = \frac{\epsilon_0}{2} \left(\mathbf{E}^2 - c^2 \mathbf{B}^2 \right) \ , \tag{2.3.1}$$

with Lagrange density $\mathcal{L}$, electromagnetic tensor $F^{\alpha\beta}$ (cp. Equation A.1.2), electric field $\mathbf{E}$ and the magnetic field $\mathbf{B}$. In the Appendix in section A.1 it is shown that L_M leads to the vacuum Maxwell equations. Thus, it is justified to take this Lagrangian as the fundamental equation for the quantization of the vacuum Maxwell field.

2.3.1. Hamiltonian

In order to derive the Hamiltonian, the Lagrangian in Equation 2.3.1 is transformed with a Legendre transformation. For the Legendre transformation of the Maxwell field, the canonical coordinates are defined. The first canonical coordinate according to the Lagrangian is

$$r_\alpha = \partial_0 A_\alpha = \frac{1}{c}\partial_t A_\alpha \ . \tag{2.3.2}$$

Without any charges, as assumed for the Maxwell field, this yields the electrical field as $\mathbf{E} = -\partial_t \mathbf{A}$. The canonical momentum is defined as

$$\Pi_\alpha = \frac{\partial \mathcal{L}}{\partial(\partial_0 A_\alpha)} = -\frac{1}{\mu_0 c} E_\alpha \ , \tag{2.3.3}$$

Thus, both coordinates include the **E**-field but with different prefactors. Therefore, the Hamiltonian for the Maxwell field reads [57]

$$
\begin{aligned}
H_M = \int d^3r \mathcal{H} &= \int d^3r \left(\mathbf{r} \cdot \mathbf{\Pi} - \mathcal{L} \right) \\
&= \int d^3r \left(\epsilon_0 \mathbf{E}^2 - \mathcal{L} \right) \\
&= \int d^3r \left(\frac{\epsilon_0}{2} \mathbf{E}^2 + \frac{1}{2\mu_0} \mathbf{B}^2 \right) \ .
\end{aligned}
\tag{2.3.4}
$$

This classical Hamiltonian describes the energy of the vacuum Maxwell field and is used in the following for the quantization.

2.3.2. Quantization

The task now is to perform the quantization of the Maxwell field. For simplicity, the representation of the fields in matter is used

$$
\mathbf{D} = \epsilon_0 \epsilon_r \mathbf{E} \ ,
\tag{2.3.5}
$$

$$
\mathbf{H} = \mu_0 \mu_r \mathbf{B} \ ,
\tag{2.3.6}
$$

but a vacuum is assumed ($\mu_r = \epsilon_r = 1$). With this, the second Maxwell equation in Equation A.1.12 reads

$$
\dot{\mathbf{D}} = \nabla \times \mathbf{H} \ .
\tag{2.3.7}
$$

In a first step, it is assumed that the fields are quantized and therefore operators $\mathbf{D} \to \hat{\mathbf{D}}$, $\mathbf{H} \to \hat{\mathbf{H}}$. For quantum mechanical operators, the equation of motion of an arbitrary (not explicitly time-dependent) operator reads

$$
-i\hbar \frac{d}{dt} \langle \hat{O} \rangle = \langle \left[\hat{H}, \hat{O} \right] \rangle \ .
\tag{2.3.8}
$$

This equation for the field operators should be in correspondence to the classical Maxwell equations. Thus, the idea is that the commutation relation of $\hat{\mathbf{D}}$ with the Hamiltonian shall yield the second Maxwell equation

$$
-i\hbar \dot{\hat{\mathbf{D}}} = \left[\hat{H}_M, \hat{\mathbf{D}} \right] = \nabla \times \hat{\mathbf{H}} \ .
\tag{2.3.9}
$$

By defining this commutation relation, the field operators are derived to generate correspondence with the second Maxwell equation

$$
\left[\hat{H}_M, \hat{D}_i \right] = \int d^3r' \left(\frac{1}{2\epsilon_0} \left[\hat{\mathbf{D}}^2(\mathbf{r}'), \hat{D}_i(\mathbf{r}) \right] + \frac{1}{2\mu_0} \left[\hat{\mathbf{B}}^2(\mathbf{r}'), \hat{D}_i(\mathbf{r}) \right] \right) \ .
\tag{2.3.10}
$$

To arrive at the second Maxwell equation, the first summand shall vanish. Therefore it is requested that the commutator $\left[\hat{\mathbf{D}}^2(\mathbf{r}'), \hat{D}_i(\mathbf{r}) \right] = 0$. This is the case if all components are linearly independent, thus the first condition on the commutator reads [58]

$$
\left[\hat{D}_i(\mathbf{r}, t), \hat{D}_j(\mathbf{r}', t) \right] = 0 \ .
\tag{2.3.11}
$$

The second summand should yield the Maxwell equation, therefore the outcome shall be the rotation with the Nabla operator. The square of the magnetic field is rewritten as $1/\mu_0 \hat{\mathbf{B}}_i^2 = \hat{H}_i \hat{B}_i$ which results in

$$\left[\hat{H}_M, \hat{D}_i\right] = \int d^3r' \frac{1}{2} \sum_j \left(\hat{H}_j(\mathbf{r}') \left[\hat{B}_j(\mathbf{r}'), \hat{D}_i(\mathbf{r})\right] + \left[\hat{B}_j(\mathbf{r}'), \hat{D}_i(\mathbf{r})\right] \hat{H}_j(\mathbf{r}')\right) . \quad (2.3.12)$$

The second Maxwell eq. is then fulfilled if the commutator obeys the condition [58]

$$\left[\hat{B}_j(\mathbf{r}', t), \hat{D}_i(\mathbf{r}, t)\right] = i\hbar\epsilon_{ijk}\frac{\partial}{\partial k}\delta(\mathbf{r} - \mathbf{r}') . \quad (2.3.13)$$

Thus, a condition for the commutator of the field operators is derived on the basis of the second Maxwell equation. However, in this thesis the formalism will be the second quantization where the light field is described by mode operators. In order to arrive at the Hamiltonian in second quantization, a mode expansion Ansatz of the fields is assumed [52]

$$\mathbf{E}(\mathbf{r}, t) = -\dot{\mathbf{A}} = \sum_{\lambda\mathbf{k}} \left[\sqrt{\frac{\hbar}{2\epsilon_0\omega_\mathbf{k} V}}\varepsilon_{\lambda\mathbf{k}}\hat{b}_{\lambda\mathbf{k}}(i\omega_\mathbf{k})e^{-i\omega_\mathbf{k} t + i\mathbf{k}\mathbf{r}} + h.c.\right] , \quad (2.3.14)$$

$$\mathbf{B}(\mathbf{r}, t) = \nabla \times \mathbf{A} = \sum_{\lambda\mathbf{k}} \left[\sqrt{\frac{\hbar}{2\epsilon_0\omega_\mathbf{k} V}}\varepsilon_{\lambda\mathbf{k}} \times (i\mathbf{k})\hat{b}_{\lambda\mathbf{k}}e^{-i\omega_\mathbf{k} t + i\mathbf{k}\mathbf{r}} + h.c.\right] , \quad (2.3.15)$$

with frequency $\omega_\mathbf{k}$ in mode $\mathbf{k}$, quantization volume V, and polarization $\varepsilon_{\lambda\mathbf{k}}$. Note that the quantization is done in assuming the coefficients for the amplitude to be operators $b_{\lambda\mathbf{k}} \to \hat{b}_{\lambda\mathbf{k}}$. The task now is to derive the commutation relation in Equation 2.3.13 for the mode operators $\hat{b}_{\lambda\mathbf{k}}$. For simplicity, this will be done for the x and y coordinates

$$\left[\hat{D}_x(\mathbf{r}), \hat{B}_y(\mathbf{r}')\right] = \left[\hat{D}_x(\mathbf{r}), \left(\nabla' \times \hat{\mathbf{A}}(\mathbf{r}')\right)_y\right]$$
$$= \partial_{z'}\left[\hat{D}_x(\mathbf{r}), \hat{A}_x(\mathbf{r}')\right] - \partial_{x'}\left[\hat{D}_x(\mathbf{r}), \hat{A}_z(\mathbf{r}')\right] . \quad (2.3.16)$$

In order to know if the mode operators obey a bosonic or fermionic commutation relation, the summands are derived by inserting the mode expansion

$$\left[\hat{D}_i(\mathbf{r}), \hat{A}_j(\mathbf{r}')\right] = \sum_{\lambda\lambda'\mathbf{k}\mathbf{k}'} \epsilon_0 i\omega_\mathbf{k}\alpha_\mathbf{k}(\varepsilon_{\lambda\mathbf{k}})_i\alpha_{\mathbf{k}'}(\varepsilon_{\lambda'\mathbf{k}'})_j \left[\left(\hat{b}_{\lambda\mathbf{k}}e^{i\mathbf{k}\mathbf{r}} - h.c.\right), \left(\hat{b}_{\lambda'\mathbf{k}'}e^{i\mathbf{k}'\mathbf{r}'} + h.c.\right)\right] , \quad (2.3.17)$$

with $\alpha_\mathbf{k} = \sqrt{\frac{\hbar}{2\epsilon_0\omega_\mathbf{k} V}}$. For simplicity, the time is set $t = 0$, as the commutation relation shall hold for all times. The commutation relation in Equation 2.3.13 is independent of the amplitude, thus the commutator in Equation 2.3.17 shall be independent of the mode operators $\hat{b}_{\lambda\mathbf{k}}$. Therefore, it is postulated that the commutation relation of the mode operator reads

$$\hat{b}_{\lambda\mathbf{k}}\hat{b}_{\lambda'\mathbf{k}'}^\dagger = \delta_{\lambda\lambda'}\delta(\mathbf{k} - \mathbf{k}') \pm \hat{b}_{\lambda'\mathbf{k}'}^\dagger\hat{b}_{\lambda\mathbf{k}} . \quad (2.3.18)$$

Inserting this into Equation 2.3.17, it becomes clear that the mode operators only vanish for a bosonic commutation relation

$$\left[b_{\lambda\mathbf{k}}, b_{\lambda'\mathbf{k}'}^{\dagger}\right] = \delta_{\lambda\lambda'}\delta(\mathbf{k} - \mathbf{k}') \ , \tag{2.3.19}$$

$$[b_{\lambda\mathbf{k}}, b_{\lambda'\mathbf{k}'}] = \left[b_{\lambda\mathbf{k}}^{\dagger}, b_{\lambda'\mathbf{k}'}^{\dagger}\right] = 0 \ . \tag{2.3.20}$$

This is shown in detail in the Appendix in section A.2.

Now it is the task to show that the mode expansion Ansatz combined with the bosonic commutation relation for the mode operators yields the commutation relation for the field operators in Equation 2.3.13. For this, the bosonic commutation relation is applied to Equation 2.3.17

$$\begin{aligned}
\left[\hat{D}_i(\mathbf{r}), \hat{A}_j(\mathbf{r}')\right] &= \sum_{\lambda\lambda'\mathbf{k}\mathbf{k}'} \epsilon_0 i\omega_{\mathbf{k}}\alpha_{\mathbf{k}}(\varepsilon_{\lambda\mathbf{k}})_i \alpha_{\mathbf{k}'}(\varepsilon_{\lambda'\mathbf{k}'})_j \times \\
&\quad \times \left(e^{i(\mathbf{k}\mathbf{r}-\mathbf{k}'\mathbf{r}')}\delta_{\lambda\lambda'}\delta(\mathbf{k}-\mathbf{k}') + e^{-i(\mathbf{k}\mathbf{r}-\mathbf{k}'\mathbf{r}')}\delta_{\lambda\lambda'}\delta(\mathbf{k}-\mathbf{k}')\right) \\
&= \sum_{\lambda\mathbf{k}} \epsilon_0 i\omega_{\mathbf{k}}\alpha_{\mathbf{k}}^2 (\varepsilon_{\lambda\mathbf{k}})_i (\varepsilon_{\lambda\mathbf{k}})_j \left(e^{i\mathbf{k}(\mathbf{r}-\mathbf{r}')} + e^{-i\mathbf{k}(\mathbf{r}-\mathbf{r}')}\right) \ . \tag{2.3.21}
\end{aligned}$$

For light, the polarization λ is transversal to its propagation. Thus, $\lambda = 1, 2$, while the third unit vector points in the direction of the propagation $\varepsilon_{3\mathbf{k}} = \mathbf{k}/|\mathbf{k}|$. A summation over all three unit vectors yields

$$\sum_{\lambda=1}^{3} (\varepsilon_{\lambda\mathbf{k}})_i (\varepsilon_{\lambda\mathbf{k}})_j = \delta_{ij} \ . \tag{2.3.22}$$

Thus, a summation over the two polarization yields [59]

$$\sum_{\lambda=1}^{2} (\varepsilon_{\lambda\mathbf{k}})_i (\varepsilon_{\lambda\mathbf{k}})_j = \delta_{ij} - \frac{k_i k_j}{\mathbf{k}^2} \ . \tag{2.3.23}$$

Inserting this into Equation 2.3.21 reads

$$\left[\hat{D}_i(\mathbf{r}), \hat{A}_j(\mathbf{r}')\right] = \sum_{\mathbf{k}} \epsilon_0 i\omega_{\mathbf{k}}\alpha_{\mathbf{k}}^2 \left(\delta_{ij} - \frac{k_i k_j}{\mathbf{k}^2}\right) \left(e^{i\mathbf{k}(\mathbf{r}-\mathbf{r}')} + e^{-i\mathbf{k}(\mathbf{r}-\mathbf{r}')}\right) \ . \tag{2.3.24}$$

The discrete sum is assumed to be a continuous integral. Furthermore, $\mathbf{k}$ is integrated from $-\infty$ to ∞ and the integrand $f(\mathbf{k})$ is a symmetric function around the origin $f(\mathbf{k}) = f(-\mathbf{k})$. Note that $\alpha_{\mathbf{k}}$ is inserted as well. With this, the commutator reads

$$\left[\hat{D}_i(\mathbf{r}), \hat{A}_j(\mathbf{r}')\right] = \frac{i\hbar}{(2\pi)^3} \int d^3k \left(\delta_{ij} - \frac{k_i k_j}{\mathbf{k}^2}\right) e^{i\mathbf{k}(\mathbf{r}-\mathbf{r}')} = \delta_{ij}^{T}(\mathbf{r} - \mathbf{r}') \ , \tag{2.3.25}$$

which is the transversal delta function [58]. By inserting the transversal delta function into the commutation relation of the field operators, it is shown that the mode expansion

Ansatz with a bosonic commutation relation for the mode operators is in correspondence to the second Maxwell equation

$$
\begin{aligned}
\left[\hat{D}_x(\mathbf{r}), \hat{B}_y(\mathbf{r}')\right] =& \partial_{z'}\delta_{xx}^T(\mathbf{r}-\mathbf{r}') - \partial_{x'}\delta_{xz}^T(\mathbf{r}-\mathbf{r}') \ . \\
=& \frac{i\hbar}{(2\pi)^3}\int d^3k\left(1-\frac{k_xk_x}{\mathbf{k}^2}\right)(-ik_z)e^{i\mathbf{k}(\mathbf{r}-\mathbf{r}')} \\
& -\frac{i\hbar}{(2\pi)^3}\int d^3k\left(\frac{k_xk_z}{\mathbf{k}^2}\right)(-ik_x)e^{i\mathbf{k}(\mathbf{r}-\mathbf{r}')} \\
=& \frac{i\hbar}{(2\pi)^3}\int d^3k(-ik_z)e^{i\mathbf{k}(\mathbf{r}-\mathbf{r}')} = -\frac{i\hbar}{(2\pi)^3}\partial_z\int d^3k e^{i\mathbf{k}(\mathbf{r}-\mathbf{r}')} \\
=& -i\hbar\partial_z\delta(\mathbf{r}-\mathbf{r}') \ .
\end{aligned}
\tag{2.3.26}
$$

This proves that the mode expansion Ansatz combined with a bosonic commutation relation for the mode operators $\hat{b}_{\lambda\mathbf{k}}$ is in correspondence to the second Maxwell equation as this is in agreement with the conditions for the commutation relation of the field operators. Furthermore, the Hamilton function H_M in Equation 2.3.4 yields the Maxwell equations as shown in the Appendix in section A.1. The mode expansion in Equation 2.3.14 and Equation 2.3.15 with the mode operators $\hat{b}_{\lambda\mathbf{k}}$ in second quantization are then inserted into the Hamiltonion of the vacuum Maxwell field in Equation 2.3.4. This leads directly to the Hamiltonian of the vacuum Maxwell field in second quantization [60]

$$
H_M = \sum_{\lambda\mathbf{k}} \hbar\omega_k\left(\hat{b}_{\lambda\mathbf{k}}^\dagger\hat{b}_{\lambda\mathbf{k}} + \frac{1}{2}\right) \ .
\tag{2.3.27}
$$

This Hamiltonian forms the basis to describe an open quantum system with a surrounding mode continuum. However, this Hamiltonian only describes the free evolution of the mode continuum. The coupling of the quantum system to its environment remains to be determined.

2.4. Two-level system in a classical electromagnetic field coupled to a continuum

To derive the coupling of an electronic system to a photonic environment, a single two-level system (TLS) is considered. This exemplary system is especially relevant as it forms the basis for the many-emitter phonon-laser in chapter 5 in Part II. The same exemplary system is considered in chapter 8 to demonstrate the effects of entangled system-reservoir interactions in Part III.

The basis to describe a single electron in an electromagnetic field forms the Lagrangian

$$
L_F(\mathbf{r}, \dot{\mathbf{r}}) = \frac{1}{2}m\dot{\mathbf{r}}^2 + q\dot{\mathbf{r}}\cdot\mathbf{A} - q\phi \ .
\tag{2.4.1}
$$

In the Appendix in section A.3 is is shown that this Lagrangian is justified as it leads directly to the fundamental Lorentz force.

Above, it has been shown that the Lagrangian L_M in Equation A.1.4 leads to the vacuum Maxwell field in second quantization. This justifies to take L_M to describe the surrounding electromagnetic field. In this section, these two Lagrangians are used to derive the Hamiltonian of an electron dipole, oscillating between two energies due to an external

classical driving field. This Hamiltonian is derived from the Lagrangian L_F. Furthermore, the electron is coupled to a bosonic mode continuum, which acts as a photonic reservoir and is described by L_M. The total Lagrangian with electron charge e then reads,

$$L = \frac{1}{2}m\dot{\mathbf{r}} + e\left(\mathbf{A} \cdot \dot{\mathbf{r}} - \phi\right) + \int d^3r \frac{\epsilon_0}{2}\left(\mathbf{E}^2 - c^2\mathbf{B^2}\right) \ . \tag{2.4.2}$$

In a first step, the dipole approximation is applied [59]. The position of the electron only varies on small distances compared to the wavelength of the external field. The reason is that the size of atoms or quantum dots is in the orders of Ångström or nanometers in contrast to the driving field, which is considered to be in the orders of hundreds of nanometers. Therefore, the interaction can be expanded around the position of the electron $\mathbf{R}$, therefore $\mathbf{r} = \mathbf{R} + \mathbf{r}_s$ and the Lagrangian

$$L = \frac{m}{2}\dot{\mathbf{r}}_s^2 + e\left[\mathbf{A}(\mathbf{R} + \mathbf{r}_s, t) \cdot \dot{\mathbf{r}}_s - \phi(\mathbf{R} + \mathbf{r}_s)\right] + \int d^3r \frac{\epsilon_0}{2}\left(\mathbf{E}^2 - c^2\mathbf{B^2}\right) \ . \tag{2.4.3}$$

The relation between the amplitudes of the electric and magnetic field reads $B_0 = E_0/c$. The amplitude of the electric field is orders of magnitudes larger than the amplitude of the magnetic field [61]. The main contribution to the Lorentz force in Equation A.3.6 will thus result from the electric field. For this reason, the magnetic contribution will be neglected $\mathbf{A}(\mathbf{R} + \mathbf{r}_s, t) \approx \mathbf{A}(\mathbf{R})$ and the expansion in the scalar field is truncated after the first order

$$\phi(\mathbf{r}) = \phi(\mathbf{R}) + \mathbf{r_s} \cdot \nabla_{\mathbf{r}_s}\phi(\mathbf{R}) \ . \tag{2.4.4}$$

With this, the Lagrangian reads

$$L = \frac{m}{2}\dot{\mathbf{r}}_s^2 + e\left[\mathbf{A}(\mathbf{R}) \cdot \dot{\mathbf{r}}_s - \phi(\mathbf{R}) - \mathbf{r_s} \cdot \nabla_{\mathbf{r}_s}\phi(\mathbf{R})\right] + \int d^3r \frac{\epsilon_0}{2}\left(\mathbf{E}^2 - c^2\mathbf{B^2}\right) \ . \tag{2.4.5}$$

Before deriving the Hamilton function, the gauge freedom of the Lagrangian is used to obtain an equation with explicit dependence on the electrical field strength. With the gauge-function

$$G = - q\mathbf{r}_s\mathbf{A}(\mathbf{R}) \tag{2.4.6}$$

$$\dot{G} = - e\dot{\mathbf{r}}_s\mathbf{A}(\mathbf{R}) + -e\mathbf{r}_s\dot{\mathbf{A}}(\mathbf{R}), \tag{2.4.7}$$

and $L' = L + \dot{G}$, the Lagrangian is expressed in terms of the electric field, because $-\dot{\mathbf{A}}(\mathbf{R}) - \nabla_{\mathbf{r}_s}\phi(\mathbf{R}) = \mathbf{E}(\mathbf{R})$. Thus, the gauged Lagrangian reads

$$L' = \frac{m}{2}\dot{\mathbf{r}}_s^2 - e\phi(\mathbf{R}) + \mathbf{d} \cdot \mathbf{E}(\mathbf{R}) + \int d^3r \frac{\epsilon_0}{2}\left(\mathbf{E}^2 - c^2\mathbf{B^2}\right) \ , \tag{2.4.8}$$

with dipole-operator $\mathbf{d} = e\mathbf{r}_s$.

This has the advantage that for L_F, the separation of kinetic and potential energy is already done, so the Hamilton function for this part can be written down directly. With the known Maxwell field Hamilton function H_M in Equation 2.3.4, combined with L_F, the total Hamiltonian reads

$$H = \frac{\mathbf{p}^2}{2m} + e\phi(\mathbf{R}) - \mathbf{d} \cdot \mathbf{E}(\mathbf{R}) + \int d^3r \left(\frac{\epsilon_0}{2}\mathbf{E}^2 + \frac{1}{2\mu_0}\mathbf{B}^2\right) \ . \tag{2.4.9}$$

2.4.1. Quantization

The quantization of the Maxwell field was already shown in Equation 2.3.27. The electronic part of the Hamilton function still remains to be quantized. The Hamiltonian reads

$$H' = \int d^3r \psi^*(\mathbf{r},t) \left(\frac{\mathbf{p}^2}{2m} + e\phi(\mathbf{R}) - \mathbf{d} \cdot \mathbf{E}(\mathbf{R}) \right) \psi(\mathbf{r},t) + H_M \;, \qquad (2.4.10)$$

where $\psi(\mathbf{r},t)$ represents the Schrödinger field of the electronic degrees of freedom.
For the second quantization, the Schrödinger field is quantized $\psi^{(*)}(\mathbf{r},t) \rightarrow \hat{\psi}^{(*)}(\mathbf{r},t)$ [62] with the mode expansion Ansatz

$$\hat{\psi}^{(*)}(\mathbf{r},t) = \sum_\lambda \hat{a}_\lambda^{(\dagger)}(t) u_\lambda^{(*)}(\mathbf{r}) \;, \qquad (2.4.11)$$

where $\hat{a}_\lambda^{(\dagger)}$ is a fermionic annihilation (creation) operator for an electron with mode λ and $u_\lambda^{(*)}(\mathbf{r})$ are orthonormal functions which solve the Eigenvalue problem of the Schrödinger equation. The energy Eigenvalues are obtained by solving

$$\varepsilon_\lambda = \sum_{\lambda'} \int d^3r \; u_\lambda^*(\mathbf{r}) \left(\frac{\mathbf{p}^2}{2m} + e\phi(\mathbf{R}) \right) u_{\lambda'}(\mathbf{r}) \;. \qquad (2.4.12)$$

With this, the Hamiltonian in second quantization of a bound electron reads

$$H_e = \sum_\lambda \varepsilon_\lambda \hat{a}_\lambda^\dagger \hat{a}_\lambda \;. \qquad (2.4.13)$$

If the number of states is restricted to a two-level system ($\lambda = 0, 1$, $|0\rangle$ is the ground- and $|1\rangle$ the excited state) and the origin is set to the ground state, the Hamiltonian can be expressed with the Pauli-spin matrices in Equation 2.2.14

$$H_e = \hbar\omega_{01} \hat{\sigma}^+ \hat{\sigma}^- , \qquad (2.4.14)$$

where $\hbar\omega_{01}$ is the energy gap between the two levels. The dipole moment of the driving term reads

$$\int d^3r \hat{\psi}^*(\mathbf{r},t) \left(\mathbf{d} \cdot \mathbf{E}(\mathbf{R}) \right) \hat{\psi}(\mathbf{r},t) = \sum_{\lambda\lambda'} \hat{a}_\lambda^\dagger \hat{a}_{\lambda'} \int d^3r \; u_\lambda^*(\mathbf{r}) \left(e\mathbf{r} \cdot \mathbf{E}(\mathbf{R}) \right) u_{\lambda'}(\mathbf{r}) \;, \qquad (2.4.15)$$

where the integral over the unit cell reduces to the c-number of the dipole moment $d_{\lambda\lambda'}$. With this the driving term of the Hamiltonian reads

$$H_I = \left(\mathbf{d}_{01} \hat{\sigma}^+ + \mathbf{d}_{10} \hat{\sigma}^- \right) \cdot \mathbf{E}(\mathbf{R}) \;. \qquad (2.4.16)$$

Within this section, the interaction of the electron with a classical field as well as with a mode continuum is considered. The reason to differentiate between a classical and a quantized field is that the two-level system is pumped with a laser light of a single frequency ω_L and high intensity. On the other hand, the mode-continuum is quantized as the photon number is very small. It will be shown in chapter 3 that the coupling to a quantized mode continuum results in the spontaneous decay of the electronic excitation. Thus, there are the quantized field and the external classical field $\mathbf{E}_{\text{ext}}(\mathbf{R})$.

To begin with the interaction with the quantized light field, the mode-expansion of the electric field in Equation 2.3.14 is inserted

$$H_{e-p} = -i\sum_{\lambda\mathbf{k}} \left(\mathbf{d}_{01}\hat{\sigma}^+ + \mathbf{d}_{10}\hat{\sigma}^-\right)\left[\sqrt{\frac{\hbar\omega_{\mathbf{k}}}{2\epsilon_0 V}}\boldsymbol{\varepsilon}_{\lambda\mathbf{k}}\hat{b}_{\lambda\mathbf{k}}e^{-i\omega_{\mathbf{k}}t+i\mathbf{k}\cdot\mathbf{r_0}} - h.c.\right] \quad . \qquad (2.4.17)$$

By defining the coupling $g_\lambda(\mathbf{k}) = i\sqrt{\frac{\omega_{\mathbf{k}}}{2\hbar\epsilon_0 V}}\mathbf{d}_{10}\cdot\boldsymbol{\varepsilon}_{\lambda\mathbf{k}}e^{-i\omega_{\mathbf{k}}t+i\mathbf{k}\cdot\mathbf{r_0}}$, the Hamiltonian reads

$$H_{e-p} = \sum_{\lambda\mathbf{k}} \hbar\left(g_\lambda(\mathbf{k})\hat{\sigma}^+\hat{b}_{\lambda\mathbf{k}} + g_\lambda^*(\mathbf{k})\hat{\sigma}^+\hat{b}_{\lambda\mathbf{k}}^\dagger + g_\lambda(\mathbf{k})\hat{\sigma}^-\hat{b}_{\lambda\mathbf{k}} + g_\lambda^*(\mathbf{k})\hat{\sigma}^-\hat{b}_{\lambda\mathbf{k}}^\dagger\right) \quad . \qquad (2.4.18)$$

At this point, the rotating wave approximation (RWA) is applied [63]. By transforming the Hamiltonian $H_e + H_{e-p}$ into a rotating frame with respect to H_e, fast-rotating terms like $e^{i(\omega_k+\omega_{01})t}$ are neglected. These terms appear in the summands $\hat{\sigma}^+b^\dagger$ and $\hat{\sigma}^-b$ while the summands $(\hat{\sigma}^+b)^{(\dagger)}$ rotate with $e^{i(\omega_k-\omega_{01})t}$. If the energy gap is much larger than the respective coupling $\omega_{01} \gg g_\lambda(\mathbf{k})$ the fast-rotating terms do not appear in the dynamics as they average out for the equations of motion on the relevant time-scale. If the RWA is valid for the respective system of the proposed experiment, the electron-photon Hamiltonian reads

$$H_{e-p} = \sum_{\lambda\mathbf{k}} \hbar\left(g_\lambda(\mathbf{k})\hat{\sigma}^+\hat{b}_{\lambda\mathbf{k}} + g_\lambda^*(\mathbf{k})\hat{\sigma}^-\hat{b}_{\lambda\mathbf{k}}^\dagger\right) \quad . \qquad (2.4.19)$$

For the classical driving field, the Rabi-frequency is defined as $\Omega(t) = \mathbf{d}_{10}\cdot\mathbf{E}_{\text{ext}}(\mathbf{r}_0)/\hbar$. Inserting this, as well as the quantized vacuum Maxwell field, the final Hamiltonian for a classical driven two-level system coupled to a continuum is obtained

$$H = \hbar\omega_{01}\hat{\sigma}^+\hat{\sigma}^- + \sum_{\lambda\mathbf{k}}\hbar\omega_{\mathbf{k}}\hat{b}_{\lambda\mathbf{k}}^\dagger\hat{b}_{\lambda\mathbf{k}} + \Omega(t)\left(\hat{\sigma}^+ + \hat{\sigma}^-\right) + \sum_{\lambda\mathbf{k}}\hbar\left(g_\lambda(\mathbf{k})\hat{\sigma}^+\hat{b}_{\lambda\mathbf{k}} + g_\lambda^*(\mathbf{k})\hat{\sigma}^-\hat{b}_{\lambda\mathbf{k}}^\dagger\right) \quad .$$
$$(2.4.20)$$

In this thesis, this Hamiltonian forms the basis to describe open system dynamics. In chapter 3, the quantum stochastic Schrödinger equation is introduced to solve the Schrödinger equation for the Hamiltonian in Equation 2.4.20. By tracing out the reservoir degrees of freedom in a reduced density matrix picture, the Lindblad form is obtained. However, this Hamiltonian also serves as a first example to describe entangled system-reservoir interaction on the basis of the quantum stochastic Schrödinger equation in chapter 8 in Part III of this thesis.

3.

Quantum stochastic Schrödinger equation (QSSE)

To calculate dynamics of a quantum system, the time-dependent Schrödinger equation forms the basis to solve the dynamics of the wavefunction $|\psi(t)\rangle$ for a given system which is described by the Hamiltonian $\mathcal{H}$. As an example the derived Hamiltonian in Equation 2.4.20 for a driven two-level system (TLS) is considered. If the coupling to the continuum described by the quantized Maxwell field is neglected, the solution of the Schrödinger equation leads straightforward to the Rabi model [59]. In this model, the wavefunction of the electronic system is a two-state system

$$|\psi(t)\rangle = c_0(t)|0\rangle + c_1(t)|1\rangle \ , \tag{3.0.1}$$

where the probability to measure the electron in the state $|i\rangle$ is given by $|c_i(t)|^2$. The coefficients at time t are determined by the solution of the Schrödinger equation in Equation 2.1.3. However, if the quantized Maxwell field is included in the calculation, the solution is not as straightforward. The surrounding photonic reservoir for the electronic TLS is then described by a mode continuum and the Ansatz for the wavefunction reads

$$|\psi(t)\rangle = \sum_{i_s=0}^{1} \sum_{n_{\omega_1}...,n_{\omega_i},...,n_{\omega_N}=0}^{\infty} c_{i_s,n_{\omega_1}...,n_{\omega_i},...,n_{\omega_N}}(t)|i_s, n_{\omega_1} \ldots, n_{\omega_i}, \ldots, n_{\omega_N}\rangle \ . \tag{3.0.2}$$

The electronic degrees of freedom are described by the TLS state $|i_s\rangle$. The photonic reservoir is described by Fock states, where n_{ω_i} is the number of photons with frequency ω_i. Thus, the electronic system couples to an infinite number of modes, resulting in an infinite number of coupled differential equations for the time-dependent coefficients by inserting $|\psi(t)\rangle$ in the Schrödinger equation. To generate a solvable set of differential equations, the number of considered photons N_i in the state states n_{ω_i} is usually cut off as well as the number of considered modes K. The relevant modes are in many cases close to the TLS frequency. However, the modes have to be discretized, resulting still in an exponential number $((2N_i)^K)$ of differential equations. To deal with this problem in this thesis, the photon creation (annihilation) operators for the mode ω are treated as noise operators. This is done in transforming the basis as well as the Hamiltonian to a time-discrete picture where the creation (annihilation) of a photon takes place in a discrete time interval Δt. The information about the mode is hidden due to the transformation. This formulation is called the quantum stochastic Schrödinger equation (QSSE) [64], which will be the basis for calculating dynamics within this thesis. By using the Itô calculus and assuming a Wiener process of the noise operators [52], the derived wavefunction allows to trace out the reservoir degrees of freedom when going to the reduced density matrix formalism. This

leads to the common Lindblad form [65], where the system of interest is coupled via rate equations to the surrounding reservoir. This Lindblad formalism forms the theoretical background for the treatment of open quantum systems with factorizing system-reservoir dynamics in Part II of this thesis. However, if the system is entangled with the reservoir, i.e. for structured reservoirs where for example the output of the system is fed back after a time delay, the QSSE with the time-discrete basis forms the theoretical background for calculating these entangled system-reservoir dynamics in Part III.

3.1. Quantum-noise operators

Starting with the Hamiltonian in Equation 2.4.20 in RWA, the polarization degrees of freedom are neglected ($\lambda = 1$). Furthermore, the discrete sum is converted into a continuous integral

$$
\begin{aligned}
H =& \hbar\omega_{01}\sigma^+\sigma^- + \int d\omega \ \hbar\omega b^\dagger(\omega)b(\omega) + \Omega(t)\left(\sigma^+ + \sigma^-\right) \\
&+ \int d\omega \ \hbar\left(g(\omega)\hat{\sigma}^+\hat{b}(\omega) + g^*(\omega)\hat{\sigma}^-\hat{b}^\dagger(\omega)\right) \ .
\end{aligned}
\tag{3.1.1}
$$

In a first step, this Hamiltonian is transformed into a rotating frame via a unitary transformation. Due to the different orders of magnitude of the free evolution ω_{01} and ω compared to the coupling frequencies $g(\omega)$ and Ω, two different time-scales are involved. The relevant time-scale shall be the one of the coupling frequencies. Thus, the whole set of equations of motion, based on the Schrödinger equation, is transformed with respect to the free evolution. This is possible as a unitary transformation with an arbitrary unitary operator U ($U^\dagger U = \mathbb{1}$) leaves the Schrödinger equation invariant

$$
\begin{aligned}
HU^\dagger U|\psi(t)\rangle =& i\hbar\partial_t\left(U^\dagger U|\psi(t)\rangle\right) \\
HU^\dagger U|\psi(t)\rangle =& i\hbar\left(\partial_t U^\dagger\right)U|\psi(t)\rangle + i\hbar U^\dagger\left(\partial_t U|\psi(t)\rangle\right) \ .
\end{aligned}
\tag{3.1.2}
$$

By defining the transformed wavefunction $|\tilde{\psi}(t)\rangle = U|\psi(t)\rangle$, and multiplying the equation from left with U, the transformed Hamiltonian $\tilde{H}$ is obtained

$$
\underbrace{\left(UHU^\dagger - i\hbar U\partial_t U^\dagger\right)}_{\tilde{H}}|\tilde{\psi}(t)\rangle = i\hbar\partial_t|\tilde{\psi}(t)\rangle \ .
\tag{3.1.3}
$$

To transform the Hamiltonian in Equation 3.1.1 into a rotating frame with respect to the free evolution, the following unitary operator is defined

$$
U = e^{\frac{i}{\hbar}t\left(\hbar\omega_{01}\sigma^+\sigma^- + \int d\omega \ \hbar\omega b^\dagger(\omega)b(\omega)\right)} \ .
\tag{3.1.4}
$$

The derivative of $U^\dagger$ cancels out with the free evolution of the Hamiltonian in Equation 3.1.1 as the free part commutes with U. Combined with the first summand in Equation 3.1.3, the transformed Hamiltonian reads

$$
\begin{aligned}
\tilde{H} =& \mathcal{E}_0\cos(\omega_L t)U\left(\sigma^+ + \sigma^-\right)U^\dagger + \int d\omega \ \hbar U\left(g(\omega)\hat{\sigma}^+\hat{b}(\omega) + g^*(\omega)\hat{\sigma}^-\hat{b}^\dagger(\omega)\right)U^\dagger \\
=& \mathcal{E}_0\left(\sigma^+ + \sigma^-\right) + \int d\omega \ \hbar\left(g(\omega)\hat{\sigma}^+\hat{b}(\omega)e^{-i(\omega-\omega_{01})t} + g^*(\omega)\hat{\sigma}^-\hat{b}^\dagger(\omega)e^{i(\omega-\omega_{01})t}\right) \ .
\end{aligned}
\tag{3.1.5}
$$

The external driving field was expressed as $\Omega(t) = \mathcal{E}_0 \cos(\omega_L t)$. In deriving this Hamiltonian, the Baker-Campbell-Hausdorff equation was used and, for simplicity, a resonant excitation of the external driving field with the TLS $\omega_L = \omega_{01}$ was assumed. If the amplitude of the external driving field $\mathcal{E}_0$ is time independent (continuous wave), the only time dependency of $\tilde{H}$ remains in the interaction with the quantized reservoir. As an approximation, the coupling constant is assumed to be frequency independent $g(\omega) \to g_0$. This is justified as long as the reservoir is not structured in an unusual way (e.g. some modes are highly occupied) because most of the coupling to the reservoir is close to the TLS frequency and thus, only small differences in ω are assumed. With this it is possible to define time-dependent operators

$$\hat{b}(t) = \frac{1}{\sqrt{2\pi}} \int d\omega \; \hat{b}(\omega) e^{-i(\omega - \omega_{01})t} \; , \tag{3.1.6}$$

and the Hamiltonian simplifies to

$$\tilde{H} = \mathcal{E}_0 \left(\sigma^+ + \sigma^- \right) + \hbar \left(\sqrt{2\pi} g_0 \hat{\sigma}^+ \hat{b}(t) + \sqrt{2\pi} g_0^* \hat{\sigma}^- \hat{b}^\dagger(t) \right) \; . \tag{3.1.7}$$

This can be interpreted as follows: The driven TLS interacts with a mode continuum via g_0. Due to the time representation of $\tilde{H}$, the information with which mode the TLS interacts is hidden within the time-dependent operators $\hat{b}(t)$. Thus, $\tilde{H}$ only provides information at which time a photon was emitted (absorbed) and not in which mode. The commutation relation of the time-dependent operators $\hat{b}(t)$ is determined from the bosonic commutation relation of the mode operators in Equation 2.3.19

$$\left[\hat{b}(t), \hat{b}^\dagger(t') \right] = \delta(t - t') \; . \tag{3.1.8}$$

In order to arrive at this commutation relation, the integral was taken from minus infinity to infinity. This is called narrow bandwidth approximation and is in agreement with the approximation of a mode independent coupling constant and that only modes close to the TLS transition frequency are relevant. With these approximations, the operator $\hat{b}(t)$ is referred to as Gaussian white noise [52]. It will be shown that by assuming the operator $\hat{b}(t)$ as a stochastic element, the Lindblad equation is generated.
The idea is to calculate the time evolution of the wavefunction $|\tilde{\psi}(t)\rangle$ by stroboscopic application of the time-evolution operator. This time-evolution operator will be discretized to infinitesimal small time steps.
A solution of the wavefunction $|\tilde{\psi}(t)\rangle$ is given by a formal integration of the Schrödinger equation

$$|\tilde{\psi}(t)\rangle = U(t, t_0)|\tilde{\psi}(t_0)\rangle \; , \tag{3.1.9}$$

with time-evolution operator

$$U(t, t_0) = \hat{T} \exp\left(-\frac{i}{\hbar} \int_{t_0}^t dt' \; \tilde{H}(t') \right) \; , \tag{3.1.10}$$

where the operator $\hat{T}$ denotes the time ordering operator for time from t_0 to t.

The discretized time-evolution operator with time increment $\Delta t = t_{k+1} - t_k$ then reads

$$U(\Delta t) = \hat{T} \exp\left(-\frac{i}{\hbar} \int_{t_k}^{t_{k+1}} dt'\ \tilde{H}(t')\right) \ , \qquad (3.1.11)$$

and the system evolves in time with time-step Δt as

$$|\tilde{\psi}(t_{k+1})\rangle = U(\Delta t)|\tilde{\psi}(t_k)\rangle \ . \qquad (3.1.12)$$

In principle, this suffices to compute time evolution of the system, described by H, via stroboscopic application of the time-evolution operator $U(\Delta t)$ on the state $|\tilde{\psi}(t)\rangle$. However, $|\tilde{\psi}(t)\rangle$ is still in the basis of the mode continuum with infinite frequency modes ω in Equation 3.0.2, as without adapting the basis, the time-dependent operators $\hat{b}(t)$ are only an abbreviation for the integral over the mode operators. From this point on, there are two options, on the one hand, the basis can be adapted by going into a time-discrete basis. The degrees of freedom of the mode continuum are then reduced by the time representation. There would be still a possible very large number of time steps, but this basis is in favor of the computation of time evolution. On the other hand, it is possible to reduce the bath degrees of freedom by tracing out the reservoir. This has to be done in the formalism of the reduced density matrix, but it is important that the tracing out of the reservoir is performed within the basis of the mode continuum. This will be discussed in more detail later on.

Either way will be used in this thesis. First, some general remarks about the QSSE are important. As the time-discrete basis allows an easier interpretation it will be introduced together with the quantum-noise operators before introducing the reduced density matrix formalism. These quantum-noise operators combined with the time-discrete basis forms the theoretical background for computing entangled system-reservoir dynamics in Part III of this thesis while the reduced density matrix formalism is used in Part II of this thesis. The quantum-noise operators are defined over the creation (annihilation) of photons in the time interval Δt

$$\Delta B^{(\dagger)}(\Delta t) = \int_{t_k}^{t_{k+1}} dt' \hat{b}^{(\dagger)}(t') \ . \qquad (3.1.13)$$

With this, the discrete time-evolution operator reads

$$U(\Delta t) = \exp\left\{-\frac{i}{\hbar}\left[\mathcal{E}_0 \Delta t \left(\sigma^+ + \sigma^-\right) + \hbar\left(\sqrt{2\pi}g_0\hat{\sigma}^+\Delta B(\Delta t) + \sqrt{2\pi}g_0^*\hat{\sigma}^-\Delta B^\dagger(\Delta t)\right)\right]\right\} \ . \qquad (3.1.14)$$

Note that due to the time increment, the time ordering $\hat{T}$ is redundant, because due to the definition of the quantum-noise operators there are no time-dependent operators in the time interval Δt as the quantum-noise operators are only defined over the time interval Δt. Without adapting the basis, also the quantum-noise operators are only an abbreviation for the mode operators $\hat{b}(\omega)$. Thus, the basis of the wavefunction needs to be adapted. To define the basis, the commutation relation of the noise operators is determined

$$\left[\Delta B(t_k), \Delta B^\dagger(t_j)\right] = \int_{t_k}^{t_{k+1}} dt \int_{t_j}^{t_{j+1}} dt' \delta(t - t') = \Delta t \delta_{k,j} \ . \qquad (3.1.15)$$

Thus, the quantum-noise operators form an orthogonal set of basis elements at different discrete times t_k. However, they are not normalized as the commutator is proportional to Δt. This leads to the assumption, that the noise operators are proportional to $\sqrt{\Delta t}$. By creating a time-discrete number basis, the proportionality to $\sqrt{\Delta t}$ is stored in the basis to obtain normalization [54]

$$|i_k\rangle = \frac{\left(\Delta B^\dagger(t_k)\right)^{i_k}}{\sqrt{i_k!(\Delta t)^{i_k}}}|\text{vac}\rangle \ . \tag{3.1.16}$$

The repeated action of the time-discrete quantum-noise operator $\Delta B^\dagger(t_k)$ within $\Delta t = t_{k+1} - t_k$ creates photons in the number basis in the state $|i_k\rangle$. This state is called time-bin at time interval $t_{k+1} - t_k$ in the following. Thus, the time-bin $|i_k\rangle$ represents the number of created photons in the reservoir at time interval Δt. In order to maintain normalization of the basis, the action of $(\Delta B^\dagger(t_k))^{i_k}$ on the state is divided by $\sqrt{(\Delta t)^{i_k}}$. By expanding $|\psi\rangle$ in the time-discrete basis and let the time-evolution operator act subsequently on $|\psi\rangle$, time evolution in the QSSE picture can be calculated. In the following it will be shown that the time-evolution operator can be brought to a similar form as the Langevin equation which justifies a stochastic calculus. This is important for the derivation of the Lindblad formalism in the reduced density matrix picture.

3.2. Itô calculus

One of the standard stochastic processes is the Brownian motion of a particle. This simple model is described by the Langevin equation with [66]

$$dv_t = -\beta v_t dt + \sigma dB_t \ . \tag{3.2.1}$$

This can be interpreted as the motion of a Brownian particle which interacts with its environment. The constant β describes a drift, where the velocity v_t of the particle is damped. the parameter σ is called the volatility to the stochastic process dB_t. The idea is that the change of momentum of the particle obeys a stochastic process. It is assumed that the number of collisions obeys a normal distribution in the interval Δt, such that at the end of each time interval, only the direction of the particle changes, corresponding to a random walk. This is one of the standard and most simple stochastic differential equations. In this section, it will be shown, that the time evolution of the state $|\psi(t)\rangle$ can be brought to a similar form which justifies the use of the Itô calculus.
In order to calculate the time evolution of the system, the action of the time-evolution operator on a given initial state $|\psi(0)\rangle$ is calculated

$$|\psi(\Delta t)\rangle = U(\Delta t)|\psi(0)\rangle \ . \tag{3.2.2}$$

The time-step Δt is a time interval which is chosen to be infinitesimal small. With this, the exponential of the time-evolution operator is expanded in orders of Δt

$$|\psi(\Delta t)\rangle \approx \left[\mathbb{1} - \frac{i}{\hbar}\left(U_{sys} + U_{res}\right) - \frac{1}{2\hbar^2}\left(U_{sys} + U_{res}\right)\left(U_{sys} + U_{res}\right)\right]|\psi(0)\rangle \ , \tag{3.2.3}$$

where U_{sys} is the first part of U in Equation 3.1.14 and U_{res} the last part which contains the quantum-noise operators ΔB. The following consideration simplifies this calculation: As

Δt is arbitrarily small, all terms proportional to $(\Delta t)^2$ can be neglected and the expansion is truncated after the first order of Δt. However, it is assumed that the quantum-noise operators are proportional to $\sqrt{(\Delta t)}$ due to the commutation relation. With this, the second order of the exponent has to be taken into account as the second-order term with the quantum-noise operators is proportional to Δt. In contrast, all terms of the second order including the system can be neglected as $U_{sys} \sim \Delta t$. Together with the quantum-noise operators this would correspond to a proportionality of $(\Delta t)^{3/2}$ of a term such as $U_{sys}U_{res}$ and $U_{sys}U_{sys} \sim (\Delta t)^2$. Thus, the only relevant part of the last summand is the term $U_{res}U_{res}$ which reads

$$
\begin{aligned}
U_{res}U_{res} = \hbar^2 2\pi \Big(& |g_0|^2 \sigma^+\sigma^- \Delta B \Delta B^\dagger + |g_0|^2 \sigma^-\sigma^+ \Delta B^\dagger \Delta B \\
& + g_0 g_0 \sigma^+\sigma^+ \Delta B \Delta B + g_0^* g_0^* \sigma^-\sigma^- \Delta B^\dagger \Delta B^\dagger \Big) \\
= \hbar^2 2\pi \Big(& |g_0|^2 \sigma^+\sigma^- (\Delta t + \Delta B^\dagger \Delta B) + |g_0|^2 \sigma^-\sigma^+ \Delta B^\dagger \Delta B \\
& + g_0 g_0 \sigma^+\sigma^+ \Delta B \Delta B + g_0^* g_0^* \sigma^-\sigma^- \Delta B^\dagger \Delta B^\dagger \Big)
\end{aligned}
\tag{3.2.4}
$$

To simplify Equation 3.2.3 further, it is possible to set conditions on $|\psi(0)\rangle$. Initially, it is assumed that the surrounding reservoir is in a vacuum state. This means, the occupation in all time-bins $|i_k\rangle$ is initially set to zero. The state of the system is left at an arbitrary state. The vacuum has occupation zero, thus initially, the time-bin occupation at all times t_k reads

$$
\left\langle \Delta B^\dagger(t_k)\Delta B(t_k) \right\rangle = 0 \ ,
\tag{3.2.5}
$$

before the system has interacted with time-bin $|i_k\rangle$. The same holds for the action of the time-bin occupation operator on the state $\Delta B^\dagger(t_k)\Delta B(t_k)|i_k\rangle = 0$ as well as for the action of the annihilation operator $\Delta B(t_k)|i_k\rangle = 0$. Furthermore, the action of $\sigma^-\sigma^-$ on the arbitrary system state yields zero as in this case it is a single TLS. With these considerations, Equation 3.2.3 reduces to

$$
|\psi(\Delta t)\rangle = |\psi(0)\rangle + \Delta t \underbrace{\left[-\frac{i}{\hbar}\mathcal{E}_0\left(\sigma^+ + \sigma^-\right) - \pi|g_o|^2\sigma^+\sigma^- \right]}_{U_{\text{eff}}} |\psi(0)\rangle - i\sqrt{2\pi}g_0^*\sigma^-\Delta B^\dagger|\psi(0)\rangle \ .
$$

$$
\tag{3.2.6}
$$

The first part contains only system operators and is defined as U_{eff}. Note that the only relevant part of the second-order expansion is the second term in U_{eff}. It will be shown that this term is crucial to generate the Lindblad equation, which clarifies the proportionality $\Delta B \sim \sqrt{\Delta t}$. This equation is now generalized to arbitrary times t. This is justified as the time-bin basis was introduced and initially all time-bins where set to the vacuum state. Thus, the time evolution for the next time step always acts on a vacuum state and only the past time-bins $|i_l\rangle$ with $l < k$ may differ from a vacuum. Defining the differential $d|\psi(t)\rangle$ results in

$$
d|\psi(t)\rangle := |\psi(t + \Delta t)\rangle - |\psi(t)\rangle = U_{\text{eff}}|\psi(t)\rangle\Delta t - i\sqrt{2\pi}g_0^*\sigma^-\Delta B^\dagger|\psi(t)\rangle \ .
\tag{3.2.7}
$$

This equation is in strong analogy to the Langevin equation in Equation 3.2.1. The first part describes the evolution of the system and does not contain a stochastic element. However, the second summand contains the quantum-noise creation operator $\Delta B^\dagger$. This

also justifies the interpretation of $\Delta B^\dagger$ as Gaussian white noise as it formally looks like a Langevin equation [52]. Furthermore, $\Delta B^\dagger$ can be interpreted as a Wiener process [64] combined with the assumption that all future time-bins are initialized in the vacuum state. The time increment is independent of the past and the mean value vanishes while the variance is defined

$$\langle \Delta B^\dagger(t_k) \rangle = 0, \quad \langle \Delta B(t_j) \Delta B^\dagger(t_k) \rangle = \delta_{j,k} \ . \tag{3.2.8}$$

This formal analogy to the Langevin equation suffices at this point to use the product rule of the Itô calculus [66]. In the following section it will be applied for the density operator $\hat{\rho} = |\psi\rangle\langle\psi|$, thus it will be derived with the differential of the density matrix. Defining the differential of $\hat{\rho}(t)$ it reads

$$d(|\psi(t)\rangle\langle\psi(t)|) = |\psi(t+dt)\rangle\langle\psi(t+dt)| - |\psi(t)\rangle\langle\psi(t)| \ . \tag{3.2.9}$$

By adding zero twice into the first summand, the Itô product rule is derived

$$\begin{aligned}
d(|\psi(t)\rangle\langle\psi(t)|) &= (|\psi(t+dt)\rangle - |\psi(t)\rangle + |\psi(t)\rangle)\,(\langle\psi(t+dt)| - \langle\psi(t)| + \langle\psi(t)|) - |\psi(t)\rangle\langle\psi(t)| \\
&= (d|\psi(t)\rangle + |\psi(t)\rangle)\,(d\langle\psi(t)| + \langle\psi(t)|) - |\psi(t)\rangle\langle\psi(t)| \\
&= d\,(|\psi(t)\rangle)\,\langle\psi(t)| + |\psi(t)\rangle d\,(\langle\psi(t)|) + d\,(|\psi(t)\rangle)\,d\,(\langle\psi(t)|) \ , \tag{3.2.10}
\end{aligned}$$

where the last term is in addition to the standard product rule and results from the stochastic process.

3.3. Lindblad form of the reduced density matrix

In the last section, the quantum stochastic Schrödinger equation was derived. Thus, the time evolution of the wavefunction is described by Equation 3.2.7. However, even if the information about the modes is hidden in the time-discrete picture, one deals with a large Hilbert space, as the photon number states of the discrete time-bins have to be taken into account. In most cases, the reservoir is not of interest and the important dynamics take place at the system of interest. This will be the case in Part II of this thesis. In order to reduce the complexity of the problem in these cases, the reservoir is traced out by going into the reduced density matrix picture. The dynamics of this reduced density matrix allows to draw conclusion about the system of interest by describing the interaction with the surrounding reservoir via a rate. In this section, it will be shown that by calculating the differential of the reduced density matrix with the product rule of the Itô calculus in Equation 3.2.10, the von-Neumann equation with the common Lindblad dissipator is obtained. The reduced density-matrix of the system is defined as

$$\hat{\rho}_s(t) = \mathrm{tr}_R(\hat{\rho}(t)) = \sum_{n_{\omega_1}\ldots,n_{\omega_i},\ldots,n_{\omega_N}=0}^{\infty} \langle n_{\omega_1}\ldots,n_{\omega_i},\ldots,n_{\omega_N}|\psi(t)\rangle\times$$
$$\times\langle\psi(t)|n_{\omega_1}\ldots,n_{\omega_i},\ldots,n_{\omega_N}\rangle \ . \tag{3.3.1}$$

In order to derive the Lindblad form, the most easiest and typical way is to perform the trace in the basis of the frequency modes ω. It is assumed that system and reservoir states factorize initially which is the Born approximation.
To perform the trace, the starting point is before the definition of the quantum-noise

operators in Equation 3.1.13. However, the same notation is used here to simplify the notation of the integrals including the integral over modes ω and the time increment Δt. This becomes clear in the following.

In the same manner as before, the time-evolution operator is expanded to the first order in Δt. By setting the initial reservoir state to a vacuum, only the action of the creation operators of the time evolution are unequal to zero (cp. Equation 3.2.6). With this, the differential of the state reads (but still in the basis of the modes ω)

$$d|\psi(t)\rangle = |\psi(t+\Delta t)\rangle - |\psi(t)\rangle = dt U_{\text{eff}}|\psi(t)\rangle + \sigma^- \Delta B_0^\dagger(dt)|\psi(t)\rangle$$
$$+ U_{sys}\sigma^- \Delta B_1^\dagger(dt)|\psi(t)\rangle + \Delta B_2^\dagger(dt)\sigma^- U_{sys}|\psi(t)\rangle \ , \tag{3.3.2}$$

with the definitions

$$\Delta B_0^\dagger(dt) = - i\sqrt{2\pi}g_0^* \int_0^{\Delta t} dt b^\dagger(t) \ , \tag{3.3.3}$$

$$\Delta B_1^\dagger(dt) = - \frac{\sqrt{2\pi}g_0^*}{\hbar} \int_0^{\Delta t} dt \int_0^t dt' b^\dagger(t') \ , \tag{3.3.4}$$

$$\Delta B_2^\dagger(dt) = - \frac{\sqrt{2\pi}g_0^*}{\hbar} \int_0^{\Delta t} dt b^\dagger(t) \int_0^t dt' \ . \tag{3.3.5}$$

It will be shown that the Lindblad equation is obtained when tracing out the reservoir degrees of freedom with the consideration of only terms proportional to dt.

As before, the reservoir is initially assumed to be in a vacuum state $|\,\text{vac}\rangle$ with all $n_{\omega_i} = 0$. Thus, the reduced density matrix reads

$$\hat{\rho}_s(t) = \sum_{\{n_\omega\}} \langle\{n_\omega\}|\psi(t)\rangle\langle\psi(t)|\{n_\omega\}\rangle = \langle\text{vac}\,|\,\text{vac}\rangle \otimes |\psi(t)\rangle_s\langle\psi(t)|_s \otimes \langle\text{vac}\,|\,\text{vac}\rangle \ , \tag{3.3.6}$$

with $\{n_\omega\} = n_{\omega_1}\ldots,n_{\omega_i},\ldots,n_{\omega_N}$. The reduced density matrix in differential form to compute time evolution is obtained by using the Itô-product rule derived in Equation 3.2.10 for the differential of $|\psi(t)\rangle$ in Equation 3.3.2

$$d\hat{\rho}_s(t) = \text{tr}_R(d\hat{\rho}(t)) = \text{tr}_R \left\{ [d(|\psi(t)\rangle)\langle\psi(t)| + h.c.] + d(|\psi(t)\rangle) d(\langle\psi(t)|) \right\} \ . \tag{3.3.7}$$

The first summand in Equation 3.3.7 reads

$$\text{tr}_R \left\{ d(|\psi(t)\rangle)\langle\psi(t)| \right\} = \sum_{\{n_\omega\}} \langle\{n_\omega\}|d(|\psi(t)\rangle)\langle\psi(t)|_s \otimes \langle\text{vac}\,|\{n_\omega\}\rangle$$
$$= \langle\text{vac}\,|d(|\psi(t)\rangle)\langle\psi(t)|_s$$
$$= \langle\text{vac}\,|\left(dt U_{\text{eff}} + \sigma^- \Delta B_0^\dagger(dt)\right)|\,\text{vac}\rangle \otimes |\psi(t)\rangle_s\langle\psi(t)|_s$$
$$+ \langle\text{vac}\,|\left(U_{sys}\sigma^- \Delta B_1^\dagger(dt) + \Delta B_2^\dagger(dt)\sigma^- U_{sys}\right)|\,\text{vac}\rangle \otimes |\psi(t)\rangle_s\langle\psi(t)|_s$$
$$= dt U_{eff}\hat{\rho}_s \ , \tag{3.3.8}$$

where each summand including a reservoir creation operator $b(\omega)^\dagger$ yields zero as a a photon is created in the ket state whereas the bra state remains the same.

To calculate the last summand of Equation 3.3.7, some considerations simplify the calculation. Each summand of higher order than dt equals zero as dt is arbitrarily small and

these terms can be neglected. This is the case for each summand already including dt due to the multiplication with the first summand of Equation 3.3.2.

With these considerations, the last summand of Equation 3.3.7 reads

$$
\begin{aligned}
tr_R\left\{d\left(|\psi(t)\rangle\right)d\left(\langle\psi(t)|\right)\right\} = tr_R\Big\{ &\sigma^-\Delta B_0^\dagger(dt)\hat\rho\sigma^+\Delta B_0(dt) + \sigma^-\Delta B_0^\dagger(dt)\hat\rho U_{sys}\sigma^+\Delta B_1(dt) \\
&+U_{sys}\sigma^-\Delta B_1^\dagger(dt)\hat\rho\sigma^+\Delta B_0(dt) \\
&+\sigma^-\Delta B_0^\dagger(dt)\hat\rho\Delta B_2(dt)\sigma^+U_{sys} \\
&+\Delta B_2^\dagger(dt)\sigma^-U_{sys}\hat\rho\sigma^+\Delta B_0(dt) \\
&+U_{sys}\sigma^-\Delta B_1^\dagger(dt)\hat\rho U_{sys}\sigma^+\Delta B_1(dt) \\
&+U_{sys}\sigma-\Delta B_1^\dagger(dt)\hat\rho\Delta B_2(dt)\sigma^+U_{sys} \\
&+\Delta B_2^\dagger(dt)\sigma^-U_{sys}\hat\rho U_{sys}\sigma^+\Delta B_1(dt) \\
&+\Delta B_2^\dagger(dt)\sigma^-U_{sys}\hat\rho\Delta B_2(dt)\sigma^+U_{sys}\Big\} \ .
\end{aligned}
\tag{3.3.9}
$$

To analyze the trace of these terms, it is convenient to have a look each combination of reservoir operators to obtain its proportionality to dt. Under cyclic permutation of the trace, the action of the reservoir operators on the vacuum state is investigated. By inserting the definitions of the terms $\Delta B_i(dt)$, it is shown that only one term is in the order of dt which is

$$
\begin{aligned}
\Delta B_0(dt)\Delta B_0^\dagger(dt)|\,\mathrm{vac}\rangle = &|g_0|^2\int_0^{\Delta t}dt\int_0^t dt'\int_0^\infty d\omega\,\hat b(\omega)e^{-i(\omega-\omega_{01})t}\times \\
&\times\int_0^\infty d\omega'\hat b(\omega')e^{i(\omega'-\omega_{01})t'}|\,\mathrm{vac}\rangle \ .
\end{aligned}
\tag{3.3.10}
$$

The action of the reservoir operators on the vacuum yields $\delta(\omega-\omega')$. Together with the integral over ω' this yields $\omega = \omega'$

$$
\begin{aligned}
\Delta B_0(dt)\Delta B_0^\dagger(dt)|\,\mathrm{vac}\rangle &= |g_0|^2\int_0^{\Delta t}dt\int_0^t dt'\int d\omega e^{-i\omega(t-t')}e^{-i\omega_{01}(t-t')}|\,\mathrm{vac}\rangle \\
&= 2\pi|g_0|^2 dt|\,\mathrm{vac}\rangle \ .
\end{aligned}
\tag{3.3.11}
$$

The combination of $\Delta B_0(dt)\Delta B_0^\dagger(dt)$ within the trace results in a term proportional to dt. This term is crucial for the Lindblad dynamics. However, all other combinations are of higher order in dt which is exemplarily shown for

$$
\begin{aligned}
\Delta B_0(dt)\Delta B_1^\dagger|\,\mathrm{vac}\rangle &= -\frac{i2\pi|g_0|^2}{\hbar}\int_0^{\Delta t}dt\,b(t)\int_0^t dt'\int_0^{t'}dt''b^\dagger(t'')|\,\mathrm{vac}\rangle \\
&= -\frac{i2\pi|g_0|^2}{\hbar}\int_0^{\Delta t}dt\int_0^t dt'|\,\mathrm{vac}\rangle = -\frac{i2\pi|g_0|^2}{\hbar}\mathcal{O}(dt^2)|\,\mathrm{vac}\rangle \ .
\end{aligned}
\tag{3.3.12}
$$

The same holds for terms such as $\Delta B_0(dt)\Delta B_2^\dagger(dt)$ and $\Delta B_1(dt)\Delta B_2^\dagger(dt)$. With this, the last summand in Equation 3.3.7 in first order of dt reads

$$
tr_R\left\{d\left(|\psi(t)\rangle\right)d\left(\langle\psi(t)|\right)\right\} = 2\pi|g_0|^2 dt\,\sigma^-\hat\rho_s\sigma^+ \ .
\tag{3.3.13}
$$

Inserting Equation 3.3.8 and Equation 3.3.13 into Equation 3.3.7 results in

$$
\begin{aligned}
d\hat{\rho}_s(t) =& U_{eff}\hat{\rho}_s(t)dt + \hat{\rho}_s(t)U_{eff}^\dagger dt + 2\pi|g_0|^2\sigma^-\hat{\rho}_s(t)\sigma^+ dt \\
=& \left[-\frac{i}{\hbar}\mathcal{E}_0\left(\sigma^+ + \sigma^-\right)dt - \pi|g_o|^2\sigma^+\sigma^-\right]\hat{\rho}_s(t) + \hat{\rho}_s(t)\left[\frac{i}{\hbar}\mathcal{E}_0\left(\sigma^+ + \sigma^-\right) - \pi|g_o|^2\sigma^+\sigma^-\right]dt \\
& + 2\pi|g_0|^2\sigma^-\hat{\rho}_s(t)\sigma^+ dt \\
=& -\frac{i}{\hbar}\left[H_{sys}, \hat{\rho}_s(t)\right]dt - \pi|g_0|^2\left\{\sigma^+\sigma^-, \hat{\rho}_s(t)\right\}dt + 2\pi|g_0|^2\sigma^-\hat{\rho}_s(t)\sigma^+ dt\ , \quad (3.3.14)
\end{aligned}
$$

with H_{sys} being the Hamiltonian of the semi-classical drive, i.e. the first term from Equation 3.1.7. By dividing the equation by dt, the von-Neumann equation is obtained

$$
\frac{d\hat{\rho}_s(t)}{dt} = -\frac{i}{\hbar}\left[H_{sys}, \hat{\rho}_s(t)\right] + \Gamma_R \mathcal{D}[\sigma^-]\hat{\rho}_s(t)\ , \quad\quad\quad (3.3.15)
$$

with $\Gamma_R = 2\pi|g_0|^2$ and Lindblad dissipator

$$
\mathcal{D}[\sigma^-]\hat{\rho}_s(t) = \sigma^-\hat{\rho}_s(t)\sigma^+ - \frac{1}{2}\left\{\sigma^+\sigma^-, \hat{\rho}_s(t)\right\}\ . \quad\quad\quad (3.3.16)
$$

Thus, by tracing out the reservoir in the reduced density matrix picture, the Lindblad form is obtained on the basis of the QSSE. This Lindblad form simplifies the calculation of open quantum system. The system-reservoir interaction is described by the rate Γ_R, where excitations of the system dissipate into the environment. This Lindblad dissipator forms the basis for calculating open quantum systems with factorized system-reservoir dynamics in Part II of this thesis. However, in Part III of this thesis, the entanglement between system and reservoir becomes relevant, which is why the reservoir states are then considered as part of the open quantum many-body system.

4.

Ergodicity versus many-body localization in closed quantum systems

When a many-body system reaches thermal equilibrium, the microscopic dynamics becomes irrelevant to describe the whole system and the description with macroscopic observables such as temperature or free energy suffices to govern the macroscopic dynamics. However, when studying systems out-of-equilibrium, the law of thermodynamics are not applicable and the description on a microscopic scale is necessary.

A system reaching thermal equilibrium is characterized by its ergodic behaviour, where the whole phase space is explored and thus, initial information is hidden in thermodynamic observables [16]. This leads to the question if an out-of-equilibrium many-body system remains out-of equilibrium for long times or if it necessarily reaches a thermal equilibrium. In the past, it has been shown that a broad class of systems shows ergodicity breaking when being subject to random disorder. This is known as many-body localization (MBL) a generalization from Anderson localization of non-interacting systems to interacting systems. These two competing concepts are sketched in Figure 4.1. As a model system it is convenient to consider electrons on a lattice potential. The electrons interact with each other due to nearest-neighbor Coulomb interaction and are allowed to tunnel through the potential barrier and thus, hop from site to site. Initially, one electron is located at each even site whereas the odd sites are unoccupied. Thus, initially the electrons obey a non-uniformly distributed density pattern which is an out-of-equilibrium situation. If the system is ergodic (top, right), at long times, the system has equilibrated and the probabilities of finding an electron at a specific site are uniformly distributed which is in agreement with a micro-canonical ensemble. In contrast, if there is strong random on-site disorder, it prevents the electron hopping and the electrons are localized at their initial position on the even sites. Thus, the out-of-equilibrium situation survives for long times. This localization also takes place in interacting systems which is surprising as the electrons constantly exchange information with each other and the entanglement entropy is growing with time. However, this entanglement growth is strongly suppressed and obeys an area-law scaling. This characteristic is referred to as MBL phase and is a new and unexpected type of ergodicity breaking [16].

The main aspect of this thesis is not to investigate MBL in detail. However, as many-body systems out-of-equilibrium form the main part of this thesis, an introduction to the topic of ergodicity and MBL is given within this chapter. In chapter 6, the transport of a many-body localizable system is investigated within the ergodic phase, already showing anomalous characteristics.

In chapter 9, the MBL phase is used to create discrete time translational symmetry breaking for a many-body system to create a robust discrete time crystal, being out-of-equilibrium for long times.

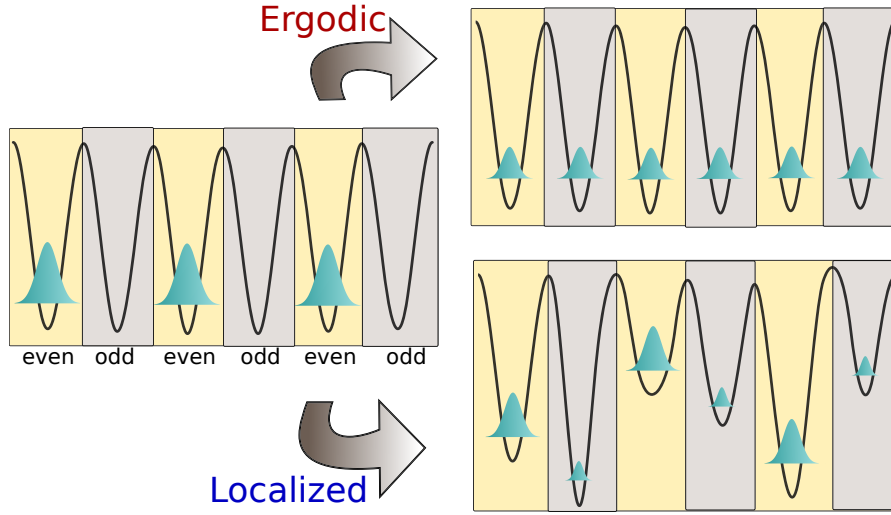Thus, this chapter serves as an introduction to these two phases of many-body quantum systems in general.

Figure 4.1.: Interacting particles are initialized in a non-uniform density pattern (only even sites are occupied, left). For an ergodic system, after unitary time evolution of the many-body quantum system, all subsystems show the same density pattern (top, right), due to thermalization with the large many-body system. In contrast, the initial information of all subsystems remains accessible in a localized system (bottom, right). This ergodicity breaking is achieved by random on-site disorder, indicated by the different on-site potentials.

4.1. Quantum thermalization

The thermalization process of classical systems in statistical mechanics is based on the ergodicity hypothesis. This predicts that over a long period of time all microscopic states of the classical system are accessed with the same probability [16]. The whole system can thus be described by thermodynamical quantities.

However, in a quantum context this concept of ergodicity cannot be adapted directly due to the linear time evolution. In classical systems, ergodic behavior is often caused by nonlinearities leading to chaotic behavior and initially stored information is lost. In contrast, nonlinear effects are not present in quantum system on a global scale. This implies that the global many-body quantum system never explores the whole phase space. This intuitive behavior of evolving a quantum system in time is demonstrated on a general example: Expanding the initial states in Eigenstates of the many-body system $|\alpha\rangle$ it can be written as $|\psi(0)\rangle = \sum_\alpha c_\alpha |\alpha\rangle$. Time evolving an initial state which is one of the many-body Eigenstates results in an additional phase factor which is the energy of that Eigenstate $\mathcal{E}_\alpha$

$$|\psi(t)\rangle = e^{-i\mathcal{H}t}|\psi(0)\rangle = \sum_\alpha c_\alpha e^{-i\mathcal{E}_\alpha t}|\alpha\rangle \ . \tag{4.1.1}$$

This shows that the probability of finding the system in a given Eigenstate $|\alpha\rangle$ is only described by the probability $|c_\alpha|^2$ and does not change over time. Thus, the probability of finding a many-body quantum system in a certain Eigenstate only depends on the initial

conditions which is clearly non-ergodic in a classical sense.

It becomes clear that globally, a quantum system never satisfies the classical ergodicity hypothesis. However, a broad class of many-body quantum system shows ergodic behavior, even under unitary time evolution, when considering small subsystems as for example a single spin in a many-body system. When describing the rest of the many-body system as a reservoir for the single spin, interactions with the many degrees of freedom results in a thermalization of the single spin with the rest of the many-body system. The reason is that the rest of the many-body quantum system acts as a heat bath for the subsystem. Thus, even when global observables cannot be described by thermodynamical quantities, local observables such as the single spin magnetization indeed show thermalizing behavior [67, 15].

An intuitive explanation of quantum ergodicity is given by the infinite time average expectation value of Eigenstates. The infinite time average of an operator $\hat{\mathcal{O}}$ is defined as [68]

$$\langle\hat{\mathcal{O}}\rangle_{\infty} = \lim_{\tau\to\infty}\frac{1}{\tau}\int_0^{\tau}dt\langle\psi(t)|\hat{\mathcal{O}}|\psi(t)\rangle = \sum_{\alpha}|c_{\alpha}|^2\langle\alpha|\hat{\mathcal{O}}|\alpha\rangle \ , \tag{4.1.2}$$

where it is assumed that off-diagonal terms of the operator oscillate at different frequencies than the diagonal terms and average out in the infinite integral [16]. Thus, the expectation value of an operator acting on global Eigenstates $|\alpha\rangle$ is given only by the choice of the initial state via $\langle\hat{\mathcal{O}}\rangle_{\infty} = \sum_{\alpha}|c_{\alpha}|^2\langle\alpha|\hat{\mathcal{O}}|\alpha\rangle$. However, the expectation value of an operator $\langle\beta|\hat{\mathcal{O}}|\beta\rangle$ with local Eigenstates $|\beta\rangle$ might become thermal [67, 15]. Note that the local Eigenstate $|\beta\rangle$ is referred to the Eigenstates of the subsystem. If a system quantum thermalizes, the assumption is that the infinite time average of an expectation value with local Eigenstates $|\beta\rangle$ agrees with the micro-canonic ensemble $\langle\hat{\mathcal{O}}\rangle_{\infty} = \langle\hat{\mathcal{O}}\rangle_{mc}$. This means a local expectation value is uniformly distributed for all local subsystems of the many-body system which is sketched in Figure 4.1 (top, right). In other words, a global expectation value of a many-body quantum system is given by the choice of the initial state. In contrast, a local expectation value becomes thermal even if initialized in an out-of-equilibrium state.

This is described by the Eigenstate thermalization hypothesis (ETH) which states that in a thermalizing quantum system, local Eigenstates have thermal expectation values for $t \to \infty$. In particular, this means, even when the global system is prepared in a many-body Eigenstate, expectation values of local subsystems agree with a thermodynamical ensemble in the infinite time average. In quantum systems, the ETH is often referred to as quantum ergodicity. Note that it is not clear if the ETH is a necessary condition for quantum thermalization. However, it has been shown that for all thermalizing quantum systems, almost all Eigenstates obey the ETH [12, 69]. The ETH has been experimentally demonstrated in the Ref. [13], where they showed that local observables indeed obey a thermal distribution while a global observable remains pure for all times due to the unitary time evolution.

Further information about quantum fluctuations in the infinite time average are necessary. Above it has been assumed that off-diagonal matrix elements of local operators average out in the infinite time average. However, strong fluctuations might be present disobeying a thermal behavior. Without going into detail, Ref. [68] introduced an Ansatz where off-diagonal matrix elements of local operators are damped by the entanglement entropy of the local subsystem which is defined as

$$S_A = -\operatorname{tr}\hat{\rho}_A\log_2\hat{\rho}_A \ , \tag{4.1.3}$$

where ρ_A is the reduced density matrix of the local subsystem. If the system obeys the ETH, the local entanglement entropy equals the thermal entropy $S_A = S_A^{th}$. Because S_A^{th} is an extensive quantity, it obeys a volume-law scaling $S_A^{th} \sim \text{vol}(A)$. This implies that quantum fluctuations in the infinite time average are bound by a volume-law scaling thermal entropy. This stands in strong contrast to an area-law scaling of the entropy for many-body localized systems which will be explained in the following section.

To conclude, the ETH states that if some local Eigenstates have thermal expectation values in the infinite time average, all local observables tend to a thermodynamical ensemble. The spreading of entanglement obeys a volume-law scaling. This is closely connected to the loss of the local initial information, which is hidden in local observables due to the strong entanglement spreading.

4.2. Many-body localization

A phenomenological explanation of quantum thermalization of a closed quantum many-body system has been given above. One broad class of systems which violate the ETH and therefore break ergodicity are Anderson localized systems [18]. These systems describe non-interacting particles in a random potential. Due to the random potential, hopping of the particles is strongly suppressed and the particles are localized at their initial position. Before explaining the concept of Anderson localization, it is convenient to introduce a standard model to describe the terms resulting in localization. The Heisenberg spin-chain with random on-site disorder reads

$$\mathcal{H} = \sum_{i=1}^{N-1} J_\perp \left(\sigma_i^x \sigma_{i+1}^x + \sigma_i^y \sigma_{i+1}^y \right) + \sum_{i=1}^{N-1} J_z \sigma_i^z \sigma_{i+1}^z + \sum_{i=1}^{N} h_i \sigma_i^z \ . \tag{4.2.1}$$

This is a model system of a one-dimensional spin-chain with N spins, where at each site i a single spin is considered. The first two terms with coupling $J_\perp$ describe spin-flips between neighboring sites. These terms do not describe interactions. This can be seen, when transforming the Heisenberg spin-chain to a model of spinless fermions via a Jordan-Wigner transformation [70]. The first two terms then describe a hopping of a single fermion from site to site. In contrast, the second term in Equation 4.2.1 describes interactions between the spins via J_z. This term is neglected when describing Anderson localization $J_z = 0$, but for MBL this is the crucial term to differentiate it from single particle localization. The last term describes random on-site disorder, which can be interpreted as a random deformation of the potentials in the particle picture (cp. Figure 4.1, bottom right). The Heisenberg spin-chain will be introduced in more detail in chapter 6.

Turning now to the explanation of Anderson localization, where the interactions are neglected $J_z = 0$. Assuming the initial state consists of a single spin-up at site i and all other spins pointing down. Considering the dynamics of this spin, if there is an Eigenstate which is localized with weight on site i, spin-flips are strongly suppressed and the spin-up survives for long times. Thus, at infinite times there is a non-zero probability of finding a spin-up at site i [14]. This stands in strong contrast to the ETH as initial information is still preserved. Without the disorder in Equation 4.2.1, within each time interval the spin might flip to neighboring sites. Thus, for $t \to \infty$ all sites have equal probability for a spin-up which is described by the micro-canonic ensemble.

If the disorder h_i is strong enough, all Eigenstates are localized which means the spin-up survives for all times and no information is exchanged with other Eigenstates. This means

that the entanglement entropy remains constant. However, this changes drastically if interactions are considered with $J_z \neq 0$. Even if spin-flips are suppressed by localized Eigenstates, interactions might suffice to close the energy gap between localized Eigenstates. The discovery of localization in the presence of interactions J_z was therefore a surprising feature and opened a new field of research called many-body localization (MBL), including experimental realizations [20, 21, 71, 72, 14, 30, 31, 33, 32, 73]. Although it has similarities to Anderson (single particle, $J_z = 0$) localization, it has strikingly different properties. Both types of localization are detected by a vanishing conductivity, which means there is no transport if the system is localized, describing a perfect insulator. Furthermore, the Eigenstate spectrum of both types is similar (at least deep in the MBL regime). However, the entanglement growth of MBL systems spreads logarithmically slow [23, 74, 24] which stands in strong contrast to the constant entanglement entropy of Anderson localization. The concept of MBL systems, including the logarithmic growth of entanglement, is explained by the so called local integrals of motions (LIOM) [75, 72, 76]. Assuming the system is deep within the MBL regime, where all Eigenstates are localized such that the Hamiltonian is diagonalized with quasi-local unitary transformations $\tau_i^z = U\sigma_i^z U^\dagger$. This results in the LIOM [16]

$$\tau_i^z = Z\sigma_i^z + \sum_n V_i^{(n)} \hat{O}_i^{(n)} , \qquad (4.2.2)$$

where Z is the overlap with the physical operator σ_i^z and the operator $\hat{O}_i^{(n)}$ contains contributions from neighboring operators with distance n. However, the overlap with the distant operators $V_i^{(n)}$ is exponentially small due to the localization. This is why the τ_i^z are called quasi-local bits (l-bit) as they have a large overlap with σ_i^z which is the key feature of localized systems. Note that this is only true for localized systems and for a system obeying the ETH, the l-bits would be highly non-local with vanishing overlap $Z\sigma_i^z$.

The exact construction of such LIOM, especially the choice of the unitary transformation U, is challenging [77, 78, 79]. However, the LIOM serve as a phenomenological model to explain MBL phenomena. Assuming the Hamiltonian can be written in terms of LIOM, the Hamiltonian the reads [75]

$$\mathcal{H}_{LIOM} = \sum_i \tau_i^z + \sum_{i,j} J_{i,j}\tau_i^z\tau_j^z + \sum_{i,j,k} J_{i,j,k}\tau_i^z\tau_j^z\tau_k^z + \dots \qquad (4.2.3)$$

In principle, every system can be diagonalized in such manner. Considering for example a many-body system obeying the ETH, each l-bit would have weight on all sites and the higher orders with couplings $J_{i,j}$ etc. would be very relevant. In contrast, for a MBL system, a description with LIOM is advantageous as each l-bit is quasi local. For example in a non-interacting localized system ($J_z = 0$), the l-bits would be the occupation in the corresponding local Eigenstate. Turning on small interactions, the l-bits become quasi local with small weight on other sites. This implies that the higher order couplings fall of exponentially with the distance due to the localization [16]

$$J_{i,j} = J_z e^{-\frac{|i-j|}{\xi}}, \quad J_{i,j,k} = J_z e^{-\frac{\max(|i-j|,|i-k|,|j-k|)}{\xi}} , \qquad (4.2.4)$$

where the length scale ξ is connected to the localization length.

The effective Hamiltonian in Equation 4.2.3 can be used to understand the Entanglement spreading. In a non-interacting system, the LIOM are truly local. Thus, they do not

exchange information with each other and the entanglement entropy remains constant [14]. Considering interactions, the LIOM become quasi local with exponentially small weight on distant sites. Considering two distant spins which are not nearest-neighbors, the two spins do not interact directly with each other but indirectly via all spins in between. The effective coupling between the two spins consists of all couplings of the spins in between. However, all couplings are exponentially small, thus, logarithmic growing entanglement is induced at time t between all spins within a distance L via $L \sim \xi \ln(J_z t)$ [14]. The logarithmic spreading of entanglement can be seen as an area-law scaling, where only the boundaries of each spin contribute to the entanglement as the coupling to further spins falls off exponentially with the distance. This stands in strong contrast to the volume-law scaling of thermalizing systems but also in contrast to constant entanglement of Anderson localized systems.

Thus, MBL describes a new robust dynamical phase of matter as it remains stable in the presence of interactions together with logarithmic growth of entanglement. Similar to Anderson localization, MBL describes a perfectly insulating system. Therefore, the transport of spin-current is an important quantity to detect localization. The transport behavior in the ergodic phase for an open quantum system will be investigated in chapter 6 of this thesis.

To truly distinguish an MBL system from Anderson localization, the logarithmic entanglement spreading provides a useful tool. From a computational point of view, the slow growth of entanglement is advantageous when simulating with matrix product state methods. As matrix product states provide a formalism which allows to truncate large parts of the Hilbert space, depending on the entanglement entropy, large system sizes in the MBL phase become numerically accessible. Matrix product states will be introduced in chapter 7 of this thesis.

In chapter 9, MBL connected with MPS methods is used to simulate a large many-body system. In contrast to isolated MBL systems introduced in this chapter, an open quantum system will be studied. It is still under debate what survives of MBL in case of an open quantum system [34]. In chapter 9 it will be shown that the time crystal within a MBL phase is stabilized against external dissipation due to feedback dynamics which are introduced in chapter 8.

PART II

Factorized system-reservoir dynamics

5.

Many-emitter phonon lasing

In this part of the thesis, open many-body systems are investigated. The focus does not lie on the reservoir degrees of freedom but on the many-body system itself. It is assumed that the investigated many-body system and external reservoir states factorize and the Born-Markov approximation is valid. Thus, the Lindblad form in Equation 3.3.16 suffices to describe the coupling to the surrounding reservoir.

As a first many-body system, quantum dots placed inside a cavity are considered with focus on many-body effects. In analogy to the standard optical laser [80, 81], the concept of coherent amplification by stimulated emission is adapted to sound waves. The idea is to create coherent vibrations, which could lead to new types of non-demolishing measurement devices [82]. Quantized vibrations of the lattice ions in a solid form the quasi-particle called phonon. The generation of coherent phonon statistics is furthermore interesting for fundamental physics itself. The idea of the so called phonon laser has led to a variety of experimental and theoretical proposals to generate coherent phonons in e.g. trapped ions [83, 84], compound microcavities [85], NV-centers [86], electromagnetic resonators [87] and semiconductor devices [88, 89, 90, 91, 92, 93]. In order to achieve lasing, the necessary ingredients are the active medium, an external pump mechanism, inversion and a cavity to confine a single mode. Thus, the design of the phonon or acoustic cavities [94, 95, 96, 97, 98, 99] forms the basis for phonon lasing. Via a combination of different lattice constants of the surrounding solid, a superlattice allows to confine a single phonon mode inside the cavity [94, 95, 96]. Quality factors up to $Q = 10^5$ have been achieved in the past [97, 98, 99]. The investigated model setup is based on a single quantum dot as an active medium [100] embedded within an acoustic cavity. Via external coherent optical excitation of the quantum dot [101], the induced Raman process [91, 92] leads to a coherent phonon population inside the acoustic cavity. The focus within this chapter lies on a generalization of the single-emitter quantum dot to a many-emitter system [102, 103]. The quantum dots are assumed to be identical and not coupled directly with each other, but via the cavity phonon field. For optical cavities this is known as the Tavis-Cummings model [104, 105]. Due to the many-emitter setup, collective effects are present. One example is superradiance, discovered by Dicke [106, 107, 108, 109]. Similar collective phenomena have been found recently for phonons as well [110, 111]. These collective processes due to a many-body setup, combined with the generation of coherent phonons by stimulated emission will be the focus of this chapter.

5.1. Model

As a model system, the semi-classical coherently driven TLS in Equation 3.1.1 forms the basis for a single emitter. For an application, the idea is to use a semiconductor quantum dot, which is modelled by a TLS [91]. Here, the single-emitter setup is generalized to many

emitters. To start with a simple model, the TLSs are assumed to be identical with frequency difference ω_{01} between the ground $|0\rangle_i$ and excited state $|1\rangle_i$ of emitter i. This will be generalized to non-identical emitters in section 5.3. The coupling to the external photon reservoir will be described by the Lindblad master equation due to factorized system-reservoir dynamics, derived in Equation 3.3.16, resulting in a rate for the spontaneous emission Γ_R of the TLS. In addition, a surrounding phonon reservoir is assumed leading to a cavity loss κ which is also described via a Lindblad dissipator.

As mentioned before, the quantum dots are embedded within a phonon cavity. This results in a single frequency ω_{ph} for the free evolution of the phonons. In this thesis, phonons are described by the operators $\hat{c}^{(\dagger)}$ to clarify the presence of a single-mode phonon cavity. Note that phonons and photons obey the same bosonic commutation relations. However, the coupling to the electronic degrees of freedom is fundamentally different, giving rise to the effects investigated within this chapter.

The Hamiltonian for the free evolution of the TLS together with the free evolution of the phonon cavity reads

$$\mathcal{H}_0 = \hbar\omega_{01}\sum_{i=1}^{N}\sigma_i^+\sigma_i^- + \hbar\omega_{ph}\hat{c}^\dagger\hat{c} \ . \tag{5.1.1}$$

The pump mechanism is described as a semi-classical laser driving each TLS. The according Hamiltonian was derived in section 2.4. The external driving field is expressed as $\Omega(t) = 2\hbar\mathcal{E}_0\cos(\omega_L t)$, where ω_L is the frequency and $\mathcal{E}_0$ the Rabi-frequency of the driving laser. in the following, the Rabi-frequency $\mathcal{E}_0$ is denoted by Ω. The rotating wave approximation (RWA) was already performed, assuming the pump strength Ω to be small in comparison to the transition frequency ω_{01}. Furthermore, the driving frequency ω_L is assumed to be close to the TLS frequency ω_{01}. Note that the driving laser is always detuned by several phonon frequencies. The RWA is still justified as the phonon cavity frequency is orders of magnitudes smaller than the TLS frequency. Introducing the electron-phonon coupling, the interaction Hamiltonian reads

$$\mathcal{H}_I = \sum_{i=1}^{N}\left[\hbar\Omega\left(\sigma_i^- e^{i\omega_L t} + \sigma_i^+ e^{-i\omega_L t}\right) + \hbar g_{ph}\left(\hat{c} + \hat{c}^\dagger\right)\sigma_i^+\sigma_i^-\right] \ . \tag{5.1.2}$$

The second part describes the interaction between the TLSs and the cavity phonons via coupling g_{ph}. This diagonal coupling is responsible for the collective effects investigated within this chapter.

The frequency of the energy-gap ω_{01} deviates orders of magnitudes from the other involved frequencies. In order to deal numerically with these two time-scales, the Hamiltonian is transformed into a rotating frame with respect to ω_{01} as shown in Equation 3.1.3

$$\mathcal{H} = \frac{\hbar\Delta}{2}\sum_{i=1}^{N}\sigma_i^z + \hbar\omega_{ph}\hat{c}^\dagger\hat{c} + \sum_{i=1}^{N}\left[\hbar g_{ph}\left(\hat{c} + \hat{c}^\dagger\right)\sigma_i^+\sigma_i^- + \hbar\Omega\sigma_i^x\right] \ . \tag{5.1.3}$$

The difference to Equation 3.1.5 is that the external driving laser is detuned from the TLS transition frequency with $\Delta = \omega_L - \omega_{01}$. This detuning is the key parameter to trigger coherent phonon excitation in this setup, which is shown in Figure 5.1. The state of the system is expressed as $\bigotimes_i^N |n_{TLS}\rangle_i \otimes |n\rangle$, where $n_{TLS} \in \{0,1\}$ is the state of the ith TLS and $n \in [0,\infty)$ is the occupation of the phonon cavity mode, expressed in the phonon number basis. The excitation laser is blue detuned at the phonon cavity frequency $\Delta \approx \omega_{ph}$.

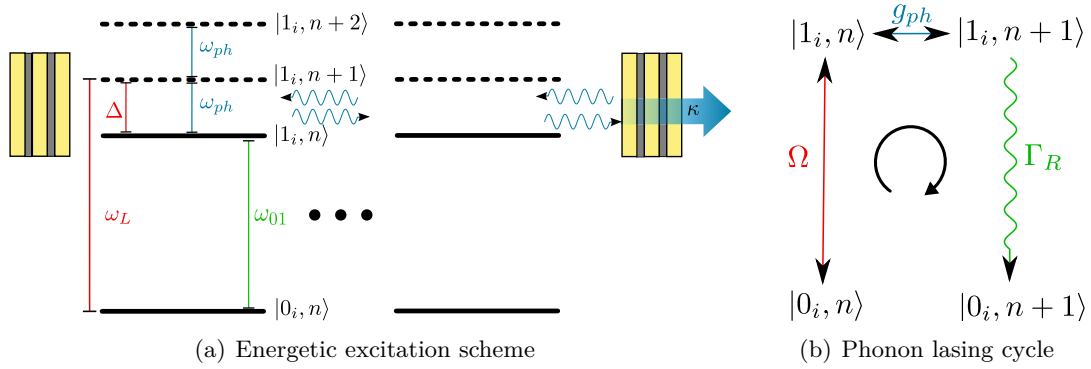(a) Energetic excitation scheme   (b) Phonon lasing cycle

Figure 5.1.: Illustration of the many-emitter setup leading to coherent phonon generation. (a) Solid lines denote the electronic energy levels with transition frequency ω_{01}. Dashed lines correspond to the virtual phonon energies ω_{ph}. The distributed Bragg-reflector structure on the level of the phonon energies symbolizes the acoustic cavity for this frequency. The cavity is subject to a phonon loss κ. The external laser ω_L is detuned at the anti-Stokes resonance $\Delta \approx \omega_{ph}$. (b) Starting in the ground state with n phonons, the TLS is excited by Ω. Due to the electron-phonon coupling g_{ph} a phonon is emitted into the cavity. The loop is closed due to a radiative decay Γ_R where the TLS ends up in the ground state again but with an additional phonon in the cavity $n + 1$.

Thus, in exciting one TLS from $|0\rangle_i$ to $|1\rangle_i$ there is additional energy left resulting in the creation of a phonon via g_{ph}. Via couplings Ω and g_{ph}, the state is brought from $|0_i, n\rangle$ to $|1_i, n+1\rangle$. If the cavity is already populated, the phonon is created due to a stimulated emission process [91]. This process is called the induced Raman process.

These processes are both reversible, indicated by the arrows in Figure 5.1(b). However, if an external mode continuum is assumed, as done in Equation 3.1.1, the TLS interacts with the photonic environment as well. For weak coupling strengths and general reservoirs, usually the Born-Markov approximation is performed to arrive at the Lindblad equation. This was shown in section 3.3 with a stochastic calculus. This stochastic calculus implies that the process in Equation 3.3.16 is an irreversible process. However, this irreversible spontaneous emission of photons to the surrounding reservoir is advantageous when it comes to phonon lasing. This process prevents the system from just going the way back from $|1_i, n+1\rangle$ to $|0_i, n\rangle$ by reabsorbing a cavity phonon. Thus, a radiative decay from $|1_i, n+1\rangle$ to $|0_i, n+1\rangle$ is a wanted process as it ensures that the lasing cycle starts from the beginning with an additional phonon inside the cavity in $|0_i, n+1\rangle$.

It was shown in section 3.3 that the Lindblad master equation is justified for factorized system-reservoir dynamics. Thus, the surrounding photon reservoir is described by Equation 3.3.16. Additionally, a surrounding phonon reservoir is assumed. This phonon reservoir is described by the Lindblad master equation as well and damps the cavity phonons via rate κ. Thus, in total the master equation for the reduced density matrix $\hat{\rho}_s$ reads

$$\dot{\hat{\rho}}_s = -\frac{i}{\hbar}[\mathcal{H}, \hat{\rho}_s] + 2\kappa \mathcal{D}[\hat{c}]\hat{\rho}_s + 2\Gamma_R \sum_{i=1}^{N} \mathcal{D}[\sigma_i^-]\hat{\rho}_s \ , \qquad (5.1.4)$$

with the dissipator $\mathcal{D}$ introduced in Equation 3.3.16.

The number of differential equations N_{DGL} of the reduced density matrix therefore scales as

$$N_{DGL} = \left(2^{N_{TLS}} N_{ph} \right)^2 \ , \tag{5.1.5}$$

where N_{TLS} is the number of emitters and N_{ph} the number state of considered phonons. Due to the open system dynamics, the phonon number of the cavity reaches a steady state for $t \to \infty$. The maximal number of considered phonons N_{ph} needs to be chosen according to the parameters such that all relevant phonon states are included. This cutoff is chosen such that the dynamics do not change for increasing N_{ph} which is in practice around $N_{ph} \sim 50$. Due to the number state for the cavity phonons and the resulting number of differential equations, the number of included emitters is restricted to a maximum of $N_{TLS} = 3$ in this chapter. However, this already results in $N_{DGL} = 16 \times 10^4$ which takes a long computation time to reach the steady state.

Initially, all TLS are set to their ground state $|0\rangle_i$. The phonons are assumed to obey a thermal distribution at temperature $T = 4K$. The set of equations is solved numerically up until all entries of the density matrix converge to their steady state value $\hat{\rho}_s(\infty)$. The relevant expectation value is then computed for the respective parameter set. The most important one is the expectation value of the phonon number $\langle n_{ph} \rangle$ of the acoustic cavity

$$\langle n_{ph} \rangle = \lim_{t \to \infty} \text{tr} \left(\hat{\rho}_s(t) \hat{c}^\dagger \hat{c} \right) \ . \tag{5.1.6}$$

This quantity measures the occupation of the phonon mode of the acoustic cavity. However, to determine whether the phonons obey a coherent statistics, the autocorrelation function $g^2(\tau)$ [112, 113] is another important quantity of this chapter. Its steady state value is defined as

$$g^2(\tau) = \lim_{t \to \infty} \frac{\left\langle \hat{c}^\dagger(t) \hat{c}^\dagger(t + \tau) \hat{c}(t + \tau) \hat{c}(t) \right\rangle}{\langle \hat{c}^\dagger(t) \hat{c}(t) \rangle^2} \ . \tag{5.1.7}$$

In this case, $\tau = 0$ is sufficient as $g^2(0) = 1$ gives a hint on coherent statistics, whereas a value $g^2(0) > 1$ is identified with thermal statistics. The autocorrelation function is computed as

$$g^2(0) = \lim_{t \to \infty} \frac{\text{tr} \left(\hat{\rho}_s(t) \hat{c}^\dagger \hat{c}^\dagger \hat{c} \hat{c} \right)}{\langle n_{ph} \rangle^2} \ . \tag{5.1.8}$$

5.2. Collective phonon processes

The induced Raman process takes place, when the TLS is excited with a blue detuned laser close to the phonon frequency $\Delta \approx \omega_{ph}$. In the Refs. [92, 93] it was shown that the exact frequency is subject to a shift with respect to the involved couplings. Maximal output is obtained for

$$\Delta = \omega_{ph} - \frac{g_{ph}^2}{\omega_{ph}} \ . \tag{5.2.1}$$

Thus, in addition to the phonon cavity frequency ω_{ph}, the energy to create coherent phonons is shifted to lower energies according to the electron-phonon coupling g_{ph}. The goal of this chapter is to show that this is only true for a single emitter and the many-emitter setup is subject to collective phenomena which include additional energy shifts. Note that in principle, the laser pump Ω also results in a shift of the driving frequency [92, 93]. To clarify the collective effects, Ω is chosen a magnitude smaller than the electron-phonon coupling g_{ph} which is why the energy shift Ω^2/Δ is neglected for the interpretation. In section 5.4 also higher pumping strengths are investigated.

In this section, the resonances for which collective phonon generation takes place will be investigated by varying Δ. In Figure 5.2 (top), the phonon number $\langle n_{ph} \rangle$ is shown for varying the optical detuning, normalized by the cavity frequency Δ/ω_{ph}. Thus, $\Delta/\omega_{ph} = 1$ would indicate the anti-Stokes resonance without additional frequency shifts. For one emitter (yellow, dashed), the resonance is red-shifted with respect to Equation 5.2.1 and reproduces the findings of Refs. [92, 93]. This resonance is called the single-emitter resonance in the following. However, for two emitters (red, dotted), the maximal phonon number is not obtained at the same resonance. The single-emitter resonance of the two-emitter case also results in lasing (cp. Figure 5.2 bottom) with a slightly higher phonon number, but does not result in double the phonon number as expected for adding a second emitter. This output is obtained at a second resonance which is even more red-shifted. This resonance is labeled the two-emitter collective resonance in the following. For three emitters (blue, solid), the single-emitter resonance as well as the two-emitter collective resonance is included, resulting in comparable phonon numbers. Furthermore, the three-emitter setup results in a third resonance which shows thrice the number of cavity phonons than the single-emitter resonance. These additional resonances are a characteristic and unexpected feature of the many-emitter phonon laser [114, 115] and are the subject of investigation of this chapter. Note, that the linewidth of the collective resonances narrow in comparison to the single-emitter resonance.

In Figure 5.2 (bottom), the steady state value of the $g^2(0)$-function is shown for varying Δ. At each resonance (the single and collective resonances), the statistics show $g^2(0) = 1$ which is associated to coherent phonon statistics. Thus, when the phonon emission is triggered by the induced-Raman process, the statistics of the cavity phonons is coherent which proves a stimulated emission of phonons. Surprisingly, this is also the case for the collective resonances including a higher number of coherent cavity phonons.

When the detuning is increased to higher driving frequencies, i.e. approximately the doubled cavity phonon frequency $\Delta \approx 2\omega_{ph}$, additional resonances appear with coherent phonon statistics $g^2(0) = 1$. Those resonances are two-phonon resonances which means that in a single laser loop two phonons are emitted due to the energy mismatch (cp. Figure 5.1). Thus, starting in $|0_i, n\rangle$ results in $|0_i, n+2\rangle$ in a single loop for a single emitter. In contrast to the one phonon resonances at $\Delta \approx \omega_{ph}$, the linewidth of the two-phonon resonances is narrowing due to the two-phonon process. However, the output of the two-phonon single-emitter resonance is twice as high as for the one-phonon single-emitter resonance. The collective two-emitter (two-phonon) resonance is also apparent for two and three emitters and results in a doubled phonon number compared to the collective two-emitter resonance at $\Delta \approx \omega_{ph}$. Note, that the three-emitter collective resonance does not appear for the investigated parameter set. This may have two reasons, on the one hand it is possible that the linewidth is too narrow to detect it by varying Δ numerically. Or, on the other hand, the pumping strength Ω might be too small to trigger this process. This will become
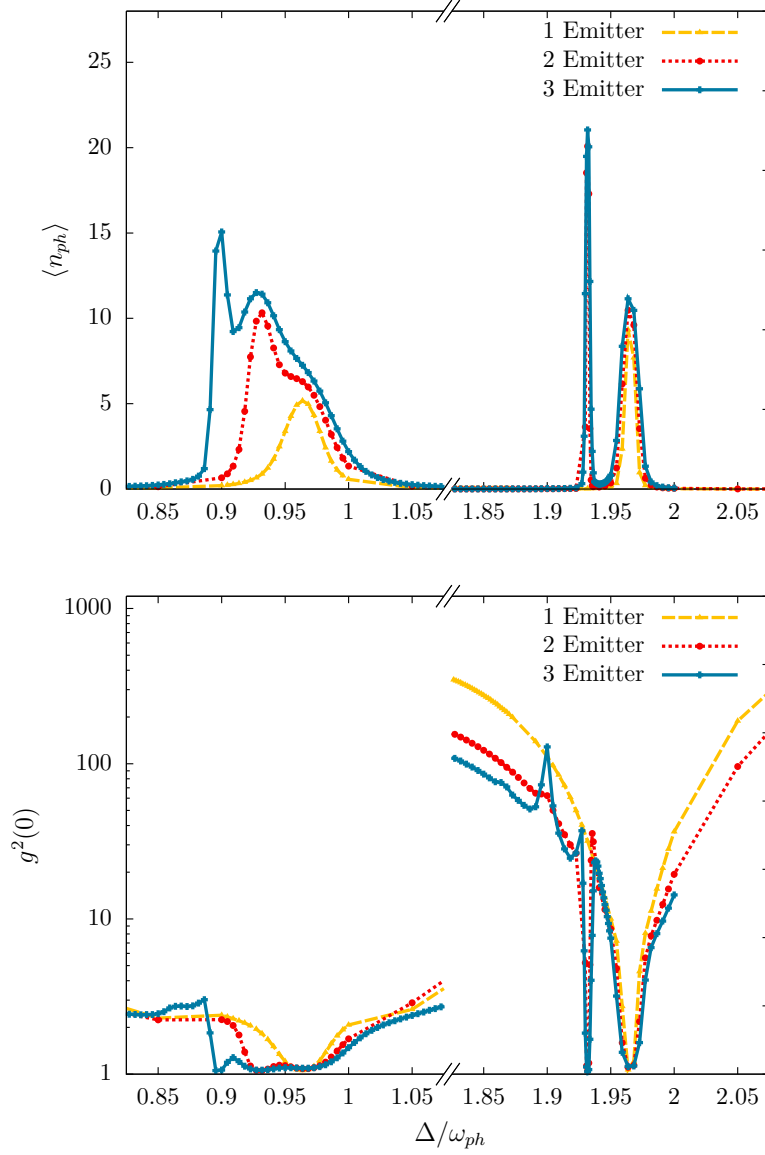
Figure 5.2.: Detuning of the TLS transition frequency Δ versus phonon number $\langle n_{ph} \rangle$ (top) and $g^2(0)$ (bottom). One emitter (yellow, dashed) shows a single resonance at $\Delta \approx \omega_{ph}$ (top, left). However, increasing the number of emitters, for two emitters (red, dashed) there are two resonances and for three emitters (blue, solid) there are three resonances. A similar pattern appears close to $\Delta \approx 2\omega_{ph}$. The second-order correlation function (bottom) shows coherent phonon statistics $g^2(0) = 1$ at the respective resonances. Parameters: $\omega_{01} = 2.28\ 1/fs$, $\omega_{ph} = 0.011\ 1/fs$, $\Omega = 4.56 \cdot 10^{-4}\ 1/fs$, $g_{ph} = 2 \cdot 10^{-3}\ 1/fs$, $\Gamma_R = 1 \cdot 10^{-5}\ 1/fs$, $\kappa = 5 \cdot 10^{-7}\ 1/fs$.

clear in the following, where the reason for the appearance of these collective resonances is investigated.

5.2.1. Effective Hamiltonian approach

To unravel the origin of the collective resonances for the many-emitter phonon laser, the idea is to transform the Hamiltonian in Equation 5.1.3 to compare it to a well-known many-emitter Hamiltonian which is the Tavis-Cummings model [104, 105]. It will become clear that when bringing the Hamiltonian in Equation 5.1.3 into a form, comparable to the Tavis-Cummings Hamiltonian, an additional term is included which is responsible for the collective resonances, resulting from the diagonal electron-phonon interaction. Similar to the Refs. [92, 116], the idea is to eliminate the first-order electronic processes and restrict it to the second-order process of cavity phonon generation. Thus, with one effective coupling constant, the electron is brought from the ground to the excited state and a phonon is created. Furthermore, the derived effective Hamiltonian will be restricted to the excitation condition $\Delta \approx \omega_{ph}$. To transform the Hamiltonian, a unitary operator S is defined such that

$$\mathcal{H}^{eff} = e^{iS}\mathcal{H}e^{-iS} \ . \tag{5.2.2}$$

A typical second-order perturbation treatment [92, 63, 59] is performed in expanding the exponential and cut the expansion such that

$$\mathcal{H}^{eff} = \mathcal{H}_0 + \mathcal{H}_I + [iS, \mathcal{H}_0] + [iS, \mathcal{H}_I] + \frac{1}{2}\left[iS\left[iS, \mathcal{H}_0\right]\right] \ . \tag{5.2.3}$$

With this, an Ansatz for the unitary operator is made such that it contains all relevant operators

$$S = \sum_{i=1}^{N}\left(\alpha_i\sigma_i^- + \alpha_i^*\sigma_i^+ + \gamma_i\sigma_i^+\sigma_i^-\hat{c} + \gamma_i^*\sigma_i^+\sigma_i^-\hat{c}^\dagger \right). \tag{5.2.4}$$

The first commutator of the expansion then reads

$$[iS, \mathcal{H}_0] = \sum_i i\hbar\Delta\left(\alpha_i\sigma_i^- - \alpha_i^*\sigma_i^+\right) + \sum_i i\hbar\omega_{ph}\sigma_i^+\sigma_i^-\left(\gamma_i\hat{c} - \gamma_i^*\hat{c}^\dagger\right) \ . \tag{5.2.5}$$

The first-order process is then eliminated by choosing appropriate coefficients. With

$$\alpha_i = \frac{i\Omega}{\Delta} \ , \ \gamma_i = \frac{ig_{ph}}{\omega_{ph}} \ , \tag{5.2.6}$$

the first commutator cancels out with the interaction Hamiltonian such that

$$[iS, \mathcal{H}_0] = -\mathcal{H}_I \ , \tag{5.2.7}$$
$$[iS\left[iS, \mathcal{H}_0\right]] = -\left[iS, \mathcal{H}_I\right] \ . \tag{5.2.8}$$

With this, the effective Hamiltonian is derived via

$$\mathcal{H}^{eff} = \mathcal{H}_0 + \frac{1}{2}\left[iS, \mathcal{H}_I\right] \ . \tag{5.2.9}$$

The commutator with the interaction Hamiltonian reads

$$[iS, \mathcal{H}_I] = \sum_i^N \left[-\frac{\hbar\Omega g_{ph}}{\Delta_i} \left(\sigma_i^- + \sigma_i^+ \right) \left(\hat{c}^\dagger + \hat{c} \right) + \frac{2\hbar\Omega^2}{\Delta_i} \sigma_i^z \right] + \frac{\hbar\Omega g_{ph}}{\omega_{ph}} \sum_i^N \left(\sigma_i^+ \hat{c}^\dagger - \sigma_i^- \hat{c}^\dagger + h.c. \right)$$
$$+ \frac{\hbar g_{ph}^2}{\omega_{ph}} \sum_{i,j}^N \left\{ -\left[\sigma_i^+ \sigma_i^- \hat{c}, \sigma_j^+ \sigma_j^- \left(\hat{c}^\dagger + \hat{c} \right) \right] + \left[\sigma_i^+ \sigma_i^- \hat{c}^\dagger, \sigma_j^+ \sigma_j^- \left(\hat{c}^\dagger + \hat{c} \right) \right] \right\} .$$

$$(5.2.10)$$

The last term describes the interaction between two emitters i and j. In general, the spin-matrices for different emitters commute with each other. However, the cavity operators do not commute. This can be interpreted as an interaction between emitters, mediated by the cavity phonons. Thus, there is a part of the last term in Equation 5.2.10 which does not reduce to a sum of a single emitter which is the crucial term for the collective resonances. Rearranging Equation 5.2.10 results in

$$[iS, \mathcal{H}_I] = \hbar \sum_i^N \left(\frac{2\Omega^2}{\Delta} \sigma_i^z - \frac{2g_{ph}^2}{\omega_{ph}} \sigma_i^+ \sigma_i^- \right) - \sum_{\substack{i,j \\ i \neq j}}^N \frac{2g_{ph}^2}{\omega_{ph}} \sigma_i^+ \sigma_i^- \otimes \sigma_j^+ \sigma_j^-$$
$$+ \hbar \sum_i^N \Omega g_{ph} \left(\frac{1}{\Delta} + \frac{1}{\omega_{ph}} \right) \left(\sigma_i^+ \hat{c}^\dagger + \sigma_i^- \hat{c} \right)$$
$$+ \hbar \sum_i^N \Omega g_{ph} \left(\frac{1}{\Delta} - \frac{1}{\omega_{ph}} \right) \left(\sigma_i^- \hat{c}^\dagger + \sigma_i^+ \hat{c} \right) .$$

$$(5.2.11)$$

The second term in the first line is the interaction between emitters. The last line can be neglected for driving close to the anti-Stokes resonance $\Delta \approx \omega_{ph}$. Inserting Equation 5.2.11 into Equation 5.2.9 and shifting the origin of the σ_i^z terms results in the effective Hamiltonian

$$\mathcal{H}^{eff} = \hbar\omega_{ph}\hat{c}^\dagger\hat{c} + \sum_i^N \hbar \left(-\Delta - \frac{2\Omega}{\Delta} - \frac{g_{ph}^2}{\omega_{ph}} \right) \sigma_i^+ \sigma_i^- - \sum_{\substack{i,j \\ i \neq j}}^N \frac{g_{ph}^2}{\omega_{ph}} \sigma_i^+ \sigma_i^- \otimes \sigma_j^+ \sigma_j^-$$
$$+ \hbar \sum_i^N \frac{\Omega g_{ph}}{2} \left(\frac{1}{\Delta} + \frac{1}{\omega_{ph}} \right) \left(\sigma_i^+ \hat{c}^\dagger + \sigma_i^- \hat{c} \right) .$$

$$(5.2.12)$$

By defining the effective transition frequency

$$\omega_{eff} = -\Delta - \frac{2|\Omega|^2}{\Delta} - \frac{g_{ph}^2}{\omega_{ph}} \tag{5.2.13}$$

and effective coupling strengths

$$g_{eff} = \frac{\Omega g_{ph}}{2} \left(\frac{1}{\Delta} + \frac{1}{\omega_{ph}} \right) , \tag{5.2.14}$$
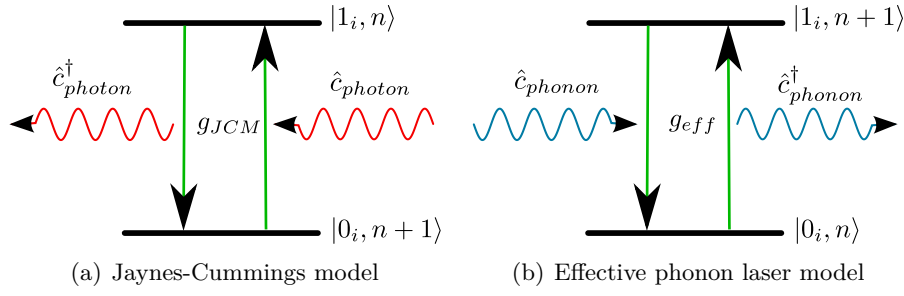
(a) Jaynes-Cummings model   (b) Effective phonon laser model

Figure 5.3.: Comparison of the Jaynes-Cummings model with the effective phonon laser for a single emitter i. (a) The interaction of a TLS with cavity photons in RWA (counter rotating terms are neglected) results in the annihilation of cavity photons when the TLS is excited via g_{JCM} and vice versa. (b) In contrast, for the effective Hamiltonian, a phonon is created when the TLS is excited via g_{eff} and vice versa.

the effective Hamiltonian becomes formally close to the Tavis-Cummings Hamiltonian. The effective Hamiltonian is split into three parts to highlight the additional interaction between emitters

$$\mathcal{H}^{eff} = \mathcal{H}_0^{eff} + \mathcal{H}_I^{eff} + \mathcal{H}_{E-E}^{eff} \ , \tag{5.2.15}$$

with $\mathcal{H}_{E-E}^{eff}$ as the many-particle interaction term

$$\mathcal{H}_0^{eff} = \sum_{i=1}^{N} \hbar\omega_{eff}\sigma_i^+\sigma_i^- + \hbar\omega_{ph}\hat{c}^\dagger\hat{c} \ , \tag{5.2.16}$$

$$\mathcal{H}_I^{eff} = \sum_{i=1}^{N} \hbar g_{eff} \left(\sigma_i^-\hat{c} + \sigma_i^+\hat{c}^\dagger\right) \ , \tag{5.2.17}$$

$$\mathcal{H}_{E-E}^{eff} = -\sum_{i\neq j}^{N} \frac{g_{ph}^2}{\omega_{ph}} \left(\sigma_i^+\sigma_i^- \otimes \sigma_j^+\sigma_j^-\right) \ . \tag{5.2.18}$$

Initially, it was assumed that all emitters are identical. Thus, Equation 5.2.16 and Equation 5.2.17 do not differ from the case of a single emitter [92] except for the sum over the number of emitters. However, Equation 5.2.18 is an additional term resulting from the interaction between emitters, mediated by the cavity phonons. This term is crucial for the resonances of the many-emitter phonon laser. Before analyzing this term in detail, the analogy to the Tavis-Cummings Hamiltonian is discussed: Although, formally it looks similar, there is a fundamental difference to the Tavis-Cummings model and photons in general. The creation and annihilation of cavity excitations is reversed for phonons as it can be seen in Figure 5.3(b). By exciting the TLS, a phonon is created via g_{eff} and vice versa. As the first-order process was eliminated, now a single process combines the excitation of the TLS via Ω as well as the creation of a phonon via g_{ph}. In contrast, for the interaction of a TLS with cavity photons in RWA, an excitation within the TLS is created by annihilating a cavity photon via coupling g_{JCM} as it can be seen in Figure 5.3(a). This illustrates the difference between a laser and the phonon laser as the electron-phonon interaction is diagonal. When comparing the effective Hamiltonian to the Tavis-Cummings
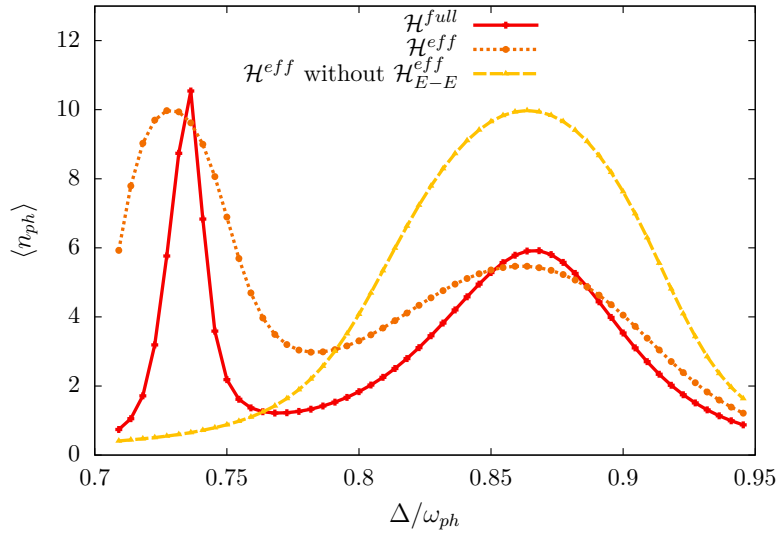
Figure 5.4.: Comparison of the full (red, solid) and the effective Hamiltonian (orange, dotted) for two emitters. Both models are in good agreement. The maximum is slightly red-shifted for the effective Hamiltonian with a smaller phonon number and a broader linewidth. When $\mathcal{H}^{eff}_{E-E}$ is not considered, the effective Hamiltonian (yellow, dashed) shows only the single-emitter resonance with twice the phonon number. The coupling strength g is chosen twice as large as before to visualize the splitting of the resonances.

Hamiltonian beyond RWA [117], the effective Hamiltonian is comparable to the counter rotating terms which are not energy conserving. For the lasing cycle, this implies that the ground state $|0_i\rangle$ can be seen as the state which has to be populated to create inversion for achieving lasing. This again clarifies the importance of a radiative decay Γ_R for the phonon lasing cycle as it is the parameter to create population inversion [91, 92].

For the many-emitter phonon laser, the most important difference is the additional term $\mathcal{H}^{eff}_{E-E}$, resulting from the interaction between emitters via the cavity phonon field. In Figure 5.4, the effective Hamiltonian for two emitters is evaluated. Comparing $\mathcal{H}^{full}$ and $\mathcal{H}^{eff}$, both are in a good agreement. Both, the single-emitter as well as the collective resonance are well described by the effective Hamiltonian, although the resonances are slightly red-shifted and the maximum and linewidth is different. This might be due to the neglected term in Equation 5.2.11 in setting $\Delta = \omega_{ph}$. As the resonances are red-shifted from the anti-Stokes resonance, this term might have small relevance. By neglecting $\mathcal{H}^{eff}_{E-E}$, it becomes clear in Figure 5.4 that this term is responsible for the splitting of the single-emitter and collective resonances. Without $\mathcal{H}^{eff}_{E-E}$, the two-emitter setup only shows the single-emitter resonance with approximately twice the number of phonons compared to the single-emitter setup.

The effective transition frequency ω_{eff} in Equation 5.2.13 consists of two terms which add up to the detuning. On the one hand $2|\Omega|^2/\Delta$ which is negligible due to the chosen parameters and on the other hand g^2_{ph}/ω_{ph} which is responsible for the red-shift of the single-emitter resonance. In addition, the many-body interaction $\mathcal{H}^{eff}_{E-E}$ has the same prefactor g^2_{ph}/ω_{ph} and also contributes to the effective transition frequency if both emitters are found in the excited state. This explains why the collective resonance for two emitters is
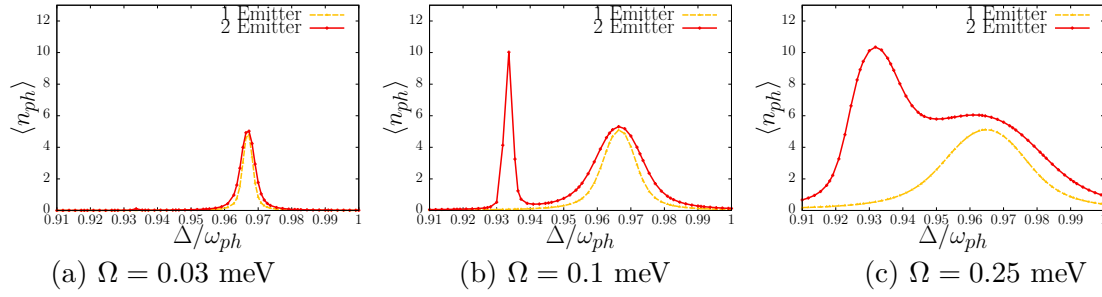
(a) $\Omega = 0.03$ meV   (b) $\Omega = 0.1$ meV   (c) $\Omega = 0.25$ meV

Figure 5.5.: Phonon number versus optical detuning for three different pump strengths Ω. For low pumping strengths (a), only the single-emitter resonance is apparent. Increasing the pumping strength (b), for two emitters it is probable for both emitters being excited at the same time such that eq. (5.2.18) becomes relevant. For higher pumping strengths (c), the collective resonance shows twice as much phonons at the collective resonance than at the single-emitter resonance. Furthermore, the resonances are broadening due to the stronger pumping, such that both resonances overlap.

red-shifted with $2g_{ph}^2/\omega_{ph}$. Knowing that $\mathcal{H}_{E-E}^{eff}$ is responsible for the collective resonances, it will be investigated in more detail in the following.

5.2.2. Collective resonances

The lasing cycle at the respective resonance is analyzed in analogy to Figure 5.1(b). For simplicity, the interpretation is limited to two emitters. For the single-emitter resonance, one of the emitters is excited at $|1_i, n\rangle$. By interacting with a cavity phonon, a second phonon is generated via a stimulated emission process resulting in $|1_i, n+1\rangle$. Due to the involved couplings, this process is most effective for a detuning calculated via Equation 5.2.13.

The same idea holds for the two-emitter collective resonance where two emitters are involved. Both emitters are excited in $|1_i, 1_j, n\rangle$ and create collectively two cavity phonons via stimulated emission resulting in $|1_i, 1_j, n+2\rangle$. In other words, both emitters collectively generate a phonon, resulting in two more phonons in the cavity. When both emitters are excited at the same time, an additional red-shift has to be considered for the excitation frequency according to Equation 5.2.18 resulting in

$$\Delta^{collective} \approx \omega_{ph} - \frac{2g_{ph}^2}{\omega_{ph}} \ . \tag{5.2.19}$$

Due to this process, the phonon number is doubled and results in a linear scaling of the phonon number with the number of emitters. In Figure 5.2 a narrowing of the linewidth is observed which indicates a longer lifetime of the collective excitation of the emitters.

In order to verify the collective red-shift in Equation 5.2.18, its dependence on the pumping strength is investigated. As it is required that both participating emitters are in the excited state, the pumping strength would have a huge impact on the collective resonance as Ω brings the TLS to the excited state. Indeed, the collective resonance disappears for small pumping strengths where the single-emitter resonance is lasing which is shown in Figure 5.5(a). For higher pumping strengths, Figure 5.5(b) shows that also the collective resonance starts lasing as it becomes probable for both emitters being in the excited state. After the resonances reach the maximal phonon number which is linear to the number

of participating emitters, a further increase of the pumping strength results in linewidth broadening Figure 5.5(c).

Thus, the recipe to address collective phonon generation is to adjust the excitation frequency according to the number of participating emitters as well as ensuring a high pumping strength Ω such that it is probable for all participating emitters to be in the excited state at the same time. However, a detuning at the single-emitter resonance only results in phonon generation of an individual emitter including a limit for the maximal phonon number. The advantage is that without knowing the exact shift-dependencies, the single-emitter limit is included in the many-emitter setup as well. Furthermore, varying the detuning allows to choose between different phonon intensities in a many-emitter setup, as long as g_{ph} is large enough that the resonances split up.

This brings up an important point: The position of the resonances is very sensible to the electron-phonon coupling g_{ph}. A comparable small g_{ph} would smear out all resonances as the position scales as $N g_{ph}^2 / \omega_{ph}$ and every resonance would be addressed close to the anti-Stokes resonance. In practice, the exact value of the electron-phonon coupling g_{ph} is often unclear. As the position of the resonances is highly sensible on g_{ph}, these findings could lead to an experimental setup to deduce the electron-phonon coupling for the involved materials as well.

5.2.3. Two-phonon resonances

Having identified the additional resonances in a many-emitter setup close to $\Delta \approx \omega_{ph}$ (cp. Figure 5.2) with collective phonon generation due to Equation 5.2.18, the resonances close to $\Delta \approx \mathbf{2}\omega_{ph}$ remain to be interpreted. In contrast to $\Delta \approx \omega_{ph}$, where additional resonances appear due to collective phonon generation of the respective number of emitters, only one additional collective resonance appears close to the two-phonon resonance. Furthermore, the phonon number for driving at the two-phonon resonance is increased approximately by a factor of two.

The first resonance close to $\Delta \approx \mathbf{2}\omega_{ph}$ is called the single-emitter two-phonon resonance. The reason is that an individual emitter is excited by the driving laser with a detuning almost twice the cavity frequency. Thus, an individual emitter is brought from $|0_i, n\rangle$ to $|1_i, n + 2\rangle$ in a single lasing loop (cp. Figure 5.1(b)). This means, in a single loop, two phonons are created in the cavity by a single emitter. This is in contrast to the two-emitter collective resonance close to $\Delta \approx \omega_{ph}$ where two phonons are created by two emitters collectively $|1_i, 1_j, n + 2\rangle$. On the one hand, two phonons are created by an individual emitter in a single loop and on the other hand, two phonons are created by two emitters collectively in a single loop. However, comparing both resonances, the phonon number as well as the linewidth is similar for both excitation schemes.

The collective resonance is also present for driving at the two-phonon resonance. This process results in a collective generation of four phonons by two emitters in a single loop. Two emitters are excited $|1_i, 1_j, n\rangle$ and create four phonons by interacting with the cavity field $|1_i, 1_j, n + 4\rangle$. In Figure 5.2 it becomes clear that a detuning at this resonance results in four times the phonons compared to the single-emitter resonance and twice the number of phonons compared to the two-emitter collective / single-emitter two-phonon resonance. Furthermore, its linewidth is very narrow compared to the other resonances. This leads to the three-emitter collective two-phonon resonance which is not apparent in Figure 5.2. This resonance is identified with a process of three emitters $|1_i, 1_j, 1_k, n\rangle$ collectively generating six phonons in a single loop $|1_i, 1_j, 1_k, n + 6\rangle$. Thus, each emitter creates two phonons simultaneously. Its linewidth is very narrow and it becomes only visible when increasing the
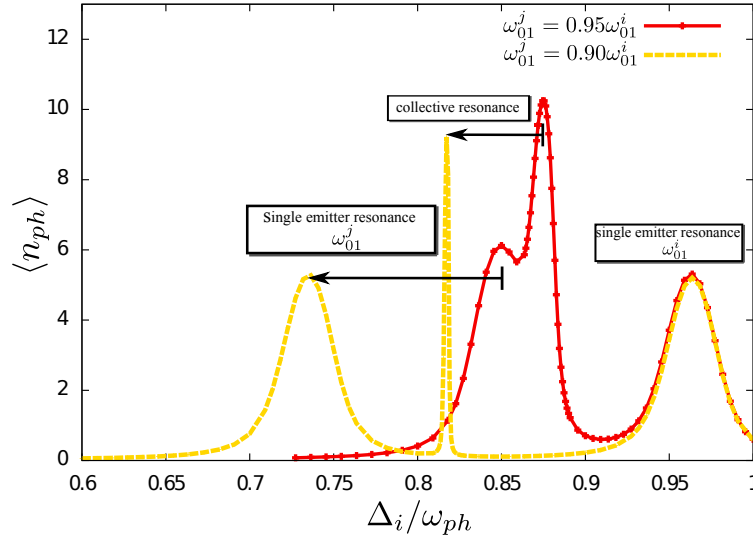
Figure 5.6.: Detuning versus phonon number for two emitters i and j which differ in the transition frequency. The second emitter has either 5% (red,solid) or 10% (yellow, dashed) difference in ω_{01}^j, while the first one is kept at the same transition frequency as before. Both emitters have different single-emitter resonances. In both cases, the collective resonance is still visible. The linewidth of the collective resonance narrows and the phonon number decreases for increasing difference in the transition frequencies. The position of the collective resonance is a mixture of both transition frequencies.

pump strength. For the investigated pump strength in Figure 5.2, no according resonance was identified. For higher pump strength it became apparent as well.

5.3. Non-identical emitters

One requirement for the Hamiltonian in Equation 5.1.3 was that all emitters are identical with respect to their transition frequencies and the electron-phonon coupling. However, realistic emitters such as quantum dots differ in size. This results in different transition frequencies ω_{01}^i and electron-phonon couplings g_{ph}^i for each emitter i [118, 119, 120, 9]. The purpose of this section is to analyze, if the collective effects found in section 5.2 also hold for non-identical emitters. In particular, it will be shown which differences in transition frequencies or electron-phonon couplings can be tolerated to still observe collective phonon generation.

Starting with a difference in the transition frequencies, the positions of the resonances are sensible for non-identical emitters as the detuning itself has to be adjusted. It is assumed, that one emitter i has the same transition frequency ω_{01}^i as before and a second emitter is assumed to have a different transition frequency ω_{01}^j. The resulting resonances are shown in Figure 5.6 for $\omega_{01}^j = 0.95\omega_{01}^i$ (red, solid) and $\omega_{01}^j = 0.90\omega_{01}^i$ (yellow, dashed). The single-emitter resonance of emitter i does not change as it still has the same transition frequency. As expected, the single-emitter resonance of emitter j is red-shifted to lower frequencies. However, the collective resonance is still apparent and for both cases found between the two single-emitter resonances. For a deviation of 10%, the collective resonance is narrowing remarkably such that it can be concluded that a higher deviation in the

transition frequencies might eliminate collective effects. As it can be seen well in Figure 5.6, the collective resonance is located at a driving frequency which is a mixture of both transition frequencies as both emitters participate collectively. The position of the collective resonance is estimated by

$$\Delta^{collective} = \omega_{ph} - \frac{\omega_1^{cv} - \omega_2^{cv}}{2} - \frac{2g_{ph}^2}{\omega_{ph}} \tag{5.3.1}$$

and agrees well with both investigated cases. For identical emitters, the second summand vanishes and yields the position of the collective resonance found in section 5.2.
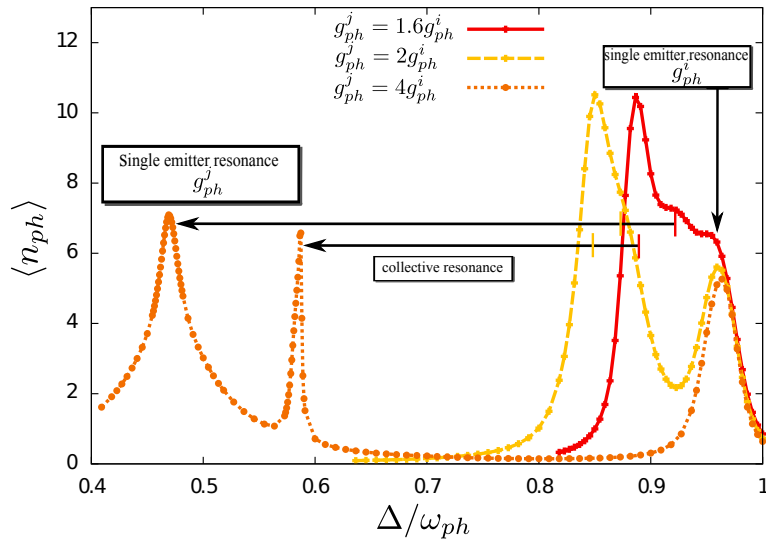

Figure 5.7.: Detuning versus phonon number for two emitters i and j which differ in the electron-phonon coupling g_{ph}. The first emitter is kept at the same electron-phonon coupling than before g_{ph}^i. As for the transition frequencies, a difference in g_{ph} results in a different single-emitter resonance, respectively. For small differences $g_{ph}^j = 1.6g_{ph}^i$ (red, solid) and $g_{ph}^j = 2g_{ph}^i$ (yellow, dashed), the single-emitter resonance of emitter j overlaps with the collective resonance. For high difference $g_{ph}^j = 4g_{ph}^i$ (orange, dotted), all resonances split up and the single-emitter resonance is at lower Δ than the collective resonance. The output of the collective resonance is smaller than for the single-emitter resonance for high difference in g_{ph}.

In contrast to the transition frequencies, where a difference of 10% already results in a narrowing of the collective resonance, collective effects are more robust against a deviation in electron-phonon coupling g_{ph}. Again one emitter i is kept at the same electron-phonon coupling as before whereas the second emitter j is assumed to be different. In Figure 5.7 three different cases are investigated: $g_{ph}^j = 1.6g_{ph}^i$ (red, solid), $g_{ph}^j = 2g_{ph}^i$ (yellow, dashed) and $g_{ph}^j = 4g_{ph}^i$ (orange, dotted). Due to the different electron-phonon coupling, the single-

emitter resonances split up according to Equation 5.2.13 (neglecting the comparably small shift due to the pump Ω)

$$\Delta_j^{single} \approx \omega_{ph} - \frac{(g_{ph}^j)^2}{\omega_{ph}} \ . \tag{5.3.2}$$

The single-emitter resonance of emitter i remains at the same position as before as collective effects do not play a role for the single-emitter resonances. In contrast to a difference in the transition frequency, the red-shift of the single-emitter resonance is comparably small such that the single-emitter resonances overlap with the collective resonances for $g_{ph}^j = 1.6 g_{ph}^i$ (red, solid) and $g_{ph}^j = 2 g_{ph}^i$ (yellow, dashed). For $g_{ph}^j = 4 g_{ph}^i$ (orange, dotted), all three resonances, the two single-emitter resonances and the collective resonance, are well separated. The collective resonance is located at a higher driving frequency than the single-emitter resonance of emitter j. Furthermore, the output of the single-emitter resonance is higher than the collective resonance for $g_{ph}^j = 4 g_{ph}^i$ which has narrowed remarkably. The reason might be that g_{ph}^j is now much higher and collective effects start to vanish for a comparable high difference in the electron-phonon coupling.

The position of the collective resonances is determined for all three cases by a mixture of both electron-phonon couplings

$$\Delta^{collective} \approx \omega_{ph} - \frac{\left(g_{ph}^j + g_{ph}^i\right)^2}{2\omega_{ph}} \ . \tag{5.3.3}$$

This agrees with the collective resonance found in section 5.2 for identical emitters.

In conclusion, non-identical emitters do not destroy the effect of collective phonon generation. For a difference in the transition frequencies of 10%, a collective resonance was still observed, although it is narrowing for increasing differences. In contrast, collective effects for emitters which differ in the electron-phonon coupling are robust up to a deviation of 400%.

5.4. Quantum yield

The different resonances close to $\Delta \approx \omega_{ph}$ in Figure 5.2 are identified with collective phonon emission. Driving at the respective collective resonance and bringing a number of emitters i to the excited state $|1_1, ..., 1_i, n\rangle$, they collectively generate coherent phonons $|1_1, ..., 1_i, n+i\rangle$, where the cavity phonon number in the steady state scales as $\langle n_{ph} \rangle \sim i$. The quantum yield, i.e. the increase of the phonon number with an increasing number of emitters, is the subject of investigation within this section. However, collective effects only occur if the pumping strength Ω is above a certain threshold. Furthermore, increasing Ω also results in a shift of the resonances. Thus in particular, the dependence of the quantum yield on Ω is the focus of this section.

In analogy to section 5.2, the number of emitters is restricted to two to simplify the interpretation. To quantify the quantum yield, a quantity called phonance witness is defined in analogy to the radiance witness of Ref. [121]

$$R = \frac{\langle \hat{c}^\dagger \hat{c} \rangle_2 - 2\langle \hat{c}^\dagger \hat{c} \rangle_1}{2\langle \hat{c}^\dagger \hat{c} \rangle_1} \ . \tag{5.4.1}$$
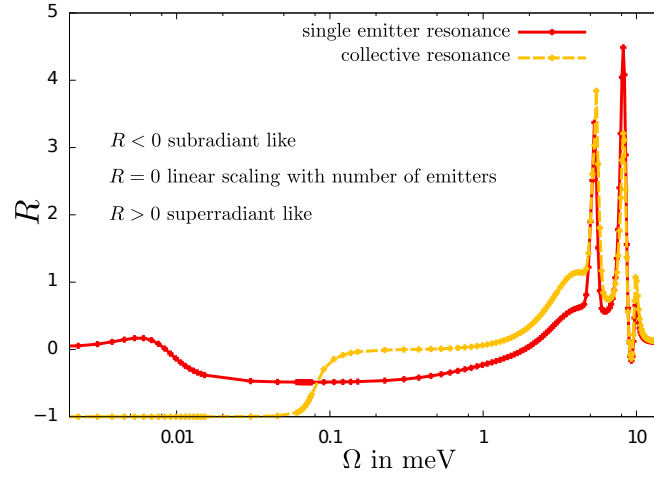
Figure 5.8.: Phonance witness R of the two-emitter phonon laser versus the external pumping strength Ω. Comparing driving at the single-emitter resonance (red, solid) with driving at the collective resonance (yellow, dashed), results in different collective behavior if Ω is increased. The one emitter case $\langle \hat{c}^\dagger \hat{c} \rangle_1$ is always driven at the single-emitter resonance. The collective resonance shows a higher quantum yield $R \geq 0$ after $\Omega = 0.1$ meV. Both cases show collective enhancements with $R > 0$, including two peaks with even $R > 1$, for $\Omega \geq 2$ meV .

The phonance witness compares the expectation value of phonon numbers for the two-emitter case $\langle \hat{c}^\dagger \hat{c} \rangle_2$ with the one emitter case $\langle \hat{c}^\dagger \hat{c} \rangle_1$. The idea is that $\langle \hat{c}^\dagger \hat{c} \rangle_2$ represents the correlated number of phonons for the two-emitter case, whereas $2\langle \hat{c}^\dagger \hat{c} \rangle_1$ represents the expected uncorrelated linear scaling with the number of emitters. Thus, $R = 0$ signifies no collective enhancements but a linear increase of the phonon number with the number of emitters. If $R < 0$ it is interpreted as a subradiant-like behavior, where the number of emitters suppresses the output [122] and $R = -0.5$ reflects the single-emitter scenario even if two emitters participate in phonon emission. In this section, the focus lies on many-emitter enhancements in increasing the pumping strength. Thus, $R > 0$ is advantageous and represents a superradiant-like behavior where the number of emitters result in an increase of the phonon number higher than the expected linear scaling.

In the previous section it has been shown that the two-emitter setup shows two resonances close to $\Delta \approx \omega_{ph}$, the single-emitter resonance and the collective resonance, whereas the one-emitter setup only shows the single-emitter resonance. The question is, how does the phonance witness change for a detuning at the collective resonance compared to a detuning at the single-emitter resonance. In Figure 5.8, the phonance witness for driving at the collective resonance (red, solid) is compared to the case where the optical laser is detuned at the single-emitter resonance (yellow, dashed) for increasing pump powers Ω. For low pump powers, driving at the single-emitter resonance shows $R > 0$, then drops below zero and for $\Omega > 1$ meV again shows superradiant-like behavior including two peaks with high quantum yield. In contrast, driving at the collective resonance shows $R = -1$ up until $\Omega = 0.1$ meV and then immediately shows $R = 0$. For higher pump powers, it shows the same behavior than for driving at the single-emitter resonance, but enters the respective regime at lower pump powers.
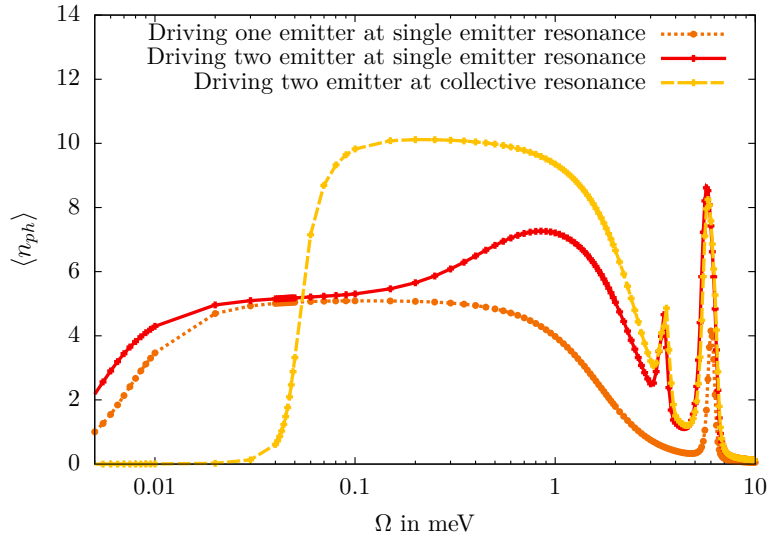
Figure 5.9.: Phonon number versus pump power for one emitter (orange, dotted), two emitters and detuning at the single-emitter resonance (red, solid) and detuning at the collective resonance (yellow, dashed). Detuning at the single-emitter resonance for one and two emitters is comparable but the two-emitter case shows a larger lasing window and an additional peak for high pump powers. Driving two emitters at the collective resonance only starts lasing at high pump powers but shows twice the phonon number.

To understand the difference in R for increasing the pump power it is useful to take a look at the phonon number of the different cases which is shown in Figure 5.9. For one emitter with a detuning at the single-emitter resonance (orange, dotted), the phonon number increases with the pump power until a maximum is reached. For high pump powers $\Omega > 1$, the phonon number decreases again until it stops lasing due to the self-quenching behavior [91, 92, 93]. In principle, the self-quenching results from the additional energy shift with Ω^2/Δ in Equation 5.2.13. Due to this shift, the resonance is brought out of the chosen detuning. This happens only for high pump powers, where the broadening of the resonance does not counteract the shifting of the resonance. However, for $\Omega \approx 9$ meV, the broadening combined with the shifting of the resonance results in addressing the two-phonon resonance as already shown in Ref. [93]. Thus, after entering the self-quenching regime, the one-emitter setup starts lasing again for certain pump powers as long as the single-emitter two-phonon resonance is addressed.

Adding a second emitter, but keeping the detuning at the single-emitter resonance, up until $\Omega = 0.1$ meV, the phonon number is comparable to the one-emitter setup. One difference is that the lasing window is increased and the two-emitter setup enters the lasing regime at lower pump powers. This explains the phonance witness $R \geq 0$ for small pump powers in driving at the single-emitter resonance in Figure 5.8 (red, solid). In reaching the maximal phonon number, the two-emitter setup shows the same phonon number than for one emitter and the phonance witness drops below zero $R < 0$. However, for $\Omega > 0.1$, the higher pump power results in linewidth broadening and the peaks of the single-emitter and collective resonances overlap for the investigated electron-phonon coupling. Thus, due to the linewidth broadening, also collective processes are addressed and the phonon

number increases (cp. Figure 5.9 (red,solid) for $\Omega \in [0.2, 1]$ meV). This is the reason why R approaches zero again for driving at the single-emitter resonance as for the one-emitter case no collective resonance is apparent.

For $\Omega > 1$ meV, the one-emitter setup is already within the self-quenching regime whereas the two-emitter case at the single-emitter resonance still overlaps with the collective resonance and shows a wider lasing window. This is why the phonance witness shows superradiant-like behavior with $R > 0$ for these pumping strength. Around $\Omega \approx 3$ meV, the two-emitter setup enters a regime, where the collective two-phonon resonance is addressed. Thus, the two-emitter setup shows a high phonon number at these pumping strengths. This resonance does not exist for the one-emitter setup which is why the phonance witness shows hyperradiance-like behavior with $R > 1$.

For $\Omega \approx 9$ meV, also the single-emitter two-phonon resonance is addressed. The one-emitter setup addresses this resonance for slightly higher pump powers which is why the phonance witness again shows hyperradiant-like behavior.

A detuning at the collective resonance $\Delta = \omega_{ph} - 2g_{ph}^2/\omega_{ph}$ shows a slightly different picture as for intermediate pumping strengths ($\Omega \in [0.1, 1]$), the expected quantum yield is obtained with $R = 0$. However, for low pump powers, the collective resonance is not lasing as it is not probable that both emitters are excited at the same time as shown in Figure 5.5. For $\Omega > 0.5$ meV, also the collective resonance enters the lasing regime and reaches the maximal phonon number which is twice as high as for the one-emitter setup. This results in the expected $R = 0$. As already explained for the single-emitter resonance, the lasing window is wider, which is why for $\Omega > 1$ the phonance witness increases and shows superradiant-like behavior, because the one-emitter setup is already within the self-quenching regime. As for driving at the single-emitter resonance, high pump powers address the collective and single-emitter two-phonon resonance which results in a high quantum yield $R > 1$. Note that due to the linewidth broadening for high pump powers, there is not much difference between driving at the single-emitter or the collective resonance for the investigated electron-phonon coupling.

5.5. Conclusion

As a first many-emitter setup, a set of two-level systems in an acoustic cavity was investigated. The system was computed with a reduced density matrix method and factorizing system-reservoir dynamics. However, the cavity phonons were considered as part of the system. Due to the combination of many emitters as well as the exact treatment of cavity phonon statistics, the number of emitters was limited to three.

In blue-detuning the external optical laser to almost the phonon cavity frequency, coherent phonon statistics were created in the acoustic cavity. It was shown that the many-emitter setup results in a variety of resonances to address coherent phonon generation by detuning the optical laser.

By mapping the full Hamiltonian to a Tavis-Cummings like Hamiltonian via a second-order perturbative treatment, it was demonstrated that the additional resonances result from collective effects of the many-emitter setup. If many emitters participate collectively in a stimulated phonon generation process, the corresponding resonance frequency is lowered by $\Delta = \omega_{ph} - Ng_{ph}^2/\omega_{ph}$. Thus, an N-emitter setup results in N corresponding resonances which positions scale with the electron-phonon coupling. A detuning at the respective collective resonance results in a linear scaling of the phonon number with the number of participating emitters. However, the linewidth is narrower which makes it more difficult to

address them for increasing number of emitters.

It was demonstrated that a detuning at the two-phonon resonance also leads to coherent phonon statistics. The collective resonances also appear in a many-emitter setup close to the two-phonon frequency. At the two-phonon resonances, the phonon number is doubled compared to the single-emitter phonon resonances but the linewidth is narrowing as well. Furthermore, it has been shown that the linewidth depends on the pump power of the external optical laser and lasing at the collective resonances disappears for decreasing pump powers, where the single-emitter resonance is still lasing.

For non-identical emitters which differ in transition frequency or electron-phonon coupling, collective effects have been demonstrated to exist as well. The position of the collective resonance depends on a mixture of the participating emitters. It has been shown that collective effects are robust for different transition frequencies up to 10% whereas for the electron-phonon coupling a difference up to 400% can be tolerated.

Investigating the quantum yield, it has been shown that the two-emitter setup has a wider lasing window and shows collective enhancements when the single-emitter setup is already within a self-quenching regime. For high pump powers, the resonances are broadening as well as shifting with the pump power such that the two-phonon resonance is addressed and a hyperradiant-like quantum yield is obtained.

6.

Boundary-driven Heisenberg spin-chain

One of the standard models to investigate generic quantum many-body interactions is the Ising spin-chain. A generalization of this model to all three spin dimensions is the Heisenberg model. The model was developed to explain ferromagnetic and anti-ferromagnetic phases of matter. However, this model also has actual relevance as the underlying quantum phase transitions are more complex in their behavior [123]. Therefore, as a second many-body system, the Heisenberg model is investigated in this thesis.

In recent experiments it became accessible to tune long-range interactions of such generic quantum spin-models [124, 125, 126, 127, 128, 129]. Long-range coupling as e.g. Coulomb interaction is far more general than the assumed nearest-neighbor coupling for this model. Thus, a generalization from nearest-neighbor coupling to long-range interactions and the connection to quantum phase transition is of fundamental importance and has drawn a lot of interest in the recent years [130, 131, 132].

One highly debated phase transition is the many-body localization (MBL) transition [20, 21, 71, 72, 14, 30, 31, 33, 32, 73], which is the generalization of Anderson localization [18] for interacting systems. The disordered Heisenberg-chain has become one of the standard models to investigate MBL. The existence of MBL in long-range interacting systems is topic of recent publications [32, 133, 134, 135].

The focus of this thesis lies on open quantum many-body systems. While the existence of MBL in closed many-body quantum systems has been demonstrated on many platforms, it is still under debate what survives of MBL in open quantum many-body systems. In closed quantum many-body systems, the MBL phase prevents a subsystem from thermalizing with the rest of the closed system. However, in case of an open quantum system, the interaction with surrounding reservoirs leads to thermalization of the quantum system with its environment. Thus, it is a challenge to prevent thermalization if surrounding thermal reservoirs are present as well [46, 47]. Especially dephasing is induced in the measurement process of optical lattice systems [48, 50, 49]. However, a well-studied approach to investigate an open quantum system in case of the Heisenberg chain is to couple the system to two magnetic reservoirs at the boundaries [136, 137, 138, 139, 140, 141, 142, 143]. The idea is to apply a voltage where on one side charge is injected and on the other side it is extracted. The generic theoretical model is described by the Lindblad master equation, where factorized system and reservoir states are assumed. Both reservoirs are kept at different potentials, e.g. spin-up at the left side and spin-down at the right side. Due to the Born-Markov approximation of the external reservoirs, the system is then kept out-of-equilibrium for all times. For nearest-neighbor coupling between the spins it has been shown that such systems exhibit negative differential conductivity (NDC) [144, 145] and anomalous transport [146, 147].

It is an open question what happens in case of strong disorder, including a possible MBL phase when boundary reservoirs are present. However, for weak disorder it has been

demonstrated that the transport of spin-current contains a transition from diffusive to subdiffusive transport [148]. This subdiffusive behavior was also found for the isolated Heisenberg chain (which is a closed quantum system) with different results: The subdiffusive regime was found close to the MBL transition [149, 150] or already for disorder approaching the clean limit [151, 152, 153].

In this chapter of the thesis, the impact of external reservoirs on the transport is investigated in detail with focus on the subdiffusive behavior. There are two processes leading to subdiffusive transport. On the one hand, weak disorder results in rare regions where disorder is locally stronger and therefore acts as a bottleneck for the transport. These are called Griffiths effects and it is under debate if this is the reason for the subdiffusive transport [149, 154]. In this chapter it will be demonstrated that on the other hand, a high potential difference of the external reservoirs also results in subdiffusive behavior. Due to the far-from-equilibrium driving, the system builds up ferromagnetic domains at the boundaries which is called a spin-blockade [145, 155]. This leads to the NDC found by Ref. [144] and results in subdiffusive transport. However, it will be demonstrated that this spin-blockade and the resulting NDC is not existent for long-range coupling. The transport of the long-range coupling scenario is independent of the external reservoir parameters [156]. As a consequence, also the transition to subdiffusive behavior in case of disorder is assumed to be independent of the open system character which would make the long-range coupled Heisenberg chain an ideal candidate to investigate the transition to MBL for open quantum systems.
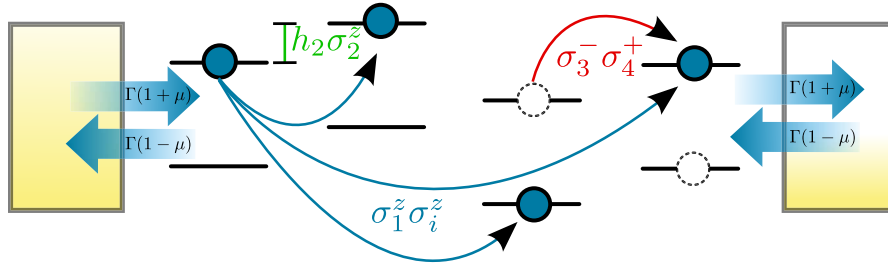
6.1. Model

Figure 6.1.: Illustration of the Heisenberg spin-chain with two boundary reservoirs: Spin-flips are illustrated as excitation hopping via $(\sigma_i^- \sigma_{i+1}^+)^{(\dagger)}$. The Ising-like interaction $\sigma_i^z \sigma_{i+l}^z$ will be either a nearest-neighbor ($l = 1$) or a long-range coupling. The system-reservoir interaction is described by four Lindblad dissipators with excitation in- and outscattering rates Γ. The two reservoirs are kept at a different potential, described by μ.

As a model system, the Heisenberg quantum spin-chain is investigated. The Heisenberg spin-chain considers interactions in all three spin dimensions. Except for the long-range coupling, only the isotropic case is considered, where all spin-coupling constants J are equal. The spin operator $\boldsymbol{S} = \frac{\hbar}{2}\boldsymbol{\sigma}$ is described by the Pauli spin-matrices $\{\sigma^x, \sigma^y, \sigma^z\}$, introduced in Equation 2.2.14.

In correspondence to the previous chapters, a single spin is imagined as a TLS. The reason is that the Heisenberg model can be transformed to a spinless fermion model [145] via a Jordan-Wigner transformation [70]. A single site is then described by a TLS with a single

fermion in analogy to chapter 5. The interactions in x and y dimension can be mapped to raising σ^+ and lowering operators σ^-. Thus, the interactions in x and y dimension describe spin-flips where the excitation at one side is annihilated and a neighboring site is excited. However, in the particle picture this is an excitation hopping and therefore not considered as an interacting term. Note that this term is also present in systems which are described by Anderson localization. When talking about interactions, the σ^z term is crucial as it describes the interactions in the spinless fermion model between sites. The Hamiltonian reads ($\hbar = 1$)

$$\mathcal{H} = \sum_{i=1}^{N-1} \frac{J}{4} \left(\sigma_i^x \sigma_{i+1}^x + \sigma_i^y \sigma_{i+1}^y \right)$$

$$+ \frac{1}{4} \frac{J}{A} \sum_{i=1}^{N-1} \sum_{l>i}^{N} \frac{1}{|l-i|^\alpha} \sigma_i^z \sigma_l^z + \sum_{i=1}^{N} \frac{h_i}{2} \sigma_i^z \tag{6.1.1}$$

$$A = \frac{1}{(N)} \sum_{i=1}^{N-1} \sum_{l>i}^{N} \frac{1}{|l-i|^\alpha} \ . \tag{6.1.2}$$

As mentioned before the first two terms describe spin-flips, as it can be seen when mapping this term to spin-raise and lower operators. The first term in the second line is an Ising-like interaction between the spins. The model system is schematically shown in Figure 6.1. In contrast to the standard Heisenberg model, the Ising interaction is assumed to be long-ranged and decays with the distance. The parameter α differs between the coupling scenarios. When $\alpha \to \infty$, the standard isotropic Heisenberg model is obtained. In this chapter the case $\alpha = 1000$ is considered as the nearest-neighbor scenario. The case $\alpha = 0.5$ is the investigated long-range scenario which is a square root decaying coupling with the distance. Note that the Ising part is normalized by A in Equation 6.1.2 to compare both coupling scenarios. The nearest-neighbor case yields $A = 1$ and $\alpha = 0$ yields $A = N/2$.

The last term in Equation 6.1.1 describes on-site random disorder of the sites. This is the crucial term which is responsible for the subdiffusive behavior resulting from Griffiths effects [149, 154, 148] and leads to MBL for the closed system [14]. The disorder is chosen randomly $h_i \in [-h, h]$ at each site and averaged out by simulating thousands of realizations with random on-site disorder. The disorder term is only investigated in the last section of this chapter where the findings of this chapter are compared to Ref. [148].

As the focus of this thesis lies on open quantum many-body systems, the Heisenberg model is investigated for a coupling to external reservoirs. In this part of the thesis factorized system-reservoir interactions are investigated, where the coupling to the external reservoir is described via a Lindblad master equation which was derived for a single TLS in section 3.3. As a generic model, the Heisenberg spin-chain is assumed to couple only at the boundaries to external magnetic reservoirs. Thus, only the boundary spins $\{1, N\}$ are subject to system-reservoir interaction. In the spin-picture the left reservoir contains spin-up and spin-down magnetization as well as the right reservoir. However, different magnetizations are assumed, i.e. the left reservoir contains more spin-up magnetization while the right reservoir contains more spin-down magnetization. If the spins are imagined as TLSs this can be viewed as two charge reservoirs, where the left reservoir contains a higher number of excitations. Thus, on the left side inscattering dominates, whereas at the right side outscattering dominates. Due

to this potential difference, the system is always kept out-of-equilibrium as the external reservoirs never change. This is modeled as

$$\partial_t \rho(t) = -i\left[\mathcal{H}, \rho(t)\right] + \sum_{\substack{j \in \{L,R\} \\ k \in \{+,-\}}} \mathcal{D}\left[L_j^k\right]\rho(t) \ , \tag{6.1.3}$$

where $\mathcal{D}$ is the Lindbald dissipator defined in Equation 3.3.16. At the left side, the operators for the Lindblad dissipator are [148]

$$L_L^+ = \sqrt{\Gamma(1+\mu)}\sigma_1^+, \ L_L^- = \sqrt{\Gamma(1-\mu)}\sigma_1^- \tag{6.1.4}$$

and the right side is the complex conjugate

$$L_R^+ = \sqrt{\Gamma(1-\mu)}\sigma_N^+, \ L_R^- = \sqrt{\Gamma(1+\mu)}\sigma_N^- \ . \tag{6.1.5}$$

The parameter μ is introduced phenomenologically to generate the bias between in and outscattering at the left and right side respectively as it can be seen in Figure 6.1. Note that $\mu \in [0,1]$. If $\mu = 0$, in- and outscattering are the same, whereas for $\mu = 1$ at the left side only inscattering is present and on the right side only outscattering. In other words, the left reservoir contains only spin-up magnetization and the right reservoir only spin-down magnetization.

The system is initialized with spin-down magnetization $\rho(0) = |\downarrow\downarrow\downarrow \ ...\rangle\langle\downarrow\downarrow\downarrow \ ...|$. As mentioned before, due to the potential difference of the external reservoirs, the system is always kept out-of-equilibrium. However, for $\lim_{t\to\infty}\rho(t)$, the system reaches a steady state. This steady state is called a non-equilibrium steady state as the bias due to the different reservoirs is still present. Thus, in the non-equilibrium steady state, the system has a specific magnetization but also a spin-current from left to right. This non-vanishing spin-current in the non-equilibrium steady state is the observable of interest in this chapter. The spin-current is derived via the continuity equation, where $\dot{\sigma}_k^z$ is the time derivative of the on-site magnetization

$$-\dot{\sigma}_k^z = \frac{j_k - j_{k-1}}{k - (k-1)} = j_{k-1} - j_k \ . \tag{6.1.6}$$

The time derivative is calculated with Heisenberg equation of motion $\dot{\sigma}_k^z = i\left[\sigma_k^z, H\right]$. The spin-current per site k then reads

$$j_k = \frac{J}{4}\left(\sigma_k^x \sigma_{k+1}^y - \sigma_k^y \sigma_{k+1}^x\right) \ . \tag{6.1.7}$$

In the non-equilibrium steady state $\lim_{t\to\infty}\rho(t)$, the spin-current does not change. Furthermore, it becomes independent of the site index k as it is then equal on all sites

$$\langle j \rangle = \lim_{t\to\infty}\text{tr}\left(\rho(t)j_k\right) \ . \tag{6.1.8}$$

In the following, the investigated observables of interest will be the magnetization of the respective site

$$\langle \sigma_k^z \rangle = \lim_{t\to\infty}\text{tr}\left(\rho(t)\sigma_k^z\right) \ , \tag{6.1.9}$$

(a) $\alpha = 1000$ (b) $\alpha = 0.5$
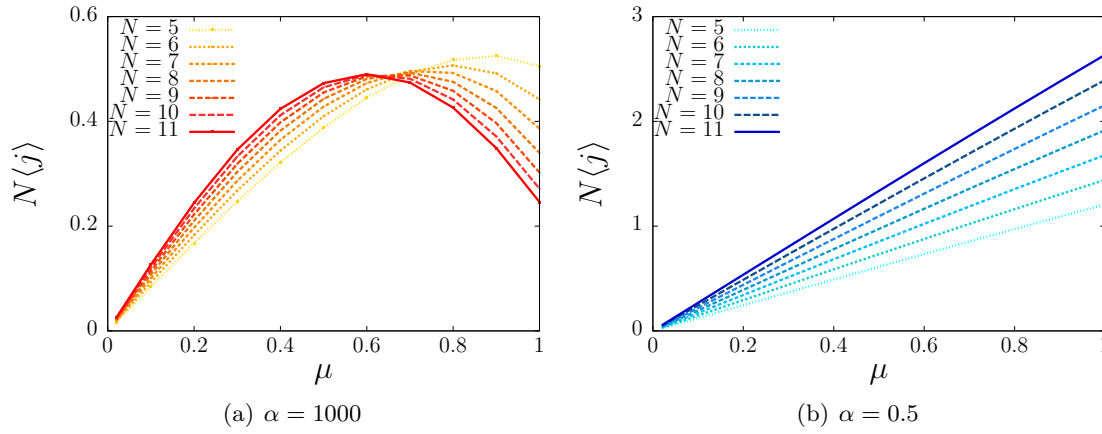
Figure 6.2.: Absolute current $N\langle j\rangle$ versus the driving strength μ for the nearest-neighbor scenario (red) (a) $\alpha = 1000$ and long-range coupling (blue) (b) $\alpha = 0.5$ for different chain lengths. Both are in a linear response regime for weak driving. Increasing the driving, nearest-neighbor coupling (a) shows a maximum. Thus, nearest-neighbor coupling results in NDC for far-from-equilibrium driving. There is a crossing of the current for different system sizes signifying diffusive transport at $\mu^{diff} \approx 0.6$. For all driving strengths μ, long-range coupling (b) shows linear response.

the single site current $\langle j\rangle$ in Equation 6.1.8 and the absolute current which is a summation of all single-site currents $N\langle j\rangle$.

6.2. Characterizing spin-transport

In this section, the transport for different external driving strengths is investigated. In particular, the interest lies on the far-from-equilibrium situation, where the strong driving $\mu = 1$ has an influence on the transport for nearest-neighbor coupling ($\alpha = 1000$). This case is compared to the long-range scenario with $\alpha = 0.5$. It will be shown that the transport for long-range coupling for all investigated reservoir parameters acts within a linear response regime. For all following plots, the spin coupling constant is set equal to the coupling to the external reservoir $J = \Gamma = 1$. In Figure 6.2, the absolute current $N\langle j\rangle$ is investigated for increasing driving strength μ. The nearest-neighbor case (a) (red) is compared to the long-range coupling scenario (b) (blue). As already shown by Refs. [145, 144], the nearest-neighbor scenario exhibits NDC for increasing the driving strength. This is a surprising feature of the far-from-equilibrium situation. Why the NDC is surprising can be understand by a simple model: When increasing the external bias, one would expect that the current of the system in between responses linearly. Considering as an example Ohms law, when one increases the voltage, the current increases linearly when the resistance is held constant. When this example is compared to the investigated setup, the driving would correspond to the voltage and the inner spin dynamics described by J correspond to the resistance. Thus, when increasing the driving, the inner dynamics change at a certain point and therefore the resistance is increased which is why NDC is present. In the Refs. [145, 144] this was explained by the spin-blockade effect, which will be explained in this chapter later on.

However, in Figure 6.2 (b) it is shown that long-range coupling acts within a linear response regime for all driving strengths. Thus, long-range coupling prevents the system from changing its resistance due to the absence of a spin-blockade.

The focus of this chapter lies on the transport behavior, i.e. the current for increasing system size N. It is assumed that the current scales as

$$\langle j \rangle \sim \frac{1}{N^\gamma} \; , \tag{6.2.1}$$

where the power-law exponent γ defines the transport scenario. The case $\gamma = 1$ is referred to as diffusive transport which corresponds to Fick's law [157]

$$j = \mathcal{D} \nabla \sigma^z, \tag{6.2.2}$$

where $\mathcal{D}$ is a diffusion constant independent of the position and chain length. However, for most cases of this chapter γ differs from one which is referred to as anomalous transport. Any $\gamma < 1$ is called superdiffusive transport, whereas any $\gamma > 1$ is called subdiffusive transport. Note that $\gamma = 0$ is called ballistic transport where the relative current becomes independent of the system size.

This brings up the point for differentiating between the relative current $\langle j \rangle$ and the absolute current $N\langle j \rangle$. The reason is that on the one hand, the transport is determined by the scaling of the relative current with the system size. On the other hand, the crossing from superdiffusive ($\gamma < 1$) to subdiffusive ($\gamma > 1$) is the most relevant change of the transport investigated here. When multiplying Equation 6.2.1 by the system size N, it becomes apparent that diffusive transport is obtained where different system sizes show the same absolute current $N\langle j \rangle$. In contrast, ballistic transport is present when different system sizes show the same relative current $\langle j \rangle$. Thus, an intersection of curves which show the relative current for different system sizes signifies ballistic transport. An intersection of curves which show the same absolute current for different system sizes signifies diffusive transport.

This is the case in Figure 6.2 (a) where the NDC sets in. At $\mu^{diff} \approx 0.6$, nearest-neighbor coupling shows diffusive transport which can be seen by the intersection of the curves of the absolute current. For smaller driving strengths, the absolute current increases with the system size, which means the transport is superdiffusive with $\gamma < 1$. For higher driving strengths, the absolute current decreases with the system size, meaning the transport is subdiffusive with $\gamma > 1$. In contrast, for long-range coupling and all driving strengths μ (Figure 6.2 (b)), the absolute current increases with the system size, meaning $\gamma < 1$. The scaling of the relative current with the system size according to Equation 6.2.1 is investigated in the following for the different driving scenarios to determine the value of γ.

6.2.1. Weak driving

Starting with the weak driving regime with $\mu = 0.02$, the power-law exponent γ is obtained by fitting Equation 6.2.1 to the values obtained for the relative current for system sizes up to $N = 11$. This is shown in Figure 6.3 (a) (red) for the nearest-neighbor case and in Figure 6.3 (b) (blue) for the long-range scenario. For nearest-neighbor coupling, the fit yields $\langle j \rangle_{\mu=0.02} \sim 1/N^{0.48}$. This value agrees well with the findings of the Refs. [138, 148] where they obtained $\gamma = 0.5$ for system sizes up to $N = 250$. Thus, within the linear response regime, the nearest-neighbor scenario shows anomalous superdiffusive transport. For the long-range scenario, the fit yields $\langle j \rangle_{\mu=0.02} \sim 1/N^{0.01}$. The power-law exponent γ

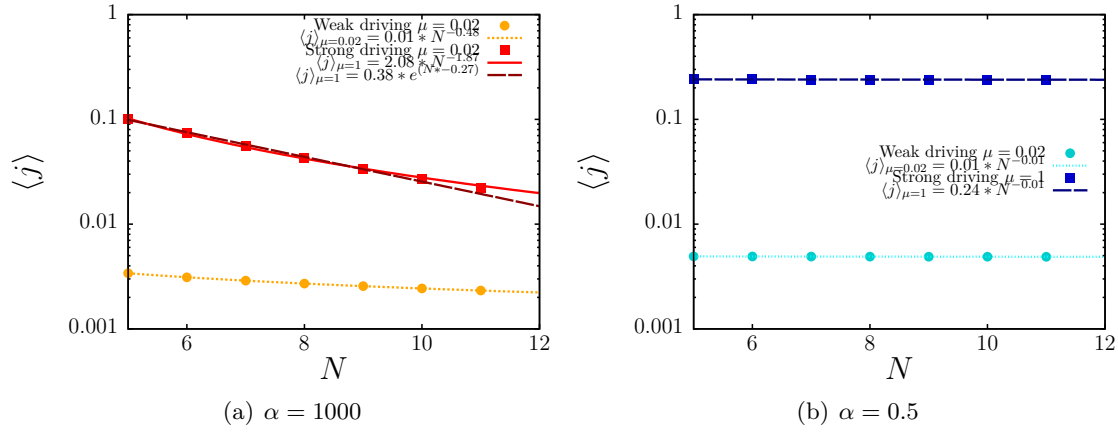(a) $\alpha = 1000$ (b) $\alpha = 0.5$

Figure 6.3.: Comparison of the transport for nearest-neighbor (red) (a) and long-range coupling (blue) (b): The scaling of the relative current $\langle j \rangle$ with the system size N is shown for weak ($\mu = 0.02$) and strong ($\mu = 1$) external driving. (a) Nearest-neighbor coupling: Weak driving yields the exponoent $\gamma = 0.48$ which is close to the known value $\gamma = 0.5$ [138] with superdiffusive transport. Strongest driving results in a change of the transport to either subdiffusive transport ($\gamma = 1.87$) or an exponential decay. (b) Long-range coupling: The transport for long-range coupling is independent of the external driving in contrast to the nearest-neighbor scenario. For weak and strong driving, the transport is nearly ballistic with $\gamma = 0.01$.

is close to zero which is nearly ballistic transport. Already for the weak driving regime there is a difference in the transport between nearest-neighbor and long-range coupling.

6.2.2. Maximal driving

For far-from-equilibrium driving, the nearest-neighbor scenario shows NDC. After crossing $\mu^{diff} \approx 0.6$, the transport changes from superdiffusive to subdiffusive transport with $\gamma > 1$. The fit in Figure 6.3 (a) for maximal driving yields $\langle j \rangle_{\mu=1} \sim 1/N^{1.87}$ which signifies subdiffusive transport. In addition, an exponential fit is also shown which would indicate an insulating system. In the Ref. [145] an exponential fit was more adequate. The data in Fig. Figure 6.3 (a) suggests subdiffusive transport. However, finite size effect might be present for the data at hand.

The data fit for long-range coupling yields $\langle j \rangle_{\mu=1} \sim 1/N^{0.01}$ which is the same than for the weak driving regime with nearly ballistic transport. This means that the transport for long-range coupling is independent of the external bias of the reservoirs μ which is a remarkable result. To further investigate the dependence of the transport on the external reservoirs, the current for different coupling strengths Γ is investigated.

6.2.3. Reservoir dependency

(a) $\alpha = 1000$, $\mu = 0.02$

(b) $\alpha = 0.5$, $\mu = 0.02$

(c) $\alpha = 1000$, $\mu = 1$
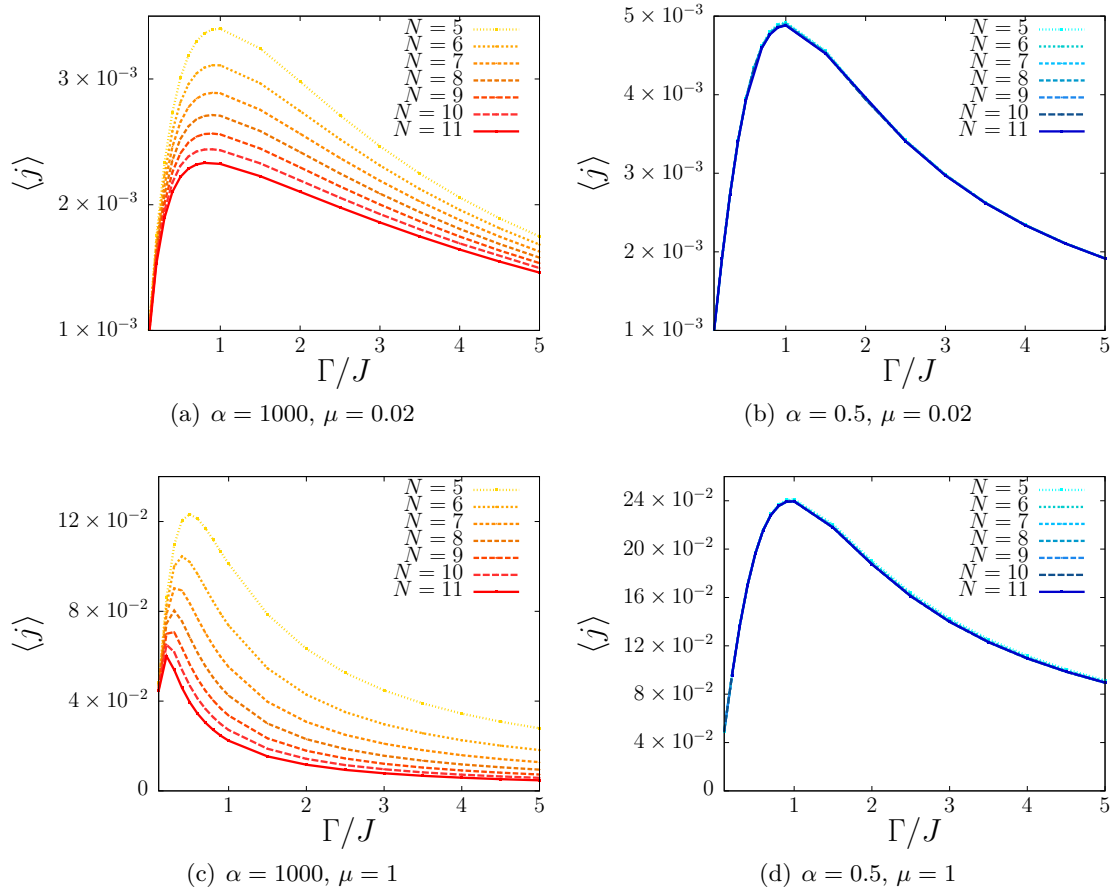
(d) $\alpha = 0.5$, $\mu = 1$

Figure 6.4.: Relative current $\langle j \rangle$ versus reservoir coupling strength Γ normalized by the spin-coupling J. Nearest-neighbor coupling (red) is compared to long-range coupling (blue) for weak driving (a, b) and strong driving (c, d). Nearest-neighbor coupling shows a different scaling with the system size with a maximum at $\Gamma = J$ (a). It changes drastically for strong driving, where the maximum tends to smaller Γ for increasing system size (c). In contrast, for long-range coupling, the relative current is the same for all coupling strength Γ, with the maximum at $\Gamma = J$ for weak (b) and strong driving (d).

It was shown that the transport for long-range coupling is robust against far-from-equilibrium effects induced by the driving strength μ. It will be shown that this is also the case for all investigated reservoir coupling strength Γ, whereas the transport for nearest-neighbor coupling changes drastically with both μ and Γ. In Figure 6.4, nearest-neighbor coupling (red) (a, c) is compared to long-range coupling (b, d). It is differentiated between weak driving $\mu = 0.02$ (a, b) and the far-from-equilibrium driving $\mu = 1$ (c, d).
If the potential difference is small (i.e. weak driving $\mu = 0.02$), both inscattering via σ^+ and outscattering σ^- is present at both side with a small bias to inscattering at the left side and outscattering at the right side. For the interpretation of the physical processes for brevity only the left side is considered. However, the same holds for the right side with dominant outscattering σ^-.

For both, nearest-neighbor and long-range coupling, the maximum is obtained at $\Gamma = J$ in the weak driving regime. At the left side, spin-up ($\Gamma(1 + \mu)$) dominates over spin-down ($\Gamma(1 - \mu)$) in the reservoir. Thus, for $\Gamma = J$, the spin coupling and the resulting spin-flips dominate over the outscattering $J > \Gamma(1 - \mu)$. In contrast, the inscattering ($\Gamma(1 + \mu)$) dominates over the spin-flips $J < \Gamma(1 + \mu)$ which is why the left side of the chain favors spin-up magnetization. This is advantageous for the current as a constant bias is present also in the non-equilibrium steady state.

When $\Gamma < J$, lesser inscattering takes places and reduces the current. The inscattering is a bottleneck for the transport. This is why with decreasing Γ in Figure 6.4 (a), the current becomes more independent of the system size. In contrast, increasing Γ also results in a higher outscattering $J < \Gamma(1 - \mu)$. For an inscattered excitation, it is more probable to scatter out before it gets transported to further sites. For this reason, the curves of different system sizes move together for increasing Γ as this process is independent of the system size. This has consequences for the transport: At the maximum, the power-law exponent shows $\gamma = 0.5$ which is superdiffusive transport. Either decreasing or increasing Γ results in a bottleneck at the boundary spins which is why the transport becomes more independent of the system size and thus, approaches the ballistic limit $\gamma \to 0$. This can be seen in Figure 6.4 (a) that the curves for different system sizes move together away from the maximum.

However, long-range coupling tells a different story. At the maximum $\Gamma = J$, different system sizes already intersect, signifying ballistic transport. Increasing or decreasing Γ changes the value of the current, but all system sizes show the same relative current. Thus, the transport is independent of the reservoir coupling Γ in the weak driving regime.

When increasing the potential difference to maximal driving $\mu = 1$, it means that the left reservoir only contains spin-up and the coupling to the reservoir becomes $2\Gamma\sigma^+$. There is no spin-down magnetization in the left reservoir, or in other words, outscattering is forbidden at the left side. The consequence is that each inscattered excitation has to be transported to the right side of the chain. The decreasing current for higher scattering rates has a different origin than in the weak driving regime. Due to the spin-up reservoir, the boundary spins of the system become polarized and reduce further interaction with the reservoir as they are already polarized with respect to the reservoir. For nearest-neighbor coupling, the spin-up polarization accumulates up to the central site which is the spin-blockade effect. Thus, the bottleneck is the central site, where the two different spin-polarizations interact with each other. This bottleneck and the accumulation of polarizations is reduced if the coupling strength is chosen smaller, as it prevents the system from building up a spin-blockade. This is why for larger chain length, the maximum moves towards smaller Γ in Figure 6.4 (c) as the spin-blockade becomes larger for larger chain lengths in the non-equilibrium steady state. At a specific coupling, e.g. $\Gamma = J$, this has a crucial consequence: The transport changes from superdiffusive to subdiffusive as for larger chain lengths the spin-blockade effect is intensified.

In case of long-range coupling, one would expect that the situation changes for the far-from-equilibrium driving. Due to the missing spin-down magnetization in the left-reservoir, the inscattering is increased and one would expect a higher current for increasing the scattering rate Γ. In contrast, the dependence on Γ does not change for maximal driving as it can be seen in Figure 6.4 (d). The curve does not change compared to the weak driving regime, but for the value of the relative current and the maximum remains at $\Gamma = J$. This is a surprising effect as one would expect a higher current for higher coupling Γ as NDC was not observed. However, even if there is no NDC, the boundary spin polarizes with

respect to the reservoir magnetization and reduces further inscattering when increasing Γ. Still, it is surprising that the transport behavior does not change for any investigated Γ or μ and remains always nearly ballistic. The reason for this effect is investigated in detail in the following section.

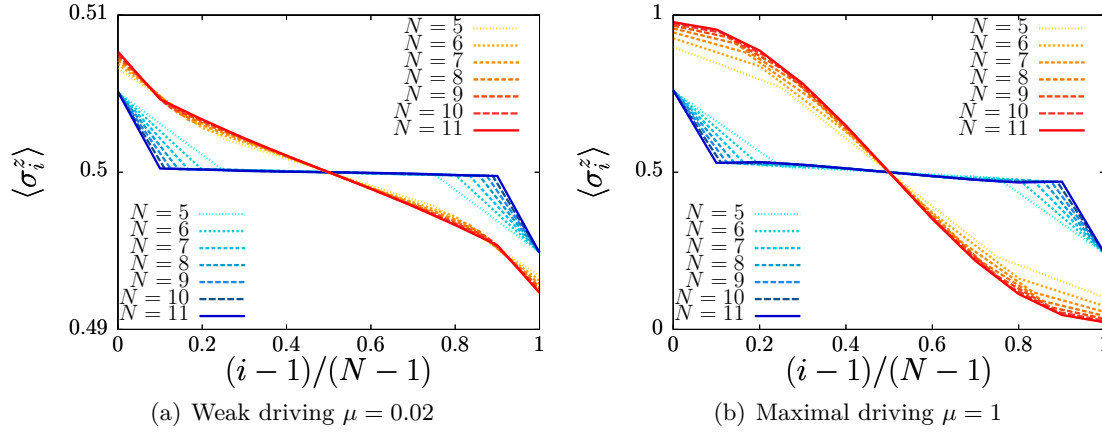## 6.3. Absence of negative differential conductivity

(a) Weak driving $\mu = 0.02$

(b) Maximal driving $\mu = 1$

Figure 6.5.: Spin-polarization (occupation probability) $\langle \sigma_i^z \rangle$ of the respective site i normalized by the chain length to compare different system sizes (zero is the left spin and one the right spin). For weak driving (a) both profiles (nearest-neighbor coupling red, long-range coupling blue) look qualitatively similar. All spins are close to $\langle \sigma_i^z \rangle \approx 0.5$ but there is a small linear decrease from the left side to the right side due to the driving. The first and the last spin show a polarization with respect to the reservoir. The gradient is different for nearest-neighbor and long-range coupling defining superdiffusive and nearly ballistic transport. For maximal driving (b), both couplings show a qualitative difference. Long-range coupling shows qualitatively the same, only the boundary spins are aligned more strongly. Nearest-neighbor coupling has changed significantly. Further sites are also aligned with respect to the reservoir polarization and a wide spin-blockade is present, resulting in subdiffusive transport.

In this section it is investigated in detail why the long-range coupling scenario does not show NDC and the transport is independent of the external reservoir parameters. The magnetization profile for nearest-neighbor-coupling (red) and long-range coupling (blue) is compared in Figure 6.5. It is differentiated between the weak driving $\mu = 0.02$ regime (a) and the far-from-equilibrium situation with maximal driving $\mu = 1$ (b).

For weak driving, all spins do not have a specific alignment $\langle \sigma_i^z \rangle \approx 0.5$. Only the boundary spins are aligned weakly with respect to the two reservoir polarizations (spin-up left and spin-down right).

Due to the potential difference of the external reservoirs, a small gradient from left to right is induced. Long-range coupling and nearest-neighbor coupling already differ in the slope of the gradient. Long-range coupling is close to horizontal alignment which signifies nearly ballistic transport. Nearest-neighbor coupling has a steeper slope which leads to superdiffusive transport which was demonstrated in section 6.2. With the magnetization

profile at hand, the transport behavior can be explained properly: The phenomenological transport law in Equation 6.2.2 shows that a linear gradient of the magnetization leads to diffusive transport. Both, long-range coupling and nearest-neighbor coupling, do not show the linear gradient which is why the transport is anomalous. Note that at μ^{diff}, the magnetization profile shows exactly this linear decrease of magnetizations for nearest-neighbor coupling.

For maximal driving in Figure 6.5 (b), the magnetization profile for nearest-neighbor coupling changes qualitatively. All spins up to the central site are polarized with respect to the two reservoirs at the boundary. This is the spin-blockade effect found by Ref. [145, 144]. Thus, the gradient is site-dependent and beyond the linear decrease of Equation 6.2.2. The transport changes from superdiffusive transport for weak driving to subdiffusive transport for strong driving. The spins align due to the magnetization of the reservoir. This polarization accumulates up to the central site and serves as a bottleneck for the transport. In Figure 6.5 (b) it is clearly visible that only the boundary spins are aligned and further spins are not affected by the reservoirs in case of long-range coupling. Thus, the transport remains nearly ballistic and NDC is absent. The reason is that long-range coupling enables interactions beyond the central site. At both sides of the chain, there are ferromagnetic domains with opposite alignment. Thus, due to the long-range coupling, both domains interact with each other and the strong alignment is reduced. This is illustrated in Figure 6.6. Due to the interaction between opposite polarized ferromagnetic domains, the strong
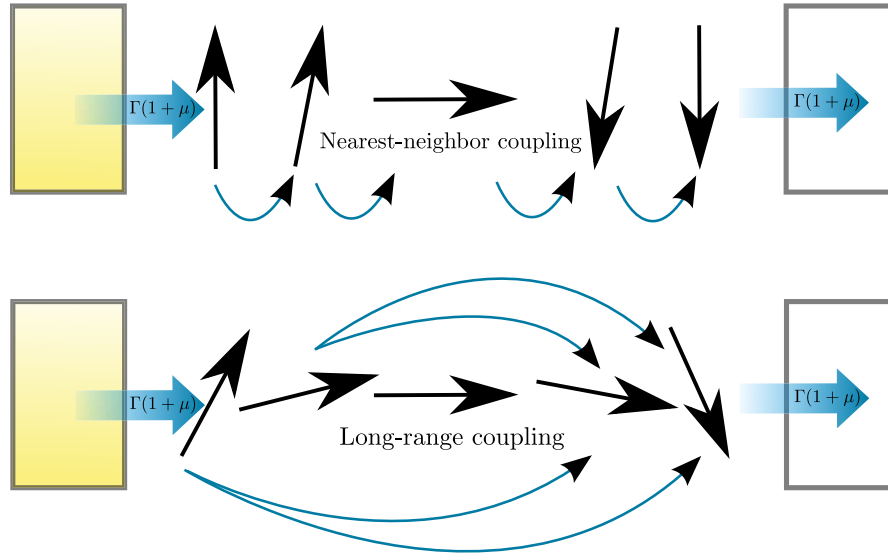

Figure 6.6.: Sketch to illustrate the spin-blockade effect for nearest-neighbor (top) as well as the missing NDC for long-range coupling (bottom) in case of maximal driving. Spin-polarizations accumulate up to the central site resulting in NDC for nearest-neighbor coupling. Long-range coupling results in an interaction between both magnetic domains and thus reducing the respective polarizations.

alignment is reduced and enables further interaction with the reservoirs. This is why the transport remains nearly ballistic for strongest driving. However, the boundary spins are still affected and counteract the interaction with the reservoir. This is the reason why increasing Γ also results in a current decrease, but not in a change of the transport (cp. Figure 6.4 (d)).

To conclude, nearest-neighbor coupling is subject to the spin-blockade effect, where spin-polarizations accumulate up to the central site and serve as a bottleneck for the transport, resulting in NDC. In contrast, long-range coupling enables interactions between the opposite polarized ferromagnetic domains and reduces the strong alignment. As a consequence, the long-range coupling scenario is robust against far-from-equilibrium effects and does not show NDC. The transport is independent of the driving and the reservoir coupling strength.

6.4. Effect of disorder

In this section, the effects found in the previous sections, namely the subdiffusive transport for nearest-neighbor coupling and the absence of NDC for long-range coupling, are combined with random disorder. This is especially relevant for ongoing research as random disorder leads to a transition to MBL in case of a closed system [14]. However, the transport for weak disorder before the MBL transition is still under discussion [149, 150, 151, 152, 153]. In case of an open quantum system it was shown by Ref. [148] that the boundary-driven nearest-neighbor coupled XXZ-chain contains a transition from diffusive to subdiffusive transport with increasing disorder. This was found for the linear response regime with weak driving. This section serves as a demonstration that this transition to subdiffusive transport not only might results from Griffiths effects but also from a spin-blockade effect in case of far-from-equilibrium driving.

Griffiths effects occur due to the randomness of disorder. This results in rare regions, where locally, between two sites, the disorder is stronger than in the rest of the system. As strong disorder suppresses spin-flips and thus the current, these regions with locally strong disorder serve as a bottleneck for the transport. Due to the averaging of random disorder realizations, for increasing disorder strengths these regions occur more often. It was assumed that these are the reason for the transition to subdiffusive transport already for disorder strengths far away from the MBL transition [149, 154]. In this section, both subdiffusive transport resulting from Griffiths effects due to disorder as well as subdiffusive transport resulting from a spin-blockade due to far-from-equilibrium driving are investigated.

In addition to the previous sections, disorder is applied which is the last term in Equation 6.1.1. For each data point in the following plots, the disorder is chosen randomly at each site with $h_i \in [-h, h]$. Thus, each realization has a specific Hamiltonian. For each Hamiltonian the current in the non-equilibrium steady state is calculated by evaluating the density-matrix dynamics. This procedure is repeated with new random disorder realizations and the averaged non-equilibrium steady state current is calculated, including all performed realizations. The simulation is completed when the averaged current does not change as well as each on-site disorder shows $\bar{h}_i \approx 0$. In practice, this is the case for around 6000 disorder averages.

It is important to mention that the density-matrix simulations are not advantageous when it comes to disorder. The fact that the number of differential equations scales as 2^{2N} is already limiting the system size to a maximum of $N = 12$ for the previous sections. However, increasing disorder needs a significant longer integration time as the current is suppressed and thus, the time to reach the non-equilibrium steady state is increased. As a further complication, the different on-site potentials due to $h_i \sigma_i^z$ result in different dynamics between all sites. As a consequence a careful adjustment of the numerical step size is important to cover all random disorder realizations for $h_i \in [-h, h]$. The step size to yield exact dynamics can be orders of magnitudes smaller than for the case without disorder of the previous sections. Note that as a numerical control parameter, the trace of
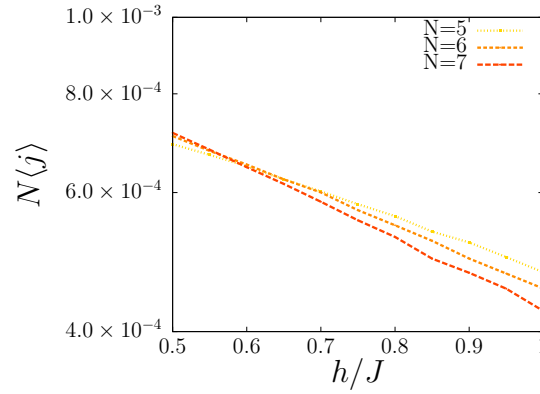
Figure 6.7.: Absolute current versus random disorder. At disorder strength $h^{diff} \approx 0.6$ the curves for different system sizes intersect, signifying diffusive transport. For $h < h^{diff}$ the system shows anomalous transport with superdiffusive transport, whereby for $h > h^{diff}$ it changes from superdiffusive to subdiffusve transport. This plot serves as a comparison to Ref. [148], where the disorder is weaker at the boundaries $h_0, h_{N-1} \in [-h/2, h/2]$.

the density matrix was carefully observed to yield one.

A more advantageous form to simulate disorder realizations is the matrix product state method which will be introduced in Part III of this thesis in chapter 7. The advantage is that due to random disorder, the entanglement between subsystems of the many-body system is suppressed (the consequence is that the transport changes to subdiffusive transport). This is advantageous for matrix product state simulations as small entanglement allows to cut off a large part of the Hilbert space. However, for the system at hand with factorized system-reservoir dynamics, a matrix product simulation in the Liouville space has to be performed to trace out the reservoir degrees of freedoms as done in Ref. [148]. This is beyond the scope of this thesis as the simulations within the matrix product state formulation are performed based on the QSSE, introduced in chapter 3.

Altogether, this is the reason why in this approach, the system size is limited to a maximum of $N \leq 8$ when considering random disorder. Note that for $N = 8$ only 1000 disorder realizations are performed due to the long integration time. The considered sytem sizes are much smaller than the thermodynamical limit and finite size effects are present. For this reason, the results obtained with the density matrix are compared to the results obtained for matrix product state simulations in the Liouville space of Ref. [148]. The focus of this section lies on a comparison of nearest-neighbor with long-range coupling, whereas the exact crossing to subdiffusive transport might differ from the thermodynamical limit.

In Figure 6.7, the absolute current $N\langle j \rangle$ for increasing random disorder is shown for different system sizes. In analogy to section 6.2 in Figure 6.2, the transition to subdiffusive transport is obtained where the curves for different system sizes intersect at h^{diff}. At this point, the absolute current does not change for increasing system size which signifies diffusive transport (cp. Equation 6.2.1). For $h < h^{diff}$, the power-law exponent is smaller than one, whereas right of the intersection the power-law exponent shows $\gamma > 1$ signifying subdiffusive transport. Note that in order to compare the transition with Ref. [148], the disorder at the boundary spins is chosen as $h_0, h_{N-1} \in [-h/2, h/2]$ for this plot.

Comparing the obtained point of the transition $h^{diff} \approx 0.6$ with $h^{diff} = 0.55$ of Ref. [148], the findings of this chapter are relative close to the reference, where they simulated up to

400 spins. Furthermore, in Ref. [148], they showed that finite size effects are present up to a certain system size N^*. The here investigated system sizes are much smaller than N^* which is why it is surprising that such small system sizes show nearly the same h^{diff}. The reason might be the different method to determine h^{diff}. In the Ref. [148] it was obtained with a fit of the relative current in analogy to Figure 6.3, whereas the here proposed method is to determine h^{diff} with an intersection of curves for different system sizes for the absolute current.

This gives rise to the assumption that the here used method to obtain the transition h^{diff} via an intersection of curves is a good method to predict h^{diff} for systems which are subject to finite size effects.

It is interesting to mention that in case of a closed system there exists a second transition at $h^{MBL} \approx 3.7$ [71, 158] where it is assumed that the scaling of the current with the system size changes from $j \sim 1/N^\gamma$ ($\gamma > 1$) to $j \sim exp(-\kappa N)$. This is referred to as the MBL transition. The scope of this chapter is not to address the question if h^{MBL} exists in boundary-driven systems, but to clarify the influence of the external reservoirs, especially for the far-from-equilibrium situation.

In section 6.2, it was shown that nearest-neighbor coupling is subject to NDC resulting from a spin-blockade effect. This leads to subdiffusive transport already for the case without disorder. However, the transport for long-range coupling is independent of the driving strength and the coupling to the external reservoirs (cp. section 6.3). This different behavior is now investigated for the effect of disorder.

In Figure 6.8, the nearest-neighbor scenario (a, c) is compared to the long-range coupled chain (b, d) for weak driving $\mu = 0.02$ (a, b) and maximal driving $\mu = 1$ (c, d). As mentioned before, the nearest-neighbor scenario shows a transition to subdiffusive transport at $h^{diff} \approx 0.6$ (Figure 6.8 (a)) in the linear response regime, where no NDC is present due to Griffiths effects. In contrast, long-range coupling shows a transition to subdiffusive transport at stronger disorder $h^{diff} \approx 0.8$ (Figure 6.8 (b)). The reason might be that the transport for the case without disorder is already different. Nearest-neighbor coupling shows superdiffusive transport with $\gamma = 0.5$, whereas long-range coupling shows nearly ballistic transport with $\gamma = 0.01$ (Figure 6.3). Thus, in case of long-range coupling, a higher disorder is needed to suppress the transport such that it becomes diffusive.

When the external driving is increased to maximal driving $\mu = 1$, the situation changes drastically for the nearest-neighbor coupling. The transition to subdiffusive transport already takes place due to the spin-blockade effect, which is why the transport is already subdiffusive for zero disorder and no h^{diff} exists (Figure 6.8 (c)). In contrast, for long-range coupling, the transition to subdiffusive transport remains at nearly the same disorder strength (Figure 6.8 (d)). The reason is that long-range coupling is robust against far-from-equilibrium effects such as NDC.

These findings prove that for nearest-neighbor coupling, the transition to subdiffusive transport is highly dependent on the external reservoir parameters. Far-from-equilibrium driving results in a spin-blockade with NDC, which is in addition to Griffiths effects in case of disorder. It might become difficult to unravel the effect of disorder from the spin-blockade effect in the presence of boundary reservoirs.

(a) $\alpha = 1000$, $\mu = 0.02$

(b) $\alpha = 0.5$, $\mu = 0.02$

(c) $\alpha = 1000$, $\mu = 1$
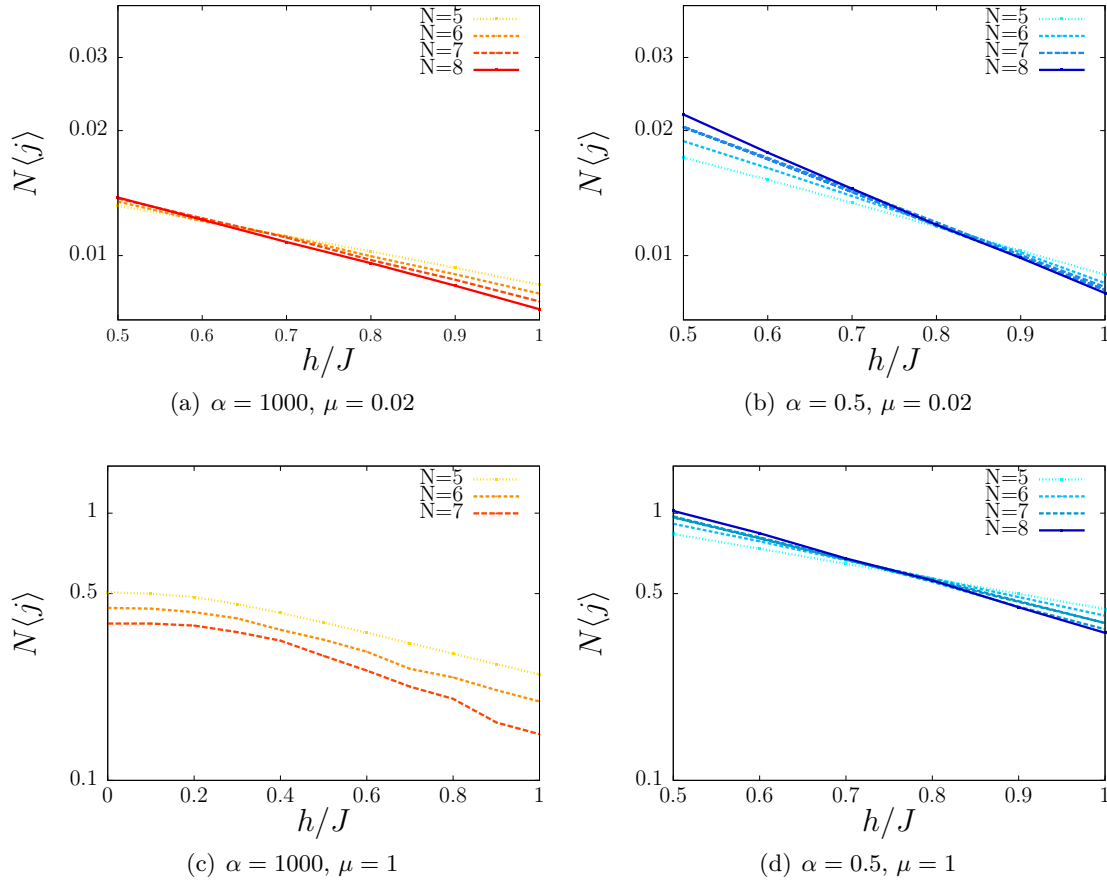
(d) $\alpha = 0.5$, $\mu = 1$

Figure 6.8.: Comparison between nearest-neighbor (a, c) and long-range coupling (b, d) for weak (a, b) and strong driving (c, d) to determine the transition to subdiffusve transport h^{diff}. Both, nearest-neighbor (a) and long-range coupling (b) show a transition to subdiffusive transport at a certain disorder strength for weak driving. For long-range coupling, the transition h^{diff} is at a higher disorder strength. However, for maximal driving $\mu = 1$, the nearest-neighbor scenario shows subdiffusive transport up until $h = 0$ (c). In contrast, for long-range coupling, h^{diff} does not change significantly (d). Due to the numerical effort, $N = 8$ was excluded in (c) as the effect becomes already clear.

However, the transport for long-range coupling is unaffected by the external reservoirs, even in the far-from-equilibrium situation. As a consequence, the transition to subdiffusive transport results purely from disorder effects and is independent of the open quantum system setup. In the case of far-from-equilibrium reservoirs, a possible transition to MBL would be unaffected by the external driving which makes the long-range coupled Heisenberg spin-chain an ideal candidate to study such effects in case of open quantum systems.

6.5. Conclusion

As a second many-body system, the isotropic Heisenberg quantum spin-chain was investigated in this thesis. This has become a standard model when investigating effects of disorder on interacting systems leading to many-body localization.

To generalize the standard model to an open quantum system, the spin-chain is coupled to two external magnetic reservoirs at the boundaries. The coupling to the reservoir is described by the Lindblad formalism, where factorized system-reservoir states are assumed. Due to strongly-correlated spins with long-range interactions, rendering typical numerical methods ineffective, the full density matrix equations of the many-body system were evaluated numerically.

In assuming a potential difference of the external reservoirs, i.e. the left reservoir contains a higher spin-up and the right reservoir a higher spin-down magnetization, a spin-current through the chain is induced. This spin-current was investigated in the non-equilibrium steady state for different system sizes to define the transport properties of the system.

For small potential differences, both, nearest-neighbor and long-range coupling, act within a linear response regime where the current increases linearly with the driving induced by the potential difference. Nearest-neighbor coupling shows superdiffusive transport, whereas long-range coupling shows nearly ballistic transport. However, for far-from-equilibrium driving, nearest-neighbor coupling exhibits negative differential conductivity resulting in a change to subdiffusive transport. In contrast, long-range coupling still acts within a linear response regime with nearly ballistic transport.

By investigating the driving strength as well as the coupling to the external reservoirs, it has been shown that the transport of the long-range coupled Heisenberg spin-chain is independent of the external reservoir parameters, whereas for nearest-neighbor coupling the transport is highly dependent on both.

These differences are explained by a spin-blockade effect which is induced by the far-from-equilibrium driving. Nearest-neighbor coupling builds up ferromagnetic domains which serve as a bottleneck for the current. For long-range coupling, these ferromagnetic domains interact with each other and vanish.

When disorder is added, both systems undergo a transition to subdiffusive transport for increasing disorder strength in the regime of a small potential difference between the reservoirs. However, the transition to subdiffusive transport is at a higher disorder strength for long-range coupling.

In the far-from-equilibrium situation, nearest-neighbor coupling shows subdiffusive transport already for zero disorder. Surprisingly, for long-range coupling, the transition to subdiffusive transport takes place at the same disorder strength than for a small potential difference.

The transport of the nearest-neighbor coupled Heisenberg chain is highly dependent on the coupling to the external reservoirs in case of an open quantum system. This makes it difficult to distinguish the effect of disorder from the reservoir induced spin-blockade. Long-range coupling shows robust transport for changing the external reservoirs. Thus, long-range coupling provides a clear understanding of disorder effects when going to a regime where MBL might be present in case of open quantum systems.

PART III

Entangled system-reservoir dynamics

7.

Introduction to matrix product states

Considering a typical one-dimensional spin-chain with N spins. Each site n_i with $i \in \{1, \ldots, N\}$ has a local state dimension of d. In practice, the local state dimension will be $d = 2$ in most cases. In general, the wave-function of an arbitrary state reads

$$|\psi\rangle = \sum_{n_1,\ldots,n_N}^{d} c_{n_1,\ldots,n_N} |n_1, \ldots, n_N\rangle \, , \tag{7.0.1}$$

where $|\psi\rangle$ can be either in a product or in a superposition state. The most simple product state is where one coefficient is nonzero and all others are zero. For example, the Néel state $|1, 0, 1, 0, \ldots\rangle$ would read $|\psi\rangle = c_{1,0,1,0,\ldots} |1, 0, 1, 0, \ldots\rangle$, with $c_{1,0,1,0,\ldots} = 1$ if $|\psi\rangle$ is normalized. However, for a many-body system the total dimension scales exponentially with the system size N. This means, the total number of coefficients $c_{n_1,\ldots,n_N}$ scales as d^N. This makes it difficult to treat arbitrary superposition states as they consist of many coefficients of the many-body system.

Calculating dynamics via a solution of the time dependent Schrödinger equation is numerically expensive as this corresponds to d^N coupled differential equations. With growing N, the total number of differential equations quickly reaches the limit of todays computational possibilities.

However, for many cases, not all states are occupied and most coefficients are zero as it is easy to see for the Néel state. Still, the time evolution with a typical many-body Hamiltonian induces correlations between subsystems and simple product states end up in a complicated superposition state after few time steps. The question is, how is it possible to judge which coefficients are relevant for the dynamics and which subsystems of the given many-body problem are truly coupled to each other. The subsystems, i.e. sets of coefficients which do not become relevant for the system dynamics, decouple and can be neglected when solving the differential equations. Neglecting these coefficients, directly reduces the exponentially many coefficients to an algebraic scaling with N, provided that the entanglement between subsystems is small.

The answer to that lies in the matrix product state (MPS) formalism and the most important operation called singular-value decomposition (SVD). It is very closely related to the Schmidt decomposition which allows to calculate bipartite entanglement between two quantum subsystems. This chapter is written in close analogy to the review on matrix product states by Ulrich Schollwöck [29].

7.1. Singular-value decomposition (SVD)

The singular-value decomposition can be viewed as a diagonalization of arbitrary rectangular matrices. Considering a matrix M of dimension $N_A \times N_B$, the SVD is a decomposition of

$$M = USV^\dagger . \tag{7.1.1}$$

Thus, the matrix M is decomposed into three matrices where the centering matrix S is diagonal and of dimension $\min(N_A, N_B) \times \min(N_A, N_B)$. The entries on the diagonal are the singular values with non-negative entries $S_{\alpha\alpha} = s_\alpha$. In the following, the SVD will be done such that the singular values are of descending order $s_1 \geq s_2 \geq \cdots \geq s_r$. The Schmidt rank r of S denotes the number of non-zero singular values.

Before making the connection of singular values and entanglement of subsystems, it is important to note some properties of the matrices U and V.

The matrix U is of dimension $N_A \times \min(N_A, N_B)$ with orthonormal columns. This implies that

$$UU^\dagger = \mathbb{1} . \tag{7.1.2}$$

This property is important when it comes to the gauge of the MPS and is called left-normalized in the following. The matrix $V^\dagger$ is right-normalized as it is of dimension $\min(N_A, N_B) \times N_B$ and has orthonormal rows with

$$V^\dagger V = \mathbb{1} . \tag{7.1.3}$$

From the context of quantum systems, the SVD is also called a Schmidt decomposition, where the Schmidt values display the entanglement between two subsystems. Getting back to the wavefunction in Equation 7.0.1, it can be divided into two subsystems A and B

$$|\psi\rangle = \sum_{ij} C_{i,j} |i\rangle_A |j\rangle_B , \tag{7.1.4}$$

where i and j contain several site indices. This grouping of indices into a single one (i and j) is called a compound index. For simplicity, the chain is divided at the half, so A contains the left half of the chain $i \in \left\{ n_1, \ldots, n_{N/2} \right\}$ and B the right half $j \in \left\{ n_{N/2+1}, \ldots, n_N \right\}$. Decomposing the coefficient matrix $C_{i,j}$ it reads

$$|\psi\rangle = \sum_{\alpha=1}^{\min(N_A, N_B)} \left(\sum_i U_{i\alpha} |i\rangle_A \right) s_\alpha \left(\sum_j V_{j\alpha}^\dagger |j\rangle_B \right) . \tag{7.1.5}$$

As the matrices U and $V^\dagger$ are orthonormal (left and right), a new basis is introduced

$$|\psi\rangle = \sum_{\alpha=1}^{\min(N_A, N_B)} s_\alpha |\alpha\rangle_A |\alpha\rangle_B . \tag{7.1.6}$$

In Figure 7.1, it is exemplarily shown, how a decomposition of the coefficient matrix is performed. The s_α are connected to the bipartite entanglement: From this new basis, the

Figure 7.1.: Singular-value decomposition of the coefficient matrix $C_{i,j}$. The singular values are the diagonal entries of the diagonal central matrix with descending order. The smallest singular values will be discarded. The left matrix $U_{i,\alpha}$ is left-normalized and the right matrix $V^\dagger_{\alpha,j}$ is right-normalized.

reduced density operators of each half respectively is given by

$$\hat{\rho}_A = \sum_{\alpha=1}^{\min(N_A,N_B)} s_\alpha^2 |\alpha\rangle_A \, {}_A\langle\alpha| \qquad \hat{\rho}_B = \sum_{\alpha=1}^{\min(N_A,N_B)} s_\alpha^2 |\alpha\rangle_B \, {}_B\langle\alpha| \; , \qquad (7.1.7)$$

from which the von-Neumann entropy is calculated via

$$S_{AB}(\psi) = -\operatorname{tr}\hat{\rho}_A \log_2\hat{\rho}_A = -\sum_{\alpha=1}^{\min(N_A,N_B)} s_\alpha^2 \log_2 s_\alpha^2 \; . \qquad (7.1.8)$$

Thus, the SVD allows to decompose a large coefficient matrix into a set of three matrices where one matrix displays the entanglement between the two subsystems A and B via the singular values s_α. The advantage in doing so is that when the entanglement S_{AB} is small, many singular values are zero as the Schmidt rank $r \le \min(N_A, N_B)$. Thus, it reduces the sum in Equations 7.1.5-7.1.7 to r summands. Furthermore, in numerical practice, one defines an approximate matrix $\tilde{S}$ with Schmidt rank $\tilde{r}$. This approximation is performed such that the norm of the approximate coefficient matrix $\tilde{C}_{i,j}$ will only deviate marginally from $C_{i,j}$

$$||C_{i,j}|| \simeq ||\tilde{C}_{i,j}|| \; . \qquad (7.1.9)$$

Now the great advantage of performing a SVD becomes clear: One can truncate the matrix S with rank $\min(N_A, N_B)$ to an approximate matrix $\tilde{S}$ with rank $\tilde{r}$. This allows to reduce the number of columns of U and the number of rows of $V^\dagger$. Thus, the SVD grants a tool to measure the entanglement between subsystems and reduce the matrix dimension according to that. If for example $|\psi\rangle$ is in a product state, the rank of S will be $r = 1$, thus for this trivial example, the dimension of $C_{i,j}$ is reduced drastically by performing a SVD. The goal of the MPS formalism is to bring any superposition state as close as possible to a product state.

7.2. Diagrammatic tensor representation

When it comes to more complex matrices and one performs more than a single SVD, the display of the corresponding tensors in a single equation becomes confusing as with each SVD, the number of indices is increased by one. To simplify the display of more complex MPS, there is the common diagrammatic form. Considering the coefficient matrix $C_{i,j}$ in Equation 7.1.4, it consists of two indices, i and j. These indices are referred to as physical indices, as they have a physical relevant label, in most cases the site index n_k. In this particular example i is a compound index of all site indices of the left half and j
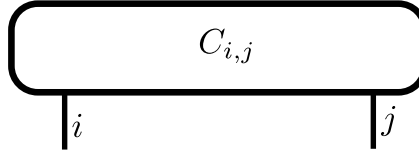
Figure 7.2.: Diagrammatic representation of the coefficient matrix. It has two physical indices i and j which are displayed as outgoing vertical lines.

of all site indices of the right half. In Figure 7.2, the diagrammatic representation of the coefficient matrix is shown. The two vertical lines represent the two physical indices which is a compound index in this example. Note that vertical lines throughout this thesis are always denoted as physical indices with local Hilbert-space dimension d ($d = 2$ for spins). The number of indices of a tensor defines its rank. The coefficient matrix in Equation 7.1.4 and Figure 7.2 has two indices and thus two outgoing lines. This makes it a tensor of rank two which is a matrix. A tensor with one single index would be a vector. The diagrammatic representation becomes really advantageous when dealing with high rank tensors $r \geq 3$. It will be shown that a common MPS mostly consists of rank three tensors. However, tensors of higher ranks are considered in this thesis as well, especially when it comes to the connection of feedback dynamics with a many-body system (cp. chapter 9).

Another advantage of the diagrammatic representation is the display of a SVD or other operations performed on tensors. The SVD of Equation 7.1.5 is shown in Figure 7.3 in diagrammatic form. The coefficient matrix with two outgoing physical indices is decomposed into three matrices: A left-normalized Matrix U with physical index i which is represented with round edges at the left side, a diagonal matrix S and a right-normalized matrix (round edges at the right side) $V^\dagger$ with physical index j. In contrast to the two vertical physical indices, there are now two horizontal indices α which connect the matrices U, S and $V^\dagger$. These indices are referred to as bond or link indices as they link the decomposed matrices. If one would contract the tensors over α by performing the sum

$$\sum_{\alpha=1}^{r} U_{i\alpha} S_{\alpha\alpha} V_{\alpha j}^{\dagger} = C_{i,j} \ , \tag{7.2.1}$$

one obtains the initial coefficient matrix. Thus, the links can be seen as an Einstein summation where in a product of tensors, a sum over the shared indices is performed. The SVD results in additional link indices which is a rewriting of the initial matrix into a set of tensors which are connected with this link index. In this thesis horizontal lines are always referred to as link indices.

It is important to mention that the MPS representation is not unique. The dimension r of the link index α is not fixed and especially by performing a time evolution, its dimension grows with each time step. Thus, depending on the problem, different representations and series of SVDs could be advantageous. This gauge of the MPS will be discussed in the following.
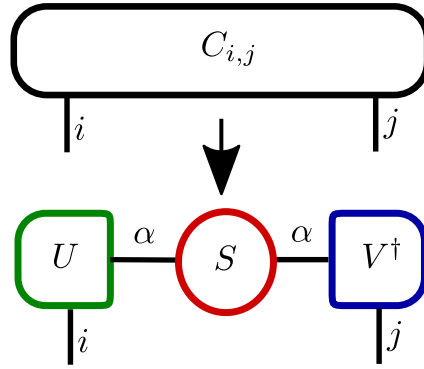
Figure 7.3.: Diagrammatic representation of the SVD, $C_{i,j}$ with two physical indices is decomposed into three matrices where the left-normalized matrix U (round edges at the left side, green) gets the vertical physical index i and the right-normalized matrix $V^\dagger$ (round edges at the right side, blue) gets the vertical physical index j. Horizontal lines represent link indices between the diagonal singular-value matrix S and U and $V^\dagger$. Connected lines are shared indices of two tensors. The two tensors will be contracted over these indices.

7.3. Canonical form of a matrix product state

In the previous section a decomposition of two subsystems was considered. The matrix dimension was reduced by neglecting all singular values s_α with $\alpha > \tilde{r}$. Thus, due to the descending order, small singular values will then be neglected. The real advantage of the MPS representation lies in performing series of SVDs and at each decomposition cut off the negligible part of the tensors. This is done by controlling the error with the norm as shown in Equation 7.1.9. In practice, this will be done for each physical site index.

Instead of writing down the equations, the advantageous diagrammatic representation will be used to display operations with tensors in the following. Note that the diagrammatic representation contains all the relevant information, but for the explicit entries of the tensors. However, the explicit entries are usually not of interest. A different gauge of the MPS results in different entries. This does not cause a problem, because a different gauge leaves the important expectation values invariant. Although, the gauge does become relevant in calculating the expectation values as this makes a huge difference in the computation time. The different relevant gauges of the MPS will be discussed within this section.

In Figure 7.4, an arbitrary coefficient tensor with N physical site indices n_i is shown. Note that physical indices are represented as vertical outgoing lines. In a first step, two subsystems are defined, one contains the first physical index n_1 and the second subsystem contains all other indices $n_2, \ldots, n_N$. Now both subsystems are decomposed as shown in Equation 7.1.5, resulting in a tensor containing only the physical index n_1 and the link to the singular-value matrix. A second tensor contains all other physical indices as well as the link index resulting from the SVD.

In the next step, the singular-value matrix and the right-normalized tensor containing indices $n_2, \ldots, n_N$ are contracted over the link l_2. Note that this step is not necessary but just a specific gauge of the MPS used in this thesis. The advantage is that the first tensor containing the physical index n_1 is left-normalized. The right tensor containing all other indices is again orthonormal and the next step can be performed. This is shown in Figure 7.5.
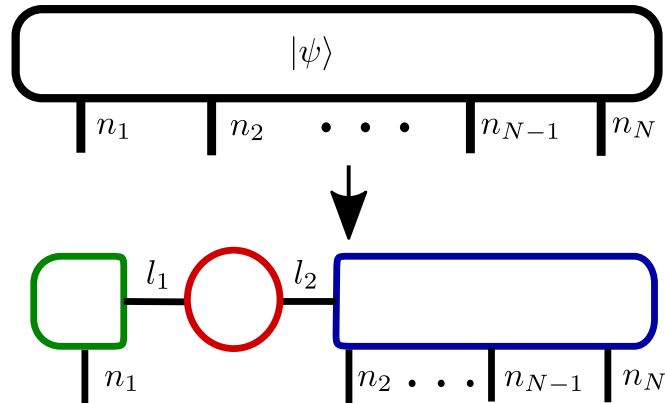
Figure 7.4.: Diagrammatic representation of the coefficient tensor of $|\psi\rangle$. It has N physical site indices n_i. In a first step, the decomposition takes place between the first site index n_1 and the rest of the system $n_2, \ldots, n_N$.
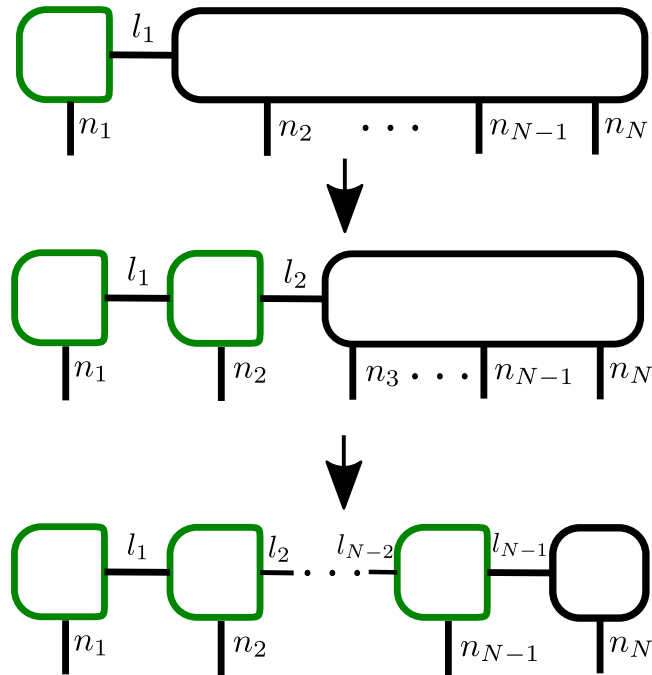

Figure 7.5.: Diagrammatic representation of the construction of a matrix product state. The MPS is constructed from the left, resulting in a left-canonical MPS. After each SVD, the singular-value matrix is contracted with the rest of the right system to create an orthogonal tensor (black box). Then the next SVD of the following physical index takes place.
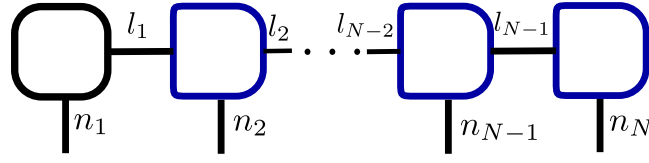
Figure 7.6.: Right-canonical MPS. The orthogonality center (OC) is at the left side (black box, round edges) and all other tensors are right-normalized (blue boxes, right round edges).

In the next step the first site tensor containing n_1 is put aside and two subsystems are defined, one containing n_2 as well as the link index l_1 and the other subsystem contains the indices $n_3, \ldots, n_N$. The SVD again decomposes the tensor and after contracting the right side with the singular-value matrix, there are two linked left-normalized tensors, one containing the index n_1 and the other the index n_2. Both share the link index l_1 resulting from the first SVD. Furthermore, the tensor containing the physical index n_2 also share a link index l_2 with the rest of the system resulting from the second SVD.

This procedure is repeated until the orthonormal matrix called orthogonality center (OC, black box) is at the right end of the system and contains only n_N as physical index.

At a first glance, the MPS formalism seems to blow up the dimension of the given problem. On a closer look, it becomes clear that indeed the formalism allows to truncate the Hilbert space: The link indices reflect the entanglement between the subsystems which are now the different sites of the chain. Within each step, the entanglement between the subsystems is reflected in the singular values. If there is no entanglement between states of the subsystems, the singular value is zero and the matrices can be truncated accordingly. In particular, after the truncation in the SVDs, all l_i have dimension one if $|\psi\rangle$ was initially in a product state. It becomes clear that series of SVDs reduce the dimension of $|\psi\rangle$ when written in a MPS as with each SVD, the dimension of the Hilbert space is reduced, depending on the entanglement of the system.

The MPS form in Figure 7.5 is called canonical form and in particular left-canonical form as all tensors are left-normalized but for the last site n_N which is the OC. This specific gauge of the MPS has advantages when it comes to calculating observables. This will be shown in detail later on. An obvious example is the calculation of the norm $\langle\psi|\psi\rangle$. The contraction of all left-normalized matrices with its complex conjugated is obsolete as they are $\mathbb{1}$ by construction. Thus, the only operation which has to be performed is a contraction of the OC (more details in the next section).

This not only holds for the left-canonical form. One can do the construction of the MPS, starting from the right side with n_N. This will end up in a right-canonical form as shown in Figure 7.6. Here, the OC is at the left side of the MPS at n_1 and all other tensors are right-normalized.

The last and most important form of used MPS in this thesis is the mixed-canonical form, shown in Figure 7.7. There, the OC is at an arbitrary position. All tensors left of the OC are left-normalized and all right of it are right-normalized. It is straightforward to arrive at the mixed canonical form from e.g. right-canonical form: The tensors n_1 and n_2 are contracted and decomposed, but now the singular-value matrix is contracted with the tensor of n_2. Thus, the OC is now at the tensor of n_2 and the n_1-tensor is left-normalized. By repeating this procedure, the OC is brought to the desired position. It becomes clear that the position of the OC is crucial for MPS algorithms.
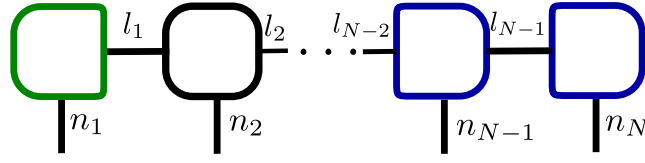
Figure 7.7.: Mixed-canonical MPS. The OC (black box, round edges) is at an arbitrary
position. All matrices left from the OC are left-normalized (green box, left
round edges) and all right from the OC are right-normalized (blue boxes, right
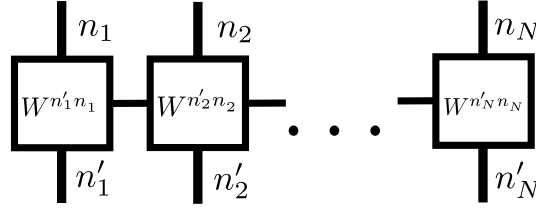round edges).

Figure 7.8.: General form of an MPO which acts on all sites. Each site has one incoming
and one outgoing physical index acting as a projector for the MPS.

In practice, the construction of the MPS does not start as shown in Figure 7.4. This has
the disadvantage that the initial coefficient matrix is already an exponentially large tensor,
which for a common many-body problem is already at computational limits. The idea
is to start in a specific product initial state as for example the Néel-state. This is easy
to write down in tensor notation as each tensor only has one occupied physical index
without being entangled with the other sites. The gauge is then achieved by contracting
the respective tensors with each other and then decomposing them before getting on with
the next index. This results in a dummy link index of dimension one between the two
tensors. This procedure is the same as for shifting the OC.

7.4. Matrix product operators

In the matrix product formalism an operator $\hat{O}$ can be seen as a projector which projects
one physical index $\mathbf{n}$ to another one $\mathbf{n}'$

$$\hat{O} = \sum_{\mathbf{n}'\mathbf{n}} W^{n'_1 n_1} \ldots W^{n'_N n_N} |\mathbf{n}'\rangle\langle\mathbf{n}| \tag{7.4.1}$$

with coefficients $W^{n_i n'_i}$. The difference to the coefficients of a matrix product state is that a
matrix product operator (MPO) has two physical indices per site, one in- and one outgoing.
In Figure 7.8, an MPO acting on all sites is demonstrated in diagrammatic form. In practice,
any operator acting on several sites can be brought in the form of Equation 7.4.1 by a
series of SVDs, but with the two physical site indices per tensor. Note that this can become
complicated for long-range coupling. However, for nearest-neighbor coupling, the MPO
formalism has the advantage that it is not necessary to contract the whole MPS when
the operator is applied. Instead, one can apply the MPO site wise, starting e.g. from the
left side. This will be explained in detail when explaining the MPS algorithms for the
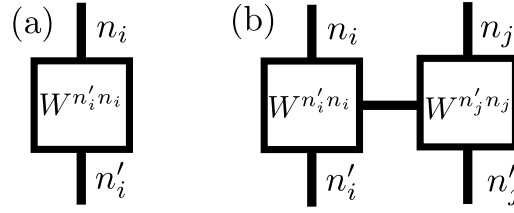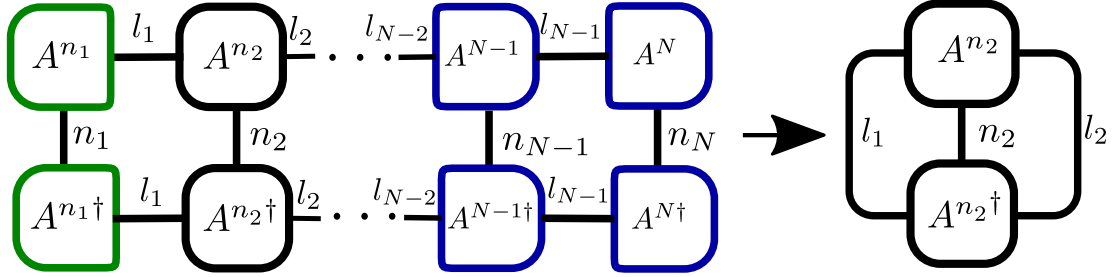respective investigated systems.

Figure 7.9.: Diagrammatic form of a (a) single-site and (b) two-site MPO.

Figure 7.10.: Calculation of the norm $\langle\psi|\psi\rangle$. One profits from a MPS in mixed canonical form as only the respective tensors at the position of the OC have to be contracted.

In this thesis, an operator acting on all sites will be the time-evolution operator $\hat{U}$ including the respective Hamiltonian. Other important operators are single-site operators (e.g. magnetization) or two-site operators for the computation of e.g. current or correlation functions as it is exemplarily shown in Figure 7.9.

Note that each tensor of the MPO contains two physical indices n_i and n_i'. The indices act on the respective MPS, n_i acts on $|\psi\rangle$, whereas n_i' acts on the complex conjugate $\langle\psi|$ which is denoted for clarity by the prime sign. This is just a new label for the respective index to avoid confusion and prevent contractions over the wrong physical indices.

7.5. Expectation values

The most simple and crucial expectation value is the norm

$$||\psi|| = \langle\psi|\psi\rangle \ . \tag{7.5.1}$$

Assuming $|\psi\rangle$ to be already a MPS in mixed-canonical form as in Figure 7.7 with vertical physical indices at the bottom, the complex conjugated $\langle\psi|$ is the same MPS with complex conjugated values. In diagrammatic form it is displayed with vertical physical indices at the top. To compute the norm, the two MPS are multiplied with each other. Thus, the MPS is contracted via a summation over shared indices which are the vertical physical indices as shown in Figure 7.10 (left). For simplicity, the tensor at the respective site n_i is named A^{n_i} and its complex conjugated is named $A^{n_i\dagger}$. Note that the tensors have also link indices in addition to the physical index appearing in the name.

When calculating expectation values, one benefits from a gauged MPS. Assuming the OC is at the tensor A^{n_2} of the MPS. As the MPS is in mixed canonical form, the left tensor A^{n_1}
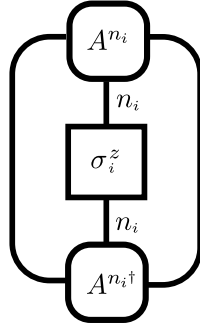
Figure 7.11.: Calculation of the single-site magnetization for a MPS in mixed-canonical form.

with physical index n_1 is left-normalized. From the property of left-normalized matrices in Equation 7.1.2, it becomes clear that the multiplication with its complex conjugated yields the identity. The same holds for all right-normalized tensors to the right of the OC as it can be seen in Equation 7.1.3. Thus, the only part of the expectation value in Figure 7.10 which has to be contracted is the OC with the two link indices at the left and right side, as the two tensors A^{n_2} and $A^{n_2\dagger}$ share the same link indices. This is the main reason why the mixed canonical form is a great advantage: One does not have to contract the whole MPS when calculating an expectation value, but just the part with the OC as it is known per construction that all left- and right-normalized matrices yield the identity when contracted in the right order. Note that a contraction over all indices yields a scalar which will be the norm in Figure 7.10.

In numerical practice, this operation is performed N-times for the norm. Starting with the OC at the first position A^{n_1}, multiply the MPS with its complex conjugate, contract the two tensors A^{n_1} and $A^{n_1\dagger}$ and thus compute the norm. Note that for this computation the physical index of the complex conjugate n_1' is unprimed to clarify the contraction over the same index. In the next step bring the OC to position two (A^{n_2}), square the MPS, contract the tensors and add the result to the norm. Repeat this procedure up to the last site results in the norm

$$||\psi|| = \frac{1}{N} \sum_{i=1}^{N} A^{n_i\dagger} A^{n_i} \ . \tag{7.5.2}$$

In practice, Equation 7.5.2 will deviate from one even when $|\psi\rangle$ is normalized, as each truncation after a SVD involves an error. If the neglected singular values are too high, this will be reflected in the norm $||\psi||$. Thus, the norm is the most important expectation value when performing MPS algorithms, as it is the control variable to check the numerical error.

The expectation value of a single-site operator is straightforward. As an example, the computation of the single-site magnetization is shown in Figure 7.11. The magnetization is calculated via the Pauli Spin-matrix σ_i^z

$$M_i = \langle n_i | \sigma_i^z | n_i \rangle \tag{7.5.3}$$

The Pauli-matrix has two physical indices, one for the rows and one for the lines, both with the same physical index n_i. The spin-matrix was defined in Equation 2.2.14. As for
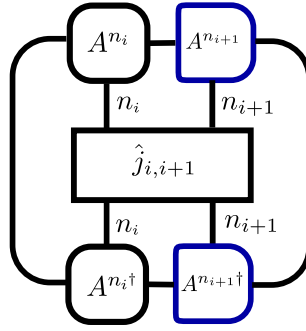
Figure 7.12.: Current $\hat{j}_{i,i+1}$ as exemplary two-site operator. The tensors on which the operator acts (i.e. $A^{n_{i+1}}$ even if its right-normalized) have to be included in the operation.
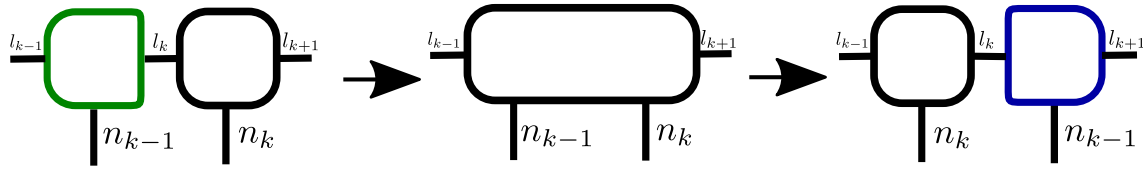

Figure 7.13.: Performing a swap operation to switch the two physical indices n_{k-1} and n_k while maintaining the link indices l_{k-i} and l_{k+1}. Note that the dimension of the link indices might change by performing this operation. After this operation n_k may be swapped with the next left tensor $A^{n_{k-2}}$.

the system norm, the multiplication of a MPS in mixed-canonical form with its complex conjugate yields the identity for left- and right-normalized tensors. However, if an operator is involved this is not the case. Thus, if an operator is applied to the MPS, the OC has to be involved in the operation. The most effective way is to bring the OC to the position where the single-site operator is acting on by performing a series of SVDs. Then, all other products of normalized tensors yield the identity and only the local tensors are involved in the operation (Figure 7.11).

Another important operation is a two-site operator, as for example the local current $\hat{j}_{i,i+1}$ in Equation 6.1.7. As for the single-site operators, it is crucial for an efficient computation that the OC is at one of the tensors the operator acts on. Otherwise, all tensor between the OC and the operator need to be contracted as well. Thus, a more efficient way is to bring the OC to the tensors involved in the operation. It is irrelevant if the OC is at A^{n_i} or at $A^{n_{i+1}}$. Note that the two-site operator $\hat{j}_{i,i+1}$ has four physical indices two for site n_i and two for site n_{i+1} as shown in Figure 7.12. As the local current operator acts on nearest-neighbors, only the respective neighboring tensors have to be included in the operation. However, if a two-site operator acts at distant tensors $\hat{O}_{i,k}$ (e.g. for the computation of a correlation function), all tensors between A^{n_i} and A^{n_k} have to be included and contracted for the operation.

Another possibility for a two-site operator acting on distant tensors, is to swap the tensor A^{n_k} with its left neighbors until it is next to A^{n_i}. In doing so, the OC is kept at A^{n_k}. This is shown in Figure 7.13. The tensors $A^{n_{k-1}}$ and A^{n_k} are contracted over the link index l_k resulting in a tensor of rank four with the two physical indices and the two link indices to the left and the right. Then a SVD is performed in maintaining the link indices at the

left and right position but switch the physical indices such that the index n_k now is left of the physical index n_{k-1}. Note that the link index l_k might change its dimension after the operation. This is repeated until A^{n_k} is the tensor next to A^{n_i}. Then, the operator $\hat{O}_{i,k}$ can be evaluated similar to $\hat{j}_{i,i+1}$ in Figure 7.12. This might be more effective for a two-site operator acting on distant sites (and depending on the size of the MPS the only possible) because otherwise all tensors in between have to be contracted as well for this operation. This swap operation will especially become relevant when performing a feedback algorithm.

8.
Feedback controlled two-photon purification

In this part of the thesis, entangled system-reservoir interaction is investigated. In this chapter, the system of interest consists of only a single TLS. However, in contrast to Part II, tracing out the reservoir degrees of freedom is not possible as system and reservoir are entangled due to a quantum feedback mechanism. The idea is to treat the reservoir as a many-body system with the matrix product state (MPS) formalism, introduced in chapter 7. It is assumed that the reservoir is structured and includes a distant mirror. Photons emitted from the TLS will interact again with the system after a time-delay, which is why any entanglement becomes relevant again in the future. The key-mechanism is, by varying the mirror distance, it is possible to control the photon statistics of the reservoir which is treated in a numerically exact manner within the MPS formalism.

Single photons are used as qubits for quantum computation protocols [159] or quantum key distribution [160]. An almost ideal single-photon source is achieved, by using a single TLS [59, 161], which is experimentally realized in, e.g., atoms [162], single quantum dots [163, 164, 165, 166, 167, 168, 169], molecules [170] and defects in solids [171]. The TLS is initialized in its ground state and inverted by excitation with a Gaussian pulse, resulting in half a Rabi-oscillation (π-pulse). After decaying radiatively, the TLS emits a single photon into the environment under spontaneous emission. However, by driving the TLS with a full Rabi-oscillation (2π-pulse), it was shown recently that the two-photon probability becomes higher than that of a single photon. This forms the idea that a single TLS acts as a source for a multi-photon state. To achieve a reliable two-photon source [172, 173, 174, 175], a high degree of control is essential. This is especially relevant if the same source should act as source for both, single and multi-photon generation [176, 177, 178, 179].

The idea of this chapter is to use a mirror, where quantum interferences manipulate the photon statistics due to an all-optical feedback mechanism.

In classical chaotic systems, time-delayed Pyragas control is used to stabilize otherwise unstable steady-states [180, 181, 182, 183]. In the quantum-regime it was successfully demonstrated that in measurement-based feedback setups non-classical light states are stabilized [184, 185], single trapped ions are cooled [186] or quantum correlations are controlled [187]. A different approach is to use structured baths [188], where reservoir engineering leads to the desired dynamics [189, 190, 191, 192, 193]. The advantage is that the quantum system is not perturbed by a measurement process.

However, the here investigated approach is to adapt the classically successful concept of a finite delay time τ of Pyragas control to quantum protocols [194, 195]: The signal of the system $s(t)$ acts as a control field, where the time-delayed signal $s(t - \tau)$ allows all-optical control while no measurement is needed.

Adapting the concept of time-delayed feedback in the quantum regime, it was shown that the

entanglement between photons emitted from a biexciton [196] as well as between nodes in a quantum network is controlled [197]. In parametric oscillators, quantum feedback enhances squeezing [198, 199]. Furthermore, unstable branches of bistabilities are stabilized using feedback in optomechanical systems [200, 201]. It was also experimentally demonstrated that feedback can manipulate the emission statistics of photonic devices [202, 203].

To achieve all-optical feedback, the light is reflected by, e.g., an external mirror or an integrated semi-infinite waveguide. The photons emitted by the system are fed back after a time-delay which is why a non-Markovian treatment is necessary. The emitted photons interact subsequently with the system after a time-delay due to the structured surrounding reservoir. Thus, a memory kernel of the reservoir is the basis to describe all-optical feedback in the theoretical approach. In this chapter, the description of quantum feedback is based on the quantum stochastic Schrödinger equation [204, 54, 205], introduced in chapter 3. The idea is to use an MPS representation as introduced in chapter 7 to treat only the most relevant part of the Hilbert space to deal with the large memory kernel. However, in the here investigated setup, there is a further complexity. Due to the time-dependent Gaussian shaped excitation, two time-scales are involved, i.e. the short pulse and the long radiative decay. The solution is to extend the MPS method based on the QSSE by going beyond the Euler-like expansion of the time evolution. The speedup in the computation also allows a non-Markovian treatment for more complex systems such as strongly-correlated [14, 148, 48, 156] or many-emitter setups [102, 103, 93, 114] which have been subject of investigation in chapter 5 and chapter 6.

However, in this chapter the focus lies on a comparable simple system and a complex structured reservoir. The findings of this chapter demonstrate a quantum interference between the system and the photon-field. In changing the distance between emitter and mirror, these interferences allow the control of the photon statistics [206]. Destructive interference results in a suppression of the one-photon probability at the simultaneous increase of the two-photon probability. For constructive interference, two-photon generation is suppressed and a single-photon emission process becomes more probable resulting in a single-photon source for a 2π-pulse.

The proposal is that a combination of the two control concepts, i.e. time-dependent excitation and time-delayed feedback allows to achieve statistics on demand, ranging from enhancing the total photon output to an increase of the two-photon probability as well as two-photon purification by suppressing single-photon events. The proposed setup allows to all-optically address individual photon probabilities in varying the external control parameters.
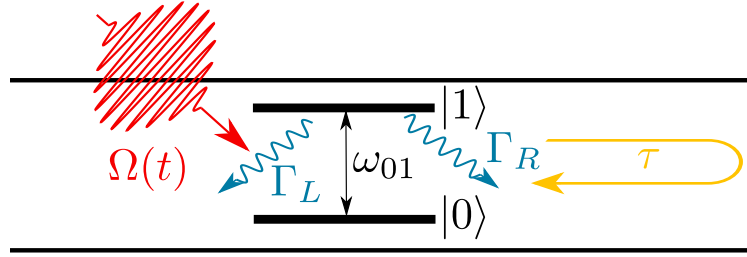
Figure 8.1.: A TLS with frequency ω_{01} is placed inside a semi-infinite waveguide. The TLS is pumped via a time-dependent external laser $\Omega(t)$. Due to spontaneous decay, a photon is emitted either to the left side with spontaneous emission rate Γ_L or to the right side with rate Γ_R. The photon emitted to the right side is reflected at the closed end and interacts again with the TLS after a time-delay τ.

8.1. Theoretical model

In chapter 3, the quantum stochastic Schrödinger equation was introduced to generate the Lindblad equation for a continuously driven TLS coupled to a continuum (Equation 3.1.1). In this chapter, an additional complexity is considered which is a structured external reservoir. As a model system, in contrast to Part II, a simple two-level system is considered. However, the reservoir degrees of freedom cannot be traced out as the TLS and the surrounding reservoir become entangled. Thus, the whole system is considered, i.e. electronic TLS and bosonic reservoir. The idea is to treat the reservoir combined with the TLS as a many-body system and describe it with the matrix product state formalism, introduced in chapter 7. In order to model the structured reservoir, a semi-infinite waveguide [207, 208] is assumed as surrounding reservoir. The TLS is placed at a specific position within the waveguide. As the waveguide is closed at one end, a boundary condition for the photon field is present. Thus, the system-reservoir interaction is modeled differently in contrast to Equation 3.1.1 and reads

$$
\begin{aligned}
\mathcal{H}_{\text{fb}} = \int d\omega \hbar \omega \hat{b}^\dagger(\omega) \hat{b}(\omega) \\
+ \int d\omega \hbar \left[G_{\text{fb}}(\omega) \hat{b}^\dagger(\omega) \sigma^- + h.c. \right] .
\end{aligned}
\tag{8.1.1}
$$

In analogy to Equation 3.1.1, the first term describes the free evolution of the reservoir resulting from the quantized vacuum Maxwell field from section 2.3. The crucial difference lies within the TLS-reservoir interaction, where the boundary condition of a closed waveguide is modeled as a frequency-dependent coupling with [209, 210, 211]

$$
G_{\text{fb}}(\omega) = g_0 \sin(\omega L/c_0) ,
\tag{8.1.2}
$$

where c_0 is the speed of light in vacuum and L the distance between the TLS and the closed end of the waveguide. The boundary condition can be interpreted as a reflecting mirror where the light field within the waveguide has a node at the closed end of the waveguide. The reflecting mirror results in a feedback loop, where photons emitted from the TLS interact again with the system after time-delay $\tau = 2L/c_0$. Note that besides this boundary condition, the coupling strengths is assumed to be a constant decay parameter $g_0 = \sqrt{\Gamma/2\pi}$ of the TLS excitation, which is associated to a Markov approximation in

analogy to section 3.1. As a further complexity, a pulsed driven TLS is considered, where the amplitude of the external driving laser becomes time dependent $\mathcal{E}_0 \to \Omega(t)$. The external coherent pulse is assumed to be resonant with the TLS frequency $\omega_L = \omega_{01}$. The whole model system is sketched in Figure 8.1. With these considerations, the total Hamiltonian reads

$$\mathcal{H}(t) = \hbar\omega_{01}\sigma^+\sigma^- + \hbar\Omega(t)\left(\sigma^+ e^{-i\omega_L t} + \sigma^- e^{i\omega_L t}\right) + \mathcal{H}_{\text{fb}} . \tag{8.1.3}$$

Note that the Hamiltonian of the pumped TLS is described in energy conserving rotating wave approximation as explained in section 2.4. The time-dependent external laser is modeled as a Gaussian pulse with frequency ω_L and time-dependent amplitude

$$\Omega(t) = \frac{A}{\sqrt{\nu^2\pi}}e^{-t^2/\nu^2} . \tag{8.1.4}$$

One of the crucial parameter within this chapter will be the pulse area A as it defines the number of Rabi-oscillations, the TLS undergoes during the pulse, i.e. for $A = \pi$ the TLS excitation is inverted due to a half Rabi-oscillation. For $A = 2\pi$, the TLS undergoes a full Rabi-Oscillation, ending up in the electronic initial state after the pulse. The parameter ν describes the linewidth of the Gaussian pulse. Due to the finite pulse width combined with a finite radiative decay to the surrounding environment, the TLS does not end up in its initial state after a full Rabi-oscillation [212] which will be described more detailed in the following section.

In contrast to chapter 3, where the Lindblad equation was derived with a reduced density matrix formalism in section 3.3, the frequency-dependent coupling $G_{\text{fb}}(\omega)$ does not allow a straightforward evaluation of the trace over the reservoir as system and reservoir are highly entangled due to the boundary condition. However, the problem can be solved numerically in the Schrödinger picture by writing the combined state of the system and reservoir as an MPS. Equation 8.1.3 is again transformed into a rotating frame via Equation 3.1.3 with respect to the free evolution ω_{01} of the system and ω of the reservoir as done in Equation 3.1.5

$$\mathcal{H}_{\text{TLS,rf}}(t) = \hbar\Omega(t)\left(\sigma^+ + \sigma^-\right), \tag{8.1.5}$$

$$\mathcal{H}_{\text{fb,rf}}(t) = \int d\omega\, \hbar\left(G_{\text{fb}}(\omega)\sigma^+\hat{b}(\omega)e^{-i(\omega-\omega_{01})t} + G_{\text{fb}}^*(\omega)\sigma^-\hat{b}^\dagger(\omega)e^{i(\omega-\omega_{01})t}\right) . \tag{8.1.6}$$

It is differentiated between photons emitted to the left Γ_L and photons emitted to the right side Γ_R. Thus, g_0 is split into the left propagating wave with $\sqrt{\Gamma_L/2\pi}$ and $\sqrt{\Gamma_R/2\pi}$ for the right propagating wave. The structured coupling in exponential form then reads

$$G_{\text{fb}}(\omega) = i\left(\sqrt{\frac{\Gamma_R}{2\pi}}e^{-i\omega\tau/2} - \sqrt{\frac{\Gamma_L}{2\pi}}e^{i\omega\tau/2}\right) . \tag{8.1.7}$$

Inserting this into the Hamiltonian in Equation 8.1.5 and Equation 8.1.6 and performing again a rotating frame transformation with Equation 3.1.3 to shift the τ dependence into one of the summands. With the unitary operator which fixes the spatial coordinates

$$U = e^{-i\int d\omega\,\omega\tau/2\hat{b}^\dagger(\omega)\hat{b}(\omega)}, \tag{8.1.8}$$

the transformed Hamiltonian reads

$$\mathcal{H}_{\text{TLS,rf}}(t) = \hbar\Omega(t)\left(\sigma^+ + \sigma^-\right), \tag{8.1.9}$$

$$\mathcal{H}_{\text{fb,rf}}(t) = -i\hbar\left(\sqrt{\frac{\Gamma}{2}}\hat{b}(t-\tau)e^{-i\phi} + \sqrt{\frac{\Gamma}{2}}\hat{b}(t)\right)\sigma^+ + h.c.. \tag{8.1.10}$$

It is assumed that the radiative decay to the left and to the right side of the waveguide are equal $\Gamma_R = \Gamma_L = \Gamma$. Furthermore, the time-dependent reservoir operators in Equation 3.1.6 have been inserted. A new parameter $\phi = \pi - \omega_{01}\tau$ is introduced, which is called the feedback phase. The fast rotating phase ϕ determines whether the feedback field is constructive or destructive with the TLS excitation, where $\omega_{01}\tau = 2n\pi$ is called constructive and $\omega_{01}\tau = (2n-1)\pi$ is called destructive interference for integer numbers n. In the following, the nomenclature constructive/destructive will become clear.

This Hamiltonian shows system-reservoir interaction at two different times. If a basis set such as in Equation 3.1.16 is introduced, the resulting time-evolution operator interacts with two different time-bins at each time step Δt. The time-bin $|i_k\rangle$ is called the current time-bin which corresponds to all operators $\hat{b}^{(\dagger)}(t)$. Without the boundary condition this is the term resulting in the Lindblad dissipation in Equation 3.3.15. However, all operators $\hat{b}^{(\dagger)}(t-\tau)$ interact with past time-bins $|i_{k-l}\rangle$, where $k - l = \tau/\Delta t$ and $k > l$. This means, any photon emitted to the right side of the waveguide interacts again with the TLS after delay τ. This is why this Hamiltonian is called the feedback Hamiltonian $\mathcal{H}_{\text{fb}}$.

This Hamiltonian already clarifies why the tracing out of reservoir degrees of freedom is not possible in this case. The resulting time-evolution operator acts on two distant time-bins. Thus, an entangled state between system and the two time-bins $|i_s, i_k, i_{k-l}\rangle$ is created at each time step Δt. A Born-Markov approximation, resulting in factorized reservoir states, as performed in section 3.3 would destroy any interference induced by the boundary condition. This is the reason, why the QSSE is used and $|\psi\rangle$ is expressed as an MPS.

8.1.1. Higher-order time-evolution operator

As in chapter 3, the time-evolution operator governs the dynamics of $|\psi\rangle$. The time-ordering operator $\hat{T}$ is redundant for the feedback Hamiltonian due to the definition of the time-increment quantum-noise operators $\Delta B^{(\dagger)}(t_k)$ and $\Delta B^{(\dagger)}(t_{k-l})$. However it is important that both commute with each other in the interval Δt. This is fulfilled as long as $\Delta t < \tau$. By adapting the numerical time step accordingly, this can be achieved in the simulation. By inserting the noise operators, defined in Equation 3.1.13, the time-evolution operator reads

$$U(t_{k+1}, t_k) = \exp\Big[-i\Delta t\Omega(\Delta t)\left(\sigma^+ + \sigma^-\right)$$

$$- \left(\sqrt{\frac{\Gamma}{2}}\Delta B(t_{k-l})e^{-i\phi} + \sqrt{\frac{\Gamma}{2}}\Delta B(t_k)\right)\sigma^+ + h.c.\Big], \tag{8.1.11}$$

where $t_k = k\Delta t$ and $t_{k-l} = t_k - \tau$. It was assumed that the amplitude of the driving laser $\Omega(\Delta t)$ at each time step only changes marginally $\Omega(t) \to \Omega(\Delta t)$, such that it is excluded from the integral over Δt. In contrast to chapter 3 and the reference introducing the method to compute the feedback Hamiltonian with the QSSE [54], in this chapter, the

time-evolution operator is expanded in second order of Δt. This has several computational reasons, one of them is that two different time-scales are involved due to the time-dependent pump $\Omega(t)$ which will be chosen comparable fast to the radiative decay Γ of the TLS. Thus, the system has to be integrated for a long time while still governing the exact dynamics during the pulse. A higher order in the time-evolution operator allows to chose a larger Δt and thus, reduce the total number of time steps. The other reasons to expand U will become clear when the feedback algorithm and the computed observables will be introduced.

To give an explicit construction of the time-evolution operator for numerical implementation, U is expressed in matrices. The operators in the exponent acting on the basis states are expressed in matrices $\mathbf{M}_{\text{TLS}}$ and $\mathbf{M}_{\text{fb}}$, respectively. Considering the basis states, the only time dependence is the amplitude of the driving laser $\Omega(t_n)$ at the respective time step t_n. An explicit expansion of the time-evolution operator then reads

$$\mathbf{U}(t_n) = \exp\left(\Omega(t_n)\mathbf{M}_{\text{TLS}} + \mathbf{M}_{\text{fb}}\right)$$
$$= \sum_{p=0}^{\infty} \frac{1}{p!}\left(\Omega(t_n)\mathbf{M}_{\text{TLS}} + \mathbf{M}_{\text{fb}}\right)^p \ , \tag{8.1.12}$$

where p is the order of the expansion and not the order in Δt. Note that the amplitude of the driving laser is separated from the Hamiltonian to deal with time-independent matrices. The reason is that with this expression, the large matrices only have to be initialized once in the beginning of the simulation.

The exponent of the time evolution is written as a matrix by multiplying the respective basis elements from left and right. The basis is labeled as $|i_S, i_k, i_\tau\rangle$, where $|i_S\rangle$ is the state of the TLS (either $|0\rangle$ or $|1\rangle$), $|i_k\rangle$ is the time-bin occupation with i_k photons at time $t_k = k\Delta t$ and $|i_\tau\rangle$ is the feedback-bin occupation with $\tau = (k-l)\Delta t$. Multiplying the basis states from left and right results in

$$\mathbf{M}_{\text{TLS}} = -\frac{i}{\hbar}\langle j_S, j_n, j_\tau| \int_{t_k}^{t_{k+1}} \frac{\mathcal{H}_{\text{TLS,rf}}}{\Omega(\Delta t)} dt |i_S, i_n, i_\tau\rangle$$
$$= -i\Delta t\left[\left(\delta_{j_S,1}\delta_{i_S,0} + \delta_{j_S,0}\delta_{i_S,1}\right)\right]\delta_{j_n,i_n}\delta_{j_\tau,i_\tau}. \tag{8.1.13}$$
$$\mathbf{M}_{\text{fb}} = -\frac{i}{\hbar}\langle j_S, j_n, j_\tau| \int_{t_k}^{t_{k+1}} \mathcal{H}_{\text{fb,rf}} dt |i_S, i_n, i_\tau\rangle$$
$$= -\left(\sqrt{\frac{\Gamma}{2}}\sqrt{i_\tau}\delta_{j_\tau+1,i_\tau}e^{-i\phi} + \sqrt{\frac{\Gamma}{2}}\sqrt{i_n}\delta_{j_n+1,i_n}\right)\delta_{j_S,1}\delta_{i_S,0}\sqrt{\Delta t}$$
$$+ \left(\sqrt{\frac{\Gamma}{2}}\sqrt{j_\tau}\delta_{j_\tau,i_\tau+1}e^{-i\phi} + \sqrt{\frac{\Gamma}{2}}\sqrt{j_n}\delta_{j_n,i_n+1}\right)\delta_{j_S,0}\delta_{i_S,1}\sqrt{\Delta t} \ . \tag{8.1.14}$$

As mentioned in chapter 3, the action of the time-bin operator $\Delta B^\dagger(t_k)$ on the state $|i_k\rangle$ creates a $\sqrt{\Delta t}$ to maintain the commutation relation in Equation 3.1.15. Thus, the matrix $\mathbf{M}_{\text{fb}} \propto \sqrt{\Delta t}$, while $\mathbf{M}_{\text{TLS,env}}(t_n) \propto \Delta t$. This is the reason, why a higher expansion in Δt of the time-evolution operator is not straightforward in the order of the expansion as both terms obey a different proportionality to Δt. For the first order in Δt, terms up to second

order of $\mathbf{M}_{\text{fb}}$ contribute as shown in chapter 3. For an expansion in the orders of $(\Delta t)^2$, terms up to the fourth order in $\mathbf{M}_{\text{fb}}$ become relevant

$$
\begin{aligned}
\mathbf{U}(t_n) \approx{}& \mathbf{U}_0 + \Omega(t_n)\mathbf{U}_1 + \frac{1}{2}\Omega(t_n)^2\mathbf{U}_2 \\
={}& \mathbb{1} + \mathbf{M}_{\text{fb}} + \frac{1}{2}\mathbf{M}_{\text{fb}}^2 + \frac{1}{6}\mathbf{M}_{\text{fb}}^3 + \frac{1}{24}\mathbf{M}_{\text{fb}}^4 \\
&+ \Omega(t_n)\big[\mathbf{M}_{\text{TLS}} + \frac{1}{2}\left(\mathbf{M}_{\text{TLS}}\mathbf{M}_{\text{fb}} + \mathbf{M}_{\text{fb}}\mathbf{M}_{\text{TLS}}\right) \\
&+ \frac{1}{6}\left(\mathbf{M}_{\text{TLS}}\mathbf{M}_{\text{fb}}^2 + \mathbf{M}_{\text{fb}}\mathbf{M}_{\text{TLS}}\mathbf{M}_{\text{fb}} + \mathbf{M}_{\text{fb}}^2\mathbf{M}_{\text{TLS}}\right)\big] \\
&+ \Omega(t_n)^2\frac{1}{2}\mathbf{M}_{\text{TLS}}^2 \ .
\end{aligned}
\tag{8.1.15}
$$

The expansion is differentiated in orders of the pump amplitude $\Omega(t)$. The reason is that the pump matrix changes with each time step and thus has to be adapted and multiplied with the corresponding matrices at each time step. By computing the matrix multiplications once in the beginning of the algorithm, at each time step only the multiplication with $\Omega(t)\mathbf{U}_1$ $(\Omega(t)^2\mathbf{U}_2)$ has to be performed. As especially the matrix $\mathbf{M}_{\text{fb}}$ might become very large, this optimizes the computation time drastically.

8.1.2. Feedback algorithm in the QSSE picture

Due to the feedback system-reservoir interaction, system and reservoir do not factorize. However, the state $|\psi\rangle$ is brought formally close to a product state when written as an MPS. As explained in chapter 7, the coefficient matrix of $|\psi\rangle$ is decomposed into a train of tensors. Thus initially, $|\psi\rangle$ is already written in the form of an MPS, even if it is initialized in a product state. The used basis is the time-bin basis of Equation 3.1.16, therefore $|\psi\rangle$ consist of infinite many future time-bins. However, it is assumed that initially all future time-bins are in the photon number state zero and are not entangled with the system or with other time-bins. Thus in practice, only one future time-bin becomes relevant at each time step. Furthermore, initially all past time-bins are in a vacuum state as well. As long as $t < \tau$, the interaction with past time-bins is not present. In Figure 8.2, the time evolution of the MPS is sketched for $t < \tau$. Note, that the MPS is always assumed to be in mixed-canonical form. If this is not the case it can be brought to the mixed-canonical gauge by a series of SVDs as explained in chapter 7.

The most relevant tensor is the system-bin with physical index i_s which describes the state of the TLS. Initially, all time-bins are set to zero and the system-bin is initialized at an arbitrary state. The MPS consists of the system- and the time-bins, where future time-bins are placed left of the system-bin and past time-bins right of the system-bin. Before $t = \tau$, the time-evolution operator is a tensor of rank four, which acts on the system-bin and the future time-bin. Thus, two indices are shared with the MPS when the time-evolution tensor is contracted with it. The primed indices are then the new state of the MPS after the first time step Δt. The resulting tensor contains the two primed indices and the link index to the past time-bins. The primed indices are unprimed to be consistent with the rest of the MPS and the tensor is decomposed via a SVD and the MPS is restructured such that the former future and now past time-bin i_0 is written right of the system-bin. Note that the OC is always kept at the system-bin. Furthermore, the link index between the system-bin and past time-bin i_0 now might be occupied, depending on the parameters
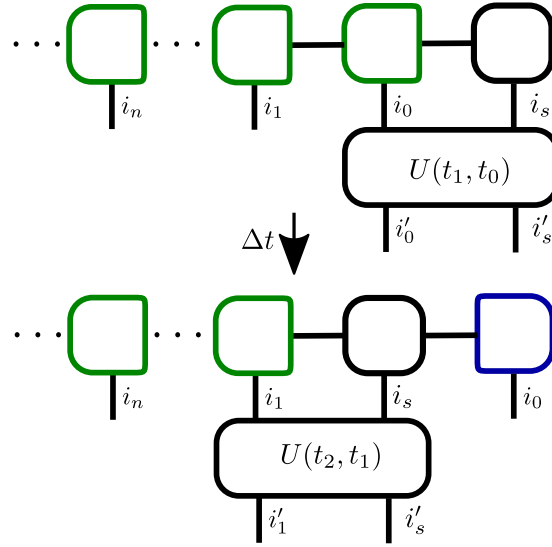
Figure 8.2.: Time evolution of the first two time steps for $t < \tau$. The time-evolution operator acts on the MPS $U(t_1, t_0)|\psi(0)\rangle$. By contracting over the two physical indices i_s (TLS index) and i_0 (first time-bin) with the time-evolution tensor, as well as the link index between the system and first time-bin, the time evolution is computed. The resulting tensor is decomposed and the outgoing physical indices i'_s and i'_0 are unprimed to restore the form of the MPS. The tensor containing the system index i_s is now left of the time-bin i_0. The system has already interacted with time-bin i_0 which is now a past time-bin and therefore right of the system-bin. It becomes clear that all time-bins right of the system-bin are past time-bins and all indices left of the system-bin are future time-bins. In the next time step the time-evolution operator acts on the indices i_s (system-bin) and i_1 (next time-bin).

in U and the cutoff of the SVD, representing entanglement between system and reservoir. Between each time step observables are derived as, e.g., the norm or the occupation of the system. This is straightforward as the OC is always at the system-bin for $t < \tau$. Afterwards, the MPS is ready to compute the next time step. Thus, the time-evolution operator now changes its index. The system index i_s remains the same but the reservoir index i_0 has changed to i_1 as $U(t_2, t_1)$ acts on the next time-bin. This is in practice realized by multiplicating the time-evolution operator with an identity tensor with two physical indices i_0 and i_1. Without changing the entries of the tensors the index i_0 is replaced with i_1 by contracting over i_0. The same is performed for the primed indices i'_0 and i'_1.

Thus within each time step, the system-bin moves one position to the left in the MPS and thus also forward in time. This procedure is repeated until $t = \tau$ is reached.

When $t > \tau$, the time-delay becomes relevant as past time-bins interact again with the system. Thus, the time-evolution operator now acts on the system-bin i_s, on the future time-bin i_k and on the feedback time-bin $i_{k-l} = \tau/\Delta t$. This poses a problem as between system-bin and feedback time-bin might be a high number of time-bins depending on Δt and τ. In order to apply the time-evolution tensor on these three tensors, one would have to contract all the time-bins between i_s and i_{k-l} as well. This can result in a very large tensor and is not practical. However, a faster possibility to deal with this long-range
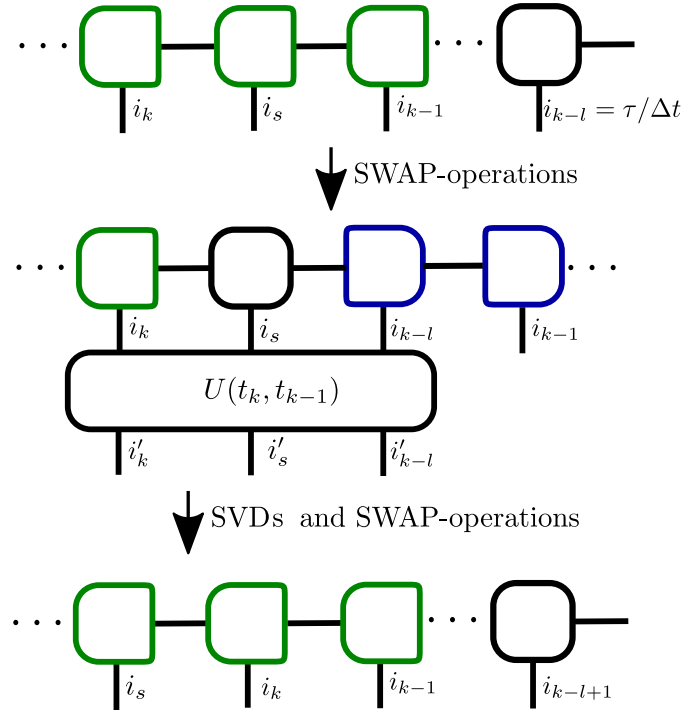
Figure 8.3.: Time evolution after time-delay τ for applying $U(t_k, t_{k-1})|\psi(t_{k-1})\rangle$. The tensor with time-bin $\tau/\Delta t = i_{k-l}$ is brought next to the system-bin by SWAP-operations. Then the time-evolution tensor being a tensor of rank six acts on the future time-bin, the system-bin and the past time-bin corresponding to the delay time τ. The resulting tensor is decomposed by SVD and the feedback-bin i_{k-l} is brought back to the original position.

coupling is by performing series of swap operations until the feedback time-bin is right to the system-bin [54]. This procedure, including the application of U, is shown in Figure 8.3. The swapping of two physical indices was introduced in Figure 7.13 in section 7.5: The OC is brought to the feedback time-bin by contractions and SVDs. Between feedback time-bin i_{k-l} and system-bin are $\tau/\Delta t$ past time-bins right of the system-bin. Thus, in a first step the feedback time-bin i_{k-l} is contracted with its left neighbor i_{k-l+1}. For the SVD, the physical index is swapped while maintaining the link indices to the left and right. The new link index between i_{k-l} and i_{k-l+1} might change in performing this operation. Then the procedure is repeated until the feedback time-bin is next to the system-bin, by keeping the OC at the feedback time-bin. In a last step, the OC is brought from the feedback time-bin to the system-bin. Observables concerning the system-bin might be computed at this point before applying the time-evolution operator.

When the feedback time-bin is next to the system-bin, the application of the time-evolution operator is the same than for $t < \tau$. The only difference is that U acts on three tensors. Thus, the resulting tensor is decomposed twice to restore the three bins. Furthermore, the tensor is decomposed such that the two time-bins are positioned right of the system-bin, because both now represent past time-bins. The OC is stored in the feedback time-bin i_{k-l}. Afterwards, the feedback time-bin is swapped back to its original position. After the last swap operation, the OC is stored in the feedback time-bin for the next time step i_{k-l+1} and the procedure is repeated until the end of the time integration is reached.

Another advantage of the higher-order time-evolution operator becomes apparent. Each time step an error is induced by a non-unitary U. This results from the expansion of the exponential in orders of Δt. When the order in Δt is higher, the same accuracy is obtained with a higher chosen Δt. For constant time-delay τ, a lower number of time-bins are needed in the delay-interval $\tau/\Delta t$ as Δt is higher. This directly leads to fewer swap operations during each time step and thus reduces drastically the computation time.

8.1.3. Computing photon probabilities from the matrix product state

In this chapter, the focus does not lie on the system observables, but on the statistics of the reservoir. The quantity of interest are the photon statistics described by photon number probabilities $p(n)$ for $t \to \infty$ after the time-dependent pulse has excited the system and the TLS is equilibrated. The MPS does not lead directly to the photon probabilities of interest. However, the photon probabilities can be obtained by calculating correlation functions [213] which are multi-site operators acting on the MPS. The operator for the total intensity emitted into the environment is defined as $\hat{I} = \sum_{j=0}^{\infty} \Delta B^{\dagger}(t_j)\Delta B(t_j)$. This results from the total intensity inside each corresponding time-bin t_j. For the numerical evaluation, it is assumed that after a large enough time $t_{\text{end}} = N\Delta t$, all excitation from the TLS is emitted into the environment, so that afterwards no photons will be observed. The mth order intensity correlation function is defined as $\langle : \hat{I}^m : \rangle$, where : indicates the normal ordering of the operators. Thus, in the time-bin basis, the correlation functions up to the third order are obtained via

$$C_1 = \sum_{k=0}^{N} \langle \Delta B^{\dagger}(t_k)\Delta B(t_k) \rangle \tag{8.1.16}$$

$$C_2 = \sum_{k=0}^{N} \sum_{l=0}^{N} \langle \Delta B^{\dagger}(t_k)\Delta B^{\dagger}(t_l)\Delta B(t_l)\Delta B(t_k) \rangle \tag{8.1.17}$$

$$C_3 = \sum_{k=0}^{N} \sum_{l=0}^{N} \sum_{m=0}^{N} \langle \Delta B^{\dagger}(t_k)\Delta B^{\dagger}(t_l)\Delta B^{\dagger}(t_m)\Delta B(t_m)\Delta B(t_l)\Delta B(t_k) \rangle \ . \tag{8.1.18}$$

The total intensity inside the reservoir is of interest, thus the photon occupations of all time-bins from the start of the integration until the end $t_i \in [0, t_{end}]$ have to be computed. For the photon intensity in Equation 8.1.16 this is straightforward, because the intensity operator $\langle \Delta B^{\dagger}(t_k)\Delta B(t_k) \rangle$ is local. Thus, the OC is shifted to the respective time-bin and the local intensity operator is computed in analogy to Figure 7.11. Then, the local intensities of the time-bins are summed up and the total photon intensity of the reservoir is obtained. However, Equation 8.1.17 and Equation 8.1.18 are two and three site operations on the MPS and the computation can be very costly. The computation of a single integrand of C_3 is shown in Figure 8.4. Note that for each operation, the OC has to be at one of the involved contracted tensors. Furthermore, all tensors between the three involved time-bins have to be contracted as well. At worst this corresponds to a contraction of $t_{end}/\Delta t$ time-bins. In order to avoid to perform this costly operation multiple times, the symmetry of the correlation function is used. Furthermore, it becomes clear that the higher order in the time-evolution operator is very advantageous when dealing with higher-order correlation functions, as the number of total time-bins is reduced by choosing a higher Δt. After computing all relevant integrands once, the third-order correlation function is then obtained by summing up all integrands in the right manner to be in correspondence with Equation 8.1.18.
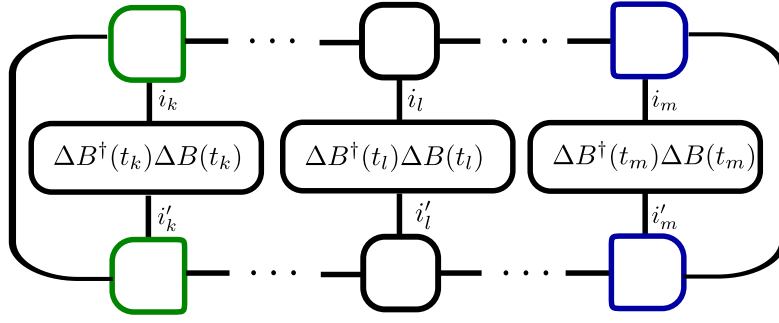
Figure 8.4.: Computation of a single integrand of the third-order correlation function C_3. The OC has to be included in the operation.

The relation between the mth order intensity correlation function and the probability of n photons $p(n)$ reads

$$C_m = \langle : \hat{I}^m : \rangle = \sum_{n=0}^{\infty} \frac{n!}{(n-m)!} p(n) \ . \tag{8.1.19}$$

The physical mechanism to generate multi-photon states in the present setup is a spontaneous decay of electronic excitation during the time-dependent pulse. Thus, during the pulse, multiple photons are created via spontaneous emission rate Γ. If the pulse width ν is chosen small in comparison to Γ, high photon probabilities can be neglected. In the investigated pump regimes, $p(2)$ dominates and $p(3)$ is very small compared to $p(1)$ and $p(2)$. This justifies, to assume any correlations higher than third order to be negligible. Thus, the expansion in Equation 8.1.19 can be cut off after the third order. By rearranging the set of equations, the photon probabilities are calculated from the correlation functions up to the third order via

$$p(1) = C_1 - C_2 + \frac{C_3}{2} \ , \tag{8.1.20}$$

$$p(2) = \frac{C_2 - C_3}{2} \ , \tag{8.1.21}$$

$$p(3) = C_3/6 \ . \tag{8.1.22}$$

8.2. Controlling photon statistics

8.2.1. Effect of the time-dependent pulse

When a single TLS is excited with a resonant pulse, the TLS undergoes Rabi-oscillations. The pulse area A determines the number of oscillations. If $A = \pi$, the TLS excitation is inverted as shown in Figure 8.5. If the TLS is initially in its ground state $|0\rangle$, after the pulse, the TLS ends up in the exited state $|1\rangle$. When the TLS is coupled to an external reservoir it is subject to spontaneous radiative decay. Thus, a photon is emitted on a long time-scale $1/\Gamma$. The inverted TLS now being in the state $|1\rangle$, decays radiatively under emission of a single photon. An excitation with a π-pulse results in an almost perfect single-photon source, as for $t \to \infty$ one would detect a single photon coming from the TLS (inset Figure 8.5).

However, if the pulse induces a full Rabi-oscillation of the TLS excitation for $A = 2\pi$, the
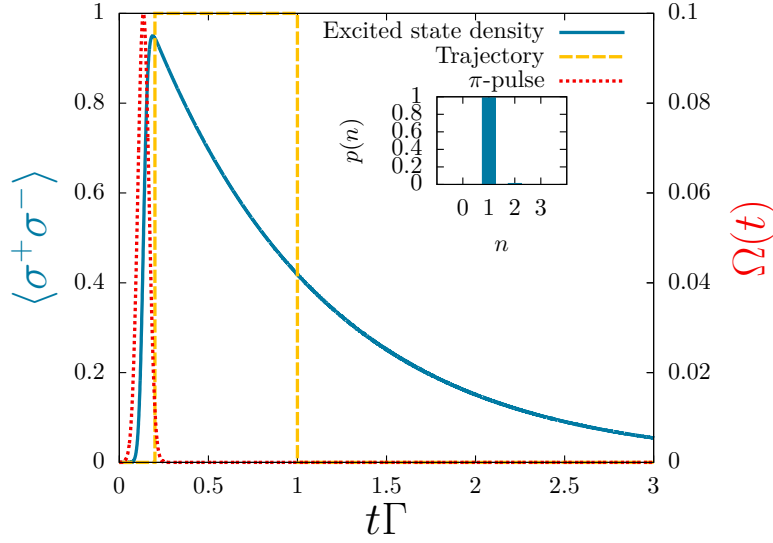
Figure 8.5.: Time evolution of the TLS excited with a pulse of $A = \pi$. The TLS excitation (blue, solid) is inverted after the pulse (red, dotted). On a long time-scale, a photon is emitted resulting in a single-photon source (see inset where $p(1)$ is dominant). An exemplary trajectory of the TLS excitation is sketched (yellow, dashed).
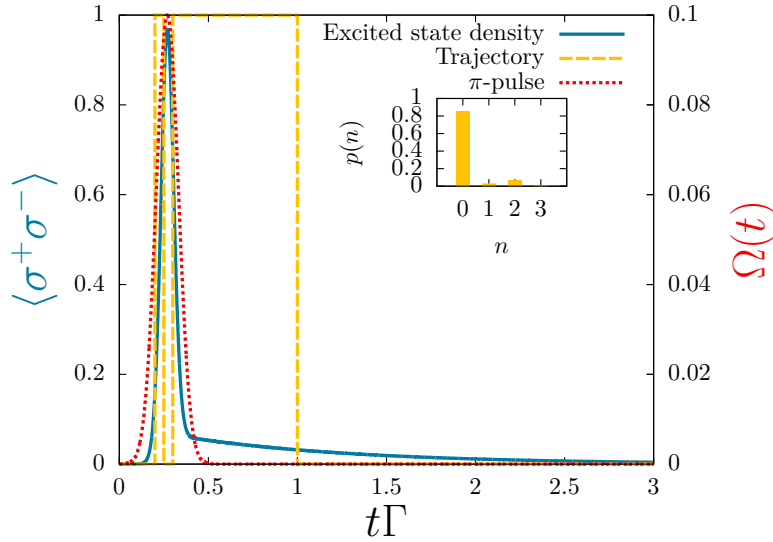

Figure 8.6.: Time evolution of the TLS excited with a pulse of $A = 2\pi$. The TLS undergoes a full Rabi-oscillation (blue, solid) after the pulse (red, dotted). Zero photons are most probable (inset for photon probabilities $p(n)$). However, due to a finite pulse width, the TLS might decay during the pulse and be re-excited again and a second photon is emitted on a long time-scale. An exemplary trajectory of the TLS excitation is sketched (yellow, dashed). This procedure results in $p(2) > p(1)$.

two-photon probability is higher than the single-photon probability [212, 214] as shown in Figure 8.6. If the pulse width would be infinitely small, the TLS undergoes a perfect full Rabi-oscillation without a photon emitted to the environment and ending up again in its initial state. Due to a finite pulse width and a finite radiative decay, there is a probability of a photon emission process during the pulse. The TLS is excited by the pulse, bringing it to the state $|1\rangle$. Due to the finite decay, there is a probability that one photon is emitted into the environment and the TLS is found in the state $|0\rangle$. However, the remaining pulse might re-excite the TLS, bringing it again to the excited state $|1\rangle$. A second photon is then emitted on a long time-scale as for driving with $A = \pi$. This results then in a probability of $p(2) > p(1)$. Thus, for a full Rabi-oscillation zero photons $p(0)$ are most probable. However, the probability in finding the TLS in the ground state after the pulse is not one as can be seen on the offset of the TLS excitation density (blue, solid) in Figure 8.6. This is due to the emission of a photon and a re-excitation during the pulse and the reason for $p(2) > p(1)$.

8.2.2. Effect of time-delayed feedback

So far, the results shown are without a structured reservoir. The key idea of this chapter is to trigger the two-photon process with a time-delay during the pulse. In the inset of Figure 8.7, a sketch of the TLS excitation density is shown for a structured reservoir with a mirror as boundary condition. In yellow, the expected TLS decay is shown for a reservoir without boundary condition and therefore without feedback field. When the feedback phase is constructive ($\omega_{01}\tau = 2n\pi$), the back-action of photons results in revivals of the TLS excitation after τ as shown in blue. In contrast, when the phase is destructive ($\omega_{01}\tau = (2n-1)\pi$), the radiative decay is effectively increased after delay τ as the interference with the feedback field triggers the photon emission process of the TLS. In Figure 8.7, the two-photon emission for different phases ϕ and delay-times τ is shown for a pulse area of $A = 2\pi$. The ratio

$$r = \frac{p(2)}{p(1)} \frac{p(1)_{nofeedback}}{p(2)_{nofeedback}} \qquad (8.2.1)$$

quantifies the two-photon purification obtained from the structured reservoir. If $r = 1$, the photon probabilities $p(n)$ of the feedback case are the same than without feedback $p(n)_{nofeedback}$. If $r > 1$, the ratio $p(2)/p(1)$, signifying two-photon purification, is higher than without feedback. If $r < 1$, single photons dominate compared to the case without feedback.

It becomes apparent that the feedback phase ϕ has a huge impact on the two-photon emission. In particular, it switches between single and two-photon emission. For constructive feedback, where the TLS excitation shows revivals after τ, single-photon emission dominates over two-photon emission with $r \to 0$. However, destructive feedback results in a higher two-photon probability compared to the case without feedback. The ratio r is increased up to a factor of two. This factor is dependent on the time-delay τ. The reason behind this increase in the two-photon probability lies within the effectively increased radiative decay during the pulse. As the dominant two-photon emission results from a spontaneous decay during the pulse, an effective increase of Γ due to feedback interference increases the two-photon emission process. Note that the ratio shows $r = 1$ if $\phi = \pi/2$. This means the feedback dynamics are then almost equal to the case without feedback.
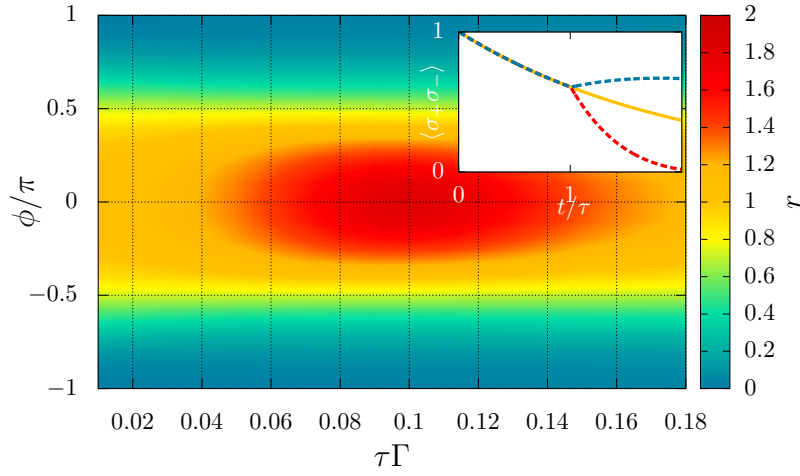
Figure 8.7.: Dependence of two-photon emission on the feedback phase ϕ and the time-delay τ for $A = 2\pi$. The color denotes the ratio $r = p(2)/p(1)$ normalized by the ratio without feedback. Thus, yellow color reproduces two-photon emission without feedback. Red color represents two-photon enhancement which is the case for destructive feedback ($\phi = 0$). Blue denotes single-photon emission. The inset sketches the effect of feedback on the TLS decay, the color matches the respective emission process.
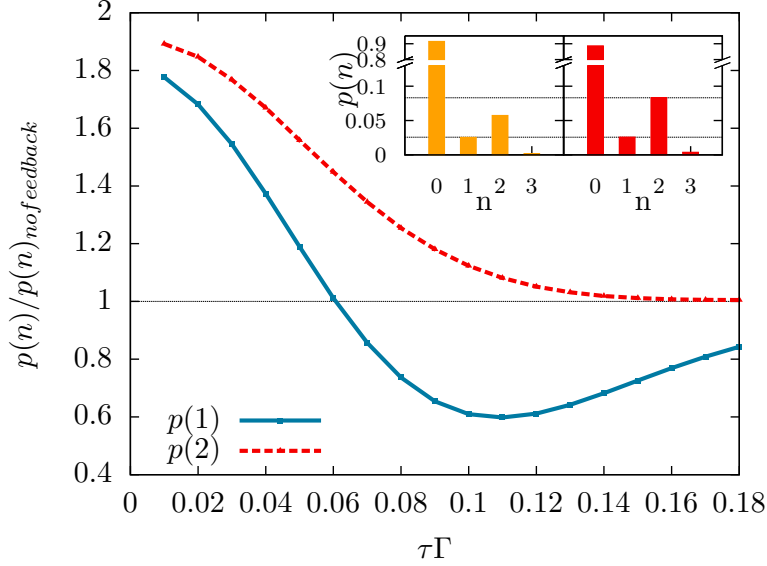

Figure 8.8.: Photon probabilities versus varying time-delay τ, scaled with Γ for a pulse area $A = 2\pi$. The probabilities are normalized by the case without feedback, the black line at one indicates the probabilities at $A = 2\pi$ for no feedback. Note that $p(1)$ (blue) and $p(2)$ (red) respond non-trivial on varying τ. Inset: Photon probabilities for $\tau\Gamma = 0.06$ for no feedback (yellow) and destructive feedback (red). Destructive feedback increases $p(2)$ by almost 50% while $p(1)$ is unaffected.

8.2.3. Controlling individual photon probabilities

This effect of triggered two-photon emission due to feedback interference enables the control of the photon emission statistics. The external control parameters for this scenario are the pulse area A and the distance L between mirror and TLS which affects both τ and ϕ. The phase ϕ represents fast oscillations with the distance and is very sensitive on varying L. As shown in Figure 8.7, destructive interference takes place in $\phi \in [-\pi/2, \pi/2]$ which corresponds to a distance of $\Delta L \approx 0.3\mu$m for a typical quantum dot with band gap of 1eV. If the system is a superconducting circuit which has usually a smaller transition frequency of, e.g., $\omega_{01}/2\pi = 6$ GHz [215], two-photon enhancement is robust for $\Delta L \approx 1.3$cm. The time-delay τ has to be adjusted dependent on the radiative decay of the respective system and the chosen pulse width ν. The pulse width ν is also a relevant control parameter. By increasing ν, higher photon probabilities become relevant. This case is beyond the scope of this chapter as higher-order correlation functions would become relevant. In this chapter the pulse width is fixed at $\nu = \frac{1}{10\Gamma}\frac{1}{\sqrt{2\ln(2)}}$.

In Figure 8.7 it was shown that the phase ϕ determines whether two-photon creation is enhanced or single-photon emission is dominant compared to the case without feedback. The question is, how much the individual probabilities can be influenced by varying the control parameters for destructive feedback in order to achieve a two-photon purification. Thus, ϕ will be chosen to yield destructive interference from now on to trigger the two-photon emission process.

In Figure 8.8, the photon probabilities are shown for varying τ. The one-photon (blue, solid) and two-photon (red, dashed) probabilities are normalized by the probabilities without feedback, respectively. The horizontal black line corresponds to the case without feedback for both probabilities. On a first glance, it becomes apparent that $p(2)$ is enhanced for all investigated time-delays τ whereas $p(1)$ is either enhanced or suppressed. For short time-delay ($\tau\Gamma < 0.06$), both probabilities are increased compared to the case without feedback. As the delay is very short, the radiative decay is already effectively increased at the beginning of the pulse. Thus, this can be interpreted as a higher global radiative decay of the TLS, induced by short delay-times τ.

The full power of the feedback control setup becomes apparent for time delays in the orders of the pulse width ν: The radiative decay is effectively increased at a certain time during the pulse. This controlled increase of the decay allows to only increase $p(2)$ while $p(1)$ is still the same than without feedback. The two-photon probability is enhanced by 50% at $\tau\Gamma = 0.06$ whereas $p(1)$ remains the same.

The interplay between finite pulse width ν and time-delay τ allows to manipulate an individual photon probability and results in a two-photon purification. For higher time-delays, the two-photon probability decreases but is still higher than without feedback. In contrast, $p(1)$ is suppressed compared to no feedback and reaches a minimum for $\tau\Gamma \approx 0.1$. This explains the highest purification of the ratio $p(2)/p(1)$ in Figure 8.7, visible as the red center at $\tau\Gamma \approx 0.1$. For increasing time-delay, both $p(1)$ and $p(2)$ approach the case without feedback. The reason is that the backaction takes place after the pulse and the two-photon emission process is not triggered by the feedback dynamics. The only difference is that the remaining excitation of the TLS decays faster.

When the amplitude of the driving laser is increased such that the pulse area corresponds to $A = 4\pi$, the TLS undergoes an additional full Rabi-oscillation. As the pulse width remains fixed, the same window of time-delays allows for a higher control, which is shown in Figure 8.9. E.g., the two-photon probability is increased by almost 50% while $p(1)$
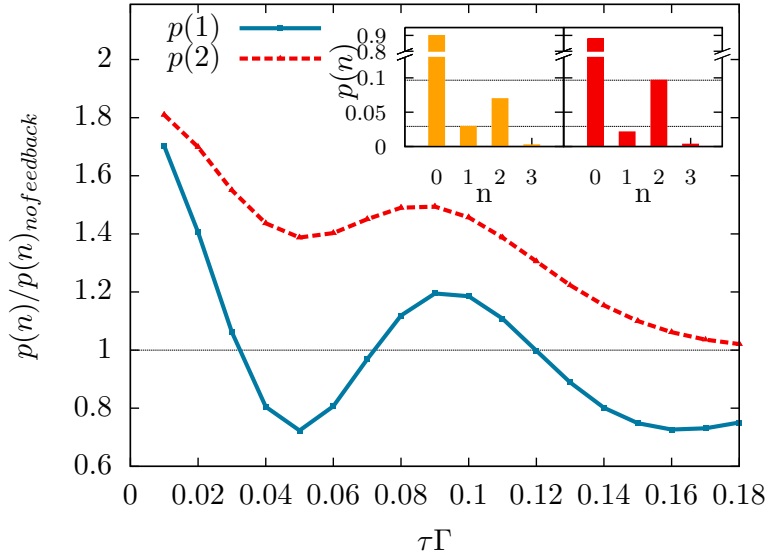
Figure 8.9.: Photon probabilities normalized by the case without feedback for a pulse area $A = 4\pi$. The TLS undergoes an additional Rabi-oscillation. This is reflected in the photon probabilities, where $p(1)$ (blue) and $p(2)$ (red) change their dependence on τ compared to $A = 2\pi$. Inset: Photon probabilities for $\Gamma\tau = 0.05$ for no feedback (yellow) and destructive feedback (red). Destructive feedback increases $p(2)$ by almost 50% and simultaneously decreases $p(1)$.

is minimal at $\tau\Gamma = 0.05$. This is an even higher achieved purification as for $A = 2\pi$. Furthermore, for $\tau\Gamma \in [0.07, 0.12]$, both probabilities are enhanced compared to the case without feedback. Again, the two-photon probability $p(2)$ is increased for all investigated time-delays while the one-photon probability responds non-trivially to a change of the time-delay.

8.3. Conclusion

In this chapter, it has been demonstrated how a structured reservoir leading to entangled system-reservoir dynamics can be simulated on the basis of the quantum stochastic Schrödinger equation. By writing the state of the system and the state of the reservoir as a matrix product state and by performing stroboscopic simulation of the time-evolution operator, the state of the system and reservoir is evolved in time. By considering the state of the reservoir as a many-body problem, it has been demonstrated how photon statistics can be evaluated, leading to the photon probabilities of the reservoir within a matrix product state representation close to an experimentally photon counting setup.

By assuming a distant mirror, it has been shown how feedback dynamics including a memory kernel are evaluated in the quantum stochastic Schrödinger picture using matrix product states. The findings of this chapter demonstrate a quantum interference effect between the photon-field and the two-level system induced by the mirror.

Having two external control parameters, i.e. the time-dependent excitation as well as the mirror distance with time-delay τ, a setup to control the photon statistics of the reservoir is proposed. By adjusting the amplitude of the driving laser as well as the mirror distance

it becomes possible to manipulate and tailor feasible parts of the photon probabilities. Constructive feedback results in a single-photon source for a pulse-area of 2π, where without feedback, the two-photon probability would be higher than the one-photon probability. However, for destructive feedback, the two-photon emission process is triggered. If the time-delay is very short in comparison to the driving pulse, both single and two-photon probabilities are increased. This is due to an effectively increased radiative decay which is global for short delay times.

However, by adjusting the pulse-duration and the time-delay it becomes possible to address individual photon probabilities. For a time-delay of the order of the pulse width, the one-photon probability responds differently than the two-photon probability. As an example, the two-photon emission is increased by 50%, whereas the one-photon probability remains the same than without feedback. In general, for destructive feedback, two-photon emission is enhanced or remains the same than without feedback whereas the one-photon probability is either enhanced or suppressed, depending on the time-delay.

In choosing a higher amplitude, i.e. a driving laser which induces two full Rabi-oscillations of the two-level system, the same window of time-delays allows for more control. This results in an even purer two-photon source as the two-photon probability is enhanced up to 50% with a simultaneous decrease of the one-photon probability.

9.

Feedback-stabilized time crystal

The concept of spontaneous symmetry breaking is uniformly used to explain phase transitions [123, 216]. The standard example in condensed matter physics is the Ising transition. The Hamiltonian displays a $\mathbb{Z}_2$-symmetry, which is spontaneously broken at zero temperature as the ground state consists of ordered spins. Another example is the continuous translational symmetry of liquids. If the symmetry is broken, the system forms a spatial crystal which is only translational invariant in discrete positions in space.

These fundamental concepts of symmetry breaking gave rise to the question, whether continuous time translational symmetry might be broken as well, forming a so called time crystal [217, 218]. Adapting the analogy of spatial crystals, a time crystal would be a many-body system with periodic behavior in time. This implies that the system returns to its initial state after discrete periods.

These considerations were followed by no-go theorems [219, 220] which stated that a time crystal can neither exist in the ground state nor in thermodynamic equilibrium due to the periodic oscillations.

However, this leaves the possible existence of a time crystal in systems being out-of-equilibrium, far away from their ground state [40, 41, 221, 222]. These so called Floquet systems are periodically driven, where the Hamiltonian is periodic in time $\mathcal{H}(t) = \mathcal{H}(t + T)$ with period T. The external driving force induces an out-of-equilibrium situation. However, for long times, the system absorbs the energy of the driving and is heating to infinite temperatures [38, 39]. This process would destroy any time crystal phenomena in reaching a thermal equilibrium, prohibiting time-dependent observables.

Ergodicity breaking due to MBL (introduction in chapter 4), prevents a system from reaching thermal equilibrium. It has been demonstrated that MBL also exists in Floquet systems [35, 36, 37].

Based on a proposal in Ref. [223], this paved the way for the demonstration of discrete time crystals (DTC) in trapped ions [42], diamond impurities [43], in a solid crystal [44] or in molecules [45]. The DTC shows oscillations in the observable with an integer number of the Floquet period. This breaks the time translation symmetry of the Floquet Hamiltonian, because the system follows a different period.

Altogether, due to the new phase of matter in an out-of-equilibrium system, the time crystal forms an application of the findings of this thesis. Similar to chapter 5 and chapter 8, the driving induces out-of equilibrium dynamics. Many-body localization, discussed in chapter 4 and chapter 6, is an important requirement to prevent thermalization in the time crystal phase due to interactions.

However, the fate of a time crystal as an open quantum system is still under debate [43]. It was argued that for Lindblad dissipators, the time crystal necessarily thermalizes with the environment [224].

In this chapter it will be demonstrated that in contrast, feedback dynamics similar to

chapter 8, stabilize a discrete time crystal against dissipation for long times.

In this thesis, the time crystal is the first many-body spin system investigated with MPS methods, introduced in chapter 7. As many-body spin systems form the standard application for the MPS method, the important aspects when simulating time evolution will be discussed in a first section with focus on the time crystal behavior.

In the second section, the system will be generalized to an open quantum system via the QSSE method introduced in chapter 3. It will be shown that the time crystal thermalizes due to the open system dynamics. A time-delayed feedback mechanism, in analogy to chapter 8, prevents the thermalization with the external reservoir. Due to the feedback dynamics, the entanglement between system and reservoir states is important and the dynamics are evaluated in the full QSSE picture without tracing out the reservoir degrees of freedom.

9.1. Closed system dynamics

9.1.1. Model

The time crystal is modeled as a driven one-dimensional Ising spin-1/2 chain. The idea is to apply different Hamiltonians at different times. The overall period of the system reads $T = T_1 + T_2$ and the Hamiltonian is periodic in time $\mathcal{H}(t) = \mathcal{H}(t + T)$. During period T_1, the Hamiltonian

$$\mathcal{H}_T = (\Omega - \epsilon) \sum_{i=1}^{N} \sigma_i^x, \quad 0 < t < T_1 \tag{9.1.1}$$

is applied. Note that for spin-models this term is called a transverse field. When mapping σ_i^x to raise σ_i^+ and lower operators σ_i^-, the transverse field of a single spin is comparable to the coherently driven two-level system of chapter 8. When choosing a pulse-area $A = \pi$, the TLS excitation is inverted after applying the pulse. This is formally the same for a single-site of the spin-flips in Equation 9.1.1 with $\Omega = \pi/2$.

Thus, when Ω is chosen as $\pi/2$ and the perturbation set to zero $\epsilon = 0$, each spin of the chain is flipped. If a spin is initialized with spin-up, after T_1 it will be flipped to spin-down and vice versa. The parameter ϵ describes a perturbation of the driving resulting in spins which are not ending up exactly in the opposite polarization after T_1. So far, the Hamiltonian does not describe a many-body system as the spins do not interact with each other. The interaction is described by the disordered Ising Hamiltonian

$$\mathcal{H}_I = \sum_{i=1}^{N-1} J\sigma_i^z \sigma_{i+1}^z + \sum_{i=1}^{N} h_i \sigma_i^z \quad T_1 < t < T_2 \ . \tag{9.1.2}$$

This Hamiltonian is formally the same as the second line in Equation 6.1.1 with nearest-neighbor coupling ($\alpha = 1000$). The nearest-neighbor interaction between different sites results in entanglement between subsystems of the many-body system under time evolution. The interaction is the crucial term for the time crystal to act against perturbation in the driving. Furthermore, the on-site random disorder is chosen such that the spins are in a many-body localized phase to prevent thermalization between subsystems of the many-body system. This will be analyzed in detail in the following sections.

In Figure 9.1, the idea of the time crystal is shown. The spins are initialized in a random initial state where all spins are polarized to either spin-up or spin-down. After applying
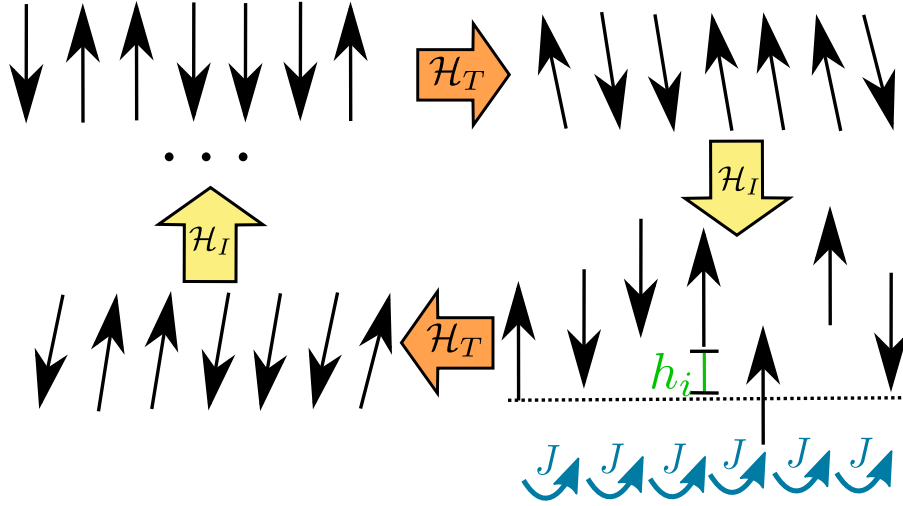
Figure 9.1.: Illustration of the $2T$ discrete time crystal. The spins are initialized in a random initial state where each spin is polarized with either spin-up or spin-down. After applying $\mathcal{H}_T$ each spin is flipped to nearly the opposite polarization with a small perturbation indicated by the tilted spins. When applying $\mathcal{H}_\mathcal{I}$, the interaction via J counteracts the perturbation in the driving and the spins are polarized again to either spin-up or spin-down but with opposite polarization compared to the initial state. The random on-site disorder h_i prevents the system from thermalizing with itself due to the interaction. After applying again $\mathcal{H}_T$ and $\mathcal{H}_I$, the system is found again in its initial configuration.

$\mathcal{H}_T$ (top left to top right), all local spins flip to the opposite polarization with a small perturbation ϵ, indicated by the tilted spins. Applying the Ising Hamiltonian $\mathcal{H}_I$ (top right to bottom right), interactions are induced by J (cp. first term in Equation 9.1.2). Furthermore, the local spins are randomly disordered via h_i. The interaction counteracts the perturbation of the driving as the Ising Hamiltonian favors energetically spin-up or spin-down polarization and not a superposition state. After applying again the driving Hamiltonian $\mathcal{H}_T$ (bottom right to bottom left), the spins are close to their initial configuration. However, the small perturbation still results in not exactly the initial state. When $\mathcal{H}_I$ is applied again, the initial configuration is restored due to the Ising interaction. Thus, after two periods $2T$, the many-body system is found again in its initial configuration even if there is a perturbation in the driving. This is the key idea of the discrete time crystal.

Before analyzing this in detail and explaining the physics behind this mechanism some remarks about the computation of many-body spin systems in the matrix product state description are necessary.

9.1.2. Computing many-body systems via matrix product states

The advantage in using the MPS formalism is that depending on the entanglement between subsystems of the many-body problem, the scaling of the Hilbert space 2^N is reduced to an algebraic scaling. Hereby, the cutoff of small singular values is controlled within each step of the computation such that the considered Hilbert space is adapted, depending on the complexity of the given dynamics. Thus initially, all spins are written in an MPS as introduced in chapter 7.

To perform the time evolution of a closed system, the time-evolution operator acts on the state

$$|\psi(t_{k+1})\rangle = U(t_{k+1}, t_k)|\psi(t_k)\rangle \;. \tag{9.1.3}$$

With the Hamiltonian in Equation 9.1.1 and Equation 9.1.2, $U(t_{k+1}, t_k)$ is an operator acting on all states of the MPS. This is in contrast to chapter 8, where the time-evolution operator only acts on a single TLS and at most on two other physical states which are the time-bins of the reservoir. There, $U(t_{k+1}, t_k)$ was a tensor of rank six in case of feedback dynamics (three ingoing and three outgoing physical indices).

In case of the many-body spin system, a straightforward tensor formulation of $U(t_{k+1}, t_k)$ would result in a tensor of rank $2N$. It is clearly visible that nothing is gained in formulating the Hamiltonian as a single tensor because the complexity still scales as 2^N as each index of the tensor of rank $2N$ has dimension of two.

The answer to that problem also lies in singular value decompositions (SVDs) of the time-evolution operator. Similar to the decomposition of the coefficient matrix of the corresponding many-body state $|\psi\rangle$ to an MPS, the operator $U(t_{k+1}, t_k)$ can be decomposed to a matrix product operator (MPO), where each tensor only contains two physical indices which was illustrated in Figure 7.8. Similar to an MPS formulation of $|\psi\rangle$, the Hilbert space of $U(t_{k+1}, t_k)$ is truncated by neglecting small singular values. Note that this induces an error within each time step.

The advantage of formulating $U(t_{k+1}, t_k)$ as an MPO is that it does not destroy the form of the MPS when acting on the state $|\psi\rangle$. This is especially relevant when dealing with a many-body problem, as with increasing N the Hilbert space grows exponentially and it becomes impossible to write down the whole coefficient matrix of the state $|\psi\rangle$. Thus, in practice, one never deals with the whole coefficient matrix but initializes it already from the beginning as an MPS. The same holds for $U(t_{k+1}, t_k)$ as it becomes exponentially difficult to write down the whole tensor.

For the driving Hamiltonian $\mathcal{H}_T$ this is straightforward as it only consists of local operators σ_i^x

$$U_T = \exp\left(-i\Delta t(\Omega - \epsilon)\sum_{i=1}^{N}\sigma_i^x\right) = \prod_{i=1}^{N}\exp\left(-i\Delta t(\Omega - \epsilon)\sigma_i^x\right) \;. \tag{9.1.4}$$

This means, to evolve a spin system in time with the driving Hamiltonian, one has to perform N single-site operations as shown in Figure 7.9(a). The MPO contains N single-site operators without links in between. This clarifies that $\mathcal{H}_T$ does not introduce entanglement between the spins as the link dimension of the MPS is not increased when U_T is applied. However, $\mathcal{H}_I$ consists of two-site operators. Furthermore, all two-site operators are connected with each other, $\sigma_1^z\sigma_2^z$ is connected to $\sigma_2^z\sigma_3^z$ and so on. This makes it impossible to write down U_I exactly in terms of single-site operators. As a solution, one could initialize the whole tensor and then decompose it as shown for the MPS in Figure 7.5 but with two physical indices per site. However, this involves the problem of an exponentially large initial tensor U_I for large system sizes.

A solution to this problem is the Suzuki-Trotter decomposition. The idea is to write the

sum in the exponential as a product of exponentials similar to Equation 9.1.4. To simplify the notation, the two-site operator is written as $\mathcal{Z}_i = \sigma_i^z \sigma_{i+1}^z$. The exponential is written as

$$
\begin{aligned}
U_I &= \exp\left(-iJ\Delta t \sum_{i=1}^{N-1} \mathcal{Z}_i - i\Delta t \sum_{i=1}^{N} h_i \sigma_i^z\right) \\
&= \prod_{i=1}^{N-2} \exp\left(-iJ\Delta t \mathcal{Z}_i - ih_i \Delta t \sigma_i^z\right) \exp\left(-iJ\Delta t \mathcal{Z}_{N-1} - ih_{N-1}\Delta t \sigma_{N-1}^z - ih_N \Delta t \sigma_N^z\right) \ .
\end{aligned}
$$

$$(9.1.5)$$

Note that the disorder is a single-site operation and thus for the last two-site operator $\mathcal{Z}_{N-1}$, the disorder term $h_N \sigma_N^z$ is included as well.

In general, for Hamiltonians such as the Heisenberg spin-chain in Equation 6.1.1, the Suzuki-Trotter decomposition introduces an error, because it is required that the exponents commute with each other to write it as a product of exponentials. However, for the problem at hand, the approximation is exact as the different exponents commute with each other. The error of the Suzuki-Trotter decomposition is given by

$$
\exp\left(\hat{A}\Delta t + \hat{B}\Delta t\right) - \exp\left(\hat{A}\Delta t\right)\exp\left(\hat{B}\Delta t\right) = \frac{1}{2}\left(\hat{B}\hat{A} - \hat{A}\hat{B}\right) + \dots \ . \tag{9.1.6}
$$

By inserting $\hat{A} = -iJ\mathcal{Z}_i - ih_i \sigma_i^z$ and $\hat{B} = -iJ\mathcal{Z}_{i+1} - ih_{i+1}\sigma_{i+1}^z$, it can be shown that Equation 9.1.6 yields zero as σ_i^z commutes for different sites i.

With this, the many-body Hamiltonian is expressed as a product of two-site operators. However, in the following, the goal is to construct an MPO which only acts on single sites. The reason is that this simplifies the application of U_I on $|\psi\rangle$ as it does not destroy the MPS form and fewer SVDs are necessary for each time step.

With the product formulation in Equation 9.1.5 it is possible to split the time-evolution operator into even and odd parts of $\mathcal{Z}_i$.

$$
U_I = \prod_{i=1}^{(N-1)/2} U_I\left(\mathcal{Z}_{2i}\right) \prod_{i=1}^{(N-1)/2} U_I\left(\mathcal{Z}_{2i-1}\right) \ , \tag{9.1.7}
$$

where $U_I\left(\mathcal{Z}_i\right)$ are the exponentials which include the respective operators including the part with the disorder. Note that the last term which includes the last sites $\mathcal{Z}_{N-1}$ includes two disorder terms as shown in Equation 9.1.5.

As the even and odd exponentials are written in a product form they can be applied after each other on the MPS. This is exemplarily shown in Figure 9.2 for $N = 6$. First, all odd parts of U_I are applied on the MPS and it is contracted over all site indices n_i as well as the link indices which are part of the two-site operation. If one would directly apply the even parts afterwards as shown in Figure 9.2 and contract over all primed site indices n_i' as well as the involved link indices, the MPS is destroyed and ends up in a tensor of rank N. This is not practical and becomes numerical impossible for growing system size N. One possibility is to decompose the tensors after applying the odd parts of $U_I(\mathcal{Z}_i)$. However, the approach chosen here is to further decompose the time-evolution operator to write it as an MPO.

The decomposition is demonstrated in Figure 9.3. Starting with the odd part which is the second product in Equation 9.1.7, each two-site operator $U_I(\mathcal{Z}_{2i-1})$ is decomposed via a SVD into two tensors acting on a single site n_i. The resulting tensors are denoted as
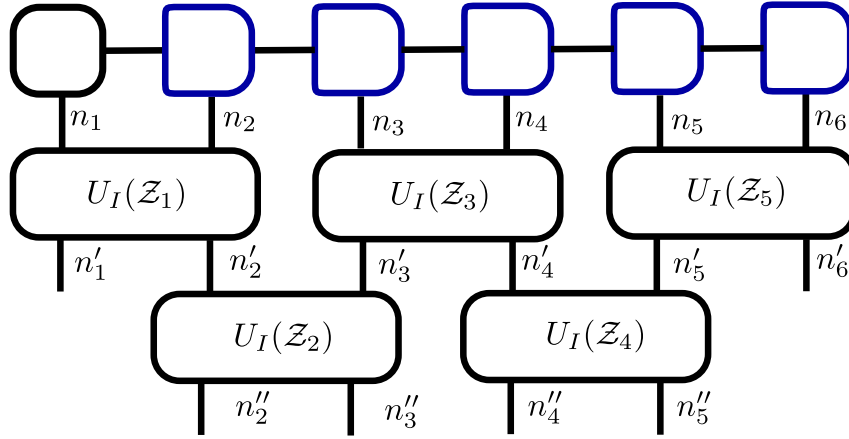
Figure 9.2.: Application of the time-evolution operator on the MPS. When written in a product form, it allows to apply even and odd parts of $U_I(\mathcal{Z}_i)$ after each other. Each $U_I(\mathcal{Z}_i)$ contains a two-site operator acting on site n_i and n_{i+1}. Note that for clarity for the even part, all indices are primed to avoid contraction over the wrong indices. After the application of U_I, all indices are unprimed to restore the MPS.
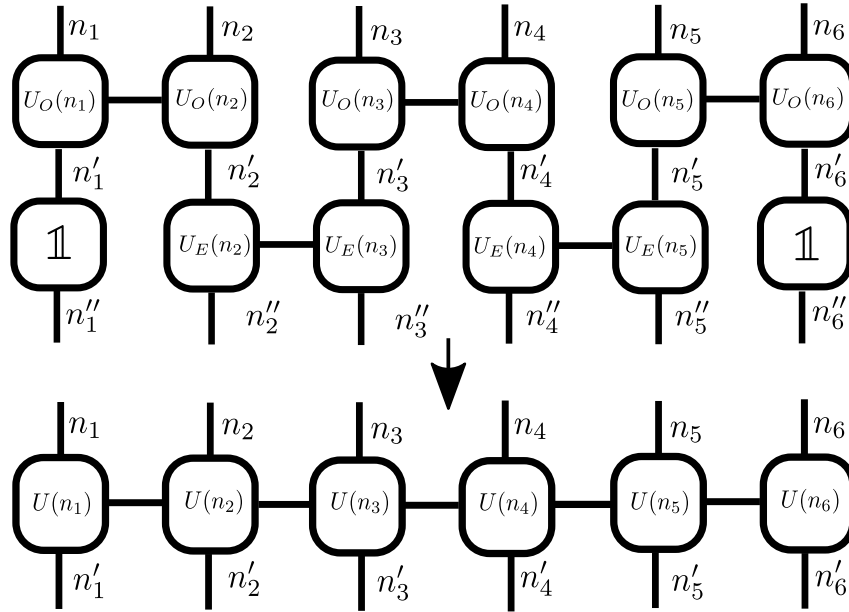

Figure 9.3.: Construction of the MPO for U_I. The time-evolution operator is split into even U_E and odd U_O parts of the two-site operators $\mathcal{Z}_i$. Each two-site operator is decomposed via SVDs into local tensors. Due to the decomposition, the decomposed tensors share a link index. This is between different tensors for the even part (first line) and the odd part (second line). The MPO is then constructed by contracting over all physical indices n_i'. Afterwards, the prime level of n_i'' is decreased by one to obtain the final MPO for U_I. Note that on the boundaries of U_E, an identity tensor is applied for a simpler multiplication within the numerics.

$U_O(n_i)$, because each tensor now acts on a single site. For numerical practice, the diagonal matrix containing the singular values S_α is multiplicated into both tensors with the entries $\sqrt{S_\alpha}$ which is why there is no OC in the MPO. Due to the SVD, the two tensors $U_O(n_{2i-1})$ and $U_O(n_{2i})$ corresponding to the two-site operator $U_I(\mathcal{Z}_{2i-1})$ now share a link index. This can be seen in Figure 9.3 (first line), where every second pair of tensors share a link index. The same procedure is repeated for the even part of U_I. It is important to mention that the link indices are between different pairs of tensors than for the odd part. Note that in the diagrammtic representation, a contraction over the same indices is performed. This is why the priming of the indices is relevant in this context. For this reason, the prime level of all indices of $U_E(n_i)$ is increased by one. Thus, with the notation here, the whole time-evolution operator is reproduced when contracting over all shared indices.

Another important point for the numerical implementation are the identities at the boundaries for the even part (cp. second line in Figure 9.3). When the total number of spins N is even, the even part does not have any tensors for the boundary sites. When the total number of spins N is odd, the first site of U_E has no tensor and needs to be filled with an identity as well as the last site of U_O.

The MPO for U_I is then constructed by contracting over all primed site indices n_i' as shown in the last line of Figure 9.3. The identities at the boundaries leave the corresponding tensors invariant but the multiplication can be formalized by writing U_O and U_E already as MPOs. With this, an MPO is constructed with links between all tensors and two physical indices at each site, one ingoing n_i and one outgoing n_i''. The prime level of all outgoing indices n_i'' is then decreased by one for the final MPO.

Now both MPOs have been constructed. On the one hand $U_T(\Delta t)$, which consists of N local operations, and on the other hand $U_I(\Delta t)$, which is a standard MPO with local tensors for each site and a link index between all neighboring sites. With this, the time evolution can be computed by repeatedly applying the MPOs on the MPS. During T_1, the time evolution MPO of the driving Hamiltonian $U_T(\Delta t)$ and during T_2 the time-evolution MPO of the Ising Hamiltonian $U_I(\Delta t)$ are applied on the MPS for each time step.

For $|\psi(0)\rangle$, all spins are initialized in a polarized state with either spin-up or spin-down with no entanglement between the sites. Thus, until the end of T_1 there exists no entanglement between the spins and one deals with N local operations at each time step.

The simulation of time evolution is shown in Figure 9.4. In a first step, $U_T(\Delta t)$ is applied on the MPS of $|\psi(0)\rangle$. Note that there are no links between the local operators of the MPO. The MPS of the next time step $|\psi(\Delta t)\rangle$ is thus obtained by contracting over all indices n_i. Afterwards all indices are unprimed for the next application of $U_T(\Delta t)$. This is repeated $T_1/\Delta t$ times until the driving period is finished and the state has evolved to $|\psi(T_1)\rangle$. Then the Ising Hamiltonian in $U_I(\Delta t)$ is applied on the system. In general, this is the same as for $U_T(\Delta t)$, by repeatedly applying $U_I(\Delta t)$, the system is evolved to $|\psi(T)\rangle$ and a full period has been computed. However, due to the link indices between the tensors of $U_I(\Delta t)$, its application on the MPS is not as straightforward as for $U_T(\Delta t)$ to maintain the MPS form of the state.

An efficient application of $U_I(\Delta t)$ on $|\psi(T_1)\rangle$ is explained in the appendix in section B.1. The algorithm is shown in diagrammatic form in Figure B.1.

By repeating this procedure, an arbitrary number of periods can be simulated with the MPS formalism. However, with each application of U_I, the link dimension of the MPS grows. By truncating the number of singular values accordingly, a large number of periods can be simulated, especially for the MBL phase where the entanglement only grows logarithmically. Of course, the total number of periods is still limited as within each time step an error is

induced by the truncation of singular values and the finite order of the expansion of the time-evolution operator. However, with the method introduced in this section, it is possible to simulate a satisfying number of periods to discuss the DTC in a closed quantum system.
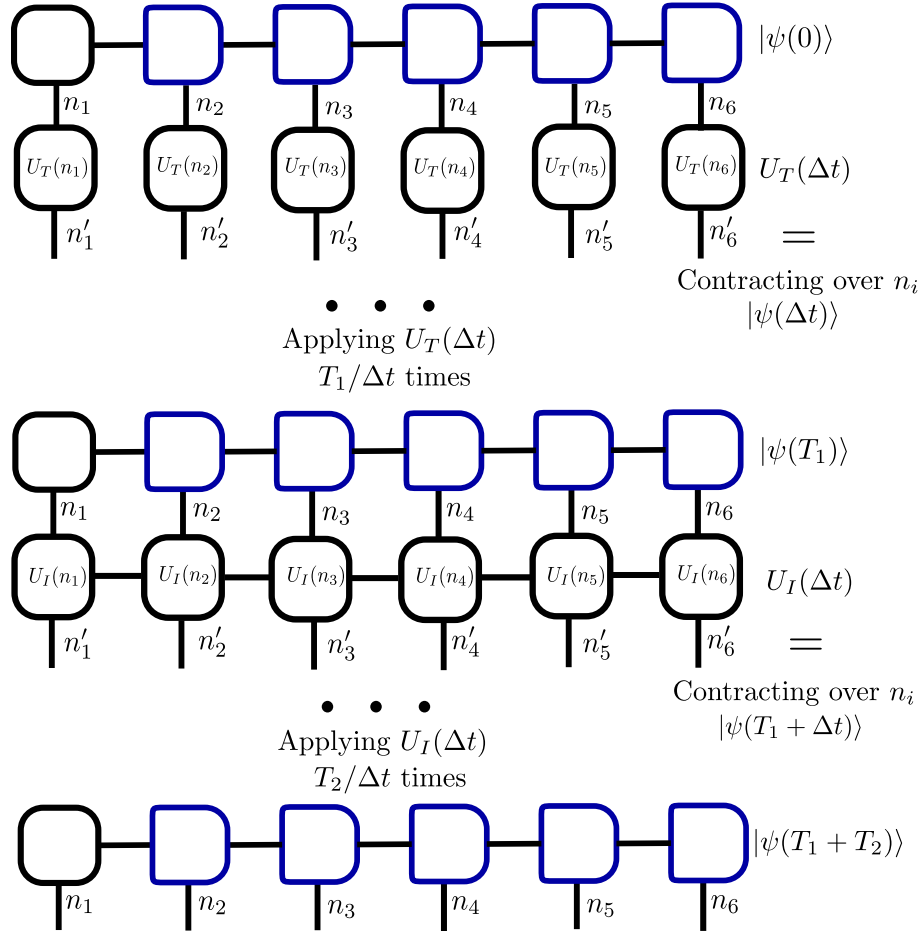

Figure 9.4.: Time evolving the MPS for one period $T = T_1 + T_2$. First, the initial state $|\psi(0)\rangle$ is evolved to $|\psi(\Delta t)\rangle$ in applying $U_T(\Delta t)$. $U_T(\Delta t)$ consists of N single-site operators, which is why no entanglement between the sites is induced and the links between the tensors do not change. However, the respective site tensors change according to $U_T(\Delta t)$. The time-evolved state $|\psi(\Delta t)\rangle$ is simply obtained by contracting over all n_i. The prime level of the indices of the resulting MPS is decreased by one afterwards. The MPS is ready for the next time step. By repeatedly applying $U_T(\Delta t)$ on the MPS, the time is evolved to the end of the first period T_1. Afterwards, during T_2, $U_I(\Delta t)$ acts repeatedly on $|\psi(T_1)\rangle$ to arrive at the end of the period $T = T_1 + T_2$. Due to the link indices of $U_I(\Delta t)$, its application is not as straightforward as for $U_T(\Delta t)$ and is explained detailed in Figure B.1. Note that within each time step Δt, the link dimension of $U_I(\Delta t)$ is added to the existing link dimension between each elements of MPS.

9.1.3. Achieving a discrete time crystal

Having demonstrated the numerical tools to simulate the time evolution of the driven disordered Ising spin-chain, the behavior of the system for different parameter setups is investigated with focus on time crystal behavior.

The system size considered is $N = 10$. To simplify the display of all spins, the initial state is not set to a random polarization of each spin, but the Néel state where spin-up and spin-down polarization are alternating from site to site $|\psi(0)\rangle = |\uparrow\downarrow\uparrow\ldots\rangle$. The observable of interest is the magnetization of each spin, but to consider all spins in a single observable, the staggered magnetization is convenient

$$\langle M \rangle = \frac{1}{N} \sum_{i=1}^{N} (-1)^i \frac{\langle \sigma_i^z \rangle}{2} \; . \tag{9.1.8}$$

The alternating minus sign is chosen in correspondence to the initial Néel state. Thus, initially $\langle M \rangle = -1/2$.

The single-site magnetization is computed according to Figure 7.11. Note that for the computation of each spin magnetization, the orthogonality center (OC) is shifted to the respective position before computing the observable. Afterwards, all single-site magnetizations $\langle \sigma_i^z \rangle$ are added up according to Equation 9.1.8.

In this section, the parameters leading to the time crystal phase of the Hamiltonians in Equation 9.1.1 and Equation 9.1.2 are investigated in detail. It is convenient to start with the most simple scenario with $\Omega = \pi/2$ and all other parameters set to zero, i.e the perturbation $\epsilon = 0$, the interaction $J = 0$ and the disorder $h_i = 0$. Initially, all spins show $\langle M \rangle = -1/2$. During the driving period T_1 with $\Omega = \pi/2$, all spins flip to the opposite polarization and the system shows $\langle M \rangle = 1/2$. During the period T_2, where the Ising Hamiltonian is applied, the MPO consists of identities and the system is left in its state with $\langle M \rangle = 1/2$, because $J = 0$ and $h_i = 0$. Thus, after a full period, the system is in the state of opposite polarization. After another period at $t = 2T$, the system is again found in the initial state with $\langle M \rangle = -1/2$ as the driving Hamiltonian induces a spin-flip of each spin and the Ising Hamiltonian has no effect as all parameters are set to zero. Thus, after $2T$, the system always ends up in the initial state. This effect of the driving with all other parameters set to zero is shown in Figure 9.5. In the inset, the time evolution of the staggered magnetization $\langle M \rangle$ is shown for $T = 10$ periods. It becomes clear that after $2T$ the spins are found in the same state. The main plot shows the Fourier spectrum, computed over $T = 500$ periods. The system locks to the subharmonic frequency of $\omega = 1/2$ according to the $2T$ periodicity of the driving.

The question is, if this is already a time crystal as a many-body spin system returns after a discrete period back to its initial state. The answer is no, for two reasons. On the one hand, it is not really a many-body system as it consists of isolated spins which do not interact with each other as $J = 0$. Each individual spin is flipped and the observable is computed adding up spin magnetizations, but due to the lack of interactions, the individual spins do not produce entanglement entropy.

On the other hand, it is not a time crystal because of the sensibility to perturbations ϵ. In Figure 9.6, the response of the systems to a perturbation in the driving with $\epsilon = 0.015$ is shown. In the inset it becomes clear that there is another enveloping oscillation of $\langle M \rangle$ due to $\epsilon \neq 0$. The Fourier spectrum is again computed over $T = 500$ periods. The system is no longer locked at the subharmonic frequency $\omega = 1/2$, because the perturbation in the driving results in a peak splitting. Furthermore, the height of the peak decreases. The
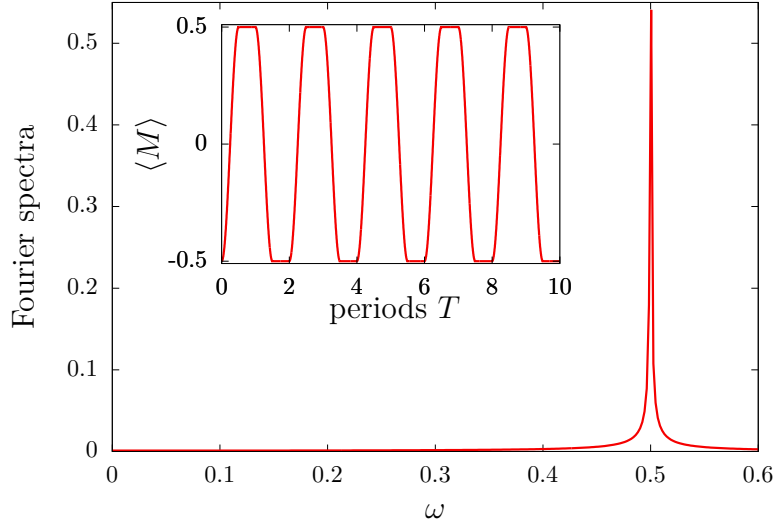
Figure 9.5.: Fourier spectrum of the Floquet driven spin-chain. During T_1, U_T is applied with $\Omega = \pi/2$ and $\epsilon = 0$. During T_2, where usually U_I is applied nothing happens as $J = 0$, $h = 0$ and U_I consists of identities. The spin system shows perfect oscillations, where after each $2T$, the system is found again in its initial state (inset). Thus, the Fourier spectrum shows $\omega = 0.5$. Note that this is not a many-body system as the spins are not interacting.
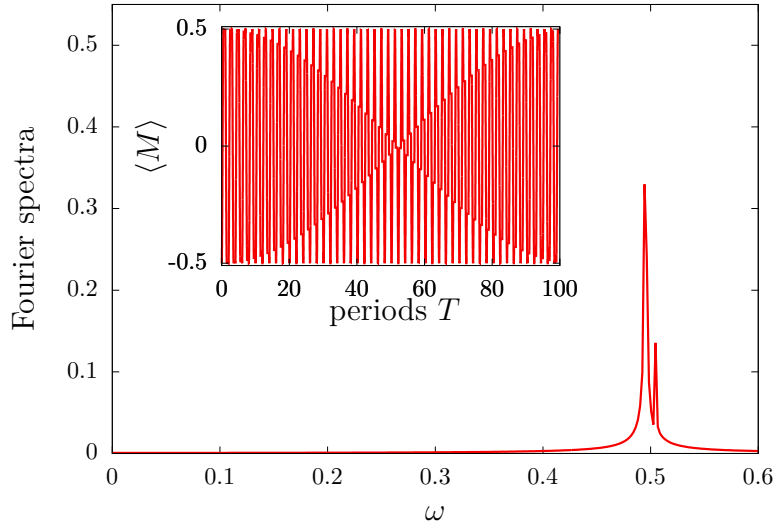

Figure 9.6.: When perturbations are turned on $\epsilon = 0.015$, the spins do not end up in their initial state after $T = 2$. This results in a peak-splitting of the Fourier spectra. The enveloping oscillation induced by the perturbation can be seen in the inset.
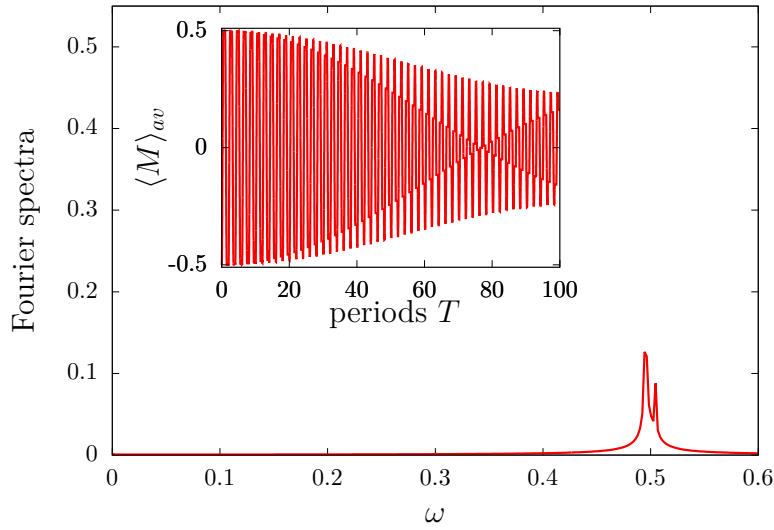
Figure 9.7.: Investigating the effect of disorder without interactions $J = 0$, it becomes clear that the system is also perturbed by the random disorder. The perturbation changes (inset) and the peak height decreases with still a splitting of the peak.

system simply follows the external dictated frequency of the driving $(\Omega - \epsilon)$.

Focusing now on the effect of the Ising Hamiltonian with the driving Hamiltonian remaining at $\Omega = \pi/2$ and $\epsilon = 0.015$, the starting point is to investigate the effect of disorder h_i without interactions $J = 0$. Each single-site disorder is chosen randomly with $h_i \in [0, 7]$, where it is known that the spin system in case of interactions is in a many-body localized phase [223]. As in section 6.4, for each random disorder realization, the time evolution and the according observable $\langle M \rangle$ of the system is computed until $T = 500$ periods. Then, a new system is initialized with random disorder and the time evolution is computed. After finishing the computation, the observable $\langle M \rangle$ is averaged over the performed disorder realizations N_{av} for every time step

$$\langle M \rangle_{av}(t) = \frac{1}{N_{av}} \sum_{i=1}^{N_{av}} \langle M \rangle_i(t) \ . \tag{9.1.9}$$

If not denoted otherwise, the number of disorder realizations will be chosen as $N_{av} = 10^3$. In Figure 9.7, the effect of disorder on the non-interacting driven system is shown. Due to the random disorder on each site, the spins precess with different Larmor rates and dephase with respect to each other [42]. This can be observed in the inset of Figure 9.7, that $\langle M \rangle_{av}$ is no longer only following the driving but has another enveloping oscillation in comparison to Figure 9.6. Thus, the splitting of the peaks is slightly different. Furthermore, the averaged staggered magnetization approaches zero for long times $\langle M \rangle_{av} \to 0$ due to the random disorder and a different response of each spin to the driving. At a first glance it seems like random on-site disorder does not favor the periodic Floquet driving and counteracts any time crystal behavior. However, it will be shown in the following that the opposite is the case: Random disorder leading to many-body localization is an important ingredient to achieve a stable DTC for long times [223].

Before coming to that, disorder is turned off with $h_i = 0$ and the interactions of the Ising Hamiltonian are turned on with $J = 0.02$ to deal with a many-body system. These
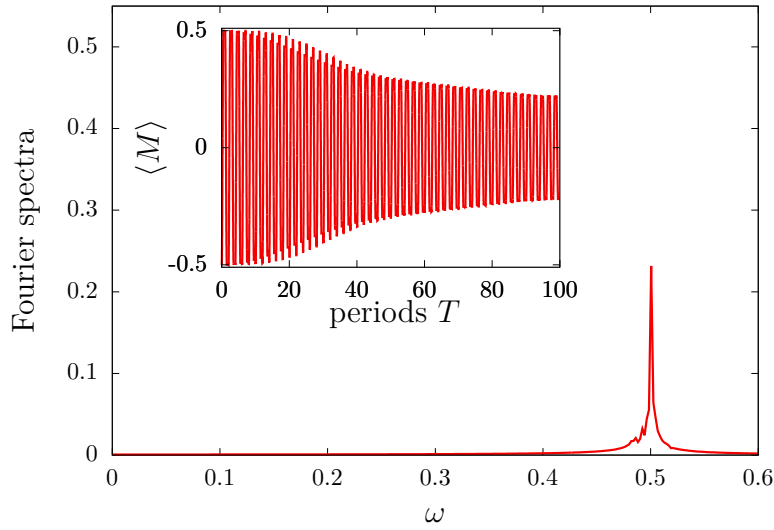
Figure 9.8.: Considering a real many-body system in turning on the interactions $J = 0.02$, the Ising interaction counteracts the perturbation and the frequency is locked at $\omega = 0.5$. However, interaction results in a build up of entanglement between the spins which is why they deviate from a polarized state. The peak height decreases and $\langle M \rangle \to 0$ (inset). Note that due to the small system size ($N = 10$) this thermalization process is not as strong as for larger systems.

interactions are crucial to form the DTC as on the one hand it is now a many-body system and on the other hand, the interactions counteract the small perturbation in the driving. In Figure 9.8, the observation of a time crystal is shown. Even in the presence of perturbations in the driving $\epsilon \neq 0$, the Fourier spectrum is locked at the subharmonic frequency $\omega = 1/2$, meaning that after $2T$, the system is found again in its initial state with $\langle M \rangle = -1/2$. Thus, collective synchronization of all spins take place due to the Ising interaction J, which counteracts the perturbation in the driving. The system favors energetically a polarization of spin-up or spin-down after applying the Ising Hamiltonian. However, it becomes apparent that the peak height of the Fourier spectrum is smaller than the one without perturbation and interactions in Figure 9.5. This is caused by the interaction J. After the Floquet period T_1, the spins are not in a polarized state due to the perturbation $\epsilon \neq 0$. Therefore, the Ising Hamiltonian induces entanglement between all spins due to the interaction. This buildup of entanglement results in $\langle M \rangle \to 0$ (inset Figure 9.8) as all spins approach a maximally entangled state for $t \to \infty$. This is a thermalization process within the many-body system. The Ising Hamiltonian introduces entanglement of a single spin with the rest of the many-body system. In the simulation, this can be directly observed in the growing number of relevant singular values and the resulting dimension of the link indices between the sites. Thus, when measuring a single-site observable such as $\langle \sigma_i^z \rangle$, the total information is hidden within all other involved spins. This results in a state of maximal entanglement entropy for a large number of periods $T \to \infty$. Approaching the thermodynamical limit with $N \to \infty$, it is a thermalization process of all subsystems with the rest of the many-body system and the staggered magnetization approaches zero $\langle M \rangle \to 0$. This would destroy the time crystal already at comparable small times which can be seen in the comparably small peak height of the Fourier spectrum and the decay of $\langle M \rangle$ in Figure 9.8. Note that for the considered system size $N = 10$, this thermalization
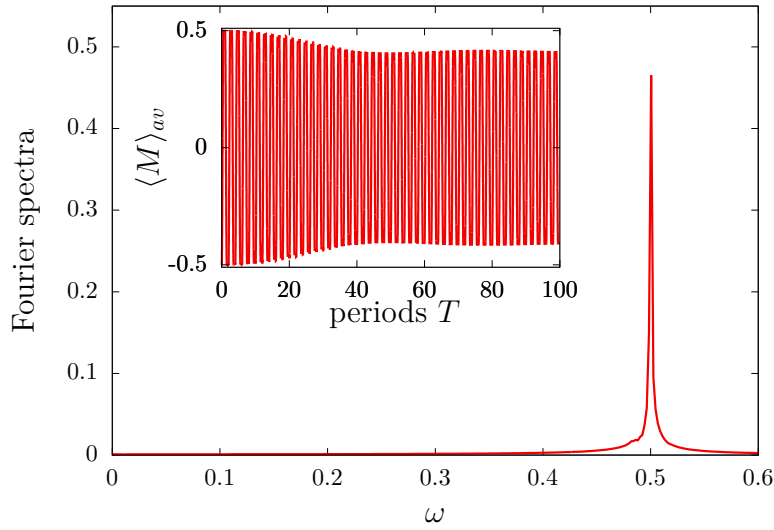
Figure 9.9.: Turning on random disorder such that the system is in a many-body localized phase and considering interactions $J = 0.02$, a stable $2T$ discrete time crystal is created even with perturbation in the driving. The frequency is locked at $\omega = 0.5$ and the peak height is almost as high as for the non-interacting case without perturbation (Figure 9.5). The many-body localization counteracts the thermalization due to spin interactions and the DTC is stable for long times (up to $T = 500$ investigated).

process is not as grave as for larger systems, as the total entanglement is limited due to the small system size compared to $N \to \infty$. Furthermore, the magnetization is subject to revivals for longer integration times which is also due to finite size effects.

To prevent this thermalization, the random on-site disorder comes into play. Now turning on interactions as well as random on-site disorder, a stable DTC is created for long times which can be seen in Figure 9.9. The Fourier spectrum shows a clear peak at the subharmonic frequency $\omega = 1/2$, corresponding to the return to the initial state of the many-body system after $2T$ periods. The peak height is almost as high as for the case without interactions and perturbations in Figure 9.5. The reason for a slightly smaller peak height is a small decay of $\langle M \rangle$ which can be seen in the inset of Figure 9.9. However, the decay is small in comparison to the case without disorder in Figure 9.8 and stabilizes at high values of $|\langle M \rangle|$ after $T \approx 40$ periods. Note that this oscillations are stable up until the end of the time integration which is $T = 500$. Thus, the Ising interaction counteracts the perturbation in the driving ϵ via J. A reason might be that the Ising Hamiltonian favors energetically full polarized spins. However, when the spins are not exactly in a full polarized state, the Ising interaction introduces entanglement between the subsystems. MBL achieved by turning on random on-site disorder, prevents this entanglement growth and the system shows time crystal behavior for long times.

To conclude, having turned on all parameters and chosen such that the system exhibits a DTC [223] it is observed that the interacting many-body system shows a discrete periodicity where it returns always after $2T$ back to its initial state. The time translational symmetry of the Hamiltonian $\mathcal{H}(t) = \mathcal{H}(t + T)$ is broken as the expectation value shows periodicity for twice the period $\langle M \rangle(t) = \langle M \rangle(t + 2T)$. This is stable against perturbations in the driving $\epsilon \neq 0$, where without interactions the system would follow the period dictated by

the driving (Figure 9.6). Due to the interaction, all spins synchronize collectively and favor the polarized state. Many-body localization due to random on-site disorder prevents the system from going into thermal equilibrium for long times.

9.2. Open system dynamics

Having shown how a stable time crystal is achieved in case of a closed quantum system, the question of interest is what happens in case of an open quantum system. It has been shown that without MBL, the closed quantum system is subject to thermalization with the closed many-body quantum system itself due to the Ising interaction. This results in a decay of the staggered magnetization $\langle M \rangle$ for long times due to the buildup of entanglement between the spins.

It has been shown by Ref. [224] that a time crystal as open quantum system with any reasonable Lindblad dissipator is subject to thermalization with its environment and melts for long times with $\langle M \rangle \to 0$. Systems subject to Lindblad dissipators were investigated in Part II of this thesis for the many-emitter phonon laser in chapter 5 and the Heisenberg spin-chain in chapter 6. The focus of this chapter lies in the computation of an open quantum system in the QSSE picture introduced in chapter 3 without tracing out the reservoir degrees of freedom leading to Lindblad dissipators. Thus, the subject of investigation is the entanglement between many-body system and the surrounding reservoirs. It has been shown in the previous section and argued in chapter 4 that many-body localization prevents the many-body system from building up entanglement within the many-body system itself and thus, prevents it from reaching thermal equilibrium.

An interaction of the many-body system with a surrounding reservoir, which is modeled as a mode continuum, leads to a build up of entanglement of the many-body system with the reservoir states. The idea of this chapter is to prevent the buildup of entanglement by structuring the external reservoir. In including a boundary condition and a sinusoidal coupling to the environment, similar to chapter 8, it will be shown that feedback dynamics stabilize a dissipative time crystal which interacts with the surrounding environment. Feedback dynamics can counteract a building up of entanglement of the many-body system with the surrounding reservoir in addition to many-body localization which prevents the build up of entanglement within the many-body system itself.

9.2.1. Reservoir model

To model an external reservoir, the idea is to assume the spins as single TLS which are subject to a radiative decay Γ, similar to the investigated TLS in chapter 8. Thus, each spin is coupled to an external mode continuum in analogy to Equation 8.1.6. The dissipative Hamiltonian is therefore modeled as

$$H_{\mathcal{D}} = \sum_{j=1}^{N} \int d\omega \hbar \omega b_j^\dagger(\omega) b_j(\omega) + \sum_{j=1}^{N} \int d\omega \hbar \left[G_j(\omega) b_j^\dagger(\omega) \sigma_j^- + h.c. \right]. \tag{9.2.1}$$

Initializing the reservoir in a vacuum state, the excitation of each single TLS is subject to radiative decay, where an excitation of an individual TLS is annihilated and inside the respective reservoir an excitation is created. In the spin-picture, the reservoir would correspond to a spin-down reservoir where any spin-up polarization of the system is subject to interaction with the spin-down polarization of the external reservoir. Note that by introducing the time-bin basis in Equation 3.1.16, the number basis in the computation
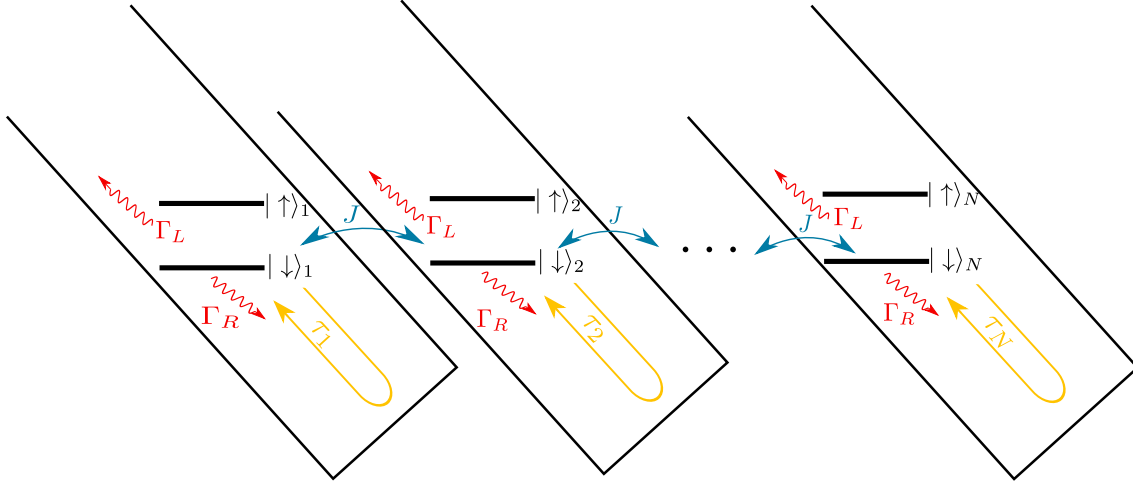
Figure 9.10.: Model of the spin-chain coupled to external structured reservoirs. Each spin is subject to a decay into its individual environment which would be a spontaneous emission process in case of a TLS coupled to a photonic reservoir. The spins are coupled to each other with Ising interaction J. Each individual reservoir contains a boundary condition which is sketched as a semi-infinite waveguide, where excitations are reflected and interact again with the system after time-delay τ. It is differentiated between a decay to the infinite side of the waveguide Γ_L and the side with the closed end Γ_R.

is restricted to two states. Thus, it is not differentiated between bosons or fermions in modeling the reservoirs. However, for simplicity and in analogy to chapter 8 it is convenient to imagine the spins as TLS with a photonic reservoir.

The coupling is modeled in analogy to chapter 8 as

$$G_j(\omega) = i \left(\sqrt{\frac{\Gamma_R}{2\pi}} e^{-i\omega\tau_j/2} - \sqrt{\frac{\Gamma_L}{2\pi}} e^{i\omega\tau_j/2} \right) \; , \qquad (9.2.2)$$

where a boundary condition leads to the sinusoidal dependence on the distance. This results in an exponential form of the dependence on the time-delay $\tau_j = 2L_j/c_o$, where c_0 would be the speed of light in vacuum in case of a photonic reservoir. Note that this changes if the reservoir consists of magnetizations. In case of a single TLS with a photonic reservoir, the boundary condition is realized as a reflecting mirror. This chapter serves as a proof of principle that such a sinusoidal coupling constant leads to a stabilization of a dissipative time crystal for long times.

The model setup is sketched in Figure 9.10. Each individual spin is put into a semi-infinite waveguide, to model the individual reservoir including a boundary condition which is the closed end of the waveguide. The Ising interaction is denoted as J between the different TLS. The interaction to the environment takes place during the whole period $T = T_1 + T_2$, which includes the driving Hamiltonian during T_1 and the Ising Hamiltonian during T_2.

9.2.2. Computing open quantum many-body systems in the QSSE picture

By going into the QSSE picture in introducing quantum noise operators $\Delta B_{n_j}^{(\dagger)}(\Delta t)$ with time increment $\Delta t = t_{k+1} - t_k$, the time-evolution operator for the dissipation reads similar to Equation 8.1.11

$$U_{\mathcal{D}}(t_{k+1}, t_k) = \prod_{j=1}^{N} \exp\left[-\left(\sqrt{\Gamma_R}\Delta B_{n_j}(t_{k-l})e^{-i\phi_{n_j}} + \sqrt{\Gamma_L}\Delta B_{n_j}(t_k) \right) \sigma_j^+ + h.c. \right] . \quad (9.2.3)$$

In introducing the quantum noise operators, the time-bin basis is constructed similar to Equation 3.1.16

$$|i_k^{n_j}\rangle = \frac{\left(\Delta B_{n_j}^{\dagger}(t_k) \right)^{i_k^{n_j}}}{\sqrt{i_k^{n_j}!(\Delta t)^{i_k^{n_j}}}} |\text{vac}\rangle . \quad (9.2.4)$$

The difference to chapter 8 is that more than a single reservoir is considered, i.e. one reservoir for each spin of the chain. Thus, N reservoirs are considered, where the upper index n_j labels the corresponding reservoir for the j-th spin.
 Due to the additional reservoirs for each spin and the exact consideration of the reservoir degrees of freedom within the MPS formalism, the total MPS is now two-dimensional. Each spin of the chain and with this, each tensor of the system MPS is coupled to an additional MPS which represents the reservoir. This is shown in Figure 9.11, where the tensors of the reservoir MPSs are sloped and dashed in the diagrammatic representation. Due to the two-dimensional form of the MPS it is even more important to keep track of the OC to calculate expectation values. Before explaining the algorithm and the computation of observables, some remarks about the construction of the MPOs when including dissipation in the QSSE picture are in order.
By applying $\Delta B_{n_j}^{\dagger}(t_k)$ on the state, an excitation is created in the time-bin $i_k^{n_j}$ corresponding to the reservoir of the spin n_j at time t_k. Note that the first summand in the exponent of Equation 9.2.3 corresponds to an interaction with the feedback time-bin $i_{k-l}^{n_j}$ with Γ_R as the radiative decay to the right side of the waveguide which includes the reflecting element. Thus, when the reservoir is assumed to be in general form, i.e. only dissipation without feedback dynamics, Γ_R is set to zero such that the system only interacts with future time-bins $i_k^{n_j}$ and not with past time bins such as $i_{k-l}^{n_j}$.
The starting point is the construction of the MPO for general (unstructured) reservoirs without a feedback algorithm. During the driving period this is straightforward as the driving Hamiltonian only consists of local operators

$$U_{T-\mathcal{D}} = \prod_{j=1}^{N} \exp\left(-i\Delta t(\Omega - \epsilon)\sigma_j^x - \left(\sqrt{\Gamma_R}\Delta B_{n_j}(t_{k-l})e^{-i\phi_{n_j}} + \sqrt{\Gamma_L}\Delta B_{n_j}(t_k) \right) \sigma_j^+ + h.c. \right) ,$$

$$(9.2.5)$$

where Γ_R is set to zero for a general (unstructured) reservoir coupling. The time-evolution operator is then expanded until the second order in Δt, similar to Equation 8.1.15, due to the proportionality of $\Delta B_{n_j}^{(\dagger)}(\Delta t) \sim \sqrt{\Delta t}$. The MPO then consists of N local operations on the system MPS. Note that local is only referred to the spin system as each operator does interact with two tensors: One is the respective system-bin of the spin system n_j and the other one is the respective time-bin of the reservoir $i_k^{n_j}$. Thus, each local operator is a
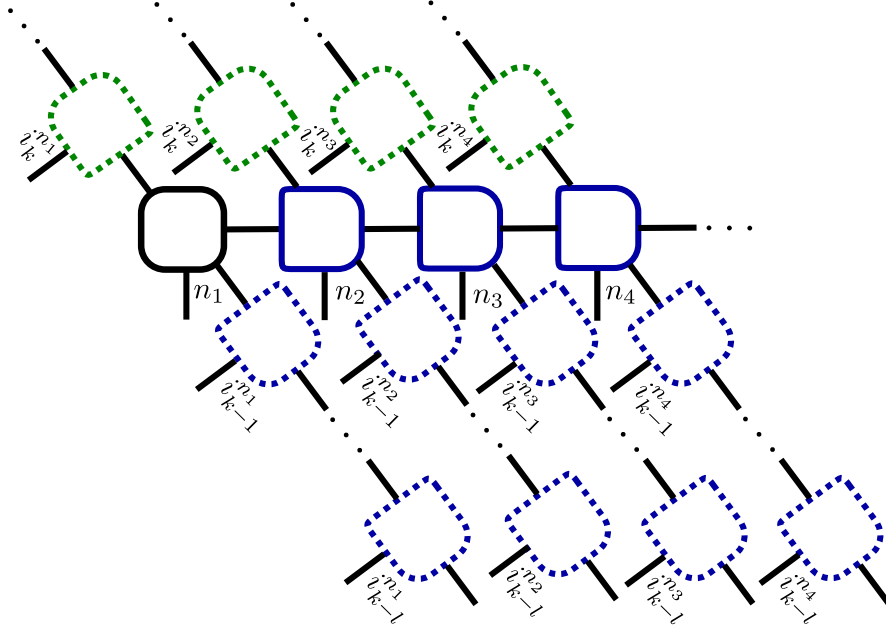
Figure 9.11.: General form of the MPS in mixed canonical gauge in case of an individual reservoir for each spin. The notation of the many-body spin system is chosen as explained within the previous chapters, with vertical lines corresponding to physical indices and horizontal lines corresponding to link indices. The black box denotes the OC (at the tensor corresponding to the physical index n_1), blue boxes show right orthogonality and green boxes left orthogonality. As each spin is coupled to a reservoir, the MPS is no longer one-dimensional, thus each spin is linked to an additional MPS which represents the respective reservoir. The reservoir MPSs are denoted as dashed sloped boxes. The physical indices are labeled with the time-bin bases $i_k^{n_j}$, whereas the link indices are not labeled in this picture. Orthogonality is denoted as for the many-body system. Note that the feedback time-bins have the physical index $i_{k-l}^{n_j}$.
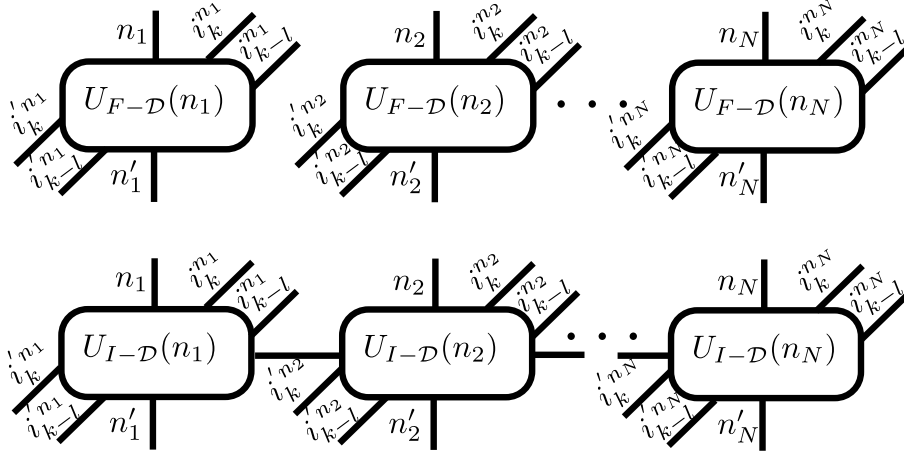
Figure 9.12.: MPO for the feedback driving time-evolution operator $U_{T-\mathcal{D}}$ (top) and for the feedback Ising time-evolution operator $U_{I-\mathcal{D}}$ (bottom). Each local operator (acting only on one site of the spin-chain) consists of six physical indices, three ingoing and three outgoing. One physical index describes interaction with the system-bin n_j, one describes interaction with the future time-bin $i_k^{n_j}$ and one describes interaction with the feedback time-bin $i_{k-l}^{n_j}$. Note that $U_{I-\mathcal{D}}$ has link indices between each local operator due to the Ising interaction.

tensor of rank four with two ingoing and two outgoing physical indices.

The Ising time evolution during T_2 is slightly more complicated, as it consists of two-site operations. However, due to the assumption of individual reservoirs for each spin for the dissipation in Equation 9.2.3, the dissipation consists of local operations on the spin-chain. Thus, in performing the Suzuki-Trotter expansion as depicted in Figure 9.3, the MPO is constructed from

$$
\begin{aligned}
U_{I-\mathcal{D}} = \exp\Bigg(&-iJ\Delta t \sum_{j=1}^{N-1} \sigma_j^z \sigma_{j+1}^z - i\Delta t \sum_{j=1}^{N} h_j \sigma_j^z \\
&- \sum_{j=1}^{N} \left(\sqrt{\Gamma_R}\Delta B_{n_j}(t_{k-l})e^{-i\phi_{n_j}} + \sqrt{\Gamma_L}\Delta B_{n_j}(t_k)\sigma_j^+ + h.c. \right) \Bigg) ,
\end{aligned}
\qquad (9.2.6)
$$

where the dissipation is included for each local operator acting on the spin-chain. The time-evolution operator is then expanded until the second order in Δt, similar to Equation 8.1.15, to have the same error in Δt as for applying the driving time-evolution operator. As for the driving time-evolution operator $U_{T-\mathcal{D}}$, each operator of the MPO of $U_{I-\mathcal{D}}$ now consists of four physical indices, two ingoing and two outgoing. One is acting on the respective system-bin of the spin-chain and one on the future reservoir time-bin $i_k^{n_j}$. In contrast to the dissipative driving time-evolution operator $U_{T-\mathcal{D}}$, the dissipative Ising time-evolution operator $U_{I-\mathcal{D}}$ has a link index between each operator due to the two-site operation of the Ising Hamiltonian as discussed in subsection 9.1.2.

If a structured reservoir is considered with $\Gamma_R > 0$, the construction of the MPOs is basically the same as for a general reservoir. The difference is that each tensor has a higher rank due to the additional interaction with past time-bins. Each local tensor consists of six physical indices similar to Figure 8.3. The MPOs used for the feedback algorithm for
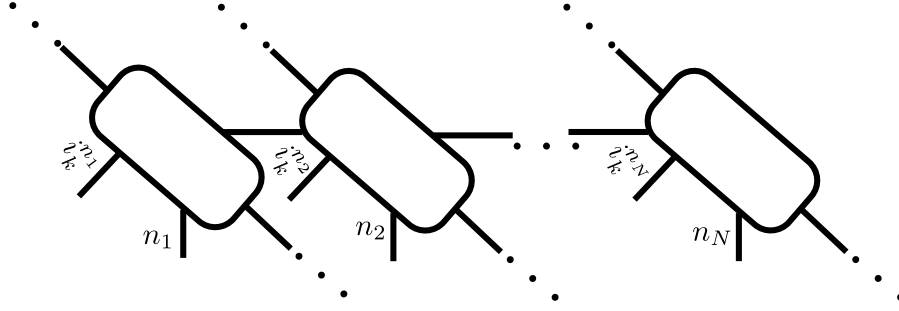
Figure 9.13.: MPS for the application of a dissipative time-evolution operator $U_\mathcal{D}$ without feedback dynamics. Each local tensor consists of two physical indices, one for the respective site index n_j (vertical) and one for the future time-bin $i_k^{n_j}$ (sloped). Furthermore, each tensor has four link indices (three if it is a boundary site). Two for the neighboring sites (horizontal) and two to the respective reservoir MPS (sloped). The upper link index to the reservoir connects to future time-bins which is why this link index has dimension one. The sloped index pointing down right connects to past time-bins.

$U_{T-\mathcal{D}}$ and $U_{I-\mathcal{D}}$ are shown in Figure 9.12.

Having now constructed the MPOs for the two time-evolution operators, including dissipative dynamics, it is possible to compute the time evolution of the system by subsequent application of the MPOs. The starting point is a general reservoir with $\Gamma_R = 0$, where each operator of the MPOs acts on one site index n_j and on the respective future time-bin $i_k^{n_j}$. To apply the time-evolution operator, the future time-bins of the reservoirs are multiplied into the respective tensor of the spin MPS. Thus, each local tensor with site index n_j is multiplied with the future time bin $i_k^{n_j}$ by contracting over the shared link index. The resulting MPS is shown in Figure 9.13. Each local tensor has the respective site index n_j and the future time-bin index $i_k^{n_j}$. Furthermore, each tensor shares two link indices with the respective reservoir, one to future time-bins and one to past time-bins. Note that orthogonality is not guaranteed in this case as the future time-bins have been multiplied into the system MPS. Besides that, the MPS is in a standard form as in Figure 9.4. Thus, the application of $U_{T-\mathcal{D}}$ during T_1 and $U_{I-\mathcal{D}}$ is straightforward. However, there is still an important difference, compared to closed system dynamics, after each application of a time-evolution operator. The tensors still include the reservoir time-bin which is now the past time-bin. Thus, each tensor is decomposed and the tensor including the past time-bin index is stored in the respective reservoir MPS. The OC is kept at the system-bin during this decomposition such that the MPS is re-gauged.

After applying the respective time-evolution operator and decomposing the tensors of the system MPS, the total two-dimensional MPS should be again in the form of Figure 9.11. This is the point to compute observables concerning the system such as the magnetization $\langle \sigma_j^z \rangle$ in Figure 7.11 as the MPS is in a mixed canonical form and the OC is at the system MPS.

There is still one step missing before computing the next time step. The MPO for the time-evolution operator still acts on the time-bin $i_k^{n_j}$, which is now a past time-bin. For the next time step, they are supposed to act on the future time-bin $i_{k+1}^{n_j}$. As the MPO itself does not change but for the physical indices, this is achieved by multiplicating each tensor of the MPO with two identity tensors, each containing two indices one with $i_k^{n_j}$ and $i_{k+1}^{n_j}$

and the other identity tensor contains $i_k'^{n_j}$ and $i_{k+1}'^{n_j}$. The past time-bin indices $i_k^{n_j}$ and $i_k'^{n_j}$ are then replaced by the future time-bin indices $i_{k+1}^{n_j}$ and $i_{k+1}'^{n_j}$, respectively. With this, the MPO then act on the future time-bin $i_{k+1}^{n_j}$ after contracting over $i_k^{n_j}$ and $i_k'^{n_j}$.

With these considerations, it is possible to compute dissipative time evolution for the DTC in the QSSE picture. However, for feedback dynamics, the algorithm becomes more complicated as swap operations have to be performed for each reservoir.

Before $t_k = \tau/\Delta t$, the time evolution is computed in the same manner as for the general reservoir, described above. As all reservoirs are initially assumed to be in a vacuum state, all past time-bins are not occupied and there is no interaction with feedback time-bins. However, after $t_k = \tau/\Delta t$ is reached, the past time-bins interact subsequently again with the system due to the reflecting element. Thus, the algorithm has to be adapted for the structured reservoir to deal with the memory kernel. The algorithm is comparable to subsection 8.1.2, with the difference that the considered system is an interacting many-body system. Therefore, as mentioned above, the MPS becomes two-dimensional and for each reservoir, swap operations have to be performed, as shown in Figure 7.13, to deal with the long-range interaction of the system with feedback time-bins.

Assuming at $t_k = \tau/\Delta t$, the two-dimensional MPS is in mixed canonical gauge in the form of Figure 9.11. If this is not the case it can be brought to this form by performing series of contractions and SVDs of neighboring tensors. Thus initially, the OC is at the tensor with physical index n_1. The OC is brought to the feedback time-bin $i_{k-l}^{n_1}$ by contracting neighboring tensors of the reservoir MPS of the first site and shifting the OC in direction of the feedback time-bin by performing SVDs. When the OC is at the feedback time-bin $i_{k-l}^{n_1}$, $\tau/\Delta t$ swap operations (because the memory kernel consists of $\tau/\Delta t$ time-bins) are performed to bring the feedback time-bin next to the system-bin n_1. In doing so, the OC is kept at the feedback time-bin $i_{k-l}^{n_1}$. When the feedback time-bin is next to the system, the OC is brought first to the system-bin n_1, then to the system-bin n_2 and then to the feedback time-bin of the second site $i_{k-l}^{n_2}$. Then this procedure is repeated until arriving at the last site n_N. The MPS is then in the form of Figure 9.14 (top), where each system-bin n_j has the future time-bin $i_k^{n_j}$ and the feedback time-bin $i_{k-l}^{n_j}$ as neighbors.

The task then is to bring the MPS in a form to apply the respective time-evolution MPO, either $U_{T-\mathcal{D}}$ or $U_{I-\mathcal{D}}$ in Figure 9.12. Thus, each tensor of the system MPS with index n_j is multiplied with the tensor of the future time-bin $i_k^{n_j}$ and the feedback time-bin $i_{k-l}^{n_j}$ in contracting over the shared link index. The system MPS is then in the form of Figure 9.14 (bottom), where each tensor has three physical indices (n_j, $i_k^{n_j}$ and $i_{k-l}^{n_j}$) as well as two link indices to neighboring sites of the many-body system (only one if its a boundary site) and two link indices to the respective reservoir, one to future time-bins (top-left for each tensor in Figure 9.14) and one to past time-bins (bottom-right for each tensor in Figure 9.14). With this, the respective MPO is applied on the MPS, shown for $U_{I-\mathcal{D}}$ in Figure 9.14 (bottom). The application of the MPO is similar to Figure B.1, but with three physical indices per tensor. After applying the MPO, the prime level of all physical indices is decreased by one. Then, each tensor is decomposed according to its physical indices. Thus, each tensor is decomposed into three tensors, where one contains the system index n_j as well as the links to neighboring sites n_{j-1} and n_{j+1} and the link to the now future time-bin $i_{k+1}^{n_j}$. The second tensor consists of the physical index $i_k^{n_j}$ and two new link indices resulting from the decomposition. The third tensor contains the feedback time-bin index $i_{k-l}^{n_j}$, and the link to the time-bin $i_{k-1}^{n_j}$ which is the neighboring past time-bin in the reservoir MPS. After the decomposition, the MPS should look like in Figure 9.15, where each system-bin is linked to the now past time bin $i_k^{n_j}$, the time-bins $i_k^{n_j}$ are linked
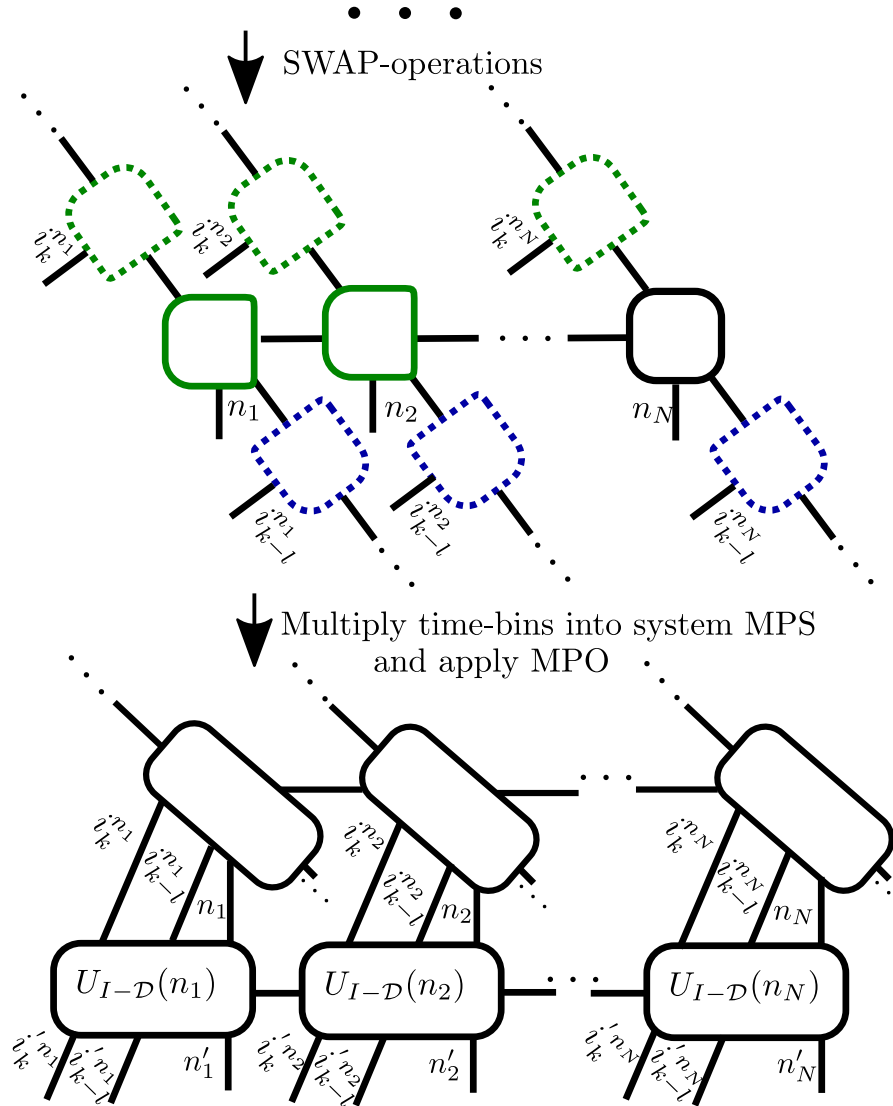
Figure 9.14.: Feedback algorithm for the many-body system coupled to N reservoirs. First, perform swap operations to bring each feedback time-bin $i_{k-l}^{n_j}$ next to the respective system-bin n_j (the starting point is the MPS in Figure 9.11). Note that the OC is kept at the respective feedback time-bin and then multiplied back into the system. Then for computing the swap operations of the next reservoir it is put into the following site n_{i+1} and brought to the feedback time-bin $i_{k-l}^{n_{j+1}}$. Afterwards, each feedback time-bin $i_{k-l}^{n_j}$ as well as each future time-bin $i_k^{n_j}$ is multiplied into the system MPS by contracting over the shared link indices. The respective MPO is applied, here shown for the Ising time-evolution operator $U_{I-\mathcal{D}}$. Then by contracting over all n_j, $i_k^{n_j}$ and $i_{k-l}^{n_j}$, the MPS for the next time step is computed in an efficient manner as depicted in Figure B.1. The prime level of all indices is decreased by one after the application of the MPO. Afterwards each tensor is decomposed to split the now past time-bin $i_k^{n_j}$ and the past feedback time-bin $i_{k-l}^{n_j}$ from the system MPS. Both are then stored in the respective MPS of the reservoirs.
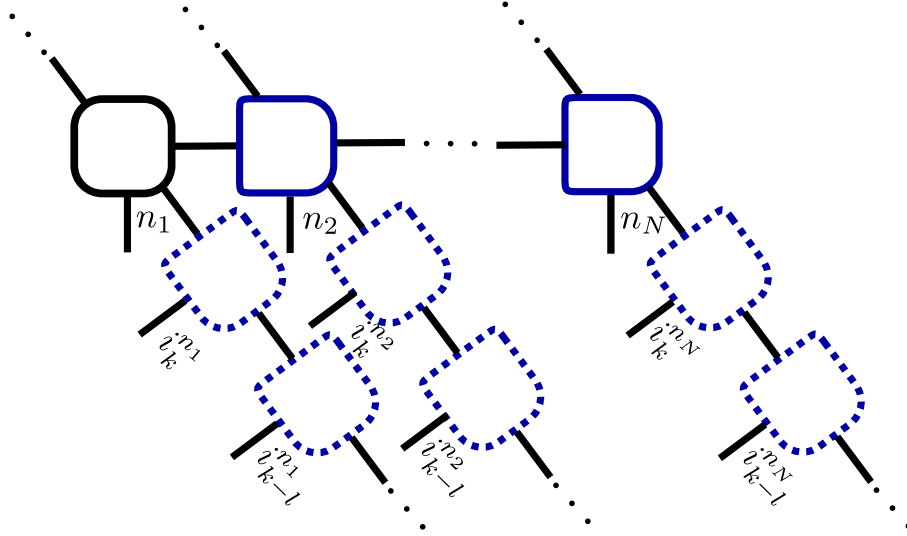
Figure 9.15.: MPS after the application of either $U_{T-\mathcal{D}}$ or $U_{I-\mathcal{D}}$. The former future time-bins $i_k^{n_j}$ are now past time-bins after the application of the MPO and are thus stored in the reservoir MPS below the system-bin. The feedback time-bin $i_{k-l}^{n_j}$ is stored below the time-bin $i_k^{n_j}$ and is linked to the past time-bin $i_{k-1}^{n_j}$. Now the MPS is re-gauged after the application of the MPO and ready for performing swap operations to bring the feedback time-bins $i_{k-l}^{n_j}$ back to their original positions.

to the feedback time-bins $i_{k-l}^{n_j}$ and the feedback time-bins are linked to $i_{k-1}^{n_j}$. Note that for simplicity, the OC is at the system-bin n_1 but might also be at the system-bin n_N dependent on from which side the MPO has been applied.

Before calculating observables, it is convenient in the algorithm to perform first the swap operations. Thus, the OC is brought to the feedback time-bin $i_{k-l}^{n_1}$ and afterwards, the feedback time-bin is brought to its original position by performing swap operations. In the last step, the OC is stored in the future feedback time-bin $i_{k-l+1}^{n_1}$. This future time-bin is then brought next to the system-bin n_1 by performing swap operations. Note that this speeds up the algorithm as one saves two times shifting the OC through the reservoir MPSs. The same procedure is repeated for each reservoir. After the swap operations, the MPS looks like in Figure 9.16. Each system-bin n_j has the future time-bin $i_{k+1}^{n_j}$ and the future feedback time-bin $i_{k-l+1}^{n_j}$ as neighboring tensors for the computation of the next time step. Furthermore, the MPS is in mixed canonical gauge which is why system observables such as the magnetization $\langle \sigma_j^z \rangle$, shown in Figure 7.11, are computed for the time t_k at this point. As done for a general reservoir, the MPOs have to be adapted for the computation of the next time step. This is done by replacing the index $i_k^{n_j}$ with the index $i_{k+1}^{n_j}$ and replacing $i_{k-l}^{n_j}$ with $i_{k-l+1}^{n_j}$ and the same for the primed outgoing indices. This is achieved in multiplying the MPOs with identities containing the index of the past time step as well as the index for the future time step as explained above. Then, the MPS and the MPO are ready for the next time step and the procedure is repeated starting with Figure 9.14.
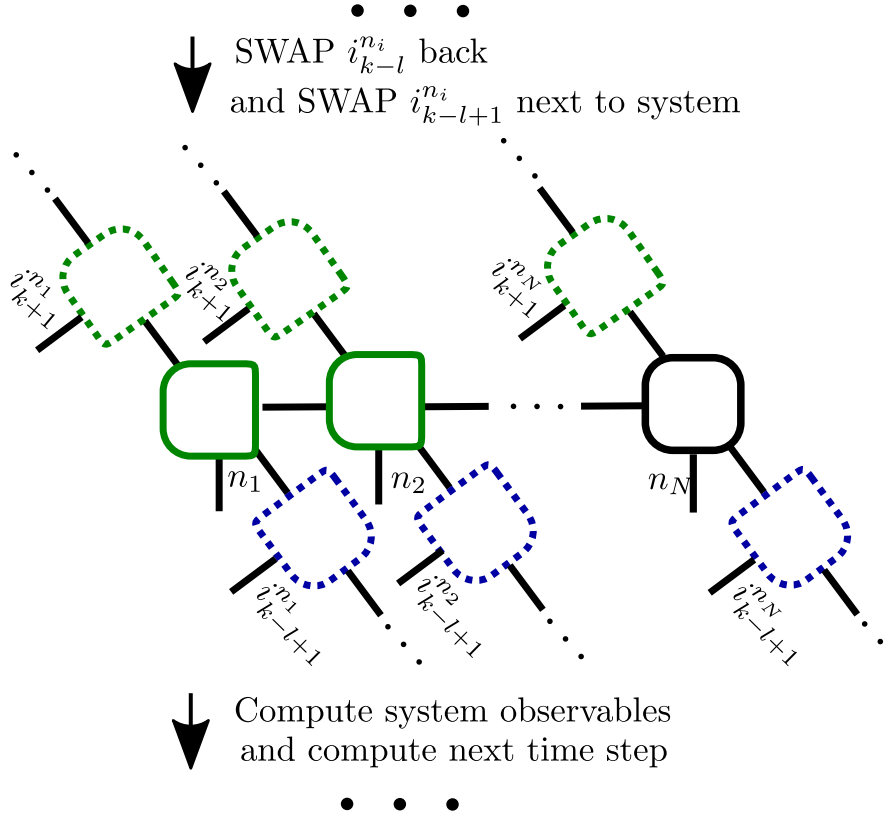
Figure 9.16.: After the application of the MPO in Figure 9.14 and the decomposition of the tensors, the feedback time-bin $i_{k-l}^{n_j}$ is brought back to its original position by performing swap operations. In doing so, the OC is kept at the feedback time-bin $i_{k-l}^{n_j}$. When arriving at its original position, the OC is then multiplied into the future feedback time-bin $i_{k-l+1}^{n_j}$. Then, the future feedback time-bin is brought next to the system bin n_j by performing swap operations. Afterwards, the OC is brought to the system-bin and then brought to the past feedback time-bin of the next reservoir $i_{k-l}^{n_{j+1}}$ and the same procedure is repeated until arriving at the end of the chain n_N. Then, observables concerning the system are computed as the MPS is in a mixed canonical gauge. The MPS is then ready for the application of the MPO for the next time step.

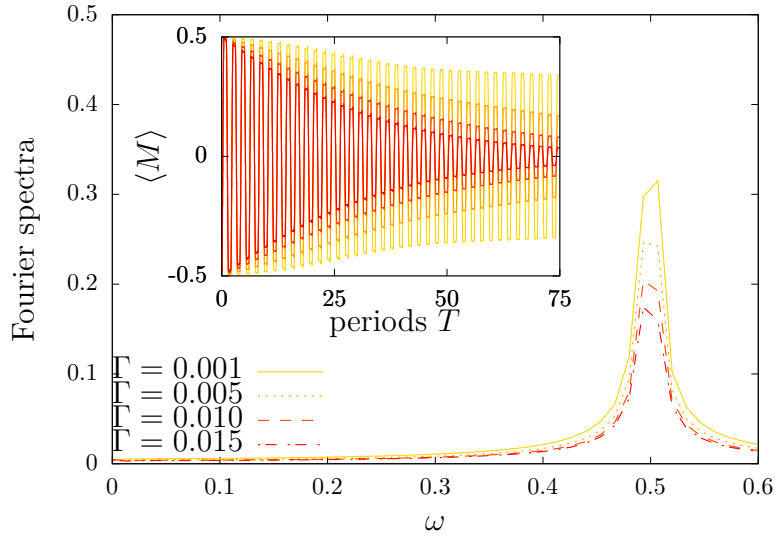### 9.2.3. Stabilizing a dissipative discrete time crystal

Figure 9.17.: Computation of a dissipative time crystal within the QSSE picture for a general (unstructured) coupling to the reservoir. The staggered magnetization $\langle M \rangle$ is subject to a decay with $\langle M \rangle \to 0$. This decay increases for increasing coupling to the reservoir Γ (inset). As a consequence, the peak height of the Fourier spectrum decreases with increasing Γ. The decay of $\langle M \rangle$ results from building up entanglement between the system and the reservoir states which is why the computation becomes very challenging already for small numbers of total time steps ($T = 75$ periods computed). Parameters are chosen as before $N = 10$, $\Delta t = 0.005$, svdcutoff$= 10e - 9$ for the spin system and svdcutoff$= 10e - 6$ between system and reservoir states, $\Omega = \pi/2$, $\epsilon = 0.015$, $J = 0.02$, $h_i \in [0, 7]$ and the number of averages between $N_{av} = 10^2$ and $N_{av} = 10^3$.

Having developed an algorithm to compute a dissipative time crystal in the QSSE picture, the interaction and buildup of entanglement between many-body spin system and the reservoir states are now investigated. First, a general reservoir is considered, where the coupling to the reservoir is constant with $\Gamma_R = 0$ and $\Gamma_L = \Gamma$. Thus, excitations are only spontaneously generated to the infinite side of each waveguide and do not interact again with the spin system. In Figure 9.17, a dissipative discrete time crystal is shown with a generic general (unstructured) coupling to N external reservoirs. In the inset of Figure 9.17, the staggered magnetization is shown. It becomes clear that $\langle M \rangle$ (Equation 9.1.8) decays faster for increasing reservoir coupling rates Γ with $\langle M \rangle \to 0$. This results in smaller peak heights with increasing Γ in the Fourier spectrum. These findings are in agreement with Ref. [224]. For a comparable small number of periods ($T = 75$), the DTC thermalizes with its environment due to build up of entanglement with reservoir states via Γ.

In contrast to computations in the Liouville space or with the density-matrix formalism as done in Part II of this thesis, the reservoir degrees of freedom are not traced out. This means that all entanglement between system and reservoir is kept during the computation within the MPS. As a consequence, the dimension of each link index grows with increasing computation time because the entanglement grows and more and more singular values
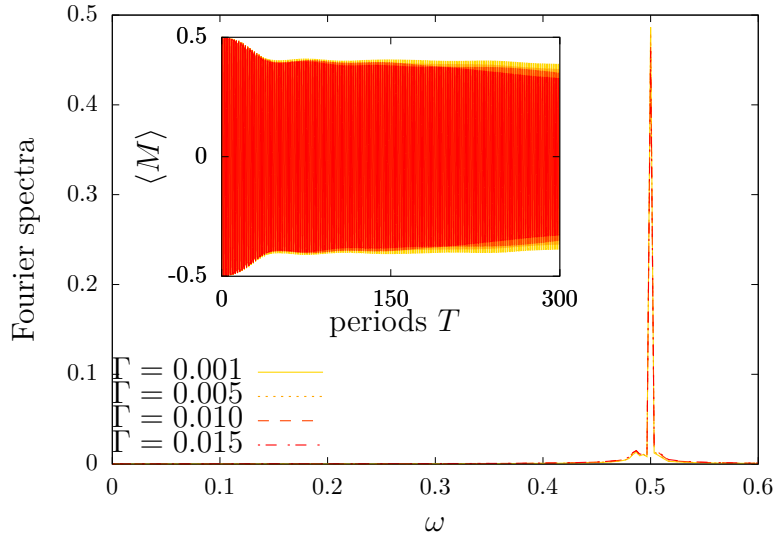
Figure 9.18.: Computation of a dissipative time crystal within the QSSE picture with constructive feedback dynamics ($\phi_{n_i} = \pi$). The subsequent interaction of the system with self-generated reservoir excitations counteracts the building up of entanglement between system and reservoir. Thus, the DTC dynamics are stabilized for a long time ($T = 300$, inset). The subharmonic frequency is locked at $\omega = 1/2$ with almost the same peakheight as without dissipation (Figure 9.9). This is also the case if the coupling to the reservoir Γ is increased. Note that $\Gamma = \Gamma_R = \Gamma_L$ and $\tau = 0.02$. The other parameters are chosen as before.

become relevant. As this setup has a high amount of link indices, i.e. one between each site index as well as link indices to each reservoir, the simulation quickly reaches a numerical limit. For this reason, the time evolution with dissipation to a general reservoir has only been computed up until $T = 75$ periods. Furthermore, Δt has to be chosen small enough to reduce the error due to the expansion to second order in Δt of the time-evolution operators. It is assumed that Δt is not small enough for $\Gamma = 0.001$, as the radiative decay is not covered by the chosen Δt. However, in choosing a smaller Δt, the truncation in the singular values has to be chosen appropriate. With smaller Δt also smaller singular values become relevant. When the truncation in the singular values is not chosen appropriate, the time crystal behavior disappears because the important Ising interaction is not covered anymore by the considered singular values. Thus, if these important singular values are neglected in the computation, the system is following the external perturbation in the driving. When this happens within a parameter setup where time crystal behavior is expected according to Ref. [223], it is a strong indicator for a too high truncation in the singular values.

However, if feedback dynamics are considered with $\Gamma = \Gamma_R = \Gamma_L$ it is possible to compute far more periods. In Figure 9.18 the dissipation including feedback dynamics is shown. It becomes clear that the feedback dynamics counteract the general dissipation in Figure 9.17. This can be seen on two things. On the one hand, the peak height is almost the same as without any dissipation (cp. Figure 9.9), because the staggered magnetization stabilizes at the same value. On the other hand, if the coupling to the surrounding reservoirs Γ is increased, the peak height as well as the oscillations of $\langle M \rangle$ remain at nearly the same value. This strongly indicates that the dissipation via Γ is suppressed by the feedback

dynamics. Another indicator is that the dimension of the link indices does not grow as much as for the general dissipation in Figure 9.17 which is why it is possible to compute up to $T = 300$ periods. This is a remarkable observation, because one would assume that the feedback algorithm would take more time. On the one hand, with each time step a lot of swap operations have to be performed, the exact number depends on the time delay $\tau/\Delta t$ and the system size. On the other hand, the dimension of each tensor of the MPS is of one higher rank and each tensor of the MPO is of higher rank two. However, the smaller dimension of the link indices, due to the suppression of entanglement with the reservoirs, counteracts this further complexity and the computation is more feasible in the QSSE picture with feedback dynamics as for general dissipation.

Having now demonstrated that feedback dynamics stabilize the dissipative DTC, a different model of the DTC is considered. The driving Hamiltonian with the transverse field $\mathcal{H}_T$ during T_1 is the same as before, but the interacting Hamiltonian $\mathcal{H}_I$ during T_2 is replaced by

$$\mathcal{H}_I = \sum_{i=1}^{N-1} J_i^z \sigma_i^z \sigma_{i+1}^z + \sum_{i=1}^{N-1} J_i^x \sigma_i^x \sigma_{i+1}^x + \sum_{i=1}^{N} h_i^x \sigma_i^x \quad T_1 < t < T_2 \ . \qquad (9.2.7)$$

The couplings J_i^z, J_i^x and the transverse field h_i^x are randomly distributed between $[-\chi, \chi]$, where χ is the respective parameter. This model is known to exhibit localization protected spatial order which is also called a MBL spin-glass [225]. Thus, a combination of spatial and temporal order is formed in this model when $\mathcal{H}_T$ and $\mathcal{H}_I$ are applied periodically [226]. Without addressing the question whether feedback dynamics also stabilize spatial order against dissipation, this might be an interesting future investigation. A possible detection of spatial order with the here used method is a modification of the Edward-Anderson order parameter, based on reduced density matrices [227].

However, the scope of this chapter is to demonstrate stabilization of temporal order against dissipation, namely the persistent oscillations of the DTC returning to its initial state after two periods. Another advantage of the model in Equation 9.2.7 is the MBL phase without using a random field in the z-dimension. Temporal order is only robust against dissipation for constructive interference $\phi_{n_i} = \pi$ of each spin n_i. The feedback phase $\phi = \pi - \omega_{01}\tau$ was introduced for a single TLS in chapter 8. The random disorder $h_i \sigma_i^z$ would modify the energy gap of each individual TLS of the many-body system according to the disorder realization. In the simulation it is possible to force each individual $\phi_i = \pi$ as done above. However, in an experiment, each individual mirror distance L_i would have to be adjusted dependent on the disorder realization. To overcome this further difficulty, the model in Equation 9.2.7 shows DTC behavior combined with MBL, without modifying the energy gap of each individual TLS and is therefore much more feasible in this context. Furthermore, it becomes possible to study the effect of a shared reservoir as all TLS have the same constructive feedback phase for this model.

The simulation of a DTC with a shared reservoir of all spins becomes very involved. The reason is that all spins share a link index to the same reservoir. Thus, a decomposition to an MPO, as explained in the previous section, is not possible. The reason is that an MPO formulation would implicate that the spins act after each other on the reservoir, starting with the first spin, then the second and so on.

Due to this, the simulation with a shared reservoir is comparable to the algorithm in chapter 8. All physical indices of the many-body system are expressed in a single compound index for the system i_s. This includes the exponential scaling of the Hilbert space with
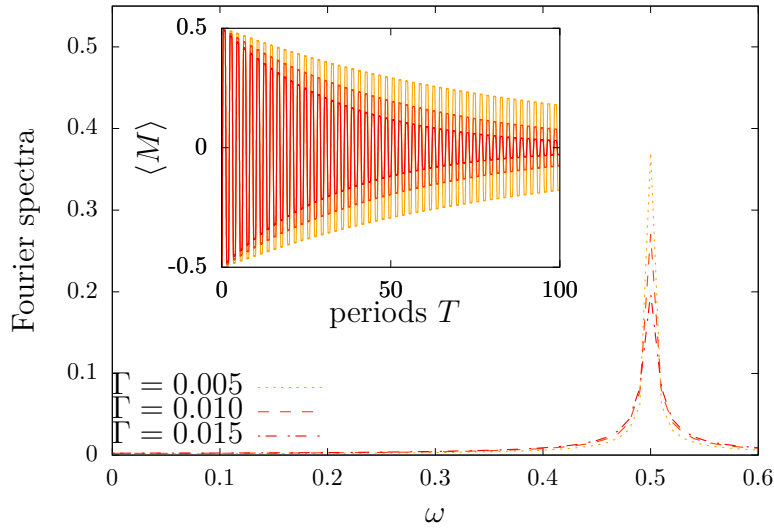
Figure 9.19.: A dissipative DTC with general (unstructured) reservoir coupling with a single reservoir for all $N = 8$ spins. The staggered magnetization decays similar to the case of individual reservoirs. Note that for computational reasons, the perturbation was set to zero $\epsilon = 0$. Parameters: $\Delta t = 0.005$, svdcutoff$= 10e-9$ for the spin system and svdcutoff$= 10e-6$ between system and reservoir states, $\Omega = \pi/2$, $\epsilon = 0$, $J^z = 0.1$, $J^x = 0.01$, $h^x = 0.01$ and the number of averages around $N_{av} = 10$.

growing system size, which is why with this approach the maximal system size is $N = 8$. However, the overall entanglement with the reservoir is smaller than for individual reservoirs for this system size, as not so many link indices to the reservoirs are involved. For this reason, the time evolution without feedback dynamics can be evaluated for a larger number of periods. The dissipation of the DTC with a shared reservoir for all spins is shown in Figure 9.19. Note that the perturbation ϵ is set to zero in this and all following plots. The reason is that this speeds up the computation time as lesser entanglement is generated within the spin system. However, the robustness of the DTC against perturbations $\epsilon > 0$ was tested for all this cases as well. It becomes clear that there is no visible difference between the dissipation to a shared reservoir compared to the individual reservoirs in Figure 9.17. For a general dissipation this is also expected as without a structured reservoir, the decay Γ is the same for all spins. As any dissipation is lost to the infinite side of the waveguide, it is not to be expected that there is a difference between individual or shared reservoirs.

In Figure 9.20 it is shown that also constructive feedback dynamics are the same as for individual reservoirs in Figure 9.18. The constructive feedback interference counteracts the buildup of entanglement and prevents the system from thermalizing with the environment, also for a shared reservoir of all spins. This is a strong finding and allows to take the case of individual reservoirs as a general example to explore much larger system sizes. This is because individual reservoirs can be computed very efficiently with the algorithm developed within previous section.

To end this chapter, an example for a large system of $N = 40$ which is beyond computation with conventional open quantum system methods is shown in Figure 9.21. This proves that temporal order for the MBL spin-glass model in Equation 9.2.7 is also stabilized
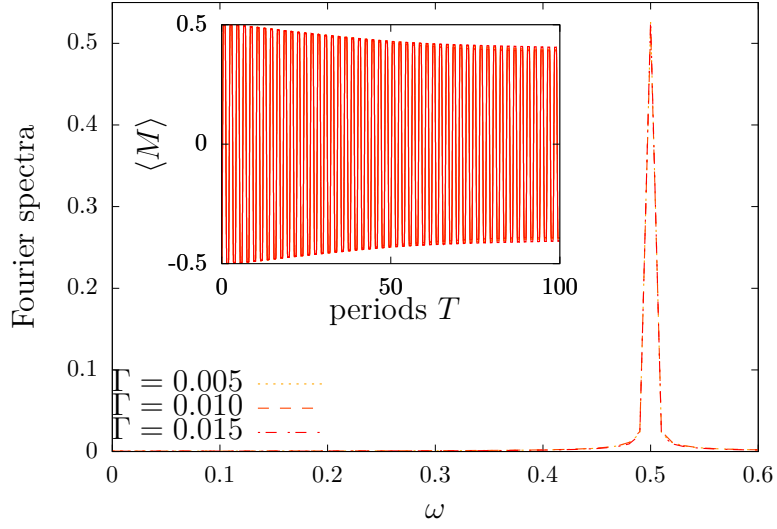
Figure 9.20.: Feedback dynamics for a shared reservoir. As for the individual reservoirs, constructive feedback stabilizes temporal order acting against dissipation. The staggered magnetization becomes independent of the coupling to the reservoir Γ. All parameters are chosen as before.
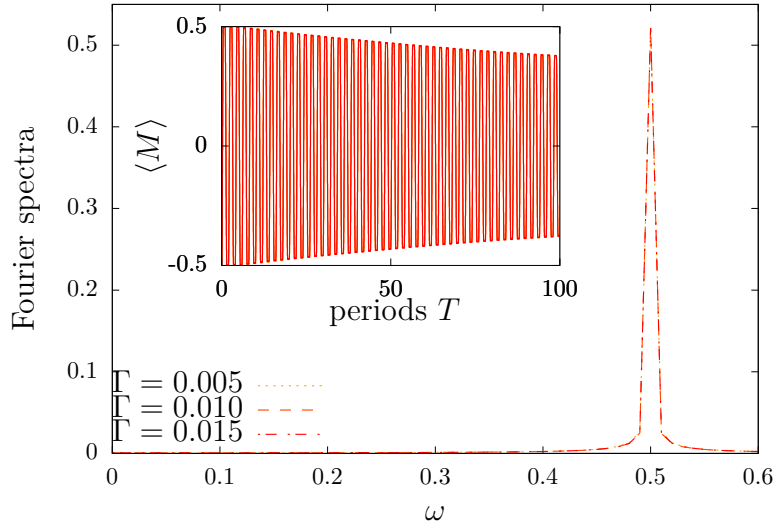

Figure 9.21.: Simulation of a large system of $N = 40$ with individual reservoirs. This proves that the developed algorithm has an efficient scaling with the system size. Furthermore, temporal order is stabilized against dissipation using constructive feedback for the MBL spin-glass system.

via feedback dynamics. Furthermore, this serves as a demonstration that the algorithm has a very efficient scaling with the system size. The main reason is that MPS methods are very efficient for systems with a small amount of entanglement. On the one hand the entanglement growth is strongly suppressed by MBL, allowing to explore large systems. On the other hand, constructive feedback suppresses entanglement with the reservoir, allowing to consider the reservoir degrees of freedom in a numerically exact method. Furthermore, this allows to draw the conclusion that not only the DTC is stabilized for long times against dissipation, but also MBL survives for an open quantum system with a structured reservoir.

9.3. Conclusion

In this chapter, an open many-body spin system has been investigated using matrix product state methods. In the first section, a closed quantum system was considered to explain standard matrix product state methods. The system of interest is a discrete time crystal, where the time translational symmetry of the Floquet Hamiltonian $\mathcal{H}(t) = \mathcal{H}(t + T)$ is broken, i.e. the staggered magnetization as observable shows oscillations at twice the period $\langle M \rangle(t) = \langle M \rangle(t + 2T)$, meaning the many-body system returns to its initial state after two periods of the Floquet Hamiltonian. This behavior is stable even against perturbations in the driving. However, the external driving results in heating of the spin system, bringing it to thermal equilibrium. Many-body localization prevents the system from absorbing the energy of the driving, and a stable discrete time crystal is achieved for long times. This makes the system an ideal candidate to use matrix product state methods due to small entanglement between subsystems.

In the second section, the many-body system was generalized to an open quantum system, adapting the method of chapter 8, where the environment was included within the many-body formulation, based on the quantum stochastic Schrödinger equation. This results in a two-dimensional matrix product state where each spin is interacting with an individual reservoir. The formulated method can be adapted to generic one-dimensional many-body quantum systems and is efficient as long as the entanglement within the many-body system is very small (i.e. any many-body localized system).

It has been demonstrated that the decay due to Lindblad dissipators is reproduced, resulting in melting of the discrete time crystal due to thermalization with the environment.

When the reservoir is structured with a reflecting element, e.g. a distant mirror, it has been demonstrated that for constructive interference, the DTC is stabilized and becomes independent of the coupling to the reservoir. The interference induced by the mirror counteracts thermalization with the environment and a stable open discrete time crystal is achieved.

Furthermore, a second model was investigated, exhibiting time translational symmetry breaking, which is a many-body localized spin-glass. In this model, a shared reservoir has been considered, showing also stabilization due to feedback dynamics. This allows to assume that the method based on individual reservoirs for each spin suffices to explain the behavior for a shared reservoir as well.

The advantage of the proposed method to simulate open many-body spin systems including feedback dynamics is that entanglement between the many-body system and the reservoir is strongly suppressed. As the many-body system itself is within a many-body localized phase, the proposed method using matrix product states has a very efficient scaling with the system size. An open system up to a number of forty spins including feedback dynamics

has been simulated, showing oscillations independent of the coupling to the reservoir. Thus, a large open quantum many-body system has been stabilized against dissipation and temporal order has been observed for a long time. This also includes that many-body localization is stable against dissipation for constructive feedback interference.

10.

Conclusion and outlook

In this thesis, different out-of-equilibrium open quantum many-body systems have been investigated. In the first part, the theoretical and physical framework for the investigated methods and effects has been provided.

The second part considered couplings to general (unstructured) reservoirs described by Lindblad dissipators based on the Born-Markov approximation via the reduced density formalism.

As a first many-body system, the many-emitter phonon laser has been investigated. Due to the coupling between different emitters over the cavity phonon mode, collective effects are present. A mapping of the Hamiltonian to a Tavis-Cummings type model has revealed additional resonances caused by collective phonon emission of many emitters. It has been demonstrated that by optically addressing these collective resonances, the phonon intensities are enhanced in the many-emitter setup. A possible future direction is to investigate interactions with reservoirs beyond Born-Markov approximation as done for different systems in the third part of this thesis. This might allow to manipulate the phonon statistics in a controllable setup.

As second many-body system, the Heisenberg spin-chain was considered. In driving the system out-of-equilibrium via two boundary reservoirs, a spin current is induced. It has been shown that the transport for the conventional nearest-neighbor coupling between the spins is very sensible on the reservoir parameters due to far-from-equilibrium effects. In contrast, the transport for long-range coupling is independent of the external reservoirs. When considering small disorder strengths, where the system is still within an ergodic phase, as well nearest-neighbor as long-range coupling show a transition to subdiffusive transport. However, the transition to subdiffusive transport for long-range coupling is independent of the external driving and thus results purely from disorder effects. This could help to understand the reason for the existence of subdiffusive transport due to disorder which is still under debate. Furthermore, it remains an open question under which conditions many-body localization exists in open boundary driven systems.

In the third part of this thesis, reservoirs with memory effects have been considered, where a common Born-Markov approximation is not possible. Dynamics have been computed via the quantum stochastic Schrödinger equation in formulating the system and reservoir as a matrix product state.

A single two-level system coupled to a structured reservoir has been considered. In exciting the emitter with a time-dependent pulse and inducing optical self-feedback via the distance to a mirror, it has been shown that individual photon probabilities are controlled. For example, the two-photon is higher than the one-photon probability and shows an enhancement of up to 50% compared to the case without feedback. The two photons generated from a single emitter could be entangled in time which remains to be shown. A computation of an observable based on Franson interferometry for matrix product state methods could be

interesting to prove time entanglement for setups with feedback dynamics, as two-photon probabilities are explicitly controlled via time-delayed feedback.

In the last chapter, a theory has been developed to consider reservoirs with memory effects combined with a many-body system. The common description via matrix product state methods has been generalized to a two-dimensional matrix product state with an individual reservoir for each site of the many-body system.

The derived methods scales very efficiently with the system size due to small entanglement within a many-body localized system. Furthermore, entanglement with the external reservoirs is suppressed using feedback dynamics. As an example, it has been shown that a discrete time crystal is stabilized against dissipation in structuring the external reservoirs. Thus, temporal order of the time crystal is stable for a long time even in the presence of an external environment. It is an interesting question, if spatial order, which is also present in these systems, is also stabilized using feedback dynamics. This might be closely connected to the performed rotating wave approximation for the coupling to the reservoir.

For the discrete time crystal up to forty spins have been investigated. However, the proposed method can be optimized in the future to even explore larger systems. Furthermore, the method is not limited to the proposed system. An investigation of other systems showing many-body localization is a promising future direction. Especially to show in detail a robustness of many-body localization for open quantum many-body systems to explore further out-of-equilibrium effects.

Acknowledgments

I would like to thank Prof. Dr. Andreas Knorr for giving me the opportunity to work on these interesting projects and the constant support he gave me in developing my research subject. Furthermore, I would like to thank him for sparking my interest in quantum mechanics already in the beginning of my studies with his inspiring lectures in the morning hours.

My thanks go to Prof. Dr. Peter Rabl for being the second reviewer of my thesis. Furthermore, I would like to thank Prof. Dr. Michael Kneissl for chairing the board of referees.

Special thanks go to Dr. Alexander Carmele. His constant support and trust in my work not only influenced the major part of this thesis, but also personally I benefited a lot from his experience. The many discussions and conversations deepened my interest in physics and created an enjoyable atmosphere which I will definitely miss in the future.

I want to thank Dr. Markus Heyl for opening my interest in many-body physics already during my master thesis. The fruitful discussions helped me developing the ideas of this thesis. Furthermore, I want to thank him and the Max-Planck-Institut für Physik komplexer Systeme for giving me the opportunity to run simulations on their cluster.

Furthermore, I would like to thank Dr. Julia Kabuss for supervising me in the beginning of my research and the development of the ideas concerning the many-emitter phonon laser.

For being the perfect collaborator, I would like to thank Dr. Nicolas Naumann. Working together on the phonon laser and developing the first simulation for feedback dynamics has improved a major part of this thesis.

I want to thank all the former and current members of the AG Knorr for the many funny moments during lunch and coffee breaks, conferences and symposias. Especially my office colleagues over the years, Shahabedin Chatraee Azizabadi, Alexander Carmele, Michael Gegg, Manuel Kraft, Nicolas Naumann and Judith Specht have made a perfect atmosphere with helpful discussions and humorous chats.

Special thanks go to Alexander Carmele, Regina Finsterhölzl, Manuel Kraft, Julian Schleibner, Malte Selig and Judith Specht for proofreading this thesis.

For the technical support and the management of the computer cluster, which I was constantly using, I thank Dr. Marten Richter and Peter Orlowski.

PART IV

Appendices

A.

Details on the Theoretical Background

A.1. Consitency with the Maxwell equations

The fundamental equations of the classical description of the electromagnetic field are the Maxwell equations. In this thesis, the equations are formulated, based on a covariant formulation of the Lagrange function. In correspondence to the Minkowski tensor, the metric tensor is defined as

$$\eta^{\alpha\beta} = \begin{pmatrix} 1 & 0 & 0 & 0 \\ 0 & -1 & 0 & 0 \\ 0 & 0 & -1 & 0 \\ 0 & 0 & 0 & -1 \end{pmatrix} . \tag{A.1.1}$$

The components of the electric field $\mathbf{E}$ and the magnetic field $\mathbf{B}$ are written into the contravariant electromagnetic tensor [61]

$$F_{\alpha\beta} = \begin{pmatrix} 0 & E_x/c & E_y/c & E_z/c \\ -E_x/c & 0 & -B_z & B_y \\ -E_y/c & B_z & 0 & -B_x \\ -E_z/c & -B_y & B_x & 0 \end{pmatrix} , \tag{A.1.2}$$

with $c = \sqrt{\epsilon_0 \mu_0}$ as the speed of light in vacuum with the corresponding electric constant ϵ_0 and magnetic permeability μ_0. The covariant form $F^{\alpha\beta}$ is obtained by raising its indices with the metric tensor (using Einstein notation)

$$F^{\gamma\delta} = \eta^{\gamma\alpha} F_{\alpha\beta} \eta^{\beta\delta} . \tag{A.1.3}$$

The Lagrange function L_M of the electromagnetic field with the electromagnetic tensor then reads [57]

$$L_M = \int d^3r \mathcal{L} , \quad \mathcal{L} = -\frac{1}{4\mu_0} F^{\alpha\beta} F_{\alpha\beta} = \frac{\epsilon_0}{2} \left(\mathbf{E}^2 - c^2 \mathbf{B}^2 \right) , \tag{A.1.4}$$

with Lagrange density $\mathcal{L}$. By defining the four-gradient and the four-potential

$$\partial^\alpha = \left(\frac{1}{c} \frac{\partial}{\partial t}, -\nabla \right) , \quad A^\alpha = (\phi/c, \mathbf{A}) , \tag{A.1.5}$$

with scalar potential ϕ and vector potential $\mathbf{A}$, the differential of the electromagnetic potentials yields the electromagnetic tensor [57]

$$F_{\alpha\beta} = \partial_\alpha A_\beta - \partial_\beta A_\alpha . \tag{A.1.6}$$

The Maxwell equations are obtained by deriving the conditions for the Euler-Lagrange equation of the Lagrangian density $\mathcal{L}\left(A_\alpha, \partial_\beta A_\alpha\right)$

$$\partial_\beta \frac{\partial \mathcal{L}}{\partial(\partial_\beta A_\alpha)} - \frac{\partial \mathcal{L}}{\partial A_\alpha} = 0 \; . \tag{A.1.7}$$

Calculating the first summand

$$\begin{aligned}
\frac{\partial \mathcal{L}}{\partial(\partial_\beta A_\alpha)} &= -\frac{1}{4\mu_0} \frac{\partial \left(F_{\mu\nu}\eta^{\mu\lambda}\eta^{\nu\sigma}F_{\lambda\sigma}\right)}{\partial(\partial_\beta A_\alpha)} \\
&= -\frac{1}{4\mu_0} \frac{\partial \left[(\partial_\mu A_\nu - \partial_\nu A_\mu)\eta^{\mu\lambda}\eta^{\nu\sigma}(\partial_\lambda A_\sigma - \partial_\sigma A_\lambda)\right]}{\partial(\partial_\beta A_\alpha)} \\
&= -\frac{1}{4\mu_0}\eta^{\mu\lambda}\eta^{\nu\sigma}\left[(\delta_\mu^\beta \delta_\nu^\alpha - \delta_\nu^\beta \delta_\mu^\alpha)F_{\lambda\sigma} + F_{\mu\nu}(\delta_\lambda^\beta \delta_\sigma^\alpha - \delta_\sigma^\beta \delta_\lambda^\alpha\right] \\
&= -\frac{1}{4\mu_0}\left[(\delta^{\beta\lambda}\delta^{\alpha\sigma} - \delta^{\beta\sigma}\delta^{\alpha\lambda})F_{\lambda\sigma} + F_{\mu\nu}(\delta^{\beta\mu}\delta^{\alpha\nu} - \delta^{\beta\nu}\delta^{\alpha\mu}\right] \\
&= -\frac{1}{4\mu_0}\left[F^{\beta\alpha} - F^{\alpha\beta} + F^{\beta\alpha} - F^{\alpha\beta}\right] \\
&= -\frac{1}{\mu_0}F^{\beta\alpha} \; ,
\end{aligned} \tag{A.1.8}$$

where in the first step the indices of the left electromagnetic tensor were lowered, then in a second step the derivative yields delta tensors. Finally the delta and the metric tensor act on the electromagnetic potentials.

The second part of Equation A.1.7 yields

$$\frac{\partial \mathcal{L}}{\partial A_\alpha} = 0 \; , \tag{A.1.9}$$

as the Lagrangian in Equation A.1.4 without the four-current has no dependency on the four-potential itself. With the condition of the Euler-Lagrange equation in Equation A.1.7

$$\partial_\beta \frac{1}{\mu_0}F^{\beta\alpha} \overset{!}{=} 0 \; , \tag{A.1.10}$$

the first two Maxwell equations are obtained. For $\beta = 0$, the first line of the covariant electromagnetic tensor is derivated yielding

$$\nabla \cdot \mathbf{E} = 0 \; . \tag{A.1.11}$$

For $\beta \in \{1, 2, 3\}$, it yields the respective part of the rotation of B_β and the time derivative of E_β resulting in

$$\nabla \times \mathbf{B} - \frac{1}{c^2}\frac{\partial \mathbf{E}}{\partial t} = 0 \; . \tag{A.1.12}$$

Note that in the Lagrangian in Equation A.1.4 the four-current was set to zero, thus the here derived Maxwell equations do not include charges or currents.
The other two Maxwell equations are derived by the Jacobian identity

$$\partial^\alpha F^{\beta\gamma} + \partial^\beta F^{\gamma\alpha} + \partial^\gamma F^{\alpha\beta} = 0 \ . \tag{A.1.13}$$

The Jacobian identity has a compact notation for the dual electromagnetic tensor $\tilde{F}^{\alpha\beta}$ which is a transformation

$$\frac{1}{c}\mathbf{E} \to \mathbf{B}, \quad \mathbf{B} \to -\frac{1}{c}\mathbf{E} \tag{A.1.14}$$

of the electromagnetic tensor. With this the Jacobian identity reads

$$\partial_\alpha \tilde{F}^{\alpha\beta} \ . \tag{A.1.15}$$

For $\alpha = 0$ the third Maxwell equation is obtained

$$\nabla \cdot \mathbf{B} = 0 \tag{A.1.16}$$

and for $\alpha \in \{1, 2, 3\}$, the rotation of $\mathbf{E}$ and time derivative of $\mathbf{B}$ is obtained

$$\nabla \times \mathbf{E} + \frac{\partial \mathbf{B}}{\partial t} = 0 \ . \tag{A.1.17}$$

With this it is shown that the Lagrangian L_M in Equation A.1.4 leads to the basic Maxwell equations for the classical electromagnetic field and will therefore be used in the following to quantize the Maxwell field.

A.2. Commutation relation of the mode operators

To determine whether the commutation relation of the mode operators is bosonic or fermionic, a general commutator is calculated with either a plus or a minus sign. Calculating the commutator in Equation 2.3.17 it reads

$$\begin{aligned}
\left[(b_{\lambda\mathbf{k}}e^{i\mathbf{k}\mathbf{r}} - h.c.), (b_{\lambda'\mathbf{k}'}e^{i\mathbf{k}'\mathbf{r}'} + h.c.)\right] &= \left[b_{\lambda\mathbf{k}}e^{i\mathbf{k}\mathbf{r}}, b_{\lambda'\mathbf{k}'}e^{i\mathbf{k}'\mathbf{r}'}\right] - \left[b_{\lambda\mathbf{k}}^\dagger e^{-i\mathbf{k}\mathbf{r}}, b_{\lambda'\mathbf{k}'}^\dagger e^{-i\mathbf{k}'\mathbf{r}'}\right] \\
&+ \left[b_{\lambda\mathbf{k}}e^{i\mathbf{k}\mathbf{r}}, b_{\lambda'\mathbf{k}'}^\dagger e^{-i\mathbf{k}'\mathbf{r}'}\right] - \left[b_{\lambda\mathbf{k}}^\dagger e^{-i\mathbf{k}\mathbf{r}}, b_{\lambda'\mathbf{k}'}e^{i\mathbf{k}'\mathbf{r}'}\right] \\
&= \left[b_{\lambda\mathbf{k}}e^{i\mathbf{k}\mathbf{r}}, b_{\lambda'\mathbf{k}'}e^{i\mathbf{k}'\mathbf{r}'}\right] - \left[b_{\lambda\mathbf{k}}^\dagger e^{-i\mathbf{k}\mathbf{r}}, b_{\lambda'\mathbf{k}'}^\dagger e^{-i\mathbf{k}'\mathbf{r}'}\right] \\
&+ e^{i(\mathbf{k}\mathbf{r}-\mathbf{k}'\mathbf{r}')}\left(\delta_{\lambda\lambda'}\delta(\mathbf{k}-\mathbf{k}') \pm b_{\lambda'\mathbf{k}'}^\dagger b_{\lambda\mathbf{k}} - b_{\lambda'\mathbf{k}'}^\dagger b_{\lambda\mathbf{k}}\right) \\
&+ e^{-i(\mathbf{k}\mathbf{r}-\mathbf{k}'\mathbf{r}')}\left(\delta_{\lambda\lambda'}\delta(\mathbf{k}-\mathbf{k}') \pm b_{\lambda\mathbf{k}}^\dagger b_{\lambda'\mathbf{k}'} - b_{\lambda\mathbf{k}}^\dagger b_{\lambda'\mathbf{k}'}\right)
\end{aligned} \tag{A.2.1}$$

With this it becomes clear that the mode operators vanish from the equation, if the plus sign is correct. With this it is shown that the mode operators obey a bosonic commutation relation

$$\left[b_{\lambda\mathbf{k}}, b^{\dagger}_{\lambda'\mathbf{k}'} \right] = \delta_{\lambda\lambda'}\delta(\mathbf{k} - \mathbf{k}') \ , \tag{A.2.2}$$

$$[b_{\lambda\mathbf{k}}, b_{\lambda'\mathbf{k}'}] = \left[b^{\dagger}_{\lambda\mathbf{k}}, b^{\dagger}_{\lambda'\mathbf{k}'} \right] = 0 \ . \tag{A.2.3}$$

A.3. Lorentz force

In this section, the Lorentz force will be derived from the Lagrangian of a charged particle with mass m and charge q in a field with vector potential $\mathbf{A}$ and scalar potential ϕ

$$L_F(\mathbf{r}, \dot{\mathbf{r}}) = \frac{1}{2}m\dot{\mathbf{r}}^2 + q\dot{\mathbf{r}} \cdot \mathbf{A} - q\phi \ . \tag{A.3.1}$$

This Lagrangian will be used later on to derive the interaction between an electron and a light field (classical as well as quantized). This section serves to prove the relevance of this Lagrangian in deriving the fundamental Lorentz force from it. The Euler-Lagrange equation reads

$$\frac{\partial L}{\partial r_i} - \frac{d}{dt}\frac{\partial L}{\partial \dot{r}_i} = 0 \ . \tag{A.3.2}$$

The first part results in

$$\frac{\partial L_F}{\partial r_i} = q\sum_l \frac{\partial A_i}{\partial r_l}\frac{dr_l}{dt} - q\frac{\partial \phi}{\partial r_i} \ , \tag{A.3.3}$$

and the second part yields

$$\begin{aligned}
\frac{d}{dt}\frac{\partial L_F}{\partial \dot{r}_i} &= \frac{d}{dt}\left(m\dot{r}_i + qA_l(\mathbf{r}(t), t) \right)\\
&= m\ddot{r}_i + q\frac{\partial A_i}{\partial t} + q\sum_l \frac{\partial A_l}{\partial r_i}\frac{dr_l}{dt} \ .
\end{aligned} \tag{A.3.4}$$

Inserting Equation A.3.3 and Equation A.3.4 into Equation A.3.2 already results in the Lorentz force

$$m\ddot{r}_i = q\left(-\frac{\partial \phi}{\partial r_i} - \frac{\partial A_i}{\partial t} \right) + q\sum_l \left(\frac{\partial A_i}{\partial r_l} - \frac{\partial A_l}{\partial r_i} \right)\frac{dr_l}{dt} \ . \tag{A.3.5}$$

The first part results in the respective part of the electric field $\mathbf{E} = -\nabla\phi - \frac{\partial \mathbf{A}}{\partial t}$ and the second part in the respective rotation of $\mathbf{B} \times \dot{\mathbf{r}}$ due to $\mathbf{B} = \nabla \times \mathbf{A}$. Thus, including all three dimensions it results in the Lorentz force

$$\mathbf{F_L} = q\mathbf{E} + q\left(\dot{\mathbf{r}} \times \mathbf{B} \right) \ . \tag{A.3.6}$$

B.

Details on Feedback-stabilized time crystal

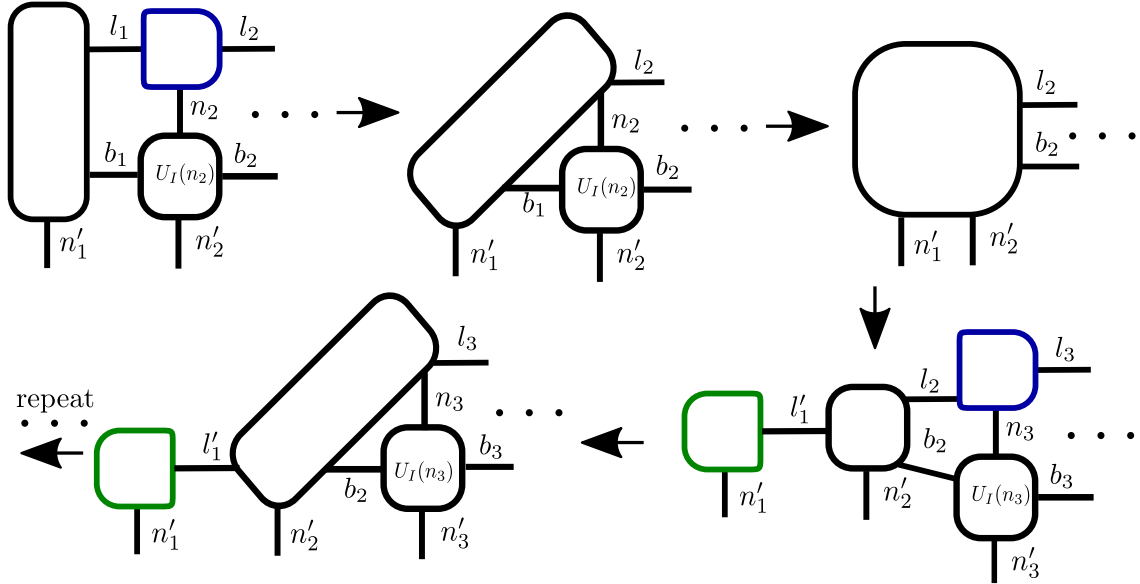## B.1. Efficient application of a matrix product operator

Figure B.1.: Efficient application of U_I on the MPS. First (top left), it is contracted over the physical index n_1. In a second step (top central) the link index l_1 is contracted. In a third and fourth step it is contracted over the link index b_1 of the MPO and then over the physical index n_2. The resulting tensor is of rank four with two physical and two link indices (top right). The tensor is decomposed such that the OC is at the tensor containing n_2' and the tensor of the first site n_1' is of rank two and left-normalized (bottom right). Note that the link index l_1' is now of higher dimension according to l_1 and b_1. The tensor at the second site now shares a link index l_2 with the tensor of the third site n_3 and a link index b_2 with $U_I(n_3)$. The procedure is repeated for the following sites starting with contracting over l_2 (bottom left).

An efficient application of $U_I(\Delta t)$ on $|\psi(T_1)\rangle$ is shown in Figure B.1. The starting point is the second diagram in Figure 9.4. At first, a contraction over the index n_1 is performed. Then the resulting tensor of rank three is contracted with the tensor of the MPS of the second site which is done in contracting over l_1. The resulting tensor of rank four is then

contracted with the MPO tensor of the second site by contracting first over b_1 and then over n_2. The resulting tensor now includes both outgoing physical indices n'_1 and n'_2. Now it is important to decompose this tensor to avoid dealing with high rank tensors in the following. Thus, the MPS form is constructed from the left side in separating the tensor containing n'_1. The resulting link index l'_1 now includes the link dimension of l_1 of the MPS and of b_1 of the MPO. Without truncation in the SVD, the link dimension b_1 would add up for each time step. Note that the OC is multiplicated into the tensor containing n'_2 to proceed with the algorithm and maintain the gauge of the MPS. The tensor containing n'_2 now shares the link index l_2 with the tensor of the MPS containing n_3 and the link index b_2 with the tensor of the MPO containing n_3. In now contracting first over l_2, then b_2, then n_3 and decomposing the resulting tensor, the procedure is repeated until the end of the MPS is reached. The resulting MPS is then in left canonical gauge and has evolved to $|\psi(T_1 + \Delta t)\rangle$. In decreasing the prime level of all indices by one and in either shifting the OC back to the left side by series of SVD or performing the application of $U_I(\Delta t)$ from the right, the MPS is ready for the next time step.

Bibliography

[1] Belén Paredes, Artur Widera, Valentin Murg, Olaf Mandel, Simon Fölling, Ignacio Cirac, Gora V Shlyapnikov, Theodor W Hänsch, and Immanuel Bloch. Tonks–girardeau gas of ultracold atoms in an optical lattice. *Nature*, 429(6989):277, 2004.

[2] Maciej Lewenstein, Anna Sanpera, Veronica Ahufinger, Bogdan Damski, Aditi Sen, and Ujjwal Sen. Ultracold atomic gases in optical lattices: mimicking condensed matter physics and beyond. *Advances In Physics*, 56(2):243–379, 2007.

[3] Axel Friedenauer, Hector Schmitz, Jan Tibor Glueckert, Diego Porras, and Tobias Schätz. Simulating a quantum magnet with trapped ions. *Nature Physics*, 4(10):757, 2008.

[4] Rainer Blatt and Christian F Roos. Quantum simulations with trapped ions. *Nature Physics*, 8(4):277, 2012.

[5] Ulrich Schneider, Lucia Hackermüller, Jens Philipp Ronzheimer, Sebastian Will, Simon Braun, Thorsten Best, Immanuel Bloch, Eugene Demler, Stephan Mandt, David Rasch, et al. Fermionic transport and out-of-equilibrium dynamics in a homogeneous hubbard model with ultracold atoms. *Nature Physics*, 8(3):213, 2012.

[6] Jens Eisert, Mathis Friesdorf, and Christian Gogolin. Quantum many-body systems out of equilibrium. *Nature Physics*, 11(2):124, 2015.

[7] J Förstner, C Weber, J Danckwerts, and A Knorr. Phonon-assisted damping of rabi oscillations in semiconductor quantum dots. *Physical review letters*, 91(12):127401, 2003.

[8] A Vagov, VM Axt, T Kuhn, W Langbein, Paola Borri, and U Woggon. Non-monotonous temperature dependence of the initial decoherence in quantum dots. *Physical Review B*, 70(20):201305, 2004.

[9] M Richter, A Carmele, S Butscher, Norbert Bücking, F Milde, Peter Kratzer, Matthias Scheffler, and Andreas Knorr. Two-dimensional electron gases: Theory of ultrafast dynamics of electron-phonon interactions in graphene, surfaces, and quantum wells. *Journal of Applied Physics*, 105(12):122409, 2009.

[10] J. I. Cirac and P. Zoller. Quantum computations with cold trapped ions. *Phys. Rev. Lett.*, 74:4091–4094, May 1995.

[11] J Ignacio Cirac and Peter Zoller. Goals and opportunities in quantum simulation. *Nature Physics*, 8(4):264, 2012.

[12] Marcos Rigol, Vanja Dunjko, and Maxim Olshanii. Thermalization and its mechanism for generic isolated quantum systems. *Nature*, 452(7189):854, 2008.

[13] Adam M. Kaufman, M. Eric Tai, Alexander Lukin, Matthew Rispoli, Robert Schittko, Philipp M. Preiss, and Markus Greiner. Quantum thermalization through entanglement in an isolated many-body system. *Science*, 353(6301):794–800, 2016.

[14] Rahul Nandkishore and David A Huse. Many-body localization and thermalization in quantum statistical mechanics. *Annu. Rev. Condens. Matter Phys.*, 6(1):15–38, 2015.

[15] Mark Srednicki. Chaos and quantum thermalization. *Phys. Rev. E*, 50:888–901, Aug 1994.

[16] Dmitry A Abanin, Ehud Altman, Immanuel Bloch, and Maksym Serbyn. Ergodicity, entanglement and many-body localization. *arXiv preprint arXiv:1804.11065*, 2018.

[17] Charles H Bennett and David P DiVincenzo. Quantum information and computation. *Nature*, 404(6775):247, 2000.

[18] P. W. Anderson. Absence of diffusion in certain random lattices. *Phys. Rev.*, 109:1492–1505, Mar 1958.

[19] Aart Lagendijk, Bart Van Tiggelen, and Diederik S Wiersma. Fifty years of anderson localization. *Phys. Today*, 62(8):24–29, 2009.

[20] D.M. Basko, I.L. Aleiner, and B.L. Altshuler. Metal–insulator transition in a weakly interacting many-electron system with localized single-particle states. *Annals of Physics*, 321(5):1126 – 1205, 2006.

[21] Vadim Oganesyan and David A. Huse. Localization of interacting fermions at high temperature. *Phys. Rev. B*, 75:155111, Apr 2007.

[22] Marko Žnidarič, Tomaž Prosen, and Peter Prelovšek. Many-body localization in the heisenberg xxz magnet in a random field. *Phys. Rev. B*, 77:064426, Feb 2008.

[23] Jens H. Bardarson, Frank Pollmann, and Joel E. Moore. Unbounded growth of entanglement in models of many-body localization. *Phys. Rev. Lett.*, 109:017202, Jul 2012.

[24] Bela Bauer and Chetan Nayak. Area laws in a many-body localized state and its implications for topological order. *Journal of Statistical Mechanics: Theory and Experiment*, 2013(09):P09005, 2013.

[25] Guifré Vidal. Efficient classical simulation of slightly entangled quantum computations. *Physical review letters*, 91(14):147902, 2003.

[26] Steven R White. Density matrix formulation for quantum renormalization groups. *Physical review letters*, 69(19):2863, 1992.

[27] Frank Verstraete, Juan J Garcia-Ripoll, and Juan Ignacio Cirac. Matrix product density operators: Simulation of finite-temperature and dissipative systems. *Physical review letters*, 93(20):207204, 2004.

[28] Steven R White and Adrian E Feiguin. Real-time evolution using the density matrix renormalization group. *Physical review letters*, 93(7):076401, 2004.

[29] Ulrich Schollwöck. The density-matrix renormalization group in the age of matrix product states. *Annals of Physics*, 326(1):96–192, 2011. January 2011 Special Issue.

[30] E. Altman and R. Vosk. Universal Dynamics and Renormalization in Many-Body-Localized Systems. *Annual Review of Condensed Matter Physics*, 6:383–409, March 2015.

[31] Michael Schreiber, Sean S. Hodgman, Pranjal Bordia, Henrik P. Lüschen, Mark H. Fischer, Ronen Vosk, Ehud Altman, Ulrich Schneider, and Immanuel Bloch. Observation of many-body localization of interacting fermions in a quasirandom optical lattice. *Science*, 349(6250):842–845, 2015.

[32] J. Smith, A. Lee, P. Richerme, B. Neyenhuis, P. W. Hess, P. Hauke, M. Heyl, D. A. Huse, and C. Monroe. Many-body localization in a quantum simulator with programmable random disorder. *Nat Phys*, 12:907–911, jun 2016.

[33] Pranjal Bordia, Henrik P. Lüschen, Sean S. Hodgman, Michael Schreiber, Immanuel Bloch, and Ulrich Schneider. Coupling identical one-dimensional many-body localized systems. *Phys. Rev. Lett.*, 116:140401, Apr 2016.

[34] Henrik P Lüschen, Pranjal Bordia, Sean S Hodgman, Michael Schreiber, Saubhik Sarkar, Andrew J Daley, Mark H Fischer, Ehud Altman, Immanuel Bloch, and Ulrich Schneider. Signatures of many-body localization in a controlled open quantum system. *Physical Review X*, 7(1):011034, 2017.

[35] Pedro Ponte, Z Papić, François Huveneers, and Dmitry A Abanin. Many-body localization in periodically driven systems. *Physical review letters*, 114(14):140401, 2015.

[36] Achilleas Lazarides, Arnab Das, and Roderich Moessner. Fate of many-body localization under periodic driving. *Physical review letters*, 115(3):030402, 2015.

[37] Dmitry A Abanin, Wojciech De Roeck, and François Huveneers. Theory of many-body localization in periodically driven systems. *Annals of Physics*, 372:1–11, 2016.

[38] Achilleas Lazarides, Arnab Das, and Roderich Moessner. Equilibrium states of generic quantum systems subject to periodic driving. *Physical Review E*, 90(1):012110, 2014.

[39] Luca D'Alessio and Marcos Rigol. Long-time behavior of isolated periodically driven interacting lattice systems. *Physical Review X*, 4(4):041048, 2014.

[40] Vedika Khemani, Achilleas Lazarides, Roderich Moessner, and Shivaji L Sondhi. Phase structure of driven quantum systems. *Physical review letters*, 116(25):250401, 2016.

[41] Dominic V Else, Bela Bauer, and Chetan Nayak. Floquet time crystals. *Physical review letters*, 117(9):090402, 2016.

[42] J Zhang, PW Hess, A Kyprianidis, P Becker, A Lee, J Smith, G Pagano, I-D Potirniche, Andrew C Potter, A Vishwanath, et al. Observation of a discrete time crystal. *Nature*, 543(7644):217, 2017.

[43] Soonwon Choi, Joonhee Choi, Renate Landig, Georg Kucsko, Hengyun Zhou, Junichi Isoya, Fedor Jelezko, Shinobu Onoda, Hitoshi Sumiya, Vedika Khemani, et al. Observation of discrete time-crystalline order in a disordered dipolar many-body system. *Nature*, 543(7644):221, 2017.

[44] Jared Rovny, Robert L Blum, and Sean E Barrett. Observation of discrete-time-crystal signatures in an ordered dipolar many-body system. *Physical review letters*, 120(18):180603, 2018.

[45] Soham Pal, Naveen Nishad, TS Mahesh, and GJ Sreejith. Temporal order in periodically driven spins in star-shaped clusters. *Physical review letters*, 120(18):180602, 2018.

[46] Rahul Nandkishore, Sarang Gopalakrishnan, and David A. Huse. Spectral features of a many-body-localized system weakly coupled to a bath. *Phys. Rev. B*, 90:064203, Aug 2014.

[47] Sonika Johri, Rahul Nandkishore, and R. N. Bhatt. Many-body localization in imperfectly isolated quantum systems. *Phys. Rev. Lett.*, 114:117401, Mar 2015.

[48] Emanuele Levi, Markus Heyl, Igor Lesanovsky, and Juan P. Garrahan. Robustness of many-body localization in the presence of dissipation. *Phys. Rev. Lett.*, 116:237203, Jun 2016.

[49] Mariya V. Medvedyeva, Tomaž Prosen, and Marko Žnidarič. Influence of dephasing on many-body localization. *Phys. Rev. B*, 93:094205, Mar 2016.

[50] Mark H Fischer, Mykola Maksymenko, and Ehud Altman. Dynamics of a many-body-localized system coupled to a bath. *Phys. Rev. Lett.*, 116:160401, Apr 2016.

[51] Howard J Carmichael and Marlan O Scully. Statistical methods in quantum optics 1: master equations and fokker-planck equations. *Physics Today*, 53(3):78, 2000.

[52] Crispin Gardiner and Peter Zoller. *Quantum noise: a handbook of Markovian and non-Markovian quantum stochastic methods with applications to quantum optics*, volume 56. Springer Science & Business Media, 2004.

[53] H.P. Breuer and F. Petruccione. *The Theory of Open Quantum Systems*. OUP Oxford, 2007.

[54] Hannes Pichler and Peter Zoller. Photonic Circuits with Time Delays and Quantum Feedback. *Phys. Rev. Lett.*, 116:093601, 3 2016.

[55] John B Parkinson and Damian JJ Farnell. *An introduction to quantum spin systems*, volume 816. Springer, 2010.

[56] Gerald D Mahan. *Many-particle physics*. Springer Science & Business Media, 2013.

[57] Florian Scheck. *Theoretische Physik 3*. Springer, 2006.

[58] William Henry Louisell and William H Louisell. *Quantum statistical properties of radiation*, volume 7. Wiley New York, 1973.

[59] M. O. Scully and S. Zubairy. *Quantum Optics*. Cambridge University Press, 2008.

[60] F. Schwabl. *Quantenmechanik für Fortgeschrittene (QM II)*. Springer-Lehrbuch. Springer, 2008.

[61] David J Griffiths. Introduction to electrodynamics, 2005.

[62] Hermann Haken. *Quantenfeldtheorie des Festkörpers*. Springer-Verlag, 2013.

[63] Claude Cohen-Tannoudji, Jacques Dupont-Roc, and Gilbert Grynberg. Atom-photon interactions: basic processes and applications. *pp. 678. ISBN 0-471-29336-9. Wiley-VCH, March 1998.*, page 678, 1998.

[64] Peter Zoller and Crispin W Gardiner. Quantum noise in quantum optics: the stochastic schrödinger equation. *arXiv preprint quant-ph/9702030*, 1997.

[65] H. Carmichael. *Statistical Methods in Quantum Optics 2: Non-Classical Fields*. Theoretical and Mathematical Physics. Springer, 2008.

[66] Thomas Deck. *Der Itô-Kalkül: Einführung und Anwendungen*. Springer-Verlag, 2005.

[67] J. M. Deutsch. Quantum statistical mechanics in a closed system. *Phys. Rev. A*, 43:2046–2049, Feb 1991.

[68] Mark Srednicki. The approach to thermal equilibrium in quantized chaotic systems. *Journal of Physics A: Mathematical and General*, 32(7):1163, 1999.

[69] Luca D'Alessio, Yariv Kafri, Anatoli Polkovnikov, and Marcos Rigol. From quantum chaos and eigenstate thermalization to statistical mechanics and thermodynamics. *Advances in Physics*, 65(3):239–362, 2016.

[70] P Jordan and Eugene P Wigner. About the pauli exclusion principle. *Z. Phys*, 47(631):14–75, 1928.

[71] Arijeet Pal and David A. Huse. Many-body localization phase transition. *Phys. Rev. B*, 82:174411, Nov 2010.

[72] Maksym Serbyn, Z. Papić, and Dmitry A. Abanin. Local conservation laws and the structure of the many-body localized states. *Phys. Rev. Lett.*, 111:127201, Sep 2013.

[73] Alexander Carmele, Markus Heyl, Christina Kraus, and Marcello Dalmonte. Stretched exponential decay of majorana edge modes in many-body localized kitaev chains under dissipation. *Phys. Rev. B*, 92:195107, Nov 2015.

[74] Maksym Serbyn, Z Papić, and Dmitry A Abanin. Universal slow growth of entanglement in interacting strongly disordered systems. *Physical review letters*, 110(26):260601, 2013.

[75] David A Huse, Rahul Nandkishore, and Vadim Oganesyan. Phenomenology of fully many-body-localized systems. *Physical Review B*, 90(17):174202, 2014.

[76] John Z Imbrie, Valentina Ros, and Antonello Scardicchio. Local integrals of motion in many-body localized systems. *Annalen der Physik*, 529(7):1600278, 2017.

[77] Frank Pollmann, Vedika Khemani, J Ignacio Cirac, and SL Sondhi. Efficient variational diagonalization of fully many-body localized hamiltonians. *Physical Review B*, 94(4):041116, 2016.

[78] John Z Imbrie. On many-body localization for quantum spin chains. *Journal of Statistical Physics*, 163(5):998–1048, 2016.

[79] M. Goihl, M. Gluza, C. Krumnow, and J. Eisert. Construction of exact constants of motion and effective models for many-body localized systems. *Phys. Rev. B*, 97:134202, Apr 2018.

[80] H. Haken. *Licht und Materie II*. B. I. Wissenschaftsverlag, Mannheim, 1994.

[81] Weng W. Chow, Stephan W. Koch, and Murray III Sargent. *Semiconductor-Laser Physics*. Springer-Verlag Berlin Heidelberg, 1994.

[82] Jacob B. Khurgin. Viewpoint: Phonon lasers gain a sound foundation. *Physics*, 3:16, 2010.

[83] Vahala K., Herrmann M., Knunz S., Batteiger V., Saathoff G., Hansch T. W., and Udem Th. A phonon laser. *Nat Phys*, 5(9):682–686, sep 2009.

[84] J. T. Mendonça, H. Terças, G. Brodin, and M. Marklund. A phonon laser in ultra-cold matter. *EPL (Europhysics Letters)*, 91(3):33001, 2010.

[85] Ivan S. Grudinin, Hansuek Lee, O. Painter, and Kerry J. Vahala. Phonon laser action in a tunable two-level system. *Phys. Rev. Lett.*, 104:083901, 2 2010.

[86] K. V. Kepesidis, S. D. Bennett, S. Portolan, M. D. Lukin, and P. Rabl. Phonon cooling and lasing with nitrogen-vacancy centers in diamond. *Phys. Rev. B*, 88:064105, 8 2013.

[87] I. Mahboob, K. Nishiguchi, A. Fujiwara, and H. Yamaguchi. Phonon lasing in an electromechanical resonator. *Phys. Rev. Lett.*, 110:127202, 3 2013.

[88] I. Camps, S. S. Makler, H. M. Pastawski, and L. E. F. Foa Torres. $GaAs-al_xga_{1-x}As$. *Phys. Rev. B*, 64:125311, 9 2001.

[89] H. C. Liu, C. Y. Song, Z. R. Wasilewski, A. J. SpringThorpe, J. C. Cao, C. Dharma-wardana, G. C. Aers, D. J. Lockwood, and J. A. Gupta. Coupled electron-phonon modes in optically pumped resonant intersubband lasers. *Phys. Rev. Lett.*, 90:077402, Feb 2003.

[90] R. P. Beardsley, A. V. Akimov, M. Henini, and A. J. Kent. Coherent terahertz sound amplification and spectral line narrowing in a stark ladder superlattice. *Phys. Rev. Lett.*, 104:085501, 2 2010.

[91] Julia Kabuss, Alexander Carmele, Tobias Brandes, and Andreas Knorr. Optically driven quantum dots as source of coherent cavity phonons: A proposal for a phonon laser scheme. *Phys. Rev. Lett.*, 109:054301, Jul 2012.

[92] Julia Kabuss, Alexander Carmele, and Andreas Knorr. Threshold behavior and operating regimes of an optically driven phonon laser: Semiclassical theory. *Phys. Rev. B*, 88:064305, Aug 2013.

[93] Nicolas L. Naumann, Leon Droenner, Weng W. Chow, Julia Kabuss, and Alexander Carmele. Solid-state-based analog of optomechanics. *J. Opt. Soc. Am. B*, 33(7):1492–1501, 7 2016.

[94] M. Trigo, A. Bruchhausen, A. Fainstein, B. Jusserand, and V. Thierry-Mieg. Confinement of Acoustical Vibrations in a Semiconductor Planar Phonon Cavity. *Phys. Rev. Lett.*, 89:227402, 11 2002.

[95] N. D. Lanzillotti-Kimura, A. Fainstein, C. A. Balseiro, and B. Jusserand. Phonon engineering with acoustic nanocavities: Theoretical considerations on phonon molecules, band structures, and acoustic Bloch oscillations. *Phys. Rev. B*, 75:024301, 1 2007.

[96] N.D. Lanzillotti-Kimura, A. Fainstein, and B. Jusserand. Towards GHz–THz cavity optomechanics in DBR-based semiconductor resonators. *Ultrasonics*, 56(0):80–89, 2015.

[97] G. Rozas, M. F. Pascual Winter, B. Jusserand, A. Fainstein, B. Perrin, E. Semenova, and A. Lemaître. Lifetime of THz Acoustic Nanocavity Modes. *Phys. Rev. Lett.*, 102:015502, 1 2009.

[98] Ö. O. Soykal, Rusko Ruskov, and Charles Tahan. Sound-based analogue of cavity quantum electrodynamics in silicon. *Phys. Rev. Lett.*, 107:235502, Nov 2011.

[99] A. Fainstein, N. D. Lanzillotti-Kimura, B. Jusserand, and B. Perrin. Strong Optical-Mechanical Coupling in a Vertical GaAs/AlAs Microcavity for Subterahertz Phonons and Near-Infrared Light. *Phys. Rev. Lett.*, 110:037403, 1 2013.

[100] S. Sauer, J. M. Daniels, D. E. Reiter, T. Kuhn, A. Vagov, and V. M. Axt. Lattice fluctuations at a double phonon frequency with and without squeezing: An exactly solvable model of an optically excited quantum dot. *Phys. Rev. Lett.*, 105:157401, Oct 2010.

[101] A. Krügel, V. M. Axt, and T. Kuhn. Back action of nonequilibrium phonons on the optically induced dynamics in semiconductor quantum dots. *Phys. Rev. B*, 73:035302, Jan 2006.

[102] Daniel Wigger, Thomas Czerniuk, Doris E Reiter, Manfred Bayer, and Tilmann Kuhn. Systematic study of the influence of coherent phonon wave packets on the lasing properties of a quantum dot ensemble. *New Journal of Physics*, 19(7):073001, 2017.

[103] T. Czerniuk, D. Wigger, A. V. Akimov, C. Schneider, M. Kamp, S. Höfling, D. R. Yakovlev, T. Kuhn, D. E. Reiter, and M. Bayer. Picosecond control of quantum dot laser emission by coherent phonons. *Phys. Rev. Lett.*, 118:133901, Mar 2017.

[104] Michael Tavis and Frederick W. Cummings. Exact Solution for an *N*-Molecule-Radiation-Field Hamiltonian. *Phys. Rev.*, 170:379–384, 6 1968.

[105] Marten Richter, Michael Gegg, T. Sverre Theuerholz, and Andreas Knorr. Numerically exact solution of the many emitter–cavity laser problem: Application to the fully quantized spaser emission. *Phys. Rev. B*, 91:035306, Jan 2015.

[106] R. H. Dicke. Coherence in Spontaneous Radiation Processes. *Phys. Rev.*, 93:99–110, 1 1954.

[107] H. A. M. Leymann, A. Foerster, F. Jahnke, J. Wiersig, and C. Gies. Sub- and Superradiance in Nanolasers. *Phys. Rev. Applied*, 4:044018, 10 2015.

[108] Wassilij Kopylov, Milan Radonjić, Tobias Brandes, Antun Balaž, and Axel Pelster. Dissipative two-mode Tavis-Cummings model with time-delayed feedback control. *Phys. Rev. A*, 92:063832, 12 2015.

[109] Yumian Su, Dieter Bimberg, Andreas Knorr, and Alexander Carmele. Collective light emission revisited: Reservoir induced coherence. *Phys. Rev. Lett.*, 110:113604, Mar 2013.

[110] Sam Genway, Weibin Li, Cenap Ates, Benjamin P. Lanyon, and Igor Lesanovsky. Generalized dicke nonequilibrium dynamics in trapped ions. *Phys. Rev. Lett.*, 112:023603, Jan 2014.

[111] Victor Ceban, Paolo Longo, and Mihai A. Macovei. Fast phonon dynamics of a nanomechanical oscillator due to cooperative effects. *Phys. Rev. A*, 95:023806, Feb 2017.

[112] S. Hong, R. Riedinger, I. Marinkovic, A. Wallucks, S. G. Hofer, R. A. Norte, M. Aspelmeyer, and S. Gröblacher. Hanbury Brown and Twiss interferometry of single phonons from an optomechanical resonator. *ArXiv e-prints*, June 2017.

[113] D. Ding, X. Yin, and B. Li. Sensing Coherent Phonons with Two-photon Interference. *ArXiv e-prints*, April 2017.

[114] Leon Droenner, Nicolas L. Naumann, Julia Kabuss, and Alexander Carmele. Collective enhancements in many-emitter phonon lasing. *Phys. Rev. A*, 96:043805, Oct 2017.

[115] Leon Droenner, Julia Kabuss, and Alexander Carmele. Quantum many-body correlations in collective phonon-excitations. In *Physics and Simulation of Optoelectronic Devices XXVI*, volume 10526, page 105260G. International Society for Optics and Photonics, 2018.

[116] Leon Droenner and Julia Kabuss. Theory of an optically driven quantum-dot phonon laser. In *Physics and Simulation of Optoelectronic Devices XXIII*, volume 9357, page 93570P. International Society for Optics and Photonics, 2015.

[117] S. Agarwal, S. M. Hashemi Rafsanjani, and J. H. Eberly. Tavis-cummings model beyond the rotating wave approximation: Quasidegenerate qubits. *Phys. Rev. A*, 85:043815, Apr 2012.

[118] Dieter Bimberg, Marius Grundmann, and Nikolai N. Ledentsov. *Quantum Dot Heterostructures*. John Wiley & Sons, 1999.

[119] P. Michler. *Single Quantum Dots: Fundamentals, Applications and New Concepts*. Physics and Astronomy Online Library. Springer, 2003.

[120] Frank Jahnke. *Quantum optics with semiconductor nanostructures*. Elsevier, 2012.

[121] Marc-Oliver Pleinert, Joachim von Zanthier, and Girish S Agarwal. Hyperradiance from collective behavior of coherently driven atoms. *Optica*, 4(7):779–785, 2017.

[122] Michael Gegg, Alexander Carmele, Andreas Knorr, and Marten Richter. Superradiant to subradiant phase transition in the open system dicke model: Dark state cascades. *New Journal of Physics*, 20(1):013006, 2018.

[123] Subir Sachdev. *Quantum phase transitions.* Cambridge university press, 2011.

[124] J. W. Britton, B. C. Sawyer, A. C. Keith, C.-C. J. Wang, J. K. Freericks, H. Uys, M. J. Biercuk, and J. J. Bollinger. Engineered two-dimensional Ising interactions in a trapped-ion quantum simulator with hundreds of spins. *Nature*, 484(7395):489–492, apr 2012.

[125] R. Islam, C. Senko, W. C. Campbell, S. Korenblit, J. Smith, A. Lee, E. E. Edwards, C.-C. J. Wang, J. K. Freericks, and C. Monroe. Emergence and frustration of magnetism with variable-range interactions in a quantum simulator. *Science*, 340(6132):583–587, 2013.

[126] P. Richerme, Z. Gong, A. Lee, C. Senko, J. Smith, M. Foss-Feig, S. Michalakis, A. V. Gorshkov, and C. Monroe. Non-local propagation of correlations in quantum systems with long-range interactions. *Nature*, 511(7508):198–201, jul 2014.

[127] P. Jurcevic, B. P. Lanyon, P. Hauke, C. Hempel, P. Zoller, R. Blatt, and C. F. Roos. Quasiparticle engineering and entanglement propagation in a quantum many-body system. *Nature*, 511(7508):202–205, jul 2014.

[128] Brian Neyenhuis, Jiehang Zhang, Paul W. Hess, Jacob Smith, Aaron C. Lee, Phil Richerme, Zhe-Xuan Gong, Alexey V. Gorshkov, and Christopher Monroe. Observation of prethermalization in long-range interacting spin chains. *Science Advances*, 3(8), 2017.

[129] P. Jurcevic, H. Shen, P. Hauke, C. Maier, T. Brydges, C. Hempel, B. P. Lanyon, M. Heyl, R. Blatt, and C. F. Roos. Direct observation of dynamical quantum phase transitions in an interacting many-body system. *Phys. Rev. Lett.*, 119:080501, Aug 2017.

[130] Anders W. Sandvik. Ground states of a frustrated quantum spin chain with long-range interactions. *Phys. Rev. Lett.*, 104:137204, Mar 2010.

[131] Lorenzo Cevolani, Giuseppe Carleo, and Laurent Sanchez-Palencia. Protected quasilocality in quantum systems with long-range interactions. *Phys. Rev. A*, 92:041603, Oct 2015.

[132] A. Bermudez, L. Tagliacozzo, G. Sierra, and P. Richerme. Long-range heisenberg models in quasiperiodically driven crystals of trapped ions. *Phys. Rev. B*, 95:024431, Jan 2017.

[133] Philipp Hauke and Markus Heyl. Many-body localization and quantum ergodicity in disordered long-range ising models. *Phys. Rev. B*, 92:134204, Oct 2015.

[134] Alexander L. Burin. Many-body delocalization in a strongly disordered system with long-range interactions: Finite-size scaling. *Phys. Rev. B*, 91:094202, Mar 2015.

[135] N. Y. Yao, C. R. Laumann, S. Gopalakrishnan, M. Knap, M. Müller, E. A. Demler, and M. D. Lukin. Many-body localization in dipolar systems. *Phys. Rev. Lett.*, 113:243002, Dec 2014.

[136] K. Saito. Strong evidence of normal heat conduction in a one-dimensional quantum system. *EPL (Europhysics Letters)*, 61(1):34, 2003.

[137] Hannu Wichterich, Markus J. Henrich, Heinz-Peter Breuer, Jochen Gemmer, and Mathias Michel. Modeling heat transport through completely positive maps. *Phys. Rev. E*, 76:031115, Sep 2007.

[138] Marko Žnidarič. Spin transport in a one-dimensional anisotropic heisenberg model. *Phys. Rev. Lett.*, 106:220601, May 2011.

[139] Tomaž Prosen. Open *xxz* spin chain: Nonequilibrium steady state and a strict bound on ballistic transport. *Phys. Rev. Lett.*, 106:217206, May 2011.

[140] D. Karevski, V. Popkov, and G. M. Schütz. Exact matrix product solution for the boundary-driven lindblad *xxz* chain. *Phys. Rev. Lett.*, 110:047201, Jan 2013.

[141] V. Popkov, D. Karevski, and G. M. Schütz. Driven isotropic heisenberg spin chain with arbitrary boundary twisting angle: Exact results. *Phys. Rev. E*, 88:062118, Dec 2013.

[142] Gabriel T. Landi and Dragi Karevski. Open heisenberg chain under boundary fields: A magnonic logic gate. *Phys. Rev. B*, 91:174422, May 2015.

[143] Cécile Monthus. Dissipative random quantum spin chain with boundary-driving and bulk-dephasing: magnetization and current statistics in the non-equilibrium-steady-state. *Journal of Statistical Mechanics: Theory and Experiment*, 2017(4):043302, 2017.

[144] Giuliano Benenti, Giulio Casati, Tomaž Prosen, and Davide Rossini. Negative differential conductivity in far-from-equilibrium quantum spin chains. *EPL (Europhysics Letters)*, 85(3):37001, 2009.

[145] Giuliano Benenti, Giulio Casati, Tomaž Prosen, Davide Rossini, and Marko Žnidarič. Charge and spin transport in strongly correlated one-dimensional quantum systems driven far from equilibrium. *Phys. Rev. B*, 80:035110, Jul 2009.

[146] Marko Žnidarič. Transport in a one-dimensional isotropic heisenberg model at high temperature. *Journal of Statistical Mechanics: Theory and Experiment*, 2011(12):P12008, 2011.

[147] Tomaž Prosen. Exact nonequilibrium steady state of a strongly driven open *xxz* chain. *Phys. Rev. Lett.*, 107:137201, Sep 2011.

[148] Marko Žnidarič, Antonello Scardicchio, and Vipin Kerala Varma. Diffusive and subdiffusive spin transport in the ergodic phase of a many-body localizable system. *Physical review letters*, 117(4):040601, 2016.

[149] Kartiek Agarwal, Sarang Gopalakrishnan, Michael Knap, Markus Müller, and Eugene Demler. Anomalous diffusion and griffiths effects near the many-body localization transition. *Phys. Rev. Lett.*, 114:160401, Apr 2015.

[150] Robin Steinigeweg, Jacek Herbrych, Frank Pollmann, and Wolfram Brenig. Typicality approach to the optical conductivity in thermal and many-body localized phases. *Phys. Rev. B*, 94:180401, Nov 2016.

[151] Yevgeny Bar Lev, Guy Cohen, and David R. Reichman. Absence of diffusion in an interacting system of spinless fermions on a one-dimensional disordered lattice. *Phys. Rev. Lett.*, 114:100601, Mar 2015.

[152] David J. Luitz, Nicolas Laflorencie, and Fabien Alet. Extended slow dynamical regime close to the many-body localization transition. *Phys. Rev. B*, 93:060201, Feb 2016.

[153] Ilia Khait, Snir Gazit, Norman Y. Yao, and Assa Auerbach. Spin transport of weakly disordered heisenberg chain at infinite temperature. *Phys. Rev. B*, 93:224205, Jun 2016.

[154] Romain Vasseur and Joel E Moore. Nonequilibrium quantum dynamics and transport: from integrability to many-body localization. *Journal of Statistical Mechanics: Theory and Experiment*, 2016(6):064010, 2016.

[155] Leon Droenner, Nicolas Naumann, Markus Heyl, and Alexander Carmele. Spin transport in a lindblad-driven isotropic quantum heisenberg spin-chain. In *Physics and Simulation of Optoelectronic Devices XXV*, volume 10098, page 100980O. International Society for Optics and Photonics, 2017.

[156] Leon Droenner and Alexander Carmele. Boundary-driven heisenberg chain in the long-range interacting regime: Robustness against far-from-equilibrium effects. *Phys. Rev. B*, 96:184421, Nov 2017.

[157] Paul Heitjans and Jörg Kärger. *Diffusion in Condensed Matter—Methods, Materials, Models.* Berlin: Springer, 2005.

[158] David J. Luitz, Nicolas Laflorencie, and Fabien Alet. Many-body localization edge in the random-field heisenberg chain. *Phys. Rev. B*, 91:081103, Feb 2015.

[159] Jeremy L. O'Brien. Optical Quantum Computing. *Science*, 318:1567–1570, 2007.

[160] Thomas Jennewein, Christoph Simon, Gregor Weihs, Harald Weinfurter, and Anton Zeilinger. Quantum cryptography with entangled photons. *Phys. Rev. Lett.*, 84:4729–4732, 5 2000.

[161] Mackillo Kira and Stephan W Koch. *Semiconductor quantum optics.* Cambridge University Press, 2011.

[162] B. Darquié, M. P. A. Jones, J. Dingjan, J. Beugnon, S. Bergamini, Y. Sortais, G. Messin, A. Browaeys, and P. Grangier. Controlled single-photon emission from a single trapped two-level atom. *Science*, 309(5733):454–456, 2005.

[163] A. J. Shields. Semiconductor quantum light sources. *Nat Photon*, 1(4):215–223, 4 2007.

[164] V. A. Gaisler. Single-photon emitters based on semiconductor nanostructures. *Bulletin of the Russian Academy of Sciences: Physics*, 73(1):77–79, 2009.

[165] Sonia Buckley, Kelley Rivoire, and Jelena Vučković. Engineered quantum dot single-photon sources. *Reports on Progress in Physics*, 75(12):126503, 2012.

[166] Heinze Dirk, Breddermann Dominik, Zrenner Artur, and Schumacher Stefan. A quantum dot single-photon source with on-the-fly all-optical polarization control and timed emission. *Nature Communications*, 6:8473, aug 2015.

[167] Clemens Matthiesen, Anthony Nickolas Vamivakas, and Mete Atatüre. Subnatural linewidth single photons from a quantum dot. *Phys. Rev. Lett.*, 108:093602, Feb 2012.

[168] AK Nowak, SL Portalupi, V Giesz, O Gazzano, C Dal Savio, P-F Braun, K Karrai, C Arnold, L Lanco, I Sagnes, et al. Deterministic and electrically tunable bright single-photon source. *Nature communications*, 5:3240, 2014.

[169] V Giesz, SL Portalupi, T Grange, C Antón, L De Santis, J Demory, N Somaschi, I Sagnes, A Lemaître, L Lanco, et al. Cavity-enhanced two-photon interference using remote quantum dot sources. *Physical Review B*, 92(16):161302, 2015.

[170] B. Lounis and W. E. Moerner. Single photons on demand from a single molecule at room temperature. *Nature*, 407:491–493, 2000.

[171] I.Aharonovich, D.Englund, and M.Toth. Solid-state single-photon emitters. *Nat Photon*, 10(10):631–641, 10 2016.

[172] Elena del Valle, Stefano Zippilli, Fabrice P. Laussy, Alejandro Gonzalez-Tudela, Giovanna Morigi, and Carlos Tejedor. Two-photon lasing by a single quantum dot in a high-q microcavity. *Phys. Rev. B*, 81:035302, Jan 2010.

[173] E del Valle, A Gonzalez–Tudela, E Cancellieri, F P Laussy, and C Tejedor. Generation of a two-photon state from a quantum dot in a microcavity. *New Journal of Physics*, 13(11):113014, 2011.

[174] P. R. Sharapova, K. H. Luo, H. Herrmann, M. Reichelt, C. Silberhorn, and T. Meier. Modified two-photon interference achieved by the manipulation of entanglement. *Phys. Rev. A*, 96:043857, Oct 2017.

[175] Alejandro Gonzalez-Tudela, Fabrice P Laussy, Carlos Tejedor, Michael J Hartmann, and Elena Del Valle. Two-photon spectra of quantum emitters. *New Journal of Physics*, 15(3):033036, 2013.

[176] L. Schneebeli, M. Kira, and S. W. Koch. Characterization of strong light-matter coupling in semiconductor quantum-dot microcavities via photon-statistics spectroscopy. *Phys. Rev. Lett.*, 101:097401, Aug 2008.

[177] Jahnke Frank, Gies Christopher, Aßmann Marc, Bayer Manfred, Leymann H. A. M., Foerster Alexander, Wiersig Jan, Schneider Christian, Kamp Martin, and Höfling Sven. Giant photon bunching, superradiant pulse emission and excitation trapping in quantum-dot nanolasers. *Nature Communications*, 7:11540, may 2016.

[178] Juan Camilo López Carreño, Elena Valle, and Fabrice P Laussy. Photon correlations from the mollow triplet. *Laser & Photonics Reviews*, 11(5), 2017.

[179] G Callsen, A Carmele, G Hönig, C Kindel, J Brunnmeier, MR Wagner, E Stock, JS Reparaz, A Schliwa, S Reitzenstein, et al. Steering photon statistics in single quantum dots: From one-to two-photon emission. *Physical Review B*, 87(24):245314, 2013.

[180] K. Pyragas. Analytical properties and optimization of time-delayed feedback control. *Phys. Rev. E*, 66:026207, 8 2002.

[181] Eckehard Schöll and Heinz Georg Schuster. *Handbook of Chaos Control*. Wiley-VCH, 2008.

[182] Eckehard Schöll, Sabine HL Klapp, and Philipp Hövel. *Control of self-organizing nonlinear systems*. Springer, 2016.

[183] R. Lang and K. Kobayashi. External optical feedback effects on semiconductor injection laser properties. *IEEE J. Quantum Electron.*, 16:347, 1980.

[184] Clement Sayrin, Igor Dotsenko, Xingxing Zhou, Bruno Peaudecerf, Theo Rybarczyk, Sebastien Gleyzes, Pierre Rouchon, Mazyar Mirrahimi, Hadis Amini, Michel Brune, Jean-Michel Raimond, and Serge Haroche. Real-time quantum feedback prepares and stabilizes photon number states. *Nature*, 477(7362):73–77, 9 2011.

[185] H. Wiseman and G. Milburn. *Quantum Measurement and Control*. Cambridge University Press, Oxford, 2006.

[186] Pavel Bushev, Daniel Rotter, Alex Wilson, François Dubin, Christoph Becher, Jürgen Eschner, Rainer Blatt, Viktor Steixner, Peter Rabl, and Peter Zoller. Feedback cooling of a single trapped ion. *Phys. Rev. Lett.*, 96:043003, Feb 2006.

[187] V. Sudhir, D. J. Wilson, R. Schilling, H. Schütz, S. A. Fedorov, A. H. Ghadimi, A. Nunnenkamp, and T. J. Kippenberg. Appearance and disappearance of quantum correlations in measurement-based feedback control of a mechanical oscillator. *Phys. Rev. X*, 7:011001, 1 2017.

[188] J. F. Poyatos, J. I. Cirac, and P. Zoller. Quantum reservoir engineering with laser cooled trapped ions. *Phys. Rev. Lett.*, 77:4728–4731, 12 1996.

[189] Heinz-Peter Breuer, Elsi-Mari Laine, Jyrki Piilo, and Bassano Vacchini. Colloquium. *Rev. Mod. Phys.*, 88:021002, 4 2016.

[190] Walter T. Strunz, Lajos Diósi, and Nicolas Gisin. Open System Dynamics with Non-Markovian Quantum Trajectories. *Phys. Rev. Lett.*, 82:1801–1805, 3 1999.

[191] Ángel Rivas, Susana F Huelga, and Martin B Plenio. Quantum non-markovianity: characterization, quantification and detection. *Reports on Progress in Physics*, 77(9):094001, 2014.

[192] A. Metelmann and A. A. Clerk. Nonreciprocal photon transmission and amplification via reservoir engineering. *Phys. Rev. X*, 5:021025, Jun 2015.

[193] Dmitry O. Krimer, Benedikt Hartl, and Stefan Rotter. Hybrid quantum systems with collectively coupled spin states: Suppression of decoherence through spectral hole burning. *Phys. Rev. Lett.*, 115:033601, Jul 2015.

[194] Chan U Lei and Wei-Min Zhang. A quantum photonic dissipative transport theory. *Annals of Physics*, 327(5):1408–1433, 2012.

[195] Arne L. Grimsmo. Time-Delayed Quantum Feedback Control. *Phys. Rev. Lett.*, 115:060402, 8 2015.

[196] Sven M. Hein, Franz Schulze, Alexander Carmele, and Andreas Knorr. Optical Feedback-Enhanced Photon Entanglement from a Biexciton Cascade. *Phys. Rev. Lett.*, 113:027401, 7 2014.

[197] Sven M. Hein, Franz Schulze, Alexander Carmele, and Andreas Knorr. Entanglement control in quantum networks by quantum-coherent time-delayed feedback. *Phys. Rev. A*, 91:052321, 5 2015.

[198] Manuel Kraft, Sven M. Hein, Judith Lehnert, Eckehard Schöll, Stephen Hughes, and Andreas Knorr. Time-delayed quantum coherent pyragas feedback control of photon squeezing in a degenerate parametric oscillator. *Phys. Rev. A*, 94:023806, 8 2016.

[199] Nikolett Német and Scott Parkins. Enhanced optical squeezing from a degenerate parametric amplifier via time-delayed coherent feedback. *Phys. Rev. A*, 94:023809, 8 2016.

[200] Nicolas L. Naumann, Sven M. Hein, Andreas Knorr, and Julia Kabuss. Steady-state control in an unstable optomechanical system. *Phys. Rev. A*, 90:043835, 10 2014.

[201] Nicolas L Naumann, Leon Droenner, Sven M Hein, Alexander Carmele, Andreas Knorr, and Julia Kabuss. Feedback control of optomechanical systems. In *Physics and Simulation of Optoelectronic Devices XXIV*, volume 9742, page 974216. International Society for Optics and Photonics, 2016.

[202] Ferdinand Albert, Caspar Hopfmann, Stephan Reitzenstein, Christian Schneider, Sven Höfling, Lukas Worschech, Martin Kamp, Wolfgang Kinzel, Alfred Forchel, and Ido Kanter. Observing chaos for quantum-dot microlasers with external feedback. *Nature Communications*, 2:366, 6 2011.

[203] C Hopfmann, F Albert, C Schneider, S Höfling, M Kamp, A Forchel, I Kanter, and S Reitzenstein. Nonlinear emission characteristics of quantum dot–micropillar lasers in the presence of polarized optical feedback. *New Journal of Physics*, 15(2):025030, 2013.

[204] C. Schön, E. Solano, F. Verstraete, J. I. Cirac, and M. M. Wolf. Sequential generation of entangled multiqubit states. *Phys. Rev. Lett.*, 95:110503, 9 2005.

[205] Pierre-Olivier Guimond, Hannes Pichler, Arno Rauschenbeutel, and Peter Zoller. Chiral quantum optics with v-level atoms and coherent quantum feedback. *Phys. Rev. A*, 94:033829, Sep 2016.

[206] Leon Droenner, Nicolas L Naumann, Andreas Knorr, and Alexander Carmele. Two-photon purification of quantum light emission via quantum feedback. *arXiv preprint arXiv:1801.03342*, 2018.

[207] S. Hughes. Coupled-cavity qed using planar photonic crystals. *Phys. Rev. Lett.*, 98:083603, Feb 2007.

[208] Yao-Lung L. Fang and Harold U. Baranger. Waveguide qed: Power spectra and correlations of two photons scattered off multiple distant qubits and a mirror. *Phys. Rev. A*, 91:053845, May 2015.

[209] U. Dorner and P. Zoller. Laser-driven atoms in half-cavities. *Phys. Rev. A*, 66:023816, 8 2002.

[210] N. Trautmann and G. Alber. Dissipation-enabled efficient excitation transfer from a single photon to a single quantum emitter. *Phys. Rev. A*, 93:053807, May 2016.

[211] Fabian M. Faulstich, Manuel Kraft, and Alexander Carmele. Unraveling mirror properties in time-delayed quantum feedback scenarios. *Journal of Modern Optics*, 0(0):1–9, 2017.

[212] Kevin A. Fischer, Lukas Hanschke, Jakob Wierzbowski, Tobias Simmet, Constantin Dory, Jonathan J. Finley, Jelena Vuckovic, and Kai Muller. Signatures of two-photon pulses from a quantum two-level system. *Nature Physics*, 13:649–654, 2017.

[213] J Lindkvist and G Johansson. Scattering of coherent pulses on a two-level system—single-photon generation. *New Journal of Physics*, 16(5):055018, 2014.

[214] Kevin A Fischer, Lukas Hanschke, Jonathan J Finley, Kai Müller, and Jelena Vučković. Pulsed rabi oscillations in quantum two-level systems: Beyond the area theorem. *arXiv preprint arXiv:1708.05444*, 2017.

[215] Andreas Wallraff, David I Schuster, Alexandre Blais, L Frunzio, R-S Huang, J Majer, S Kumar, Steven M Girvin, and Robert J Schoelkopf. Strong coupling of a single photon to a superconducting qubit using circuit quantum electrodynamics. *Nature*, 431(7005):162, 2004.

[216] Paul M Chaikin, Tom C Lubensky, and Thomas A Witten. *Principles of condensed matter physics*, volume 1. Cambridge university press Cambridge, 1995.

[217] Frank Wilczek. Quantum time crystals. *Physical review letters*, 109(16):160401, 2012.

[218] Tongcang Li, Zhe-Xuan Gong, Zhang-Qi Yin, HT Quan, Xiaobo Yin, Peng Zhang, L-M Duan, and Xiang Zhang. Space-time crystals of trapped ions. *Physical review letters*, 109(16):163001, 2012.

[219] Patrick Bruno. Impossibility of spontaneously rotating time crystals: a no-go theorem. *Physical review letters*, 111(7):070402, 2013.

[220] Haruki Watanabe and Masaki Oshikawa. Absence of quantum time crystals. *Physical review letters*, 114(25):251603, 2015.

[221] Curt W von Keyserlingk and Shivaji L Sondhi. Phase structure of one-dimensional interacting floquet systems. ii. symmetry-broken phases. *Physical Review B*, 93(24):245146, 2016.

[222] Curt W von Keyserlingk, Vedika Khemani, and Shivaji L Sondhi. Absolute stability and spatiotemporal long-range order in floquet systems. *Physical Review B*, 94(8):085112, 2016.

[223] Norman Y Yao, Andrew C Potter, I-D Potirniche, and Ashvin Vishwanath. Discrete time crystals: rigidity, criticality, and realizations. *Physical review letters*, 118(3):030401, 2017.

[224] Achilleas Lazarides and Roderich Moessner. Fate of a discrete time crystal in an open system. *Physical Review B*, 95(19):195135, 2017.

[225] David A. Huse, Rahul Nandkishore, Vadim Oganesyan, Arijeet Pal, and S. L. Sondhi. Localization-protected quantum order. *Phys. Rev. B*, 88:014206, Jul 2013.

[226] Sthitadhi Roy, Achilleas Lazarides, Markus Heyl, and Roderich Moessner. Dynamical potentials for nonequilibrium quantum many-body phases. *Phys. Rev. B*, 97:205143, May 2018.

[227] Younes Javanmard, Soumya Bera, and Markus Heyl. Accessing eigenstate spin-glass order from reduced density matrices. *arXiv preprint arXiv:1806.02571*, 2018.